

1-1-1989

# Kinematic models of cometary comae.

Lowell Evan Tacconi-Garman  
*University of Massachusetts Amherst*

Follow this and additional works at: [https://scholarworks.umass.edu/dissertations\\_1](https://scholarworks.umass.edu/dissertations_1)

---

## Recommended Citation

Tacconi-Garman, Lowell Evan, "Kinematic models of cometary comae." (1989). *Doctoral Dissertations 1896 - February 2014*. 1769.  
[https://scholarworks.umass.edu/dissertations\\_1/1769](https://scholarworks.umass.edu/dissertations_1/1769)

This Open Access Dissertation is brought to you for free and open access by ScholarWorks@UMass Amherst. It has been accepted for inclusion in Doctoral Dissertations 1896 - February 2014 by an authorized administrator of ScholarWorks@UMass Amherst. For more information, please contact [scholarworks@library.umass.edu](mailto:scholarworks@library.umass.edu).



312066007583108

KINEMATIC MODELS OF COMETARY COMAE

A Dissertation Presented

by

LOWELL EVAN TACCONI-GARMAN

Submitted to the Graduate School of the  
University of Massachusetts in partial fulfillment  
of the requirements for the degree of

DOCTOR OF PHILOSOPHY

May 1989

Department of Physics and Astronomy

©Copyright by Lowell Evan Tacconi-Garman 1989

All Rights Reserved

KINEMATIC MODELS OF COMETARY COMAE

A Dissertation Presented

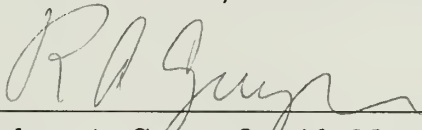
by

LOWELL EVAN TACCONI-GARMAN

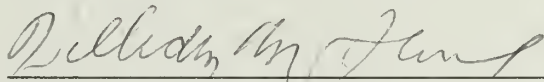
Approved as to style and content by:



F. Peter Schloerb, Committee Chairperson



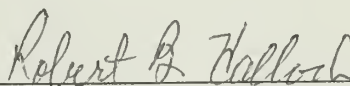
Robert A. Guyer, Outside Member



William M. Irvine, Member



David J. van Blerkom, Member



Robert B. Hallock, Department Head  
Department of Physics and Astronomy

## ACKNOWLEDGEMENTS

As I sit here on the couch at Pete, Holly, and Amy's house I am reminded of the incredible hospitality they have extended to me and Linda over the past several months. Finishing a thesis is not easy, especially when it is being done from another continent. Their acceptance of us as members of the family, however, has made the task infinitely easier and I thank them for that.

Of course, no thesis is completed without the guidance of an advisor and the rest of the committee. For such guidance and support I thank Pete, Bob, Bill, and David. Special thanks goes to two members of my committee, David and Pete. David did a great deal for me throughout the course of my graduate career, from teaching me of the splendors of the Monte Carlo method (which figures prominently in this thesis) to helping me through some rough times before I started this thesis. Pete also helped during those trying days in the best way possible, by taking me on as his student. I thank him for showing faith in me in the early stages of this work and continuing that faith throughout. In fact, in all modesty, the following quote from a biography of Linnaeus (the famous Swedish botanist) by Benjamin Daydon Jones seems particularly appropriate for Pete:

A professor can never better distinguish himself in his work than by encouraging a clever pupil, for the true discoverers are among them, as comets among the stars.

Which leads me to the subject of comets. Pete is also to be commended for

his ability to change my opinion about comets from the oft encountered “yeah, so what do you work on that’s *interesting*” to “how come more people don’t study these things?”.

In addition to my committee members, I thank the rest of the members of the faculty for, as I said at the beginning of my defense talk, making the past  $n$  years (where  $n$  is a large number) both productive and enlightening. Particular thanks goes to Judy Young for helping me through it all, showing me the joys of extragalactic research, and being a good friend. Thanks also to the postdocs, both past and present, for their support and entertainment. I especially thank Mark Claussen for his efforts in obtaining the data used in this thesis and for his helping me during my trips to Green Bank to observe Comet Wilson.

I also thank Mike Combi for driving out to Amherst from Boston for my defense talk. His work, both past and present, has played a critical role in the modeling and analysis of these cometary data. I thank him for allowing me to incorporate his most recent work, prior to its publication, into this thesis.

And then there are the graduate students. Without their companionship throughout the years I would have gone bonkers, and for saving me from that fate I thank you all. There are a few graduate students which deserve particular thanks. Pat Knezek has been a close friend since she entered UMass and has bailed Linda and me out by loaning us her car on more than one occasion. Billy (or is it William Howard?) Waller has provided countless

light moments over the years. I thank Jim Morgan and Alan Welty for their computer expertise. Without the assistance of Wayne Kinzel I would probably still be trying to reduce the Halley data. I also thank Dave and Denise Taylor for the numerous splendiferous dinners and outings which helped to relieve stresses and strains. Finally, I thank Lori Allen for the many interesting conversations, company in the computer room (boy, does she have great taste in music!), and for her help in the final stages of this thesis.

When I think of all the people who have helped me over the years I also think of Sally, Jackie, Denise, Susan, Barb, and Karen, that is, the crack crew of the FCRAO office (if I've left anyone out I'm terribly sorry). These folks have been a constant source of bemusement, and they are incredibly efficient! Jackie is to be particularly commended for her ability to keep funds flowing, her aid during our move to Holland, and her faithful addiction to her MacIntosh (which is always fun to watch).

Speaking of fun, I have especially enjoyed my trips to Paris during the past couple of years, courtesy of Pete. Not only have I found that city to be an extremely pleasant place to visit, but I have also found those trips to be very productive professionally. The reasons for this productivity are four astronomers at the observatory at Meudon, Eric Gérard, Jacques Crovisier, Dominique Bockelée-Morvan, and Pierre Colom. They have provided numerous suggestions for my work and have laid a lot of groundwork on which this thesis is based. For all their help I say, in my incredibly bad french accent, *merci*.



And while I am on the subject of european observatories, I would be remiss if I were to neglect thanking the astronomers and everyone else at the Radiosterrenwacht Dwingeloo for their kind hospitality during the completion of this thesis. They have allowed me the complete freedom and facilities to carry out this research and have made me feel very welcome. For all their help I say, in my (incredibly?) bad dutch accent, *dank u wel*.

Well, thus far I have mentioned several people who have played substantial roles in my years at UMass and in the completion of my thesis. My family, of course, also belongs on that list. My parents have been amazingly supportive and encouraging throughout my entire education, both undergraduate and graduate. Thanks, Mom and Dad! And the rest of my family, my brother Glenn, sister-in-law Linda, and nieces Sheena and Kaley, and my sister Beth have been equally encouraging and supportive (although at this stage in her life Kaley's means of being supportive is to eat her vegetables). I thank and love you all.

Finally, I love and thank Linda. She has been, and continues to be, a source of joy to me. She has offered me support, advice, love, friendship, and compassion. There is no doubt that I owe the completion of this thesis to her. It is for that reason, and everything else she has done for me, that I dedicate this thesis to her.

## ABSTRACT

### KINEMATIC MODELS OF COMETARY COMAE

MAY 1989

LOWELL EVAN TACCONI-GARMAN

B.S., RENSSELAER POLYTECHNIC INSTITUTE

Ph.D., UNIVERSITY OF MASSACHUSETTS

Directed by: Professor F. Peter Schloerb

As a first step towards understanding the kinematics of cometary comae we have undertaken an analysis of the 18-cm OH lines in comets. This work builds on past OH excitation and kinematic studies to meld them into a complete and self-consistent model for a cometary coma. We model the kinematics via the vectorial formalism and employ the powerful Monte Carlo technique in an effort to reproduce the high sensitivity, high spectral resolution 18-cm OH line profiles of Comets Halley, Giacobini-Zinner, Hartley-Good, Thiele, and Wilson which were obtained at the 43 meter telescope of the National Radio Astronomy Observatory at Green Bank, West Virginia. We have applied for the first time a "zeroth order"  $\Lambda$ -doublet quenching correction to the 18-cm data and find that we can account for the long standing UV/radio gas production rate disparity. We have derived gas expansion velocities and coma anisotropies from observations covering a wide range of heliocentric distances and gas production rates. The inferred ratio of dayside gas emission to nightside gas emission for all comets in this study,

except P/Giacobini-Zinner, is approximately two. This value is consistent with that derived from *in situ* observations of the neutral gas in the coma of Comet Halley and is independent of both gas productivity and heliocentric distance. For P/Giacobini-Zinner we infer anomalously high gas outflow anisotropies for which there is no clear explanation. The derived outflow velocities are consistent with those derived from a variety of other indicators of the coma expansion velocity and suggest that the gas production of a comet plays a critical role in determining the coma kinematics for active comets near the sun. We find, however, that the outflow velocities at large heliocentric distances are consistently lower than the predictions of one-dimensional coma dynamic models.

# TABLE OF CONTENTS

	Page
ACKNOWLEDGEMENTS .....	iv
ABSTRACT .....	viii
LIST OF TABLES .....	xii
LIST OF FIGURES .....	xiii
Chapter	
1 INTRODUCTION .....	1
1.1 Cometary Observations Old and New .....	1
1.2 Molecular Excitation in Comets .....	4
1.3 Coma Kinematics .....	9
1.4 The Present Work .....	12
2 THE DATA .....	15
2.1 Global and Local Observations .....	15
2.2 NRAO 18-cm Cometary Observations .....	16
2.3 The Epoch Average Spectra .....	24
2.4 Other Data Sets .....	60
3 THE KINEMATIC MODEL .....	64
3.1 A Comparison of Two Models .....	64
3.2 The Birth of the Parents (H <sub>2</sub> O Molecules) .....	68
3.3 The Death of the Parents .....	69
3.4 The Death of the Daughters (OH Radicals) .....	72
3.5 Parent Velocity Distribution .....	74
3.6 Parent Outflow Morphology .....	77
3.7 Daughter Velocity and Spatial Distributions .....	82
3.8 Inversion Weighting .....	84
3.9 Beam Weighting and Velocity Binning .....	85
4 MODEL RESULTS .....	89
4.1 Introduction .....	89
4.2 Gas Production Rates .....	90

4.3	The Model Results .....	94
4.3.1	General Remarks .....	94
4.3.2	AP Results .....	154
4.3.3	$V_p$ Results .....	162
5	SUMMARY .....	175
	BIBLIOGRAPHY .....	181

## LIST OF TABLES

	Page
2.1 Observations of Comet Halley .....	20
2.2 Observations of Comets Giacobini-Zinner, Hartley-Good, Thiele, and Wilson .....	22
2.3 Sun-Comet-Earth Geometry and Line Characteristics .....	59
4.1 Line Integrals and Production Rates for Comet Halley .....	95
4.2 Line Integrals and Production Rates for Comets Giacobini-Zinner, Hartley-Good, Thiele, and Wilson .....	96
4.3 Kinematic Model Results for Comet Halley .....	155
4.4 Kinematic Model Results for Comets Giacobini-Zinner, Hartley-Good, Thiele, and Wilson .....	156
5.1 Model Parameters .....	177

## LIST OF FIGURES

	Page
1.1	The detailed structure of the lowest rotational level of the ground electronic state of OH ..... 7
2.1a	The average 1667 MHz OH line from Comet Halley over the period 20–23 September 1985 ..... 25
2.1b	The average 1667 MHz OH line from Comet Halley over the period 19–21 October 1985 ..... 26
2.1c	The average 1667 MHz OH line from Comet Halley over the period 13–19 November 1985 ..... 27
2.1d	The average 1667 MHz OH line from Comet Halley over the period 10–12 December 1985 ..... 28
2.1e	The average 1667 MHz OH line from Comet Halley over the period 03–05 January 1986 ..... 29
2.1f	The average 1667 MHz OH line from Comet Halley over the period 18–20 February 1986 ..... 30
2.1g	The average 1667 MHz OH line from Comet Halley over the period 15–19 March 1986 ..... 31
2.1h	The average 1667 MHz OH line from Comet Halley over the period 03–05 May 1986 ..... 32
2.1i	The average 1667 MHz OH line from Comet Giacobini-Zinner over the period 10–11 July 1985 ..... 33
2.1j	The average 1667 MHz OH line from Comet Giacobini-Zinner over the period 24–26 August 1985 ..... 34
2.1k	The average 1667 MHz OH line from Comet Giacobini-Zinner over the period 19,21 October 1985 ..... 35
2.1l	The average 1667 MHz OH line from Comet Hartley-Good over the period 18–21 October 1985 ..... 36

2.1m	The average 1667 MHz OH line from Comet Hartley-Good over the period 12–17 November 1985 .....	37
2.1n	The average 1667 MHz OH line from Comet Thiele over the period 12,14–18 November 1985 .....	38
2.1o	The average 1667 MHz OH line from Comet Wilson over the period 28–30 March 1987 .....	39
2.1p	The average 1667 MHz OH line from Comet Wilson over the period 18–19 May 1987 .....	40
2.2a	The data of Figure 2.1a with the best fitting Gaussian curve (top), and the associated residuals (bottom) .....	42
2.2b	The data of Figure 2.1b with the best fitting Gaussian curve (top), and the associated residuals (bottom) .....	43
2.2c	The data of Figure 2.1c with the best fitting Gaussian curve (top), and the associated residuals (bottom) .....	44
2.2d	The data of Figure 2.1d with the best fitting Gaussian curve (top), and the associated residuals (bottom) .....	45
2.2e	The data of Figure 2.1e with the best fitting Gaussian curve (top), and the associated residuals (bottom) .....	46
2.2f	The data of Figure 2.1f with the best fitting Gaussian curve (top), and the associated residuals (bottom) .....	47
2.2g	The data of Figure 2.1g with the best fitting Gaussian curve (top), and the associated residuals (bottom) .....	48
2.2h	The data of Figure 2.1h with the best fitting Gaussian curve (top), and the associated residuals (bottom) .....	49
2.2i	The data of Figure 2.1i with the best fitting Gaussian curve (top), and the associated residuals (bottom) .....	50
2.2j	The data of Figure 2.1j with the best fitting Gaussian curve (top), and the associated residuals (bottom) .....	51
2.2k	The data of Figure 2.1k with the best fitting Gaussian curve (top), and the associated residuals (bottom) .....	52



2.2l	The data of Figure 2.1l with the best fitting Gaussian curve (top), and the associated residuals (bottom) .....	53
2.2m	The data of Figure 2.1m with the best fitting Gaussian curve (top), and the associated residuals (bottom) .....	54
2.2n	The data of Figure 2.1n with the best fitting Gaussian curve (top), and the associated residuals (bottom) .....	55
2.2o	The data of Figure 2.1o with the best fitting Gaussian curve (top), and the associated residuals (bottom) .....	56
2.2p	The data of Figure 2.1p with the best fitting Gaussian curve (top), and the associated residuals (bottom) .....	57
2.3	In this figure we have plotted the Full Width at Half Maximum (FWHM) of the OH lines used in this thesis as a function of heliocentric distance .....	61
3.1	A flow diagram for the model used in this work .....	66
3.2	The coordinate systems used in our modeling .....	78
3.3	The Earth-Sun-Comet geometry .....	87
4.1	Comparison of radio and UV gas production rates .....	97
4.2a	The $\chi^2_{\nu}$ surfaces derived from model fits to the September 1985 P/Halley spectrum .....	100
4.2b	The $\chi^2_{\nu}$ surfaces derived from model fits to the October 1985 P/Halley spectrum .....	101
4.2c	The $\chi^2_{\nu}$ surfaces derived from model fits to the November 1985 P/Halley spectrum .....	102
4.2d	The $\chi^2_{\nu}$ surfaces derived from model fits to the December 1985 P/Halley spectrum .....	103
4.2e	The $\chi^2_{\nu}$ surfaces derived from model fits to the January 1986 P/Halley spectrum .....	104
4.2f	The $\chi^2_{\nu}$ surfaces derived from model fits to the February 1986 P/Halley spectrum .....	105

4.2g	The $\chi^2_\nu$ surfaces derived from model fits to the March 1986 P/Halley spectrum .....	106
4.2h	The $\chi^2_\nu$ surfaces derived from model fits to the May 1986 P/Halley spectrum .....	107
4.2i	The $\chi^2_\nu$ surfaces derived from model fits to the July 1985 P/Giacobini-Zinner spectrum .....	108
4.2j	The $\chi^2_\nu$ surfaces derived from model fits to the August 1985 P/Giacobini-Zinner spectrum .....	109
4.2k	The $\chi^2_\nu$ surfaces derived from model fits to the October 1985 P/Giacobini-Zinner spectrum .....	110
4.2l	The $\chi^2_\nu$ surfaces derived from model fits to the October 1985 P/Hartley-Good spectrum .....	111
4.2m	The $\chi^2_\nu$ surfaces derived from model fits to the November 1985 P/Hartley-Good spectrum .....	112
4.2n	The $\chi^2_\nu$ surfaces derived from model fits to the November 1985 C/Thiele spectrum .....	113
4.2o	The $\chi^2_\nu$ surfaces derived from model fits to the March 1987 C/Wilson spectrum .....	114
4.2p	The $\chi^2_\nu$ surfaces derived from model fits to the May 1987 C/Wilson spectrum .....	115
4.3a	A representative sample of model spectra generated using the Despois inversion curve superimposed on the spectrum of P/Halley from September 1985 .....	117
4.3b	A representative sample of model spectra generated using the Despois inversion curve superimposed on the spectrum of P/Halley from October 1985 .....	118
4.3c	A representative sample of model spectra generated using the Despois inversion curve superimposed on the spectrum of P/Halley from November 1985 .....	119

4.3d	A representative sample of model spectra generated using the Despois inversion curve superimposed on the spectrum of P/Halley from December 1985 .....	120
4.3e	A representative sample of model spectra generated using the Despois inversion curve superimposed on the spectrum of P/Halley from January 1986 .....	121
4.3f	A representative sample of model spectra generated using the Despois inversion curve superimposed on the spectrum of P/Halley from February 1986 .....	122
4.3g	A representative sample of model spectra generated using the Despois inversion curve superimposed on the spectrum of P/Halley from March 1986 .....	123
4.3h	A representative sample of model spectra generated using the Despois inversion curve superimposed on the spectrum of P/Halley from May 1986 .....	124
4.3i	A representative sample of model spectra generated using the Despois inversion curve superimposed on the spectrum of P/Giacobini-Zinner from July 1985 .....	125
4.3j	A representative sample of model spectra generated using the Despois inversion curve superimposed on the spectrum of P/Giacobini-Zinner from August 1985 .....	126
4.3k	A representative sample of model spectra generated using the Despois inversion curve superimposed on the spectrum of P/Giacobini-Zinner from October 1985 .....	127
4.3l	A representative sample of model spectra generated using the Despois inversion curve superimposed on the spectrum of C/Hartley-Good from October 1985 .....	128
4.3m	A representative sample of model spectra generated using the Despois inversion curve superimposed on the spectrum of C/Hartley-Good from November 1985 .....	129
4.3n	A representative sample of model spectra generated using the Despois inversion curve superimposed on the spectrum of C/Thiele from November 1985 .....	130

4.3o	A representative sample of model spectra generated using the Despois inversion curve superimposed on the spectrum of C/Wilson from March 1987 .....	131
4.3p	A representative sample of model spectra generated using the Despois inversion curve superimposed on the spectrum of C/Wilson from May 1987 .....	132
4.4a	A representative sample of model spectra generated using the inversion curve of SA superimposed on the spectrum of P/Halley from September 1985 .....	133
4.4b	A representative sample of model spectra generated using the inversion curve of SA superimposed on the spectrum of P/Halley from October 1985 .....	134
4.4c	A representative sample of model spectra generated using the inversion curve of SA superimposed on the spectrum of P/Halley from November 1985 .....	135
4.4d	A representative sample of model spectra generated using the inversion curve of SA superimposed on the spectrum of P/Halley from December 1985 .....	136
4.4e	A representative sample of model spectra generated using the inversion curve of SA superimposed on the spectrum of P/Halley from January 1986 .....	137
4.4f	A representative sample of model spectra generated using the inversion curve of SA superimposed on the spectrum of P/Halley from February 1986 .....	138
4.4g	A representative sample of model spectra generated using the inversion curve of SA superimposed on the spectrum of P/Halley from March 1986 .....	139
4.4h	A representative sample of model spectra generated using the inversion curve of SA superimposed on the spectrum of P/Halley from May 1986 .....	140
4.4i	A representative sample of model spectra generated using the inversion curve of SA superimposed on the spectrum of P/Giacobini-Zinner from July 1985 .....	141

4.4j	A representative sample of model spectra generated using the inversion curve of SA superimposed on the spectrum of P/Giacobini-Zinner from August 1985 .....	142
4.4k	A representative sample of model spectra generated using the inversion curve of SA superimposed on the spectrum of P/Giacobini-Zinner from October 1985 .....	143
4.4l	A representative sample of model spectra generated using the inversion curve of SA superimposed on the spectrum of C/Hartley-Good from October 1985 .....	144
4.4m	A representative sample of model spectra generated using the inversion curve of SA superimposed on the spectrum of C/Hartley-Good from November 1985 .....	145
4.4n	A representative sample of model spectra generated using the inversion curve of SA superimposed on the spectrum of C/Thiele from November 1985 .....	146
4.4o	A representative sample of model spectra generated using the inversion curve of SA superimposed on the spectrum of C/Wilson from March 1987 .....	147
4.4p	A representative sample of model spectra generated using the inversion curve of SA superimposed on the spectrum of C/Wilson from May 1987 .....	148
4.5	The May 1985 P/Halley spectrum (top) and relevant portions of the Despois and SA inversion curves (bottom) .....	151
4.6	The Despois and SA inversion curves .....	152
4.7	The difference between AP and $V_P$ values derived using the Despois and SA inversion curves .....	153
4.8	Adopted AP values as a function of heliocentric distance .....	158
4.9	Adopted AP values as a function of the Log of the derived gas production rate .....	159
4.10	Adopted parent gas outflow velocity as a function of heliocentric distance .....	163

4.11	Comparison of adopted $V_P$ values and other indicators of the coma gas expansion velocity .....	164
4.12	Adopted parent gas outflow velocity as a function of the log of the gas production rate .....	170
4.13	Outflow velocity as a function of the log of the gas production rate and heliocentric distance .....	171
4.14	Comparison of derived parent gas outflow velocities with the dusty-gas-dynamic/Monte Carlo modeling predictions .....	173

# CHAPTER 1

## INTRODUCTION

### 1.1 Cometary Observations Old and New

Comets have been observed since antiquity. Evidence for this comes from both verbal and nonverbal records left behind by many cultures. Indeed, amongst the most complete of these ancient cometary records are those appearing in the *Chin-shu*, a history of China's Chin Dynasty (265–460 A.D.) which was compiled in 644 A.D. by the members of the *T'ai-ch'ang* (the "Astronomical Bureau") (Clark and Stephenson 1977). These accounts, however accurate they were, were primarily phenomenological in nature with little insight into the scientific significance of comets. This astronomical importance eluded humankind, especially in the West, for many centuries following the writing of the *Chin-shu*, and as a result, the apparitions of comets were frequently viewed as omens of disastrous events.

It was Tycho Brahe who began to lift the veil of folklore from comets. By not finding any sign of diurnal parallax in his carefully taken cometary position data, he determined that comets were not the atmospheric phenomena they were believed to be. In fact, his measurements placed the comets beyond the Moon (Harwit 1981). Some 130 years later, Edmund Halley made a prediction, based on the then new theory of gravitation, that the comets of 1531, 1607, and 1682 were actually the same comet reappearing. Furthermore,

he forecast the return of that comet for 1759. When Halley's Comet (as it came to be known) actually did appear in December of 1758, it became clear that comets were nothing more than celestial bodies obeying the same physical laws as all other bodies. Thereafter, the mystery and legend surrounding comets gradually faded (Harwit 1981). (One should note, though, that there was still enough superstition surrounding comets during the 1973 apparition of Comet Kohoutek to make a number of charlatans profit from the sales of books which predicted disasters (Abell 1982)!)

Since the appearance of Halley's Comet in 1758–1759 much progress has been made in our understanding of comets. Three major breakthroughs in cometary science came in the 1950's. The first of these was in the study of the location of comets. Oort (1950) advanced a theory, based on the work of Öpik (1932) and van Woerkom (1948), which entailed a "general cloud" of some  $10^{11}$  comets at distances of 50,000 to 150,000 A.U. from the sun. He also postulated that perturbations from passing stars could cause comets in this cloud to enter the inner solar system. This has since become the most widely accepted theory on the origin of comets (*cf.* Bailey, Clube, and Napier 1986). The second advancement in our understanding of comets is the now generally accepted "dirty snowball" model for the nucleus of a comet (Whipple 1950, 1951, 1955; see also Whipple 1976). This model explains, amongst other things, the non-gravitational motions observed for most comets. The last major contribution to the study of comets to come from that decade was that of Biermann (1951),



who suggested that a solar wind was responsible for the morphology and kinematics of the ion tails of comets. This is now also generally accepted, and in many ways, the 1950's can be viewed as the decade when modern cometary science was born.

Since that time many new observational techniques have played ever increasing roles in determining the nature of comets (for a comprehensive review of the recent progress in UV and IR cometary astronomy see Spinrad 1987 and references therein). In particular, within the last 10 years or so a great deal of new and interesting information on the physical processes and kinematics of cometary comae has come from the theoretical and observational work on the radio lines of OH. This new information by itself is interesting and important in its applications to the problem of molecular abundances in the coma. Almost all ground based cometary molecular abundance studies rely on kinematic information derived from models of the comae. Therefore, it is the purpose of this thesis to build on the past observational and theoretical studies and derive a consistent kinematic model for the cometary coma.

The past work on which this thesis is based breaks naturally into two categories, studies of the excitation of the OH molecules in comets and studies of the kinematics of the coma gas. These two subjects are taken up in the following two sections. In Section 1.4 we discuss the impetus for this project and give an outline of the problem.

## 1.2 Molecular Excitation in Comets

The study of the excitation of molecules in the comae of comets is not a new one. Early this century astronomers began to try to understand the mechanism responsible for producing the observed molecular lines. For example, Fowler (1910) ascribed the illumination of the coma and tail of a comet to “negatively charged particles issuing either from the head of a comet or from the Sun”. Another method of illuminating the tail of a comet was suggested by Deslandres (1909). He noticed the similarity between the spectrum of Comet Morehouse (1908 III) and a terrestrial auroral display and inferred from this that both phenomena could be explained if the sun emitted “kathode [*sic.*] rays.” Lastly, Newall (as cited in Fowler 1910) evoked a mechanism of rapidly moving dust particles travelling through the gasses of interplanetary space to provide the tail luminosity.

About the same time that these theories were proposed, Schwarzschild and Kron (1911) suggested that the molecular band emission could be caused by a fluorescence phenomenon stimulated by the absorption of solar radiation. Subsequently, this theory was formalized (Zanstra 1928, Wurm 1934a, b) and was subjected to two tests. Öhman (1941) determined that the degree of polarization in the C<sub>2</sub> and CN bands of Comets Cunningham (1941 I) and De Kock-Paraskevopoulos (1941 IV) were what was to be expected for a coma in which the molecular energy level populations are governed strictly by fluorescence (*i.e.* pure fluorescence equilibrium). The more stringent test,

however, was done by McKellar (1942, 1943) and Swings (1943). These authors found that by using the solar ultraviolet spectrum *appropriately shifted by a heliocentric velocity correction* in a pure fluorescence calculation they could reproduce the CN band profiles for a number of comets to reasonable precision; this marked the end for the corpuscular theories of comet excitation. This heliocentric velocity dependence of the excitation of cometary molecules, now known as the Swings effect, also applies in the case of the excitation of other molecules in the coma including the subject of this work, OH.

A second order excitation effect was first noted by Greenstein (1958) in his observations of the violet (0,0) band of CN in Comet Mrkos (1957 V). What seemed unusual to him at the time was that the ratios of certain lines in the P- and R-branches (*e.g.* R10/R9, P3/P5) changed from the east side of the coma to the west side. At the time of his observations Comet Mrkos was situated such that east was roughly tailward and west was roughly sunward. Thus, the best explanation for the line ratio differences was that there was gas travelling towards the sun in the west and in an antisunward direction in the east. This differential motion with respect to the sun led to a *differential* Swings effect across the coma. This phenomenon, now called the Greenstein effect, also plays a role in the excitation of the radio lines of OH.

Specifically, in the case of the excitation of the OH molecules in the coma, the absorption of photons of one of a dozen wavelengths of solar ultraviolet radiation (Mies 1974, see also below) excites the molecule from the

X  $^2\Pi_{3/2}$  ground electronic state to the A  $^2\Sigma_{1/2}^+$  state. Subsequent cascading via ultraviolet and infrared emission (the IR cascading occurs between the vibrational levels of the X  $^2\Pi_{3/2}$  state) returns the molecules to the X  $^2\Pi_{3/2}$  state. Since the timescale for this cascading is much shorter (of order  $10^{-6}$  sec) than for the excitation of the molecules (either via collisions or radiatively (Mies 1974)) most of the molecules occupy the lowest rotational level of the ground electronic state (X  $^2\Pi_{3/2}$  J=3/2) (*cf.* Schleicher and A'Hearn 1988).

A closer examination of this X  $^2\Pi_{3/2}$  state reveals that each of its rotational energy levels is split into two levels. This splitting, called  $\Lambda$ -doubling, is due to the interaction of the component of the electronic orbital angular momentum which lies along the internuclear axis and the angular momentum due to the molecular rotation (see Herzberg 1950 for further details). Further splitting of these  $\Lambda$ -doublet levels arises from the hyperfine interaction of the magnetic moment of the molecule with the spin of the hydrogen nucleus. Thus, the X  $^2\Pi_{3/2}$  J=3/2 level actually consists of 4 levels, shown in Figure 1.1 which are connected by transitions at 1667, 1665, 1720, and 1612 MHz, the 18-cm lines of OH.

The intensity of the 18-cm emission depends on a number of factors, including the population in the ground rotational state. The depletion of that state is controlled primarily by the rate of UV excitation to the A  $^2\Sigma_{1/2}^+$  state (Schleicher and A'Hearn 1988). Owing to the many Fraunhofer lines in the solar UV spectrum, the  $\Lambda$ -doublet levels of the ground rotational state are

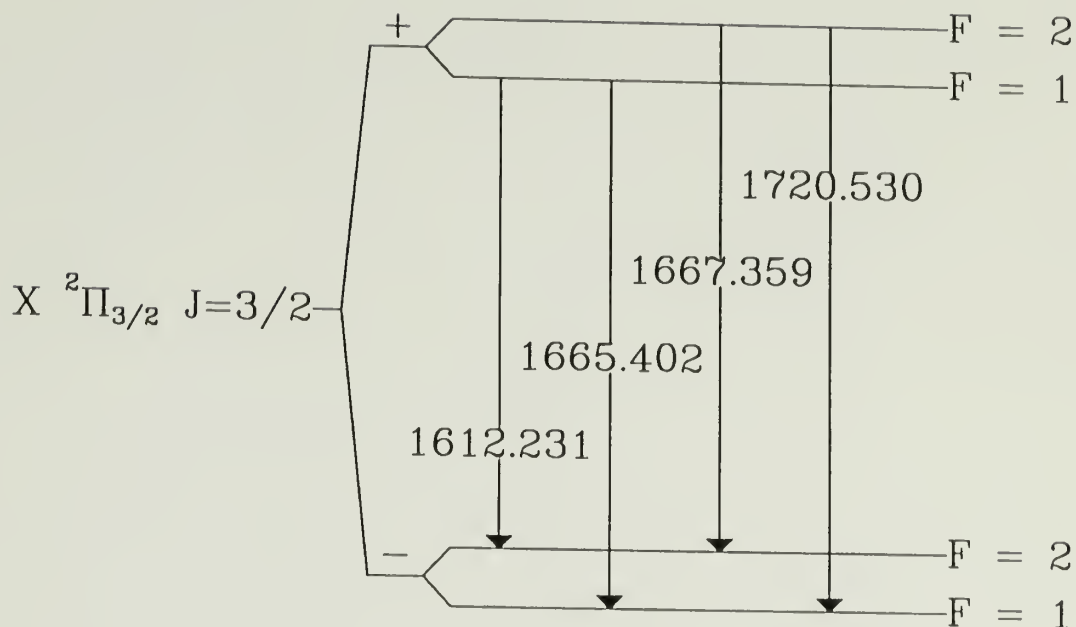


**Figure 1.1:** The detailed structure of the lowest rotational level of the ground electronic state of OH. The level is split due to  $\Lambda$ -doubling (these levels are labelled  $+/-$  for the parity). Each of these levels is further split due to the hyperfine interaction arising from the spin of the hydrogen nucleus. These hyperfine levels are labelled by their total angular momentum quantum number, while the 18-cm transitions of OH are shown as arrows. The numbers on these arrows indicate the transition frequency, in MHz.

selectively pumped. Moreover, since the solar spectrum exhibits extremely fine structure in the vicinity of the major pumping lines, small variations in the velocity of the comet, which lead to Doppler shifting of the incident solar radiation, result in large differences in the rate at which these levels are pumped (Schleicher and A'Hearn 1982, 1988). Thus the intensity of the 18-cm lines is a strong function of the heliocentric velocity of the comet. In a quantitative sense, this concept is usually expressed through the inversion parameter,  $i$ , which is a function of the heliocentric velocity and is defined to be

$$i = \frac{n_u - n_l}{n_u + n_l},$$

where  $n_{u(l)}$  represents the population in the upper (lower) state of the hyperfine transition. Using this nomenclature, when  $i$  is positive there are more molecules in the upper level of the transition (*i.e.* the population is inverted) and the coma will act as an amplifying maser for the background. When  $i$  is negative, on the other hand, the molecules in the coma are anti-inverted and the coma will be seen in absorption against the 2.7K (microwave) background.

A number of authors have calculated theoretical values for the inversion, either at specific heliocentric velocities (Mies 1974) or for a run of heliocentric velocities (plots of inversion as a function of heliocentric velocity are known as inversion curves; Biraud *et al.* 1974; Despois *et al.* 1981; Elitzur 1981; Schleicher and A'Hearn 1982, 1988). There is general agreement among their

results and between the theoretical predictions and the observations, although some minor differences continue to exist.

### 1.3 Coma Kinematics

Aside from excitation studies, much work has gone into theoretical coma kinematic models and the interpretation of 18-cm OH cometary data in light of such models. The basic outcome of the theoretical effort are two models for the propagation of molecules in the coma.

The first of these models, proposed and subsequently named for Haser (1957, 1966), is a pure radial flow scheme. In this picture the parent molecules leave the nucleus and proceed away radially until they are dissociated. From that point the daughter molecules *continue* to flow radially away from the nucleus. While this model is quite analytically tractable, it does fall short when one uses it to predict line profiles and parent scalelengths.

Despois *et al.* (1981) were the first to calculate what one would expect to see for 18-cm line profiles given the pure radial flow of the Haser model. These profiles, which ranged from box-like to double-peaked depending on the extent to which the coma was resolved by the beam (see also Schloerb and Gérard 1985), were clearly different from their observed profiles although they stopped short of making any statement to that effect, instead citing insufficient spectral resolution. Later, Bockelée-Morvan and Gérard (1984) made direct comparisons of their higher resolution spectra of comets C/Meier (1978 XXI)

and C/Austin (1982g) with theoretical Haser model spectra. Their conclusion was that the data could exclude the Haser model in the case of monokinetic parents, though for other parent velocity distributions the case against the Haser model was less clear.

A difficulty in using the Haser model arises in the deduction of parent scale lengths from radial brightness distributions. From the molecular lifetime data of Potter and Del Duca (1964), Stief, De Carlo, and Mataloni (1965), and Stief (1966) and measured outflow velocities one infers size scales of order  $10^4$ – $10^5$  km for the inner (parent species dominated) coma. Such dimensions are typically larger than those determined by employing the Haser model to observed radial brightness distributions of radicals in the coma (Combi and Smyth 1988a). Since the daughter molecules are likely to be produced isotropically from their parents (see below) rather than radially, the scale lengths deduced from the analysis of cometary brightness profiles in light of the Haser model are not the true scale lengths, but the *radial projections* of the true scale lengths (Combi and Delsemme 1980a). Combi and Delsemme further note that one can use the Haser model to determine true coma gas scale lengths providing the ratio of the parent and daughter velocities is known.

Lastly, it is physically unrealistic to expect the photodissociation products of a parent molecule to continue travelling through the coma in the same direction as their parent, *i.e.* radially, as the Haser model envisions.



Rather, isotropic ejection of the offspring molecules *in the rest frame of the parent* seems more physically plausible.

The second kinematic model used to describe the gas flow in cometary comae is the vectorial model. In this model, which was independently proposed by Combi and Delsemme (1980a) and Festou (1981a), each daughter molecule is released in a random direction from its parent, with an equal probability of being released into any solid angle. At the time of the photodissociation, any excess energy the photon might have is converted into kinetic energy of the offspring molecules. This additional velocity is added *vectorially* to the original parent velocity to produce the final daughter velocity.

Monte Carlo applications of this model (see Combi and Delsemme 1980a and Chapter 3) have been used successfully in a number of studies. Combi and Delsemme (1980a) demonstrated that a photometric profile of such species as CN and C<sub>2</sub> without the effect of radiation pressure can be generated from averages of sunward and tailward profiles as was assumed by Delsemme and Moreau (1973) (see also Combi and Delsemme 1980b and Combi 1980 for further applications of this technique). Bockelée-Morvan and Gérard (1984) have used the vectorial model in Monte Carlo calculations of synthetic spectra which closely resemble their data from C/Meier, C/Bradfield (1979 X), and C/Austin. Lastly, Combi and Smyth (1988b) have used a Monte Carlo vectorial model in conjunction with a simple gas dynamical model to

explain the observed morphology of the Lyman  $\alpha$  coma of Comet Kohoutek (1973 XII).

#### 1.4 The Present Work

Understanding the nucleus of a comet is, of course, one of the ultimate goals of cometary science. However, in the absence of direct probes a necessary step in attaining this understanding is to comprehend the workings of the surrounding coma. With the recent apparition of Halley's Comet came an unprecedented surge of cometary observations, coordinated by the International Halley Watch, covering a broad range of wavelengths. As participants in this global project, we have made high sensitivity, high spectral resolution observations of the 18-cm lines of OH in Comets Halley, Giacobini-Zinner, Hartley-Good, Thiele, and, more recently, Comet Wilson. These data have served as the impetus for the kinematic modeling performed for this thesis, as they are the best cometary OH radio data ever taken. Therefore, the major thrust of the present work is to build on the past OH excitation and kinematic studies to meld them into a complete and selfconsistent kinematic model of a cometary comae, using our OH radio data as an observational backbone.

The comparison data base is by no means limited to single dish 18-cm OH data. On the contrary, it also includes the HCN data from P/Halley of Schloerb *et al.* (1986a) which also exhibit good pre- and post-perihelion

coverage and which have been useful in constraining parent molecular velocities. Additional constraints on the parent outflow velocities have come from the infrared observations of H<sub>2</sub>O in Halley's Comet (Larson *et al.* 1986; Mumma *et al.* 1986). The VLA observations of the 18-cm lines of OH from C/Austin (1982 VI) and P/Crommelin (1983n)(Schenewerk *et al.* 1986) as well as from Comet Halley (de Pater, Palmer, and Snyder 1986) have been useful for outflow morphology comparison purposes (*cf.* Schloerb 1988). The list of data sources presented here, however, is not complete (see Chapter 2 for a comprehensive summary).

As a further guide in this modelling effort we have also used the results of some previous theoretical studies (in addition to those already mentioned). Both Festou (1981b) and Crovisier (1988) have studied the velocity distribution of the OH and H offspring which are created during the photodissociation of H<sub>2</sub>O. As a benchmark for the parent outflow velocities we have used the results of one dimensional hydrodynamic calculations for the gas flow in the inner coma (Crovisier 1984, 1987; see also Combi 1989). These results have also been used to demonstrate the predicted behavior of this outflow velocity as a function of the total gas production rate of a comet. Lastly, and perhaps most importantly, the framework of our kinematic model code comes from the work of Combi and Delsemme (1980a), who were the first to suggest the implementation of the Monte Carlo technique for the vectorial scheme.

The problem to be addressed by this work is to describe, through a model, the kinematics of cometary comae as a function of the heliocentric distance and gas production rate of the comet. To this end, we will investigate two key properties of the coma gas flow, the parent gas outflow velocity and the sunward/antisunward outflow distribution. The determination of correct parent outflow velocities is an important contribution to cometary science as a whole, since most studies aimed at determining coma molecular abundances rely on these velocities (and molecular lifetimes) to correct the observations for the effects of resolution (see Feldman 1982; Schloerb, Claussen, and Tacconi-Garman 1986). Estimates of the coma gas flow anisotropy from the analysis of radio OH data from comets have been and will continue to be useful for comparisons with 2- and perhaps 3-dimensional models of the coma (*e.g.* Kitamura 1986, 1987). Such models attempt to describe the gas and dust flow in the coma using physical parameters for the nucleus as an inner boundary condition. Thus, indirectly, estimates of the coma gas flow morphology may lead to a better understanding of the underlying cometary nucleus.

In the following chapter, we describe the data sets which have been used to constrain and compare with the model results. Chapter 3 contains a complete description of the modelling technique, from the input parameters through the workings of the code itself and finally to the output at the other end. Chapter 4 details the results of our analysis, while Chapter 5 contains a summary and concluding remarks.

## CHAPTER 2

### THE DATA

#### 2.1 Global and Local Observations

During its most recent journey into the inner solar system Halley's Comet was greeted with an unparalleled worldwide observational effort as ground based telescopes from around the world were trained on this famous comet. In addition, for the first time, spacecraft were sent to make *in situ* observations of the comet. The product of all these observations is a grand data archive which is presently being compiled by the International Halley Watch (Newburn 1983; Irvine, Schloerb, and Gérard 1983) and is due for release to the scientific community in the fall of 1990.

The contributions of the cometary studies group at the University of Massachusetts<sup>1</sup> to this archive include the data collected during our program to monitor Comet Halley in the 18-cm transition of OH. These observations were conducted at the 43-meter telescope of the National Radio Astronomy Observatory (NRAO) in Green Bank, West Virginia<sup>2</sup>. This thesis presents primarily the model analysis of these data. During the monitoring program, however, other comets presented themselves as viable observational sources and some of this data also has been included in the analysis (see Chapter 4).

---

<sup>1</sup>This group includes, in alphabetical order, M.J. Claussen (currently at the Naval Research Laboratory in Washington, D.C.), W. Ge, W.M. Irvine, W.M. Kinzel, F.P. Schloerb, D.A. Swade (presently at Computer Sciences Corporation), and L.E. Tacconi-Garman.

<sup>2</sup>NRAO is operated by Associated Universities, Inc., under contract with the National Science Foundation.

Finally, our successes with the Halley observations have given us the impetus to continue observing bright comets from that site (whenever possible); our data from Comet Wilson attest to the quality of the 43-meter antenna and its associated instrumentation (model results for these data also appear in Chapter 4). Our observational technique while at NRAO is detailed in the following section. In Section 2.3 we present the data themselves and discuss their general properties. Finally, the last section contains a discussion of the other data sets which have been helpful in guiding our choice of model parameters and in evaluating the validity of our model results.

## 2.2 NRAO 18-cm Cometary Observations

The observations of the 18-cm radiation from Comet Halley reported here were obtained between September 1985 and May 1986 using the 43-meter telescope of the NRAO. During this period we had eight observing sessions, with each session lasting from 3 to 7 days. In addition, we observed Comet Wilson on two separate occasions, one in March 1987 and the other in May 1987. We have modeled these data as well as some of the spectra from Comets Giacobini-Zinner, Hartley-Good, and Thiele obtained during the Halley monitoring project.

During all of the sessions, we simultaneously made observations of the  $^2\Pi_{3/2}$   $J=3/2$   $F=2-2$  transition at 1667 MHz and the  $^2\Pi_{3/2}$   $J=3/2$   $F=1-1$  transition at 1665 MHz. During the November 1985 observing run, when the

1667 and 1665 MHz emission from Halley was particularly strong, we also made observations of the  ${}^2\Pi_{3/2}$   $J=3/2$   $F=2-1$  transition at 1720 MHz for purposes of determining the 1665/1720 and 1667/1720 hyperfine ratios as probes of the excitation conditions in the coma. Such an excitation analysis is only marginally possible given the quality of the 1720 MHz data and is not germane to the present work. At all frequencies, we observed both right- and left-circularly polarized (RCP and LCP) emission. Because any net polarization which might be present in these data is extremely weak (see *e.g.* Gérard 1985), we routinely present and model the combined RCP + LCP data. Furthermore, since the certainty of our kinematic modeling results depends directly upon the signal to noise ratio of the data, we have chosen to model only the 1667 MHz line, the strongest of the hyperfine lines.

The 43 meter telescope was equipped with a dual-channel, FET amplifier (except for the May 1987 observations of C/Wilson which were made with a HEMT amplifier) which receives orthogonal linear polarizations and mixes them in the IF to produce right- and left-circular polarizations. The system temperature with the FET amplifier was typically  $\gtrsim 25$  K, while that obtained with the HEMT amplifier was  $\sim 28$  K (since these observations were made at low elevations, this includes a contribution from ground pickup).

Using Right Ascension and Declination scans through 3C286, we determined the half-power beamwidth (HPBW) of this telescope to be  $18'.0$  at 18-cm wavelength. Therefore, the physical dimension of this beam at the

distances of the comets observed ranges from  $0.38 \times 10^6$  to  $3.35 \times 10^6$  km (see Tables 2.1 and 2.2). Telescope pointing was checked periodically during each observing run by observing 3C286. Pointing was determined to be accurate to within  $\sim \text{HPBW}/100$ , thus system related pointing errors are not considered to be a problem. Cometary positions for each observing session were generated using the most contemporary cometary orbital elements as input to the ephemeris generation programs EPHGEN (EPHemeris GENERator) and TBEG (Two-Body Ephemeris Generator) written by M.S.W. Keesey and D.K. Yeomans and distributed by the International Halley Watch. These positions and the topocentric velocity of the comets (the velocity with respect to a particular position on the surface of the Earth) were updated every 9 minutes. The position shifts of the comets over this time interval were typically only 2–4% of the HPBW. Therefore, the smearing of the source over the beam is negligible. The velocity shifts over this same interval were  $\lesssim 0.02 \text{ km sec}^{-1}$  ( $\lesssim 1/10$  channel, see below), making spectral smearing of no concern.

The 18-cm data were obtained by frequency switching the signal in the backends (see below) by 45, 78, or 90 kHz. The choice of frequency shift was made to ensure that we did not overlap the signal and reference profiles; the larger shifts were used at times when the line was anticipated to be broad. Calibration was achieved by observing the standard radio source 3C286 which was assumed to have a constant flux density of 13.6 Jy at 18-cm (Baars *et al.* 1977). The sensitivity of this system was typically  $0.33 \text{ K Jy}^{-1}$ ; checks on the



Notes for Table 2.1:

<sup>1</sup>Geocentric (Earth-Comet) distance

<sup>2</sup>Heliocentric (Sun-Comet) distance and heliocentric velocity

<sup>3</sup>Phase (Sun-Comet-Earth) angle

<sup>4</sup>Physical dimension of the beam at the distance of the comet

Table 2.1 Observations of Comet Halley						
Epoch	$\Delta^1$ A.U.	$R_h^2$ A.U.	$\dot{R}_h^2$ km s <sup>-1</sup>	$\beta^3$ °	Beamsize <sup>4</sup> 10 <sup>6</sup> km	
20-23 September 1985	2.39-2.30 2.35	2.49-2.45 2.47	-22.3 to -22.5 -22.40	23.7-24.1 23.9	1.87-1.80	
19-21 October 1985	1.46-1.40 1.44	2.10-2.07 2.09	-23.7 to -23.8 -23.76	25.2-24.9 25.1	1.14-1.10	
13-19 November 1985	0.78-0.67 0.72	1.75-1.66 1.71	-25.1 to -25.4 -25.25	8.8-1.4 5.2	0.61-0.52	
10-12 December 1985	0.73-0.77 0.74	1.35-1.32 1.34	-26.5 to -26.6 -26.54	45.7-48.0 46.4	0.57-0.60	
03-05 January 1986	1.20-1.24 1.21	0.98-0.95 0.97	-26.3 to -26.1 -26.24	52.6-51.5 52.3	0.94-0.97	
18-20 February 1986	1.46-1.43 1.44	0.62-0.63 0.63	+11.5 to +13.7 +12.96	31.2-35.4 33.9	1.14-1.12	
15-19 March 1986	0.94-0.84 0.90	0.92-0.98 0.94	+25.8 to +26.3 +26.02	64.8-66.1 65.3	0.74-0.66	
03-05 May 1986	0.86-0.92 0.89	1.66-1.69 1.67	+25.4 to +25.3 +25.39	29.7-30.3 29.9	0.67-0.72	

Notes for Table 2.2:

<sup>1</sup> Geocentric (Earth-Comet) distance

<sup>2</sup> Heliocentric (Sun-Comet) distance and heliocentric velocity

<sup>3</sup> Phase (Sun-Comet-Earth) angle

<sup>4</sup> Physical dimension of the beam at the distance of the comet

Table 2.2  
Observations of Comets Giacobini-Zinner, Hartley-Good, Thiele, and Wilson

Comet	Epoch	$\Delta^1$ A.U.	$R_h^2$ A.U.	$\dot{R}_h^2$ km s <sup>-1</sup>	$\beta^3$ °	Beamsize <sup>4</sup> 10 <sup>6</sup> km
P/Giacobini-Zinner	10-11 July 1985	0.773-0.765 0.77	1.293-1.285 1.29	-13.7 to -13.6 -13.65	51.8-52.3 52.0	0.61-0.60
P/Giacobini-Zinner	24-26 August 1985	0.49-0.48 0.485	1.043-1.039 1.040	-4.1 to -3.4 -3.68	72.6-73.2 73.0	0.383-0.378
P/Giacobini-Zinner	19,21 October 1985	0.65-0.66 0.66	1.20-1.21 1.21	+11.9 to +12.3 +12.2	56.3-55.3 55.6	0.51-0.52
C/Hartley-Good	18-21 October 1985	0.55-0.57 0.56	1.21-1.18 1.19	-25.0 to -24.9 -24.9	54.5-57.3 56.0	0.43-0.45
C/Hartley-Good	12-17 November 1985	0.84-0.90 0.87	0.88-0.83 0.85	-20.7 to -18.5 -19.6	70.0-69.6 69.8	0.66-0.70
C/Thiele	12,14-18 November 1985	0.58-0.69 0.64	1.43-1.40 1.41	-9.7 to -8.4 -8.9	32.5-41.4 38.2	0.45-0.54
C/Wilson	28-30 March 1987	1.38-1.32 1.36	1.253-1.245 1.25	-7.8 to -7.2 -7.5	44.0-45.5 44.8	1.08-1.03
C/Wilson	18-19 May 1987	0.89-0.92 0.91	1.275-1.281 1.28	+9.1 to +9.4 +9.25	52.0-51.6 51.8	0.70-0.72

constancy of this sensitivity through the course of an observing run were made periodically by observing the standard galactic OH source W12.

Velocity resolution was provided by a 1024 channel autocorrelator which was divided into  $4 \times 256$  channel backends to allow simultaneous observations of two polarizations at two frequencies. Each quarter of the autocorrelator yielded a total bandwidth of  $56.2 \text{ km sec}^{-1}$  and a spectral resolution of  $0.22 \text{ km sec}^{-1}$ .

For each of the days observations, we have produced a final spectrum via a multistep operation. This process started with folding each individual 9 minute frequency switched spectrum over onto itself. We then removed a linear baseline from each spectrum, thereby removing instrumental effects and determining the rms noise level ( $\sigma$ ). These spectra were then weighted by  $1/\sigma^2$  and averaged together to form a single spectrum which represents 6–8 hours of observational data. From the daily average spectra we then removed another linear baseline, to eliminate any longer term instrumental effects and determine the rms noise level for the daily average (hereafter referred to as  $\sigma_j$ ).

To arrive at an epoch (2–8 day) average spectrum we have averaged together all of the individual daily average spectra. In this averaging process we have weighted each spectrum by  $1/\sigma_j^2$ , which is equivalent to weighting by the integration time for each spectrum since the system temperature was stable throughout an observing run. The resulting spectra appear in the following section.

We have also used this weighting scheme when we determined the appropriate values for  $\Delta$  (Earth-Comet distance),  $R_h$  (Sun-Comet distance),  $\dot{R}_h$  (heliocentric velocity), and  $\beta$  (Sun-Comet-Earth angle, or phase angle), for our model. Line one for each epoch listed in Tables 2.1 and 2.2 shows the variation in each of these parameters over the course of the observations, while line two for each epoch lists the  $1/\sigma_j^2$  weighted average value which we have adopted for our modeling.

### 2.3 The Epoch Average Spectra

The results of our data reduction are shown in Figures 2.1a-h (for P/Halley) and Figure 2.1i-p (for P/Giacobini-Zinner, C/Hartley-Good, C/Thiele, and C/Wilson). The velocity scale in each of these figures represents the velocity of the coma gas relative to the cometary nucleus along the line of sight to the comet. A brief descriptive look at the data follows (for a more complete treatment the reader is referred to Chapter 4).

The spectrum of Halley in January 1986 (Figure 2.1e) is noticeably broader than those from the preceding months (Figures 2.1a-d). The additional feature seen in Figure 2.1e from  $V_{\text{COMET}} = -10$  to  $-6$  km sec<sup>-1</sup> is a background source. In Figures 2.1f and 2.1g (P/Halley, February 1986 and March 1986 epochs) we again see quite wide lines. In addition, the spectrum from March 1986 has a rather flattened top to it. Finally, the Halley spectrum from May 1986 (Figure 2.1h) marks a return to a narrower line. The spike

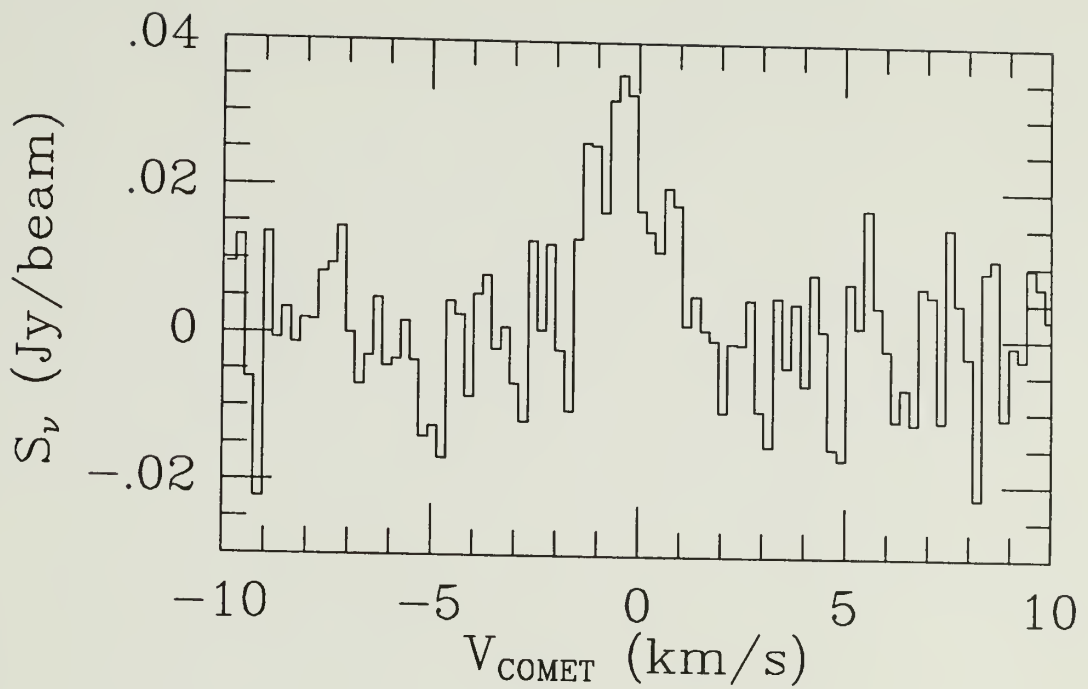


**Figure 2.1a:** The average 1667 MHz OH line from Comet Halley over the period 20–23 September 1985.

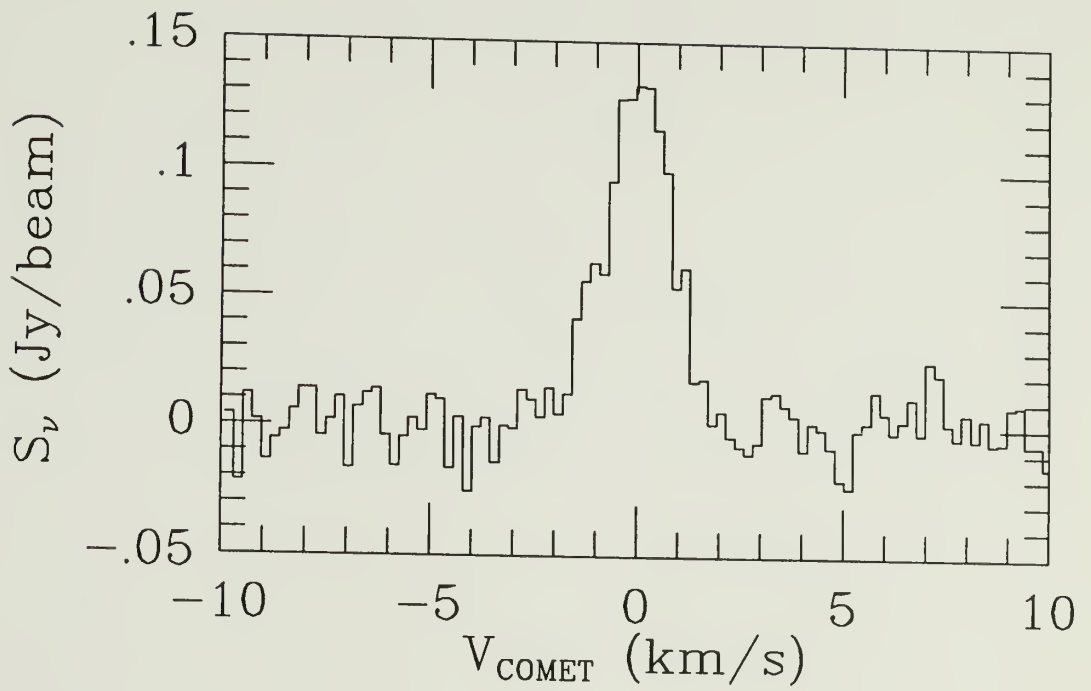
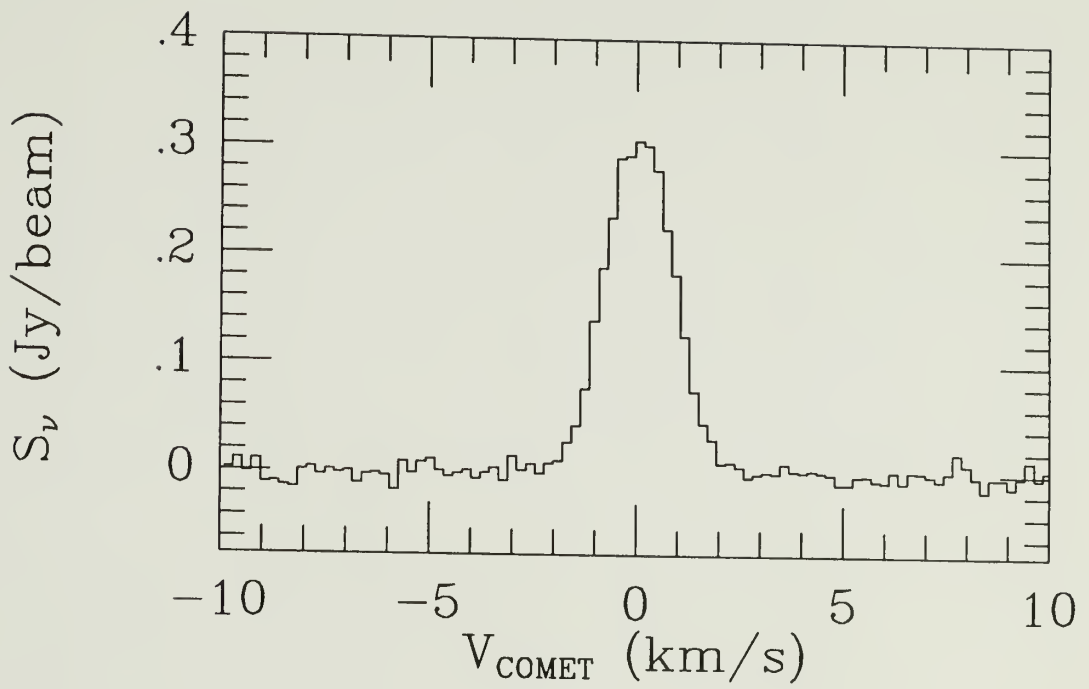


Figure 2.1b: The average 1667 MHz OH line from Comet Halley over the period 19–21 October 1985.





**Figure 2.1c:** The average 1667 MHz OH line from Comet Halley over the period 13–19 November 1985.

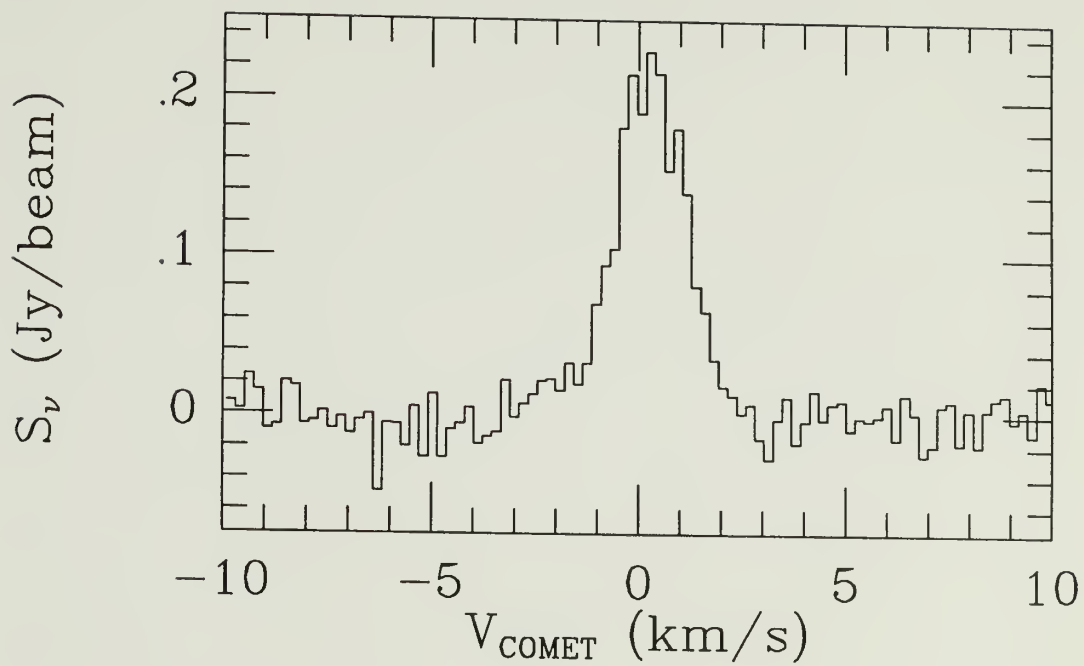
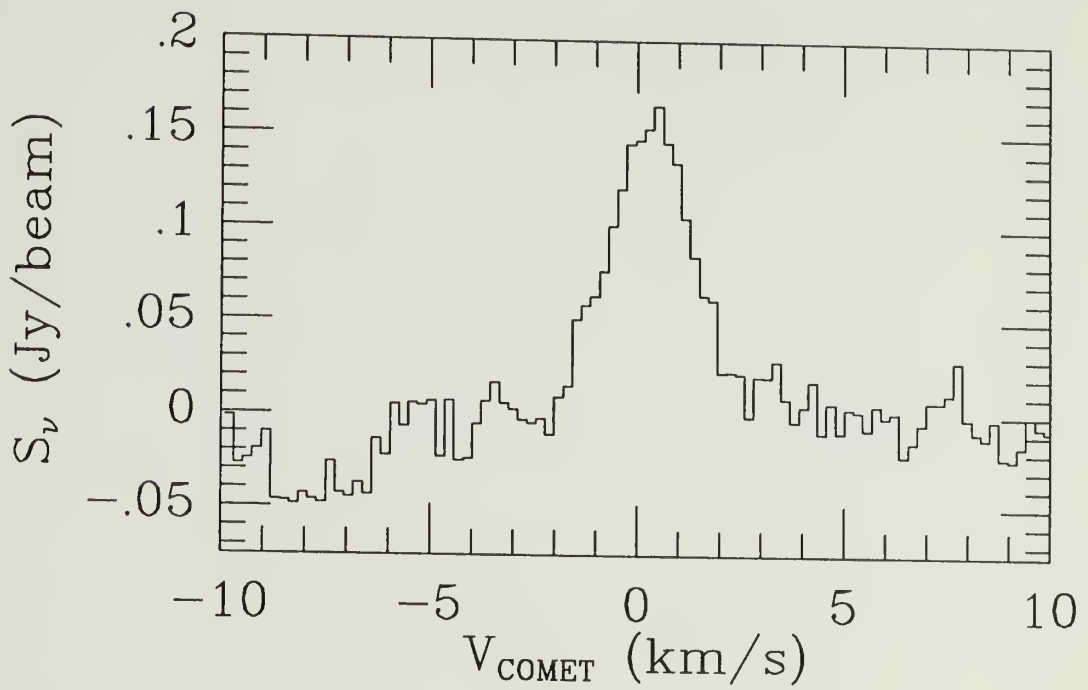
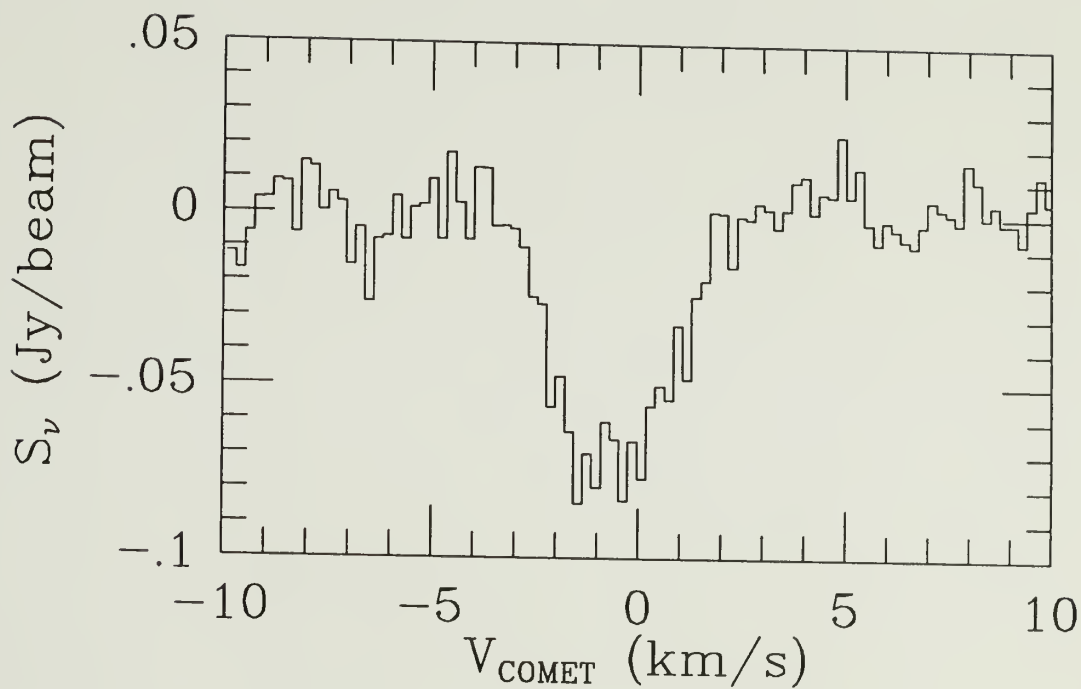


Figure 2.1d: The average 1667 MHz OH line from Comet Halley over the period 10–12 December 1985.



**Figure 2.1e:** The average 1667 MHz OH line from Comet Halley over the period 03–05 January 1986.



**Figure 2.1f:** The average 1667 MHz OH line from Comet Halley over the period 18–20 February 1986.

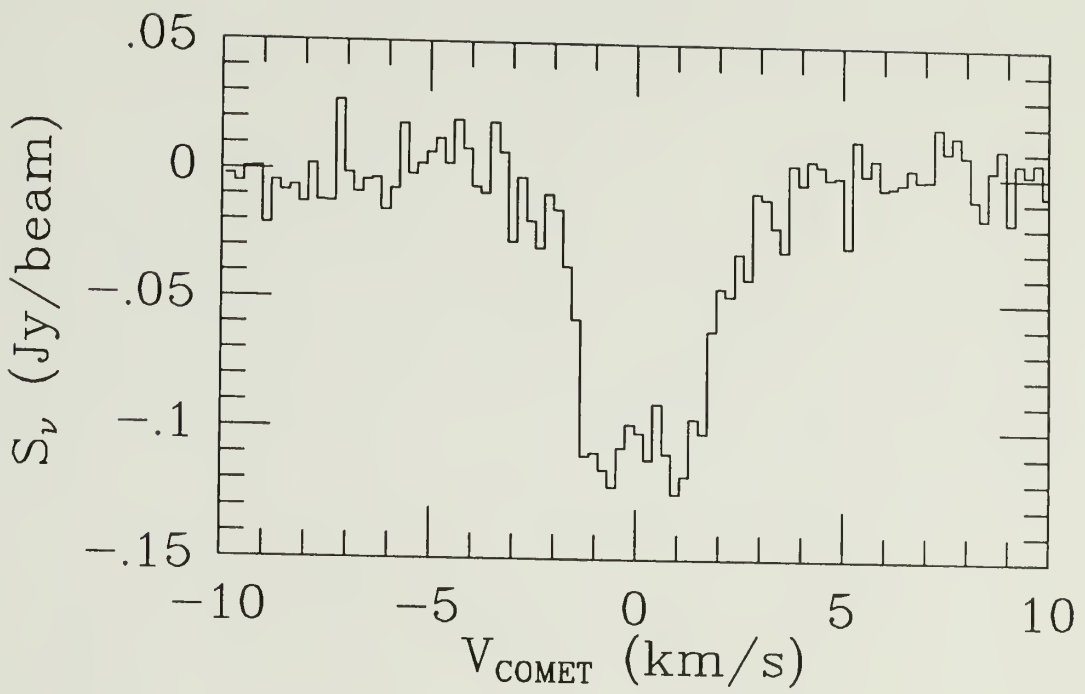


**Figure 2.1g:** The average 1667 MHz OH line from Comet Halley over the period 15–19 March 1986.

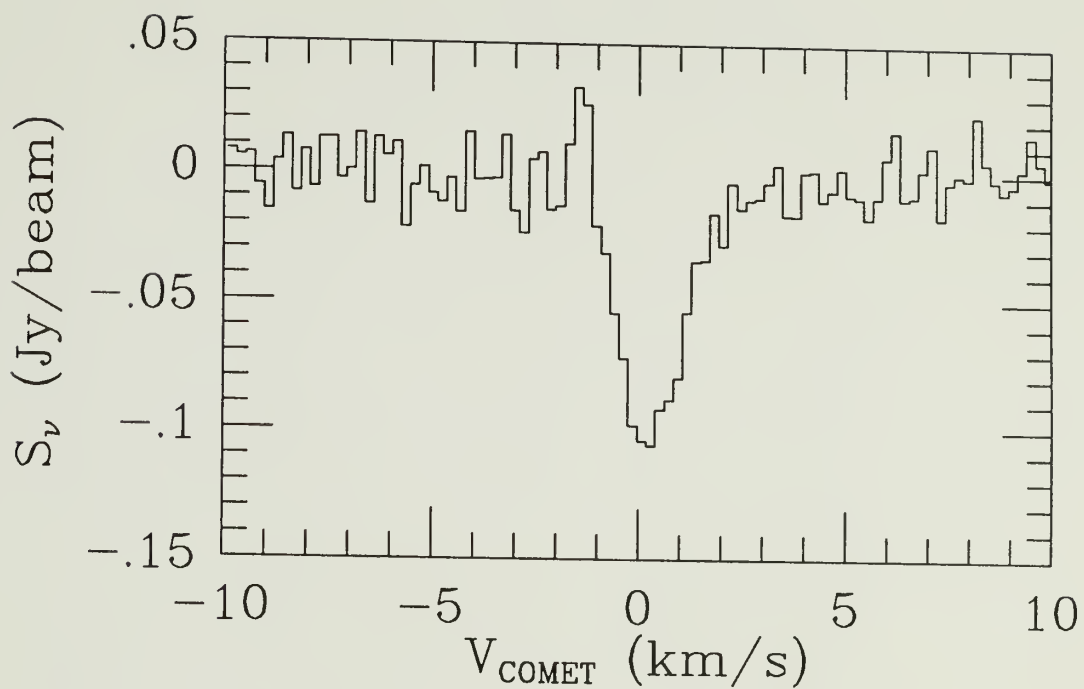


**Figure 2.1h:** The average 1667 MHz OH line from Comet Halley over the period 03–05 May 1986.

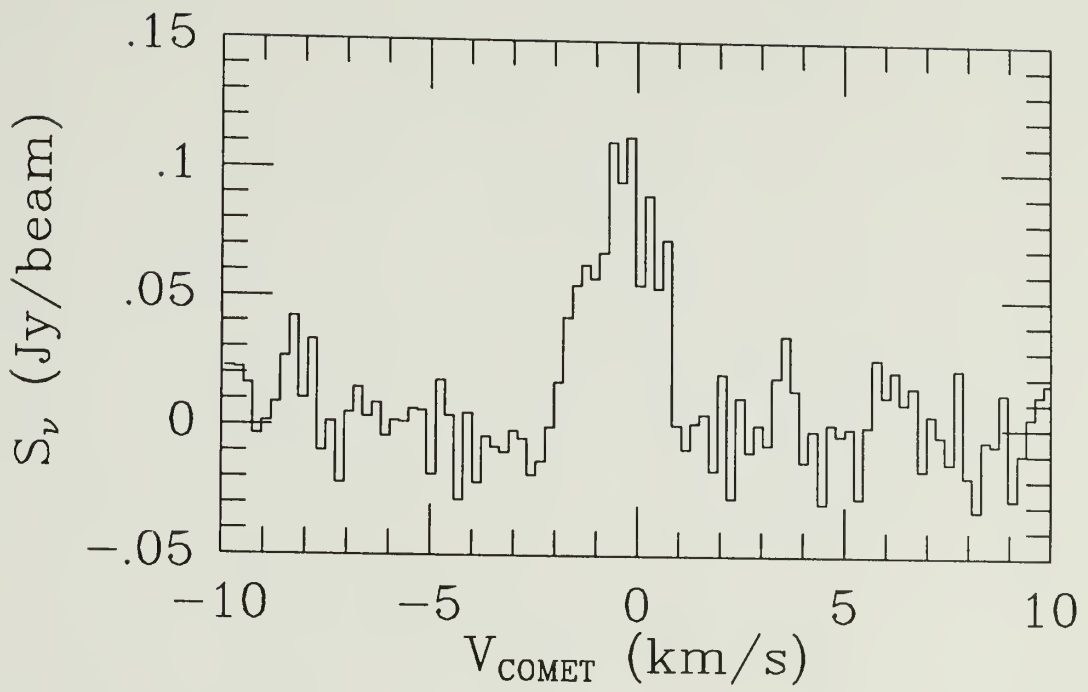


**Figure 2.1i:** The average 1667 MHz OH line from Comet Giacobini-Zinner over the period 10–11 July 1985.

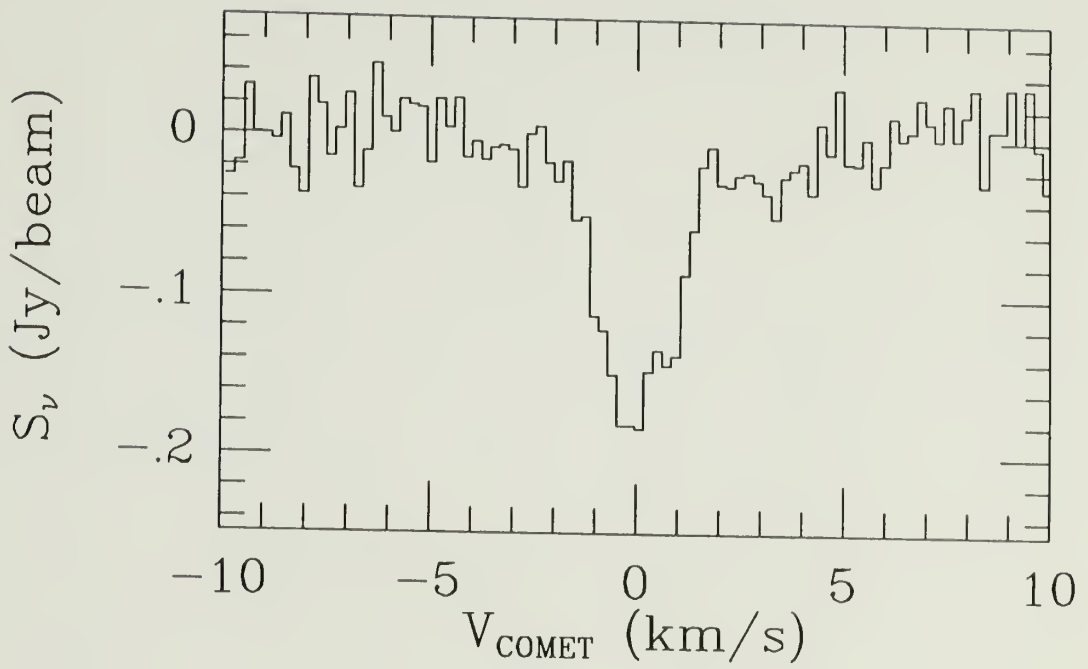


**Figure 2.1j:** The average 1667 MHz OH line from Comet Giacobini-Zinner over the period 24–26 August 1985.



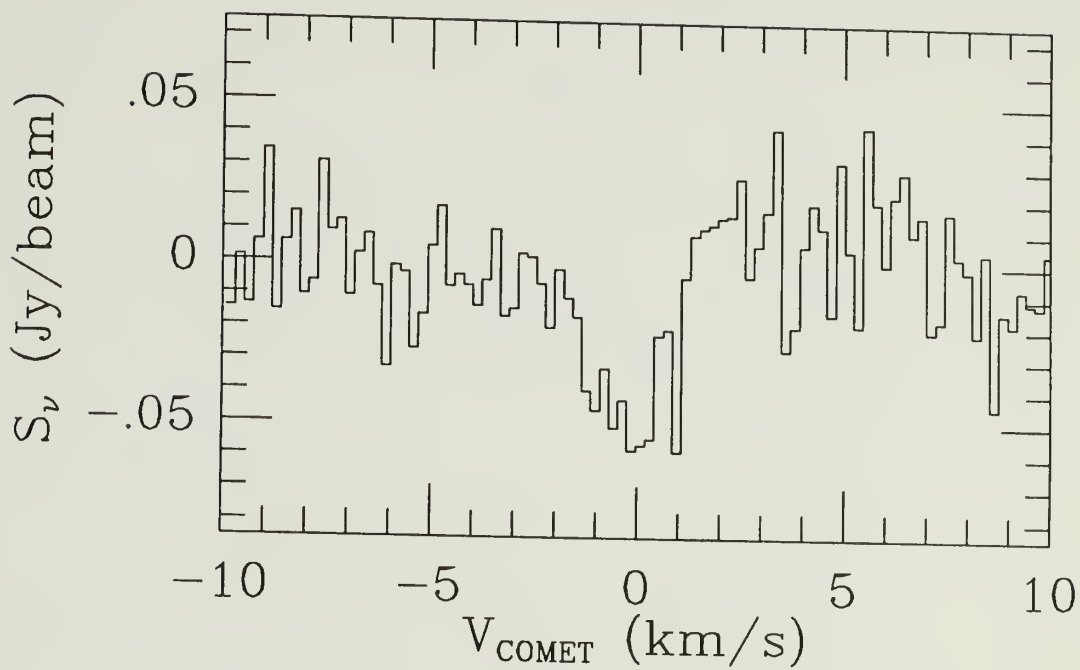


**Figure 2.1k:** The average 1667 MHz OH line from Comet Giacobini-Zinner over the period 19,21 October 1985.

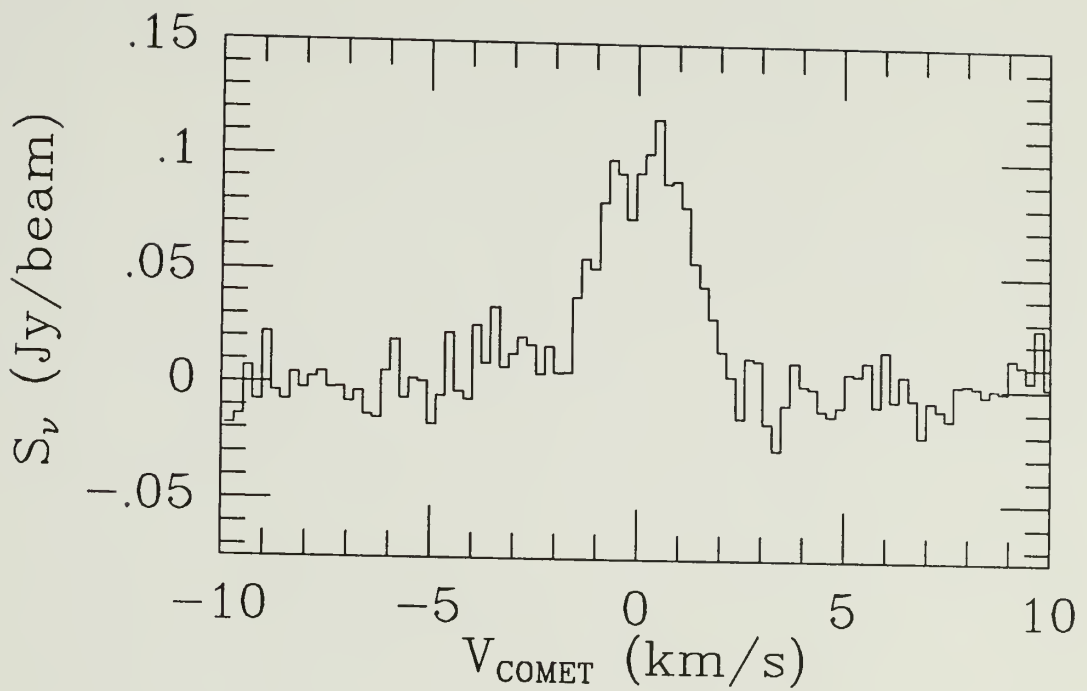


**Figure 2.11:** The average 1667 MHz OH line from Comet Hartley-Good over the period 18–21 October 1985.

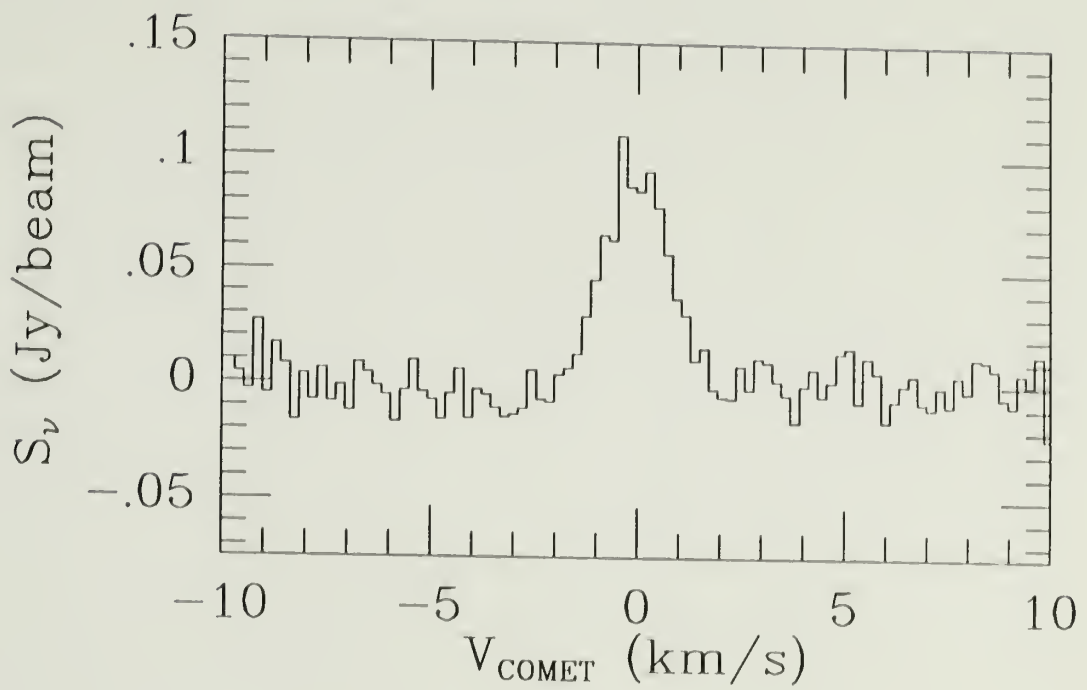
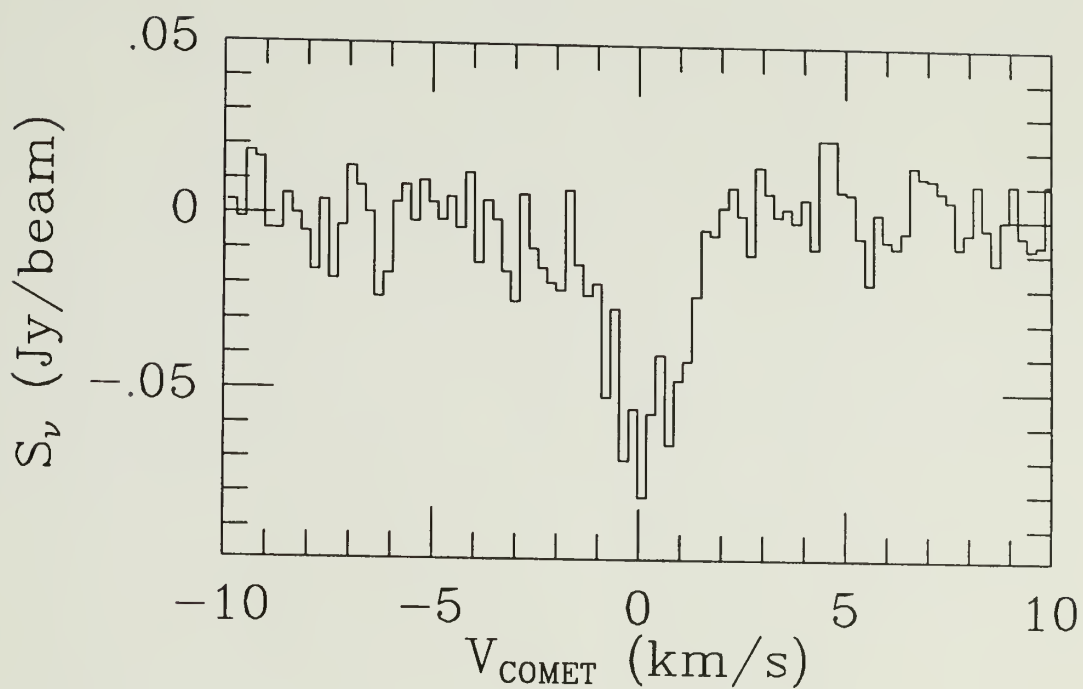
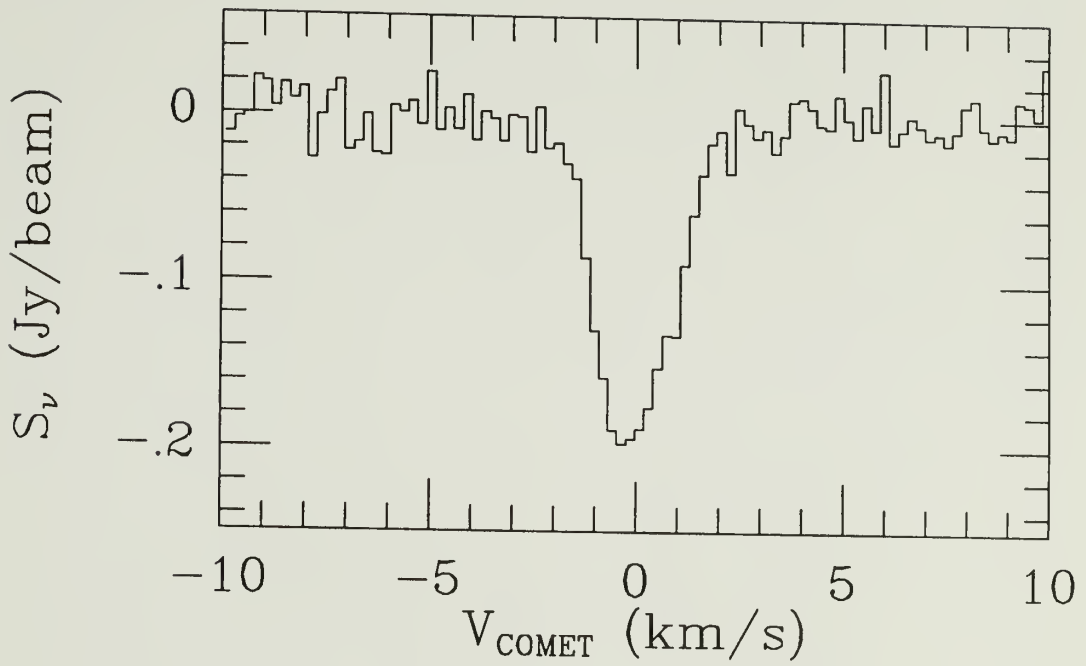


Figure 2.1m: The average 1667 MHz OH line from Comet Hartley-Good over the period 12–17 November 1985.



**Figure 2.1n:** The average 1667 MHz OH line from Comet Thiele over the period 12,14-18 November 1985.



**Figure 2.1o:** The average 1667 MHz OH line from Comet Wilson over the period 28–30 March 1987.

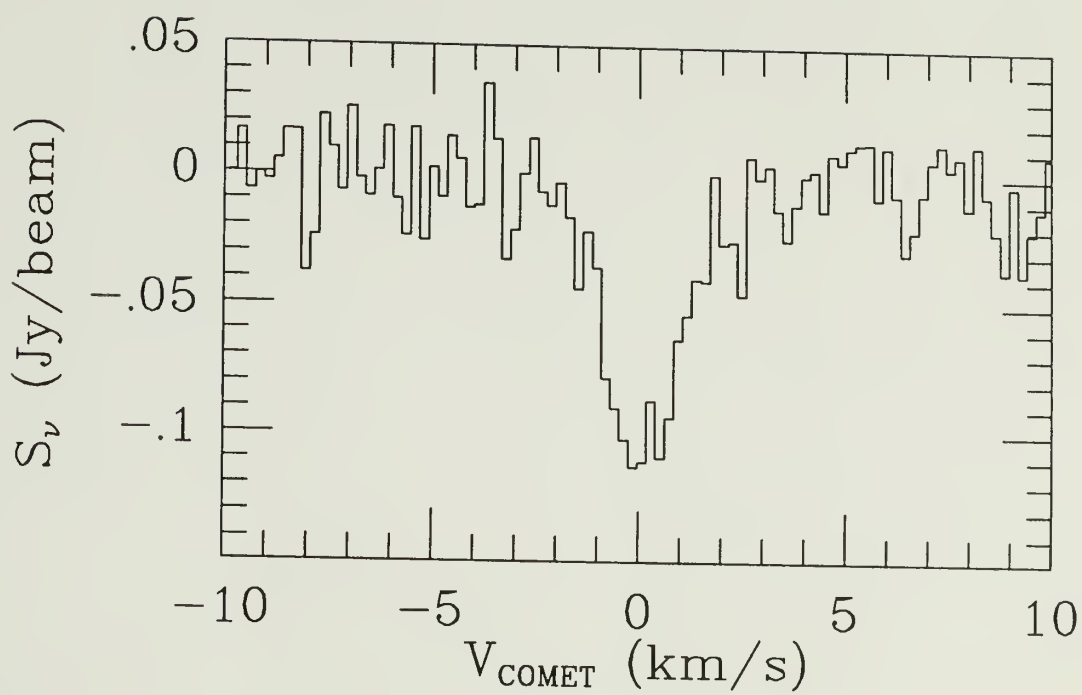


**Figure 2.1p:** The average 1667 MHz OH line from Comet Wilson over the period 18–19 May 1987.

near the left side of the absorption line in this figure is real, and appears prominently in both the 03 and 05 May daily average spectra. Indeed, emission at this velocity is *expected* based on the inversion curve of Despois *et al.* (1981; see also Chapter 4).

The spectra from the other comets used for this thesis (Figures 2.1i–p) look completely normal with two possible exceptions. First, the spectrum of P/Giacobini-Zinner in July 1985 (Figure 2.1i) exhibits a sharp edge on its red side. Such a sharp feature is not seen in any of the other spectra, although there is some suggestion of a sharp edge on the blue side of the P/Halley data from March 1985 (Figure 2.1g). Second, the spectrum from C/Hartley-Good from November 1985 (Figure 2.1m) is unusually narrow given the heliocentric distance for that comet at the time the observations were made (Table 2.2; see also below).

Since all of the spectra are essentially Gaussian in shape, we have chosen to fit the lines by a Gaussian curve and to use the fitting results to characterize the data. The best fitting Gaussian curves are shown in Figures 2.2a–p, where in the top panel we have superposed the fit on the data. The bottom panel of each of these figures shows the data after the Gaussian curve has been subtracted. From this series of figures we see that, with the exception of the P/Halley spectrum from March 1986 (Figure 2.2g), the Gaussian curves are a good representation of the data. Table 2.3 contains a summary of our fitting results. We have plotted the widths of the lines as a function of heliocentric

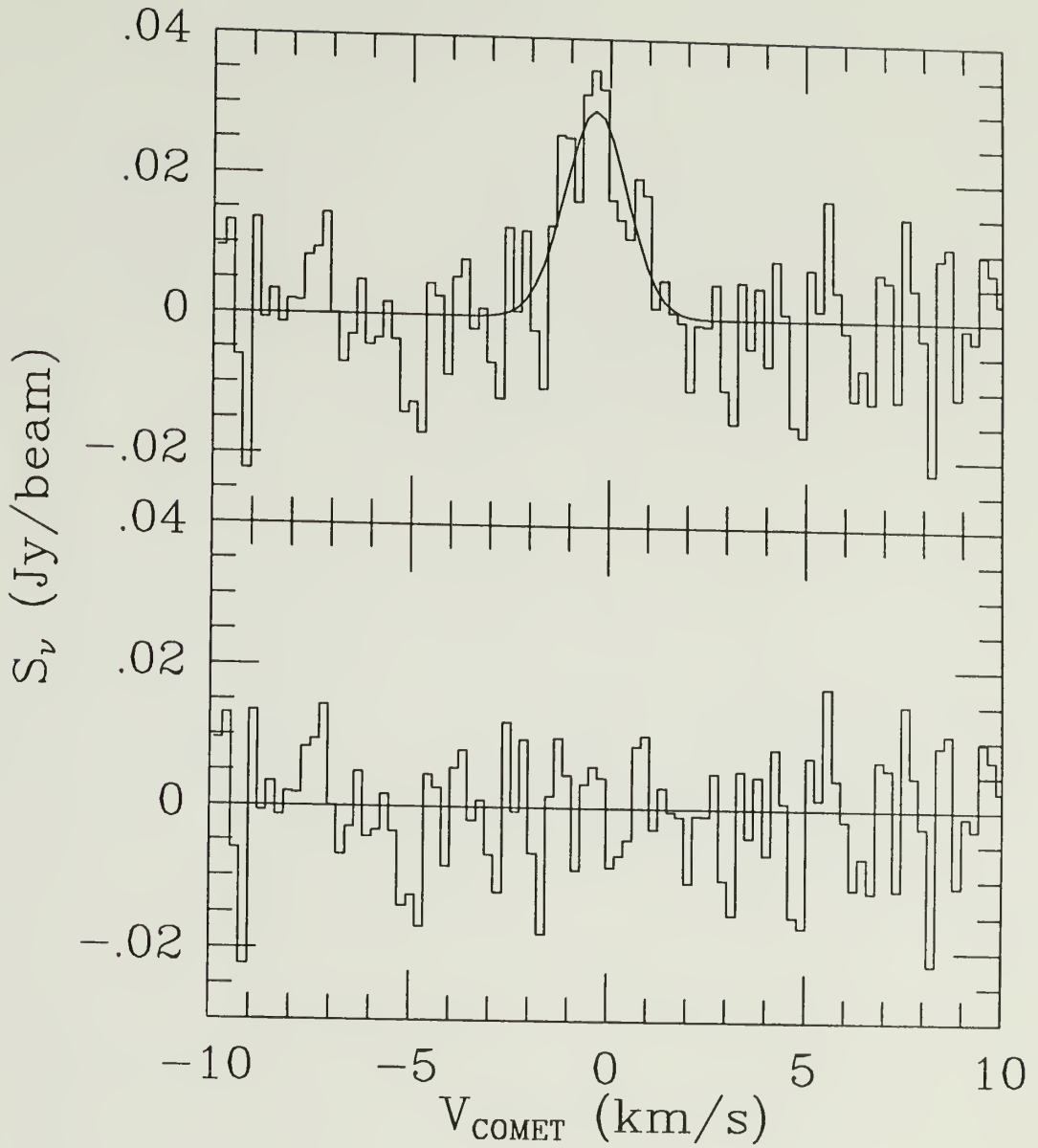


**Figure 2.2a:** The data of Figure 2.1a with the best fitting Gaussian curve (top), and the associated residuals (bottom).



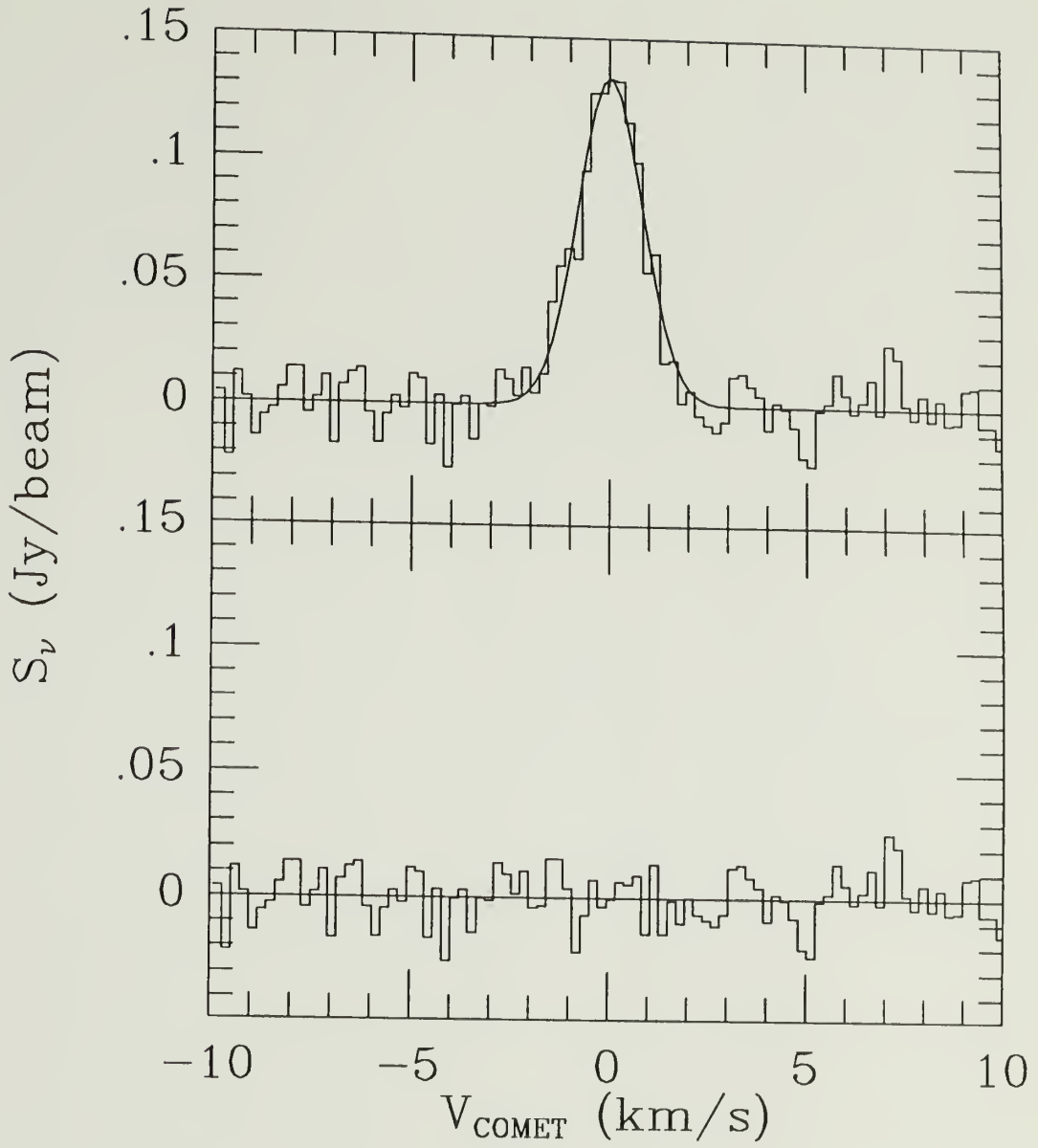


**Figure 2.2b:** The data of Figure 2.1b with the best fitting Gaussian curve (top), and the associated residuals (bottom).

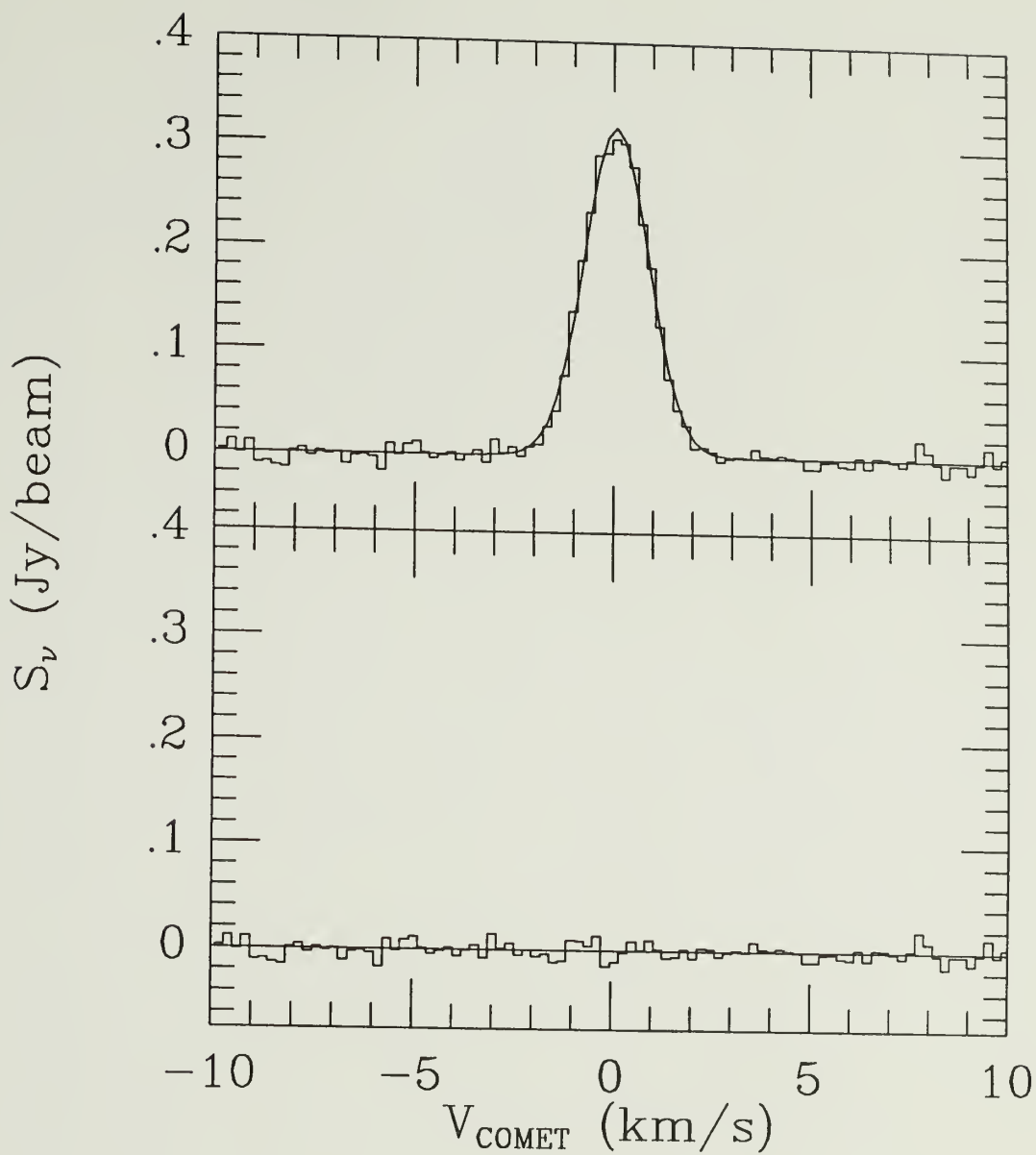


**Figure 2.2c:** The data of Figure 2.1c with the best fitting Gaussian curve (top), and the associated residuals (bottom).

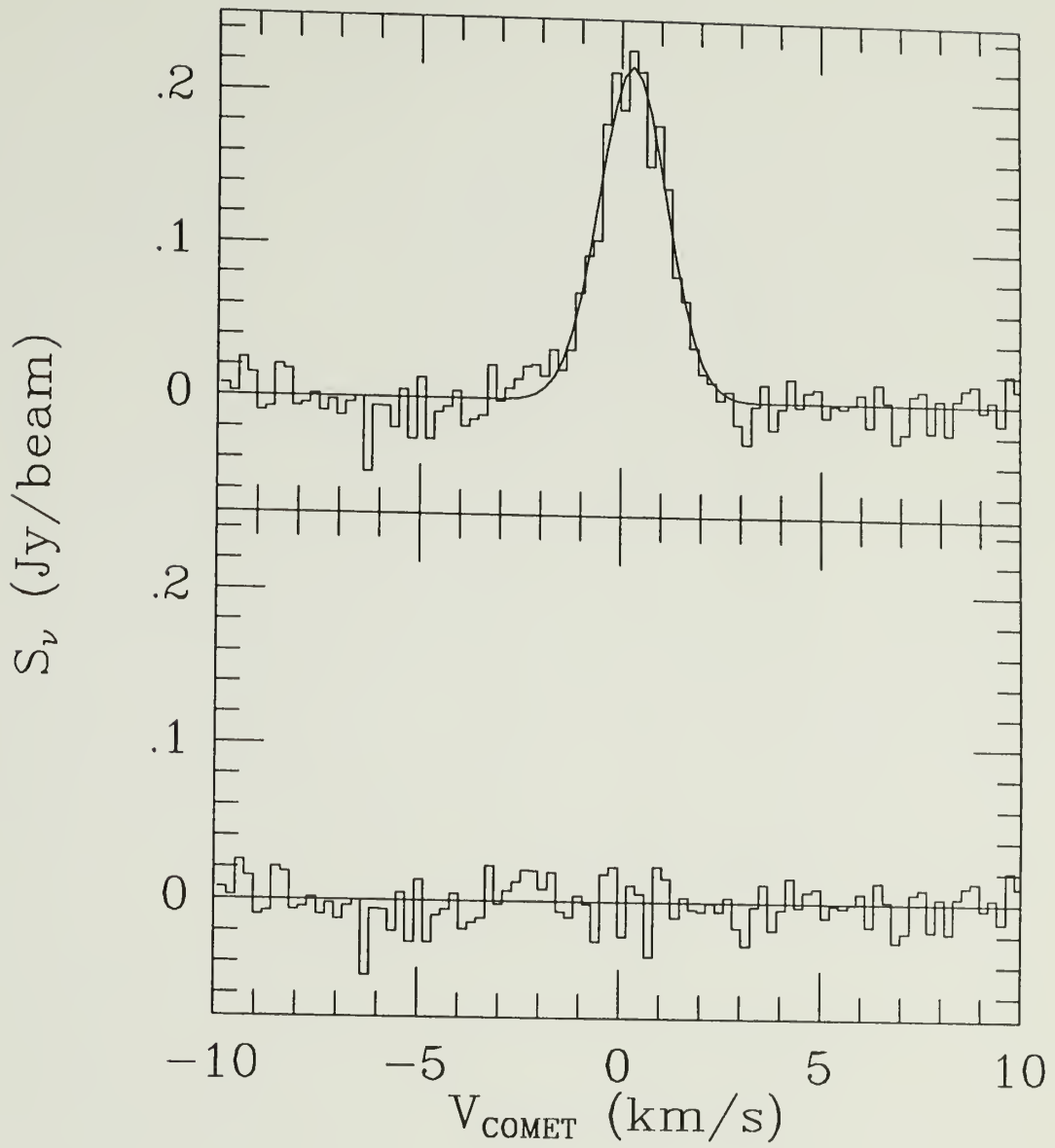


**Figure 2.2d:** The data of Figure 2.1d with the best fitting Gaussian curve (top), and the associated residuals (bottom).

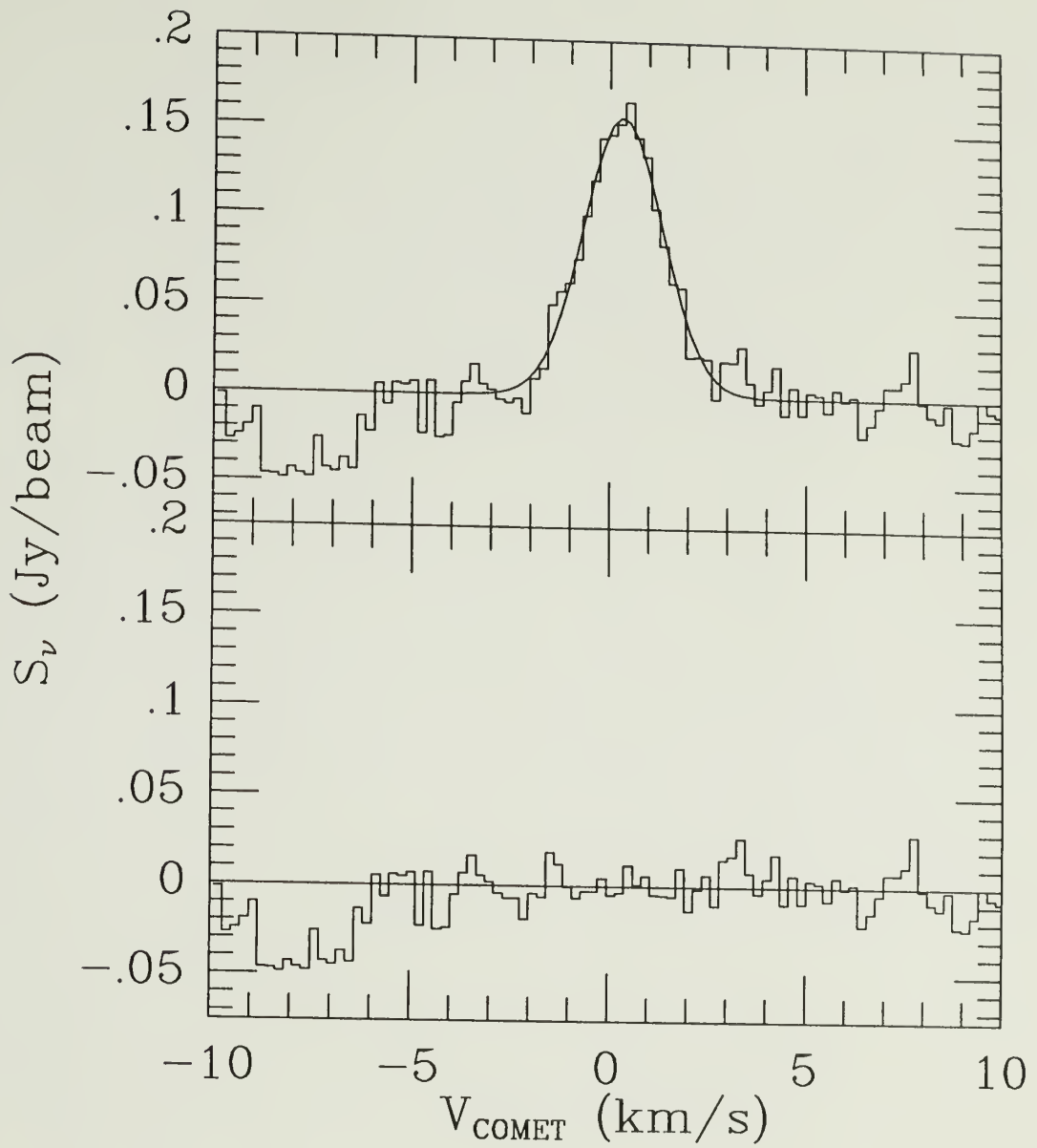


**Figure 2.2e:** The data of Figure 2.1e with the best fitting Gaussian curve (top), and the associated residuals (bottom).

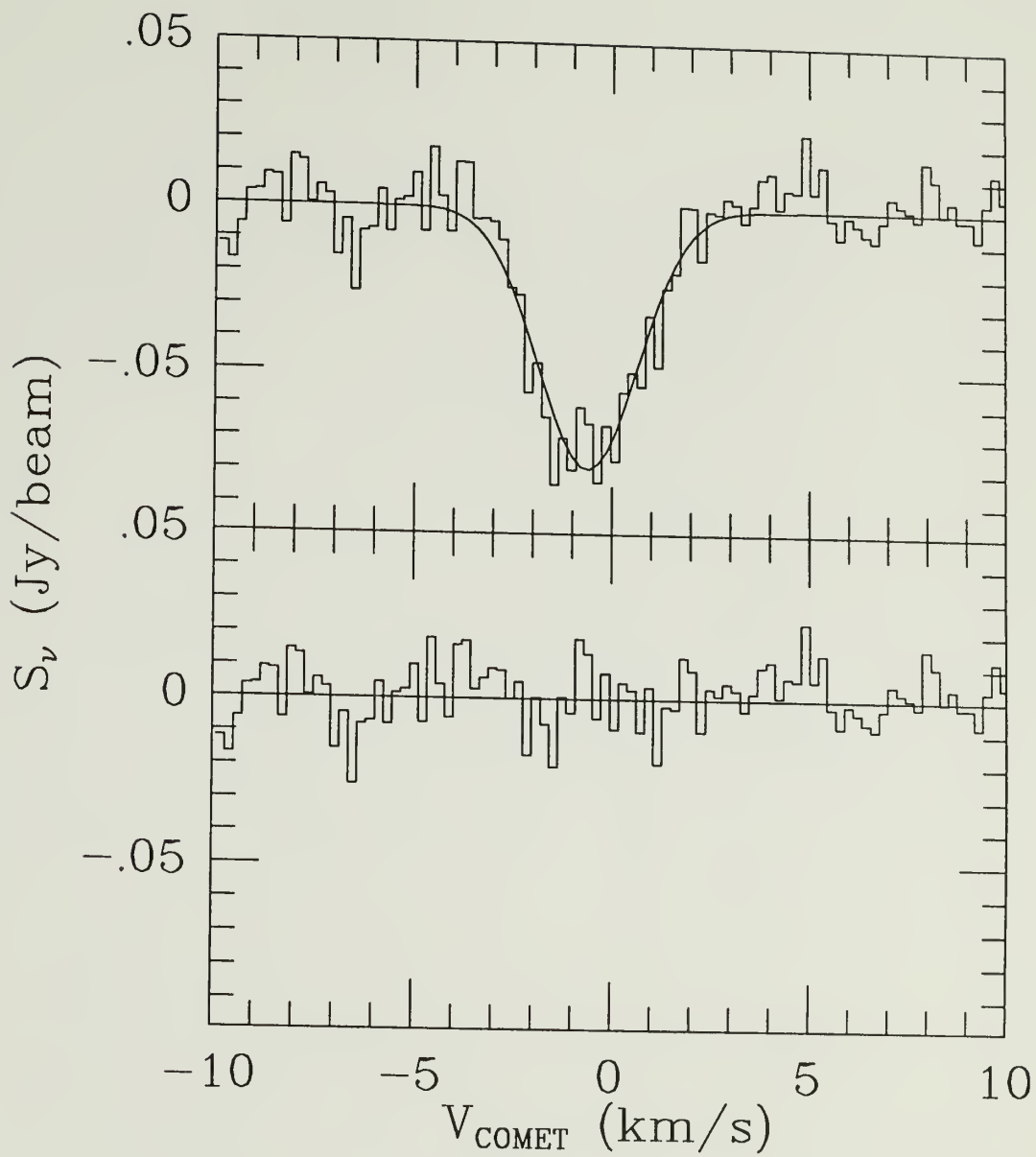


**Figure 2.2f:** The data of Figure 2.1f with the best fitting Gaussian curve (top), and the associated residuals (bottom).

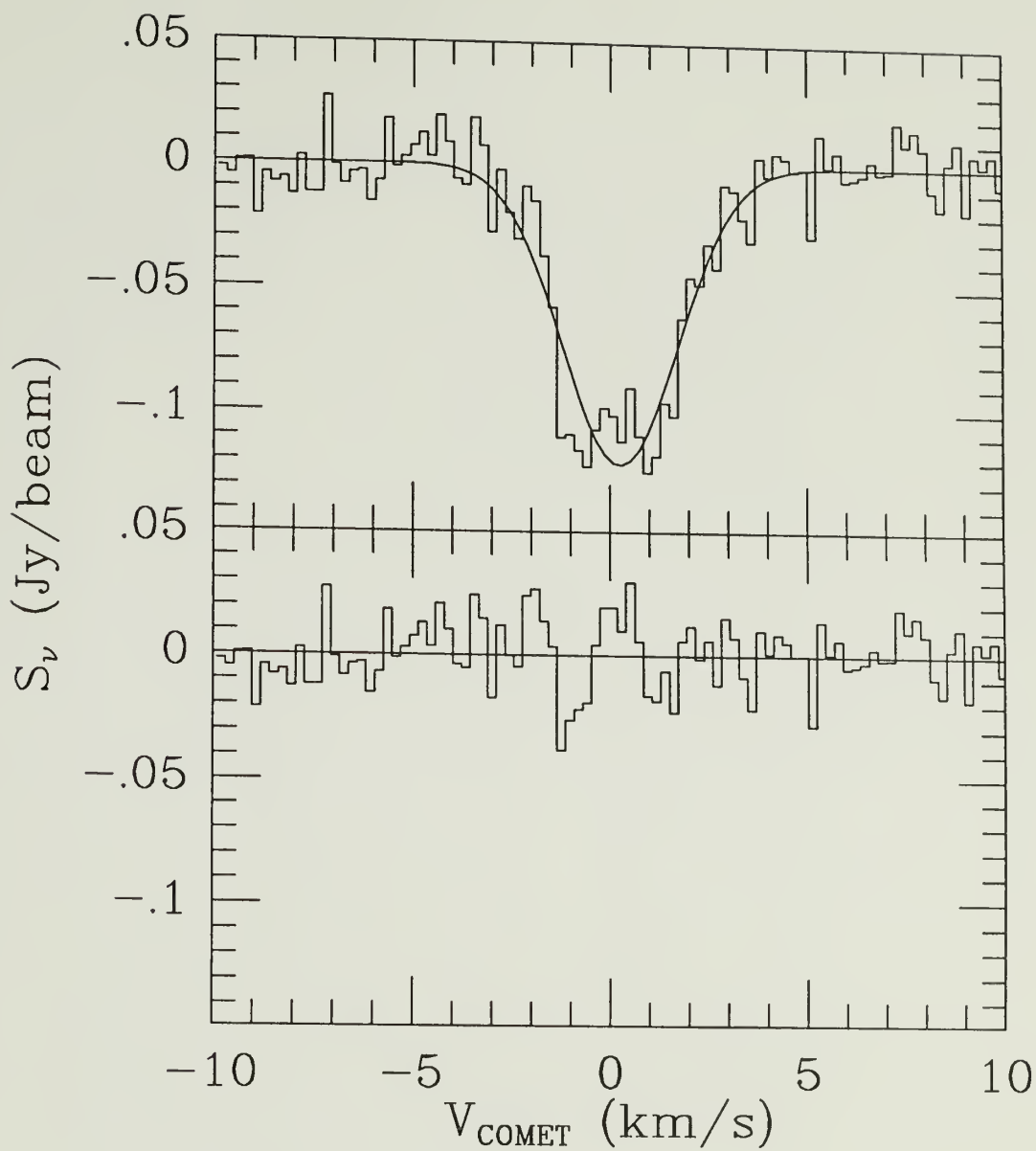


**Figure 2.2g:** The data of Figure 2.1g with the best fitting Gaussian curve (top), and the associated residuals (bottom).

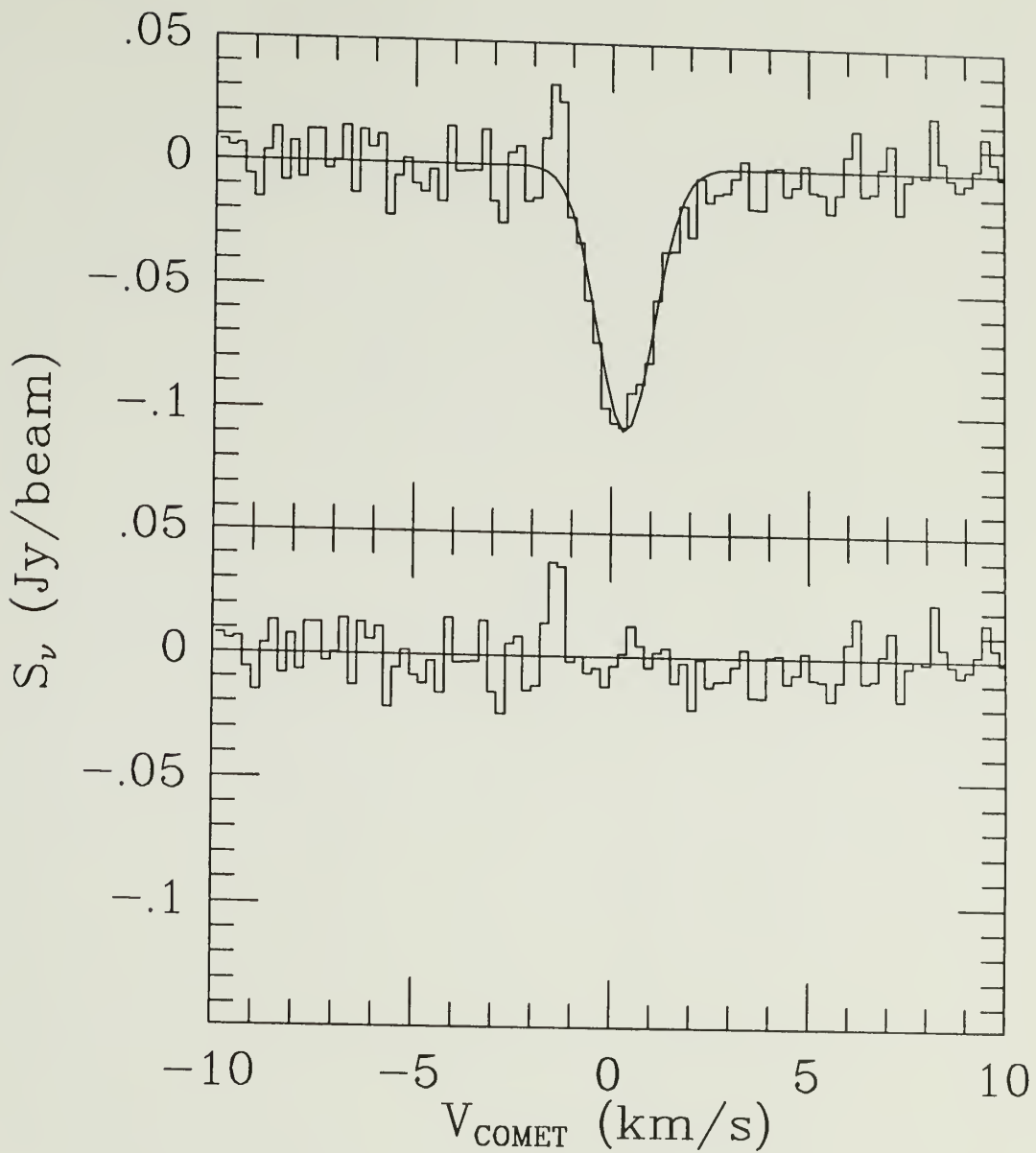


**Figure 2.2h:** The data of Figure 2.1h with the best fitting Gaussian curve (top), and the associated residuals (bottom).

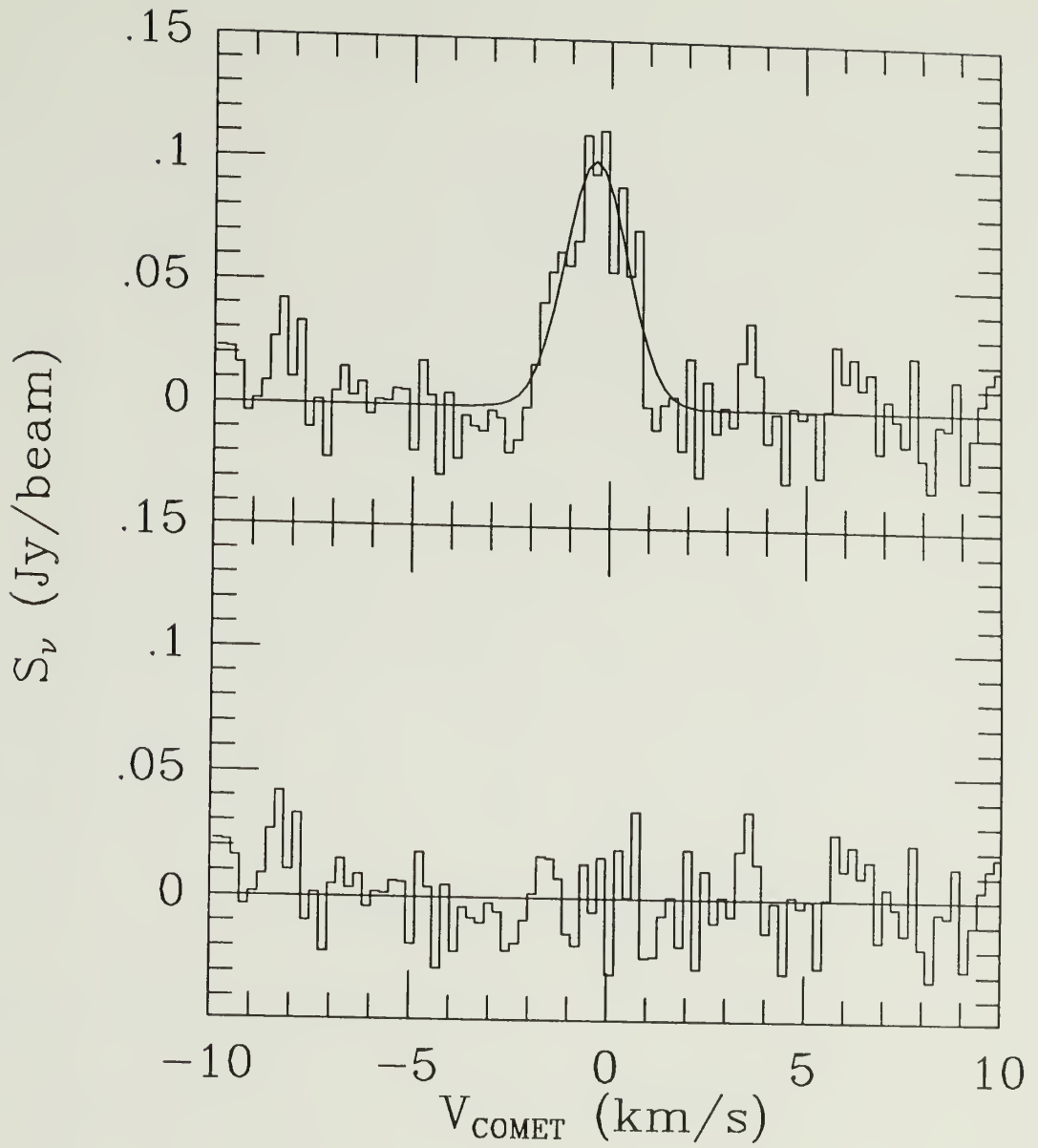


**Figure 2.2i:** The data of Figure 2.1i with the best fitting Gaussian curve (top), and the associated residuals (bottom).



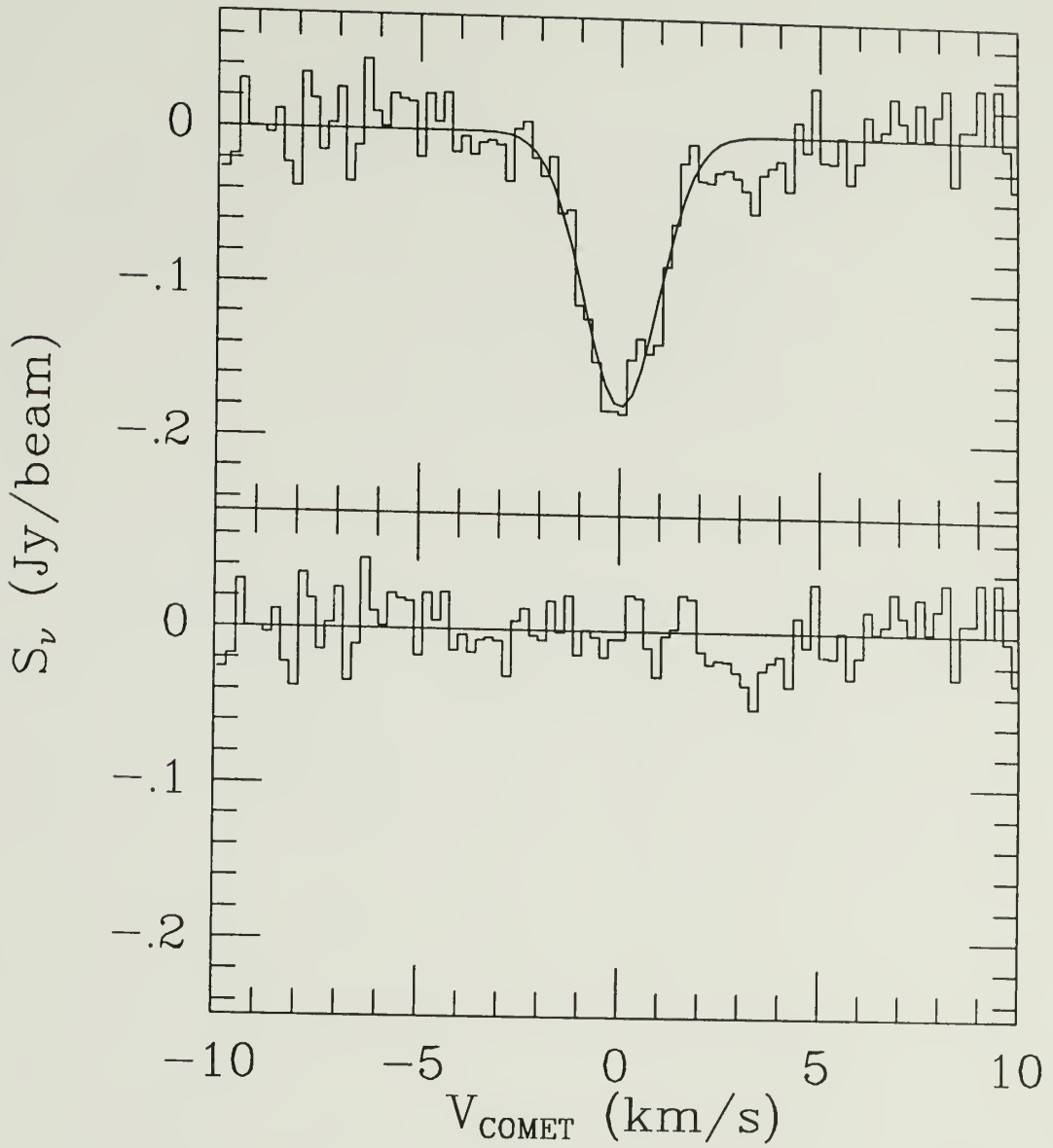


**Figure 2.2j:** The data of Figure 2.1j with the best fitting Gaussian curve (top), and the associated residuals (bottom).

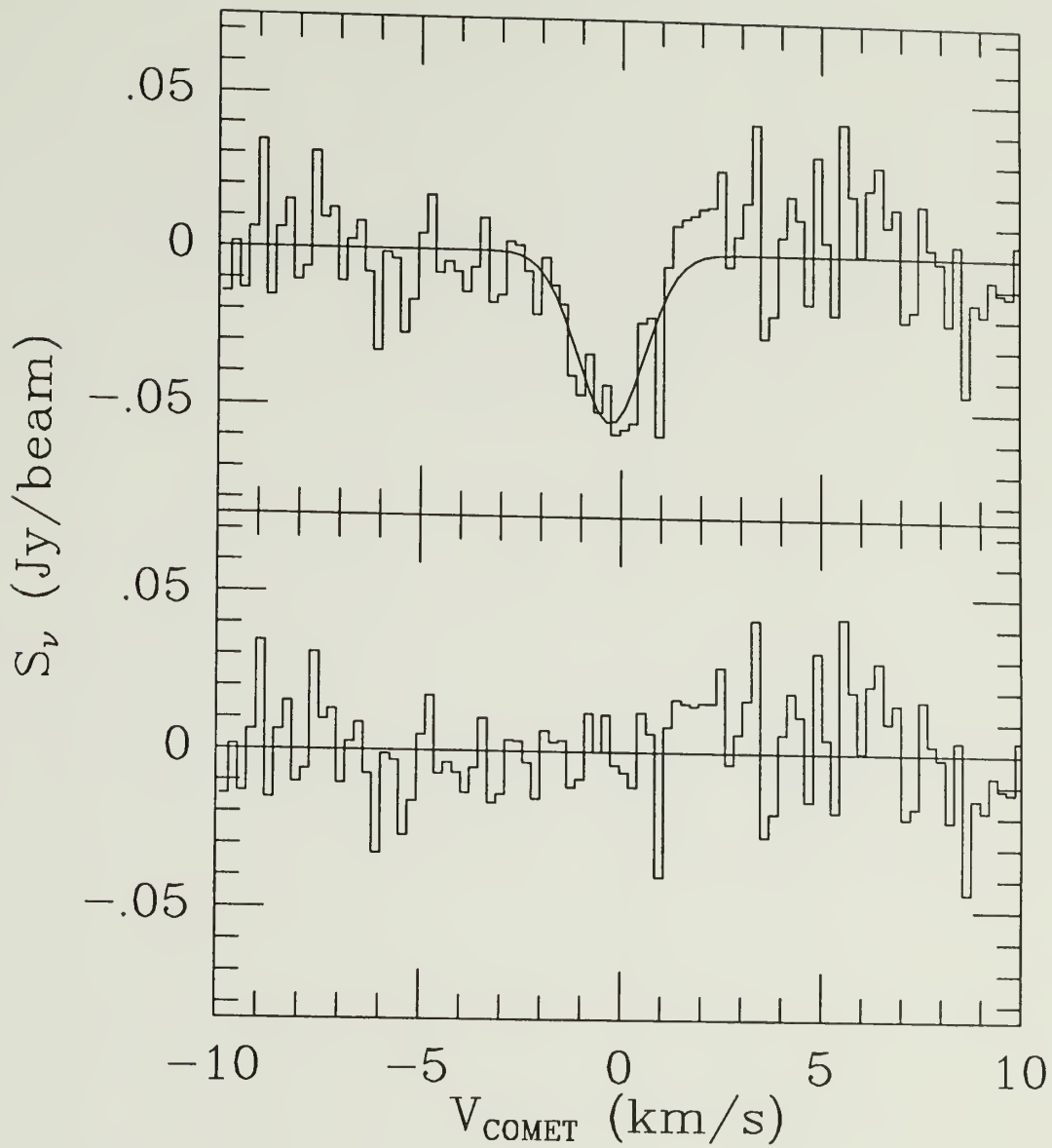


**Figure 2.2k:** The data of Figure 2.1k with the best fitting Gaussian curve (top), and the associated residuals (bottom).

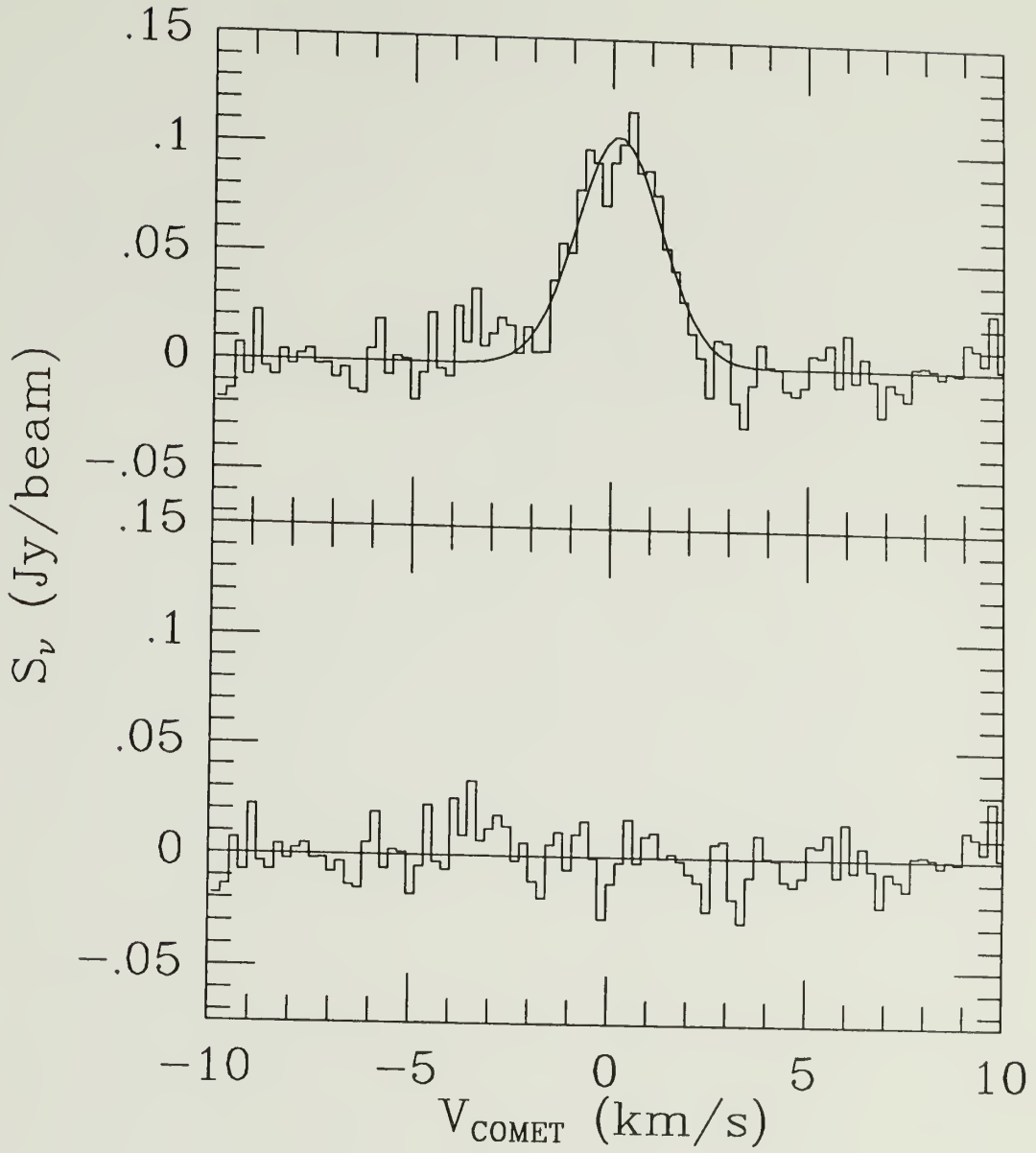


**Figure 2.2l:** The data of Figure 2.1l with the best fitting Gaussian curve (top), and the associated residuals (bottom).

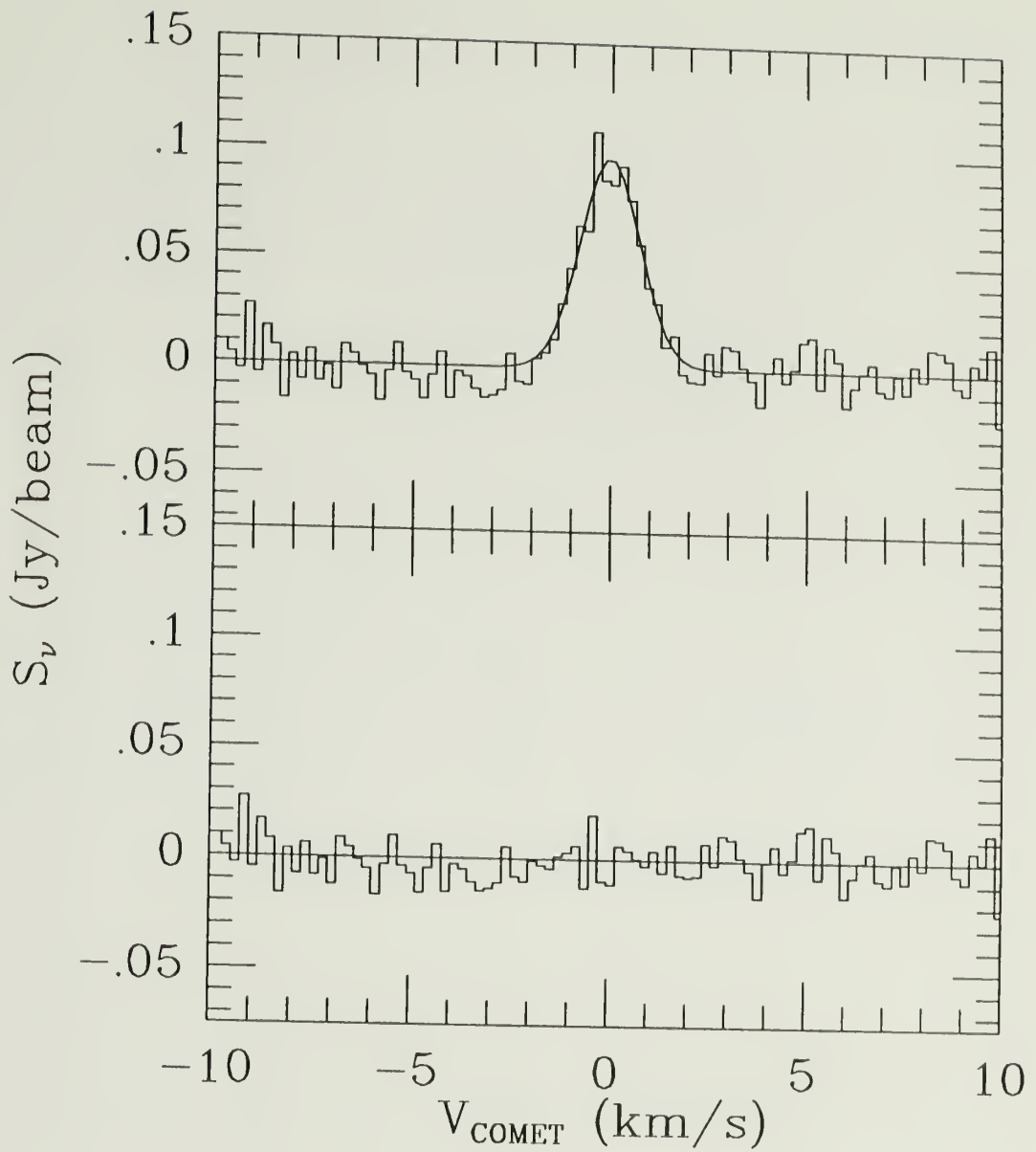
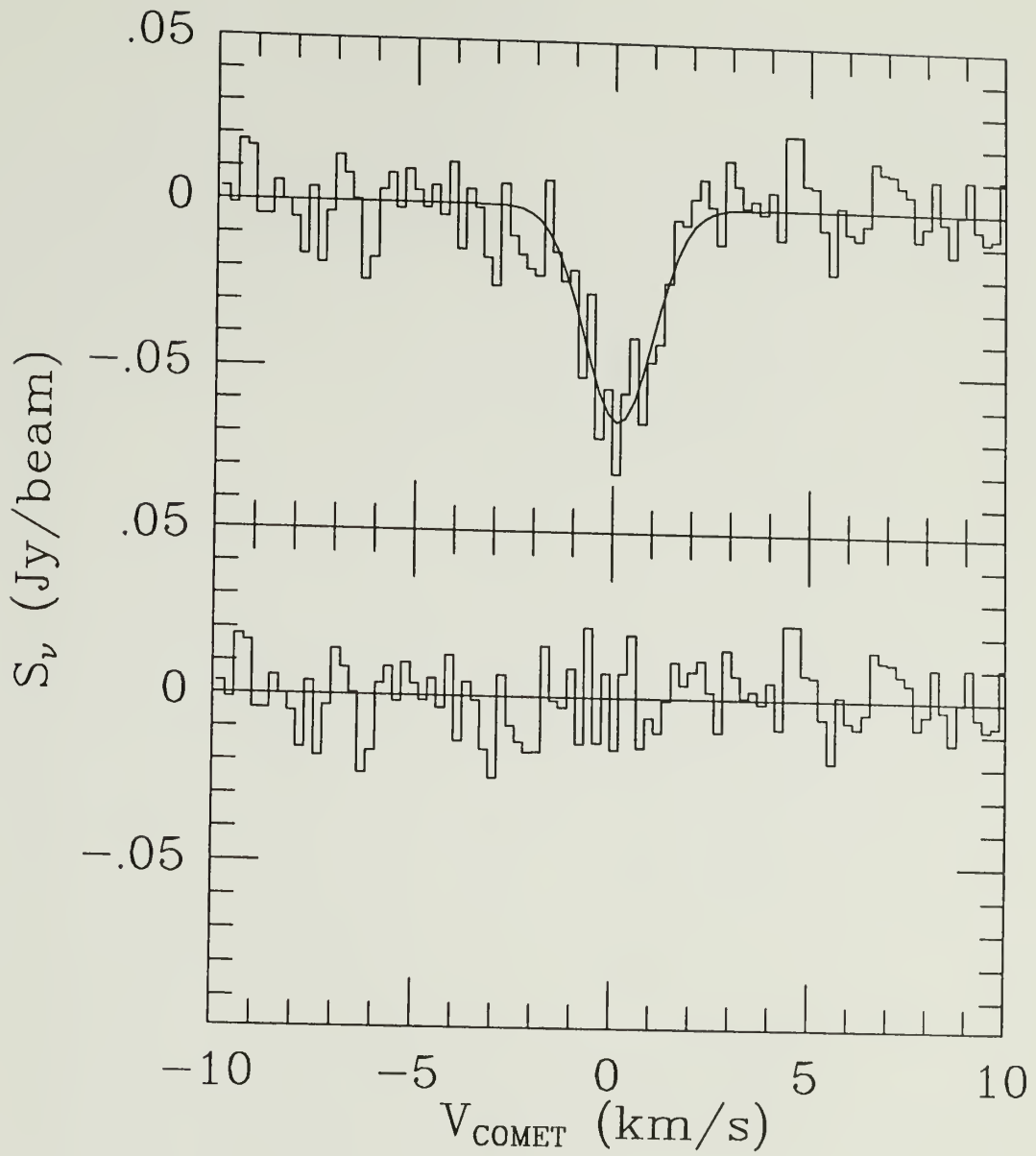


Figure 2.2m: The data of Figure 2.1m with the best fitting Gaussian curve (top), and the associated residuals (bottom).



**Figure 2.2n:** The data of Figure 2.1n with the best fitting Gaussian curve (top), and the associated residuals (bottom).

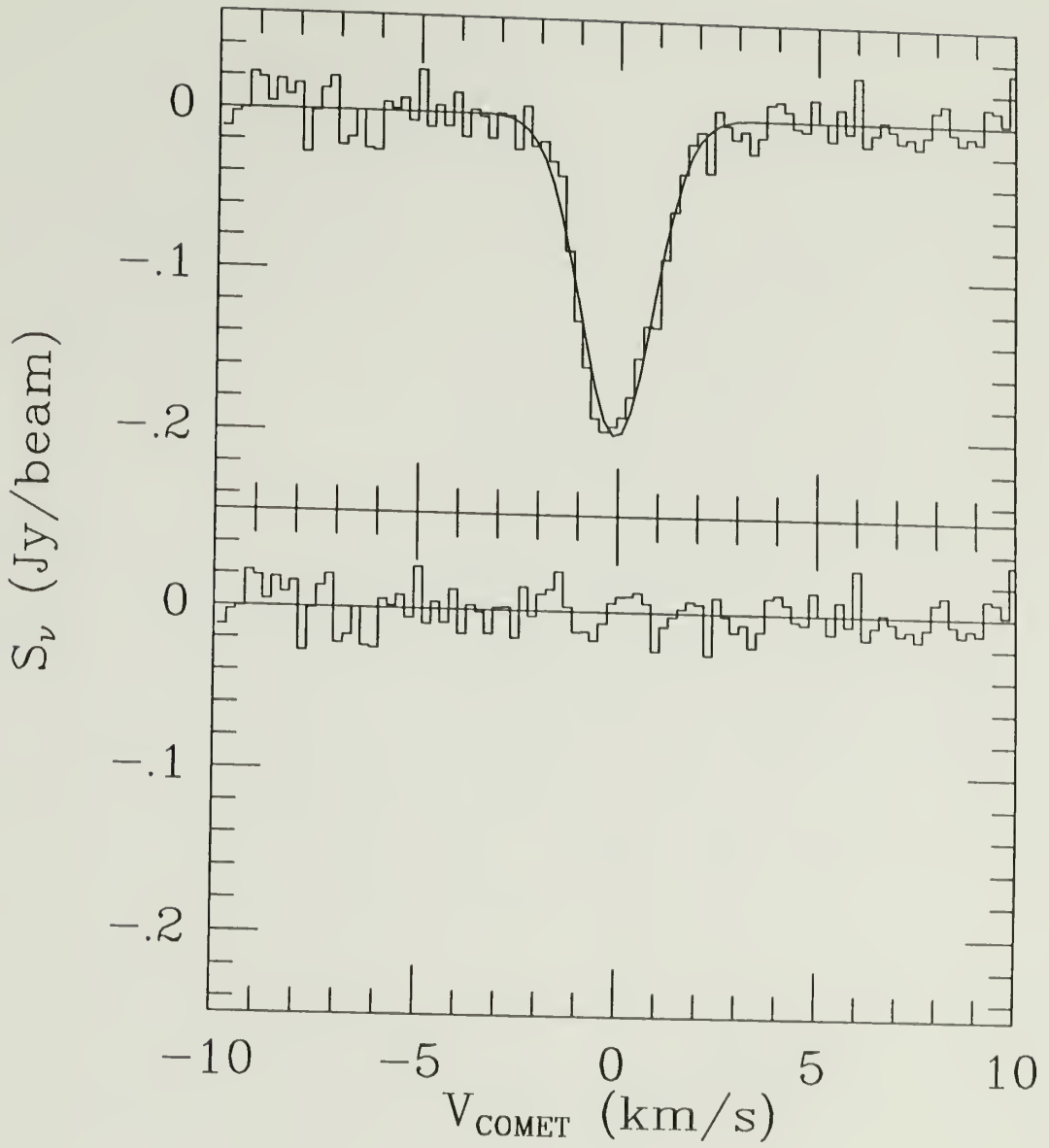
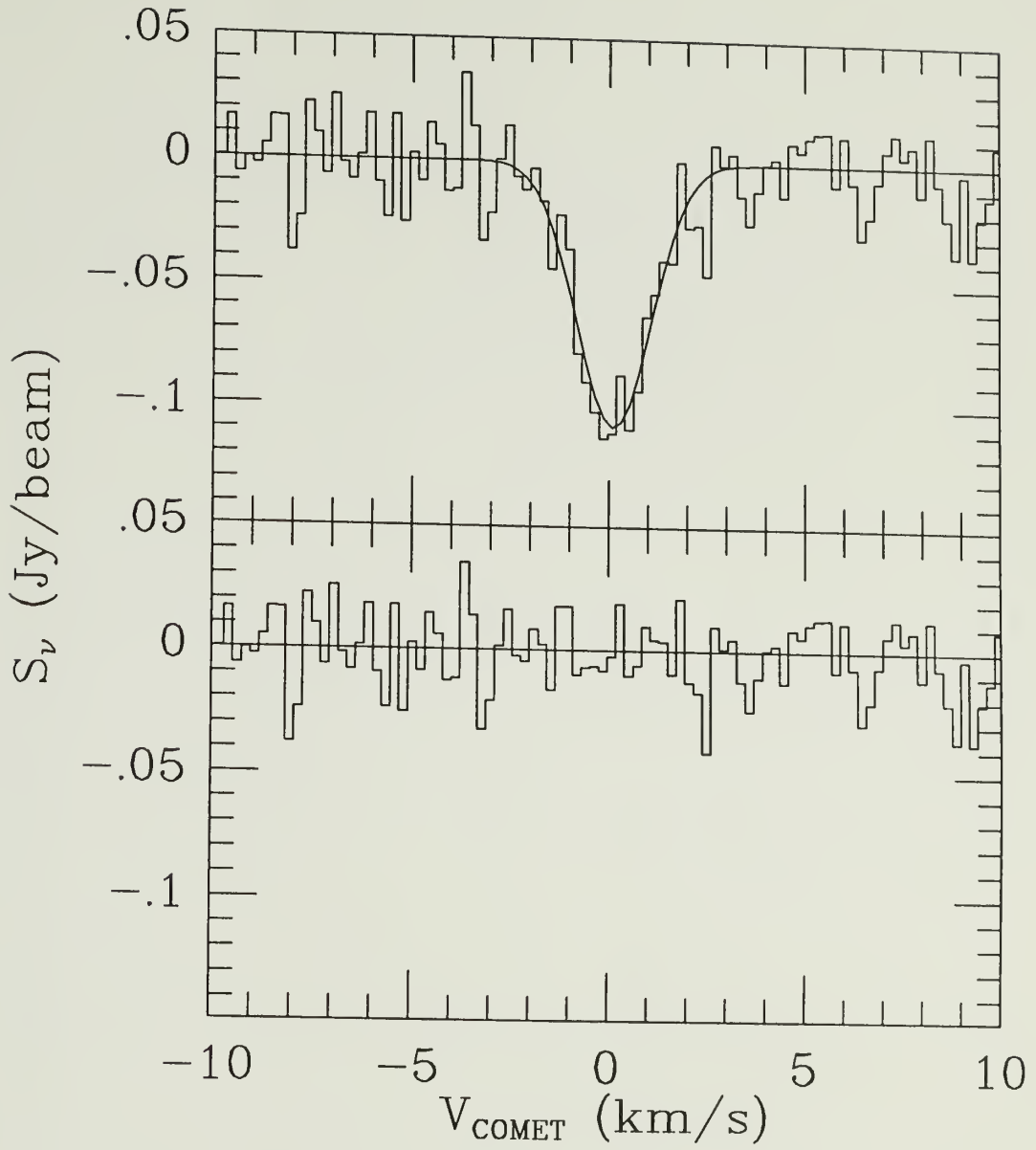


Figure 2.2o: The data of Figure 2.1o with the best fitting Gaussian curve (top), and the associated residuals (bottom).



**Figure 2.2p:** The data of Figure 2.1p with the best fitting Gaussian curve (top), and the associated residuals (bottom).

Notes for Table 2.3:

<sup>1</sup>Geocentric (Earth-Comet) distance

<sup>2</sup>Heliocentric (Sun-Comet) distance

<sup>3</sup>Phase (Sun-Comet-Earth) angle

<sup>4</sup>from a Gaussian fit to the data;  $\Delta V$  is the mean velocity relative to the nucleus.



Table 2.3  
Sun-Comet-Earth Geometry and Line Characteristics

Comet	Epoch	$\Delta^1$ A.U.	$R_h^2$ A.U.	$\beta^3$ °	$S_{\nu, \text{peak}}^4$ Jy/beam	$\Delta V^4$ km s <sup>-1</sup>	FWHM <sup>4</sup> km s <sup>-1</sup>
P/Halley	Sept 1985	2.35	2.47	23.9	0.030 (0.004)	-0.37 (0.13)	1.86 (0.26)
P/Halley	Oct 1985	1.44	2.09	25.1	0.134 (0.005)	0.01 (0.04)	1.92 (0.08)
P/Halley	Nov 1985	0.72	1.71	5.2	0.318 (0.003)	0.06 (0.01)	1.90 (0.02)
P/Halley	Dec 1985	0.74	1.34	46.4	0.219 (0.005)	0.28 (0.03)	1.98 (0.06)
P/Halley	Jan 1986	1.21	0.97	52.3	0.157 (0.005)	0.33 (0.04)	2.37 (0.09)
P/Halley	Feb 1986	1.44	0.63	33.9	-0.080 (0.003)	-0.63 (0.06)	2.96 (0.11)
P/Halley	Mar 1986	0.90	0.94	65.3	-0.122 (0.003)	0.25 (0.05)	3.44 (0.10)
P/Halley	May 1986	0.89	1.67	29.9	-0.108 (0.004)	0.34 (0.04)	1.71 (0.07)
P/GZ	Jul 1985	0.77	1.29	52.0	0.101 (0.006)	-0.38 (0.07)	1.86 (0.12)
P/GZ	Aug 1985	0.49	1.04	73.0	-0.178 (0.008)	-0.01 (0.06)	2.20 (0.12)
P/GZ	Oct 1985	0.66	1.21	55.6	-0.055 (0.007)	-0.28 (0.15)	1.99 (0.26)
C/HG	Oct 1985	0.56	1.19	56.0	0.105 (0.004)	0.16 (0.06)	2.53 (0.11)
C/HG	Nov 1985	0.87	0.85	69.8	0.097 (0.004)	-0.05 (0.04)	1.78 (0.08)
C/Thiele	Nov 1985	0.64	1.41	38.2	-0.066 (0.004)	0.11 (0.07)	2.06 (0.14)
C/Wilson	Mar 1987	1.36	1.25	44.8	-0.201 (0.005)	-0.06 (0.03)	2.16 (0.06)
C/Wilson	May 1987	0.91	1.28	51.8	-0.108 (0.006)	0.11 (0.08)	2.24 (0.16)

distance in Figure 2.3. This figure illustrates that there is a nominal linewidth of  $1.9 \pm 0.1 \text{ km sec}^{-1}$  for comets observed beyond  $\sim 1$  A.U. from the sun.

Comets at smaller heliocentric distances tend to show much broader lines (the exception to this is the anomalous C/Hartley-Good line from November 1985). This broadening of lines at small heliocentric distances has been noted before for observations of OH (Schloerb, Claussen, and Tacconi-Garman 1987; Gérard *et al.* 1987a, b) as well as HCN (Schloerb *et al.* 1987) and has usually been ascribed to increases in the parent gas outflow velocity near the sun.

The mean velocities,  $\Delta V$ , for the spectra are also listed in Table 2.3. These mean velocities are all displaced from the rest velocity of the nucleus by less than  $0.70 \text{ km sec}^{-1}$  in magnitude. The Greenstein effect is largely responsible for these shifts, although anisotropies in the coma gas flow can also cause such shifts (see Claussen and Schloerb 1987).

## 2.4 Other Data Sets

While data from other sources have not been modeled as part of this work, they are nevertheless important as a basis for comparison with our model results. Observations of the  $\text{H}_2\text{O}$  molecule in Comets Halley and Wilson (Mumma *et al.* 1986; Larson *et al.* 1986; Larson, Mumma, and Weaver 1987; Larson, private communication) have proven to be valuable as they trace both the parent outflow velocity and outflow morphology. VLA images of the 18-cm

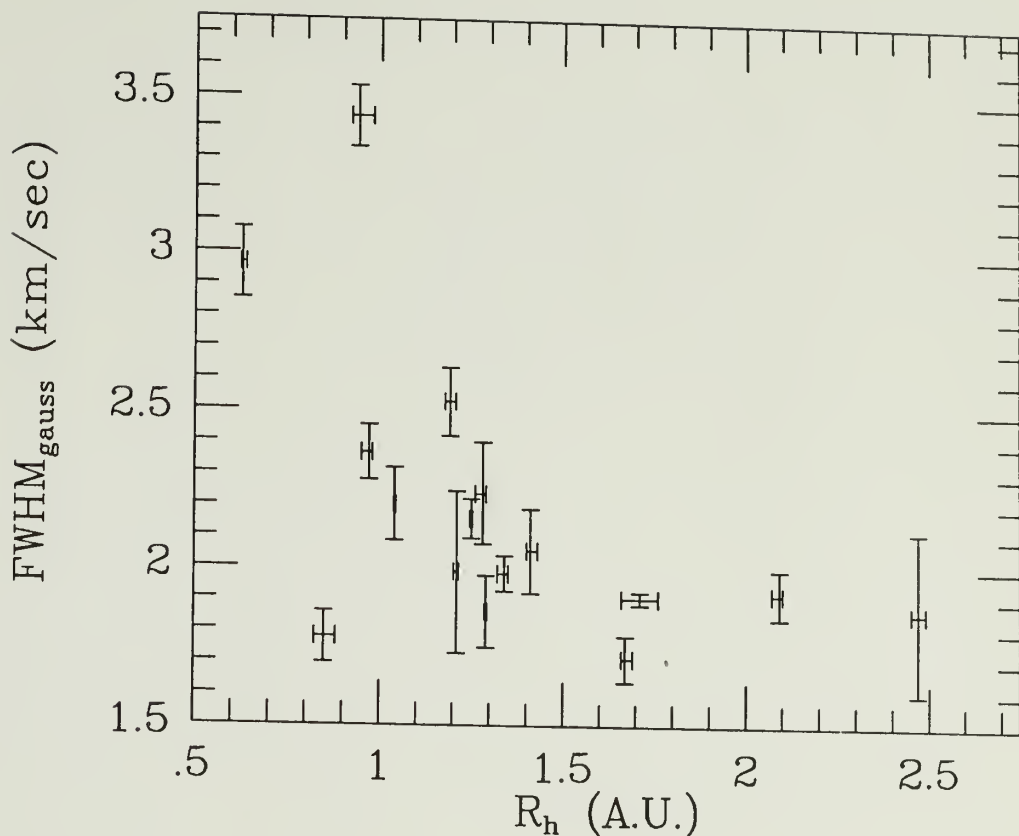


**Figure 2.3:** In this figure we have plotted the Full Width at Half Maximum (FWHM) of the OH lines used in this thesis as a function of heliocentric distance. The FWHM values are derived from the Gaussian fits to the data which, in most cases, represent the data well. The possible exceptions to that are the spectra from Comet Halley in March 1986 (see Figure 2.2g) and May 1986 (see Figure 2.2h). In the former case the profile is rather flat topped with steep edges, leading to a FWHM value which is perhaps a bit large. In the latter case, however, FWHM may be an underestimate since the fitting routine does not take into account the real *emission* feature seen to the left of the main absorption line. This figure illustrates, though, that there is a nominal linewidth of  $1.9 \pm 0.1 \text{ km sec}^{-1}$  for comets observed beyond  $\sim 1 \text{ A.U.}$  from the sun. Comets at smaller heliocentric distances show much broader lines as illustrated here.

line of OH in the coma of Comet Halley (de Pater, Palmer, and Snyder 1986) are also potentially useful indicators of the coma gas anisotropy.

Observations of the HCN molecule (Bockelée-Morvan *et al.* 1986 and Schloerb *et al.* 1987) provide further constraints on the parent outflow velocity. In fact, these data are even more useful than the H<sub>2</sub>O data owing to their more extensive temporal coverage. Rounding out the coverage are the observations of CN Jets/Shells (A'Hearn *et al.* 1986; Schlosser, Schultz, and Koczet 1986) which also yield determinations of the coma outflow velocity.

In addition to the above gas outflow velocity estimates, an *in situ* determination was made (Lämmerzahl *et al.* 1986) with data collected by the neutral mass spectrometer experiment (NMS) on board the Giotto spacecraft. Lämmerzahl *et al.* have used data from the NMS to derive the bulk velocity of water molecules at distances less than 10<sup>4</sup> km from the nucleus. Because this is the only *in situ* velocity determination, it is uniquely important for comparison with our model results from about the same epoch.

Revealing *in situ* images taken by the Giotto and Vega 1 and Vega 2 spacecraft (Keller *et al.* 1986a, b; Sagdeev *et al.* 1986b) have also been used for reference with our gas flow anisotropy model results. These data, however, represent only the distribution of the *dust* in the vicinity of the nucleus and therefore direct comparison is not possible. However, we can compare our anisotropy results with that inferred from the 1.38  $\mu\text{m}$  water data collected by the three-channel spectrometer (TKS) onboard the Vega 2 spacecraft

(Krasnopolsky *et al.* 1986, 1987). Additional comparisons can be made with anisotropies inferred from the neutral particle density results from the PLASMAG-1 instruments on Vega 1 and Vega 2 (Remizov *et al.* 1986) and the Neutral Gas Experiment (NGE) onboard Vega 1 (Curtis *et al.* 1986; Hsieh *et al.* 1987). A full discussion of our results in light of all the work referenced in this section appears in Chapter 4.

## CHAPTER 3

### THE KINEMATIC MODEL

#### 3.1 A Comparison of Two Models

The two principal models used to describe the gas kinematics of cometary comae are the Haser model (Haser 1957, 1966) and the vectorial model (Combi and Delsemme 1980a; Festou 1981a, b). Both models describe the flow of both the parent and daughter species within the coma, and agree (to first order) in their descriptions of the kinematics of the parent molecules. The parent molecules leave the nuclear region and travel radially outward into the coma. Some time later, these parent molecules are photodissociated by incident solar UV radiation, and excess energy involved in this photodissociation is converted to kinetic energy of the radicals. At this point the two kinematic models begin to differ strongly. In the Haser model the daughter molecules produced during the photodissociation *continue* to travel radially away from the nucleus. In the vectorial formalism, on the other hand, the direction taken by the daughter molecules is only constrained by conservation of momentum. The name vectorial comes from the fact that in this picture the final velocity of the daughter molecule is determined by the vectorial addition of the original parent velocity and the additional velocity impulse attained during the photodissociation of the parent molecule.

In choosing a model to describe a particular phenomenon, one is often confronted with a choice between ease of computation on one hand and physical reality in the form of observational evidence and plausibility on the other. The Haser model, with its uncluttered mathematics, seems at first to be the model of choice. However, when this model is applied to the calculation of expected daughter molecular scale lengths one finds that the predicted values are typically larger than those actually observed (Combi and Delsemme 1980a and references therein). The vectorial model, on the contrary, is quite complex mathematically as exemplified by the analytical treatment of Festou (1981a). However, Combi and Delsemme (1980a) have pointed out that the vectorial nature of the kinematics need not result in a complicated treatment of the problem. Indeed, their suggestion of applying the Monte Carlo technique to the vectorial model was a powerful breakthrough in this field. This technique allows one to introduce a variety of detailed effects with the only cost being that of computer time.

Given the above arguments, we have adopted the vectorial formalism in our effort to generate synthetic spectra, and employ the Monte Carlo method for increased flexibility. A flow chart for our model calculations is presented in Figure 3.1; we proceed as follows (complete details are found starting in Section 3.2):

- A parent ( $\text{H}_2\text{O}$ ) molecule is generated at some time  $t_i$  which lies in the range  $0 \leq t_i < t_{\text{obs}}$ . This observation time,  $t_{\text{obs}}$ , is chosen to be five times the

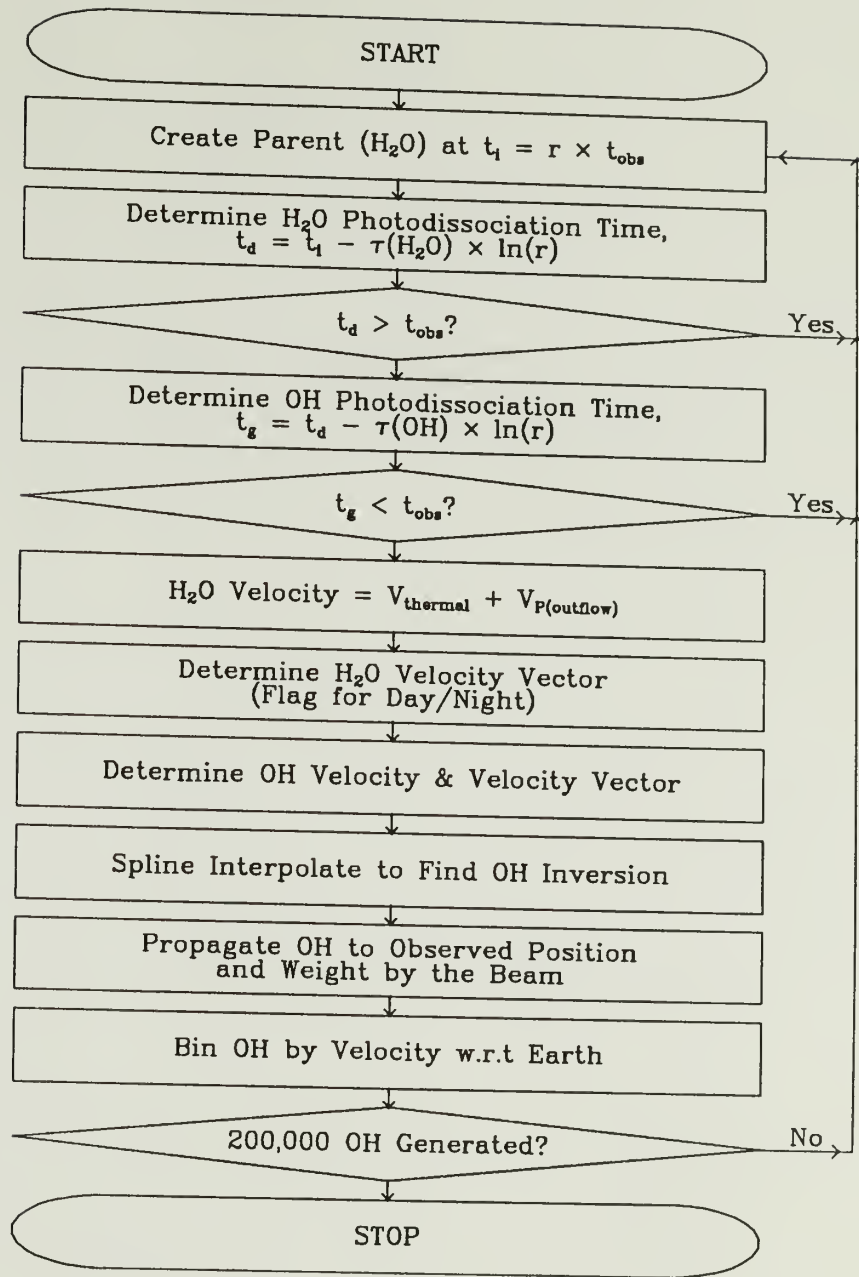


**Figure 3.1:** A flow diagram for the model used in this work. The variable  $r$  in some of the steps denotes a random number in the range  $[0,1)$  (see text).



sum of the parent and daughter lifetimes against photodissociation (see Section 3.2), thus the important parameters in this step are these lifetimes.

- The time at which that molecule photodissociates,  $t_d$ , is then calculated. If this time is after the time of our model observation of the comet then this parent molecule was unproductive for our purposes; we then go back to the top and generate another candidate parent molecule. For this step we need the lifetime of water.

- The next step is to determine when the OH radical itself will photodissociate. If it is dissociated prior to our model observation then it is not worth pursuing any further; again, we go to the top and generate another candidate parent molecule. This step requires a value for the lifetime of OH.

- If we have made it to this step it means we have a successful parent/daughter combination. Thus we now determine the parent and daughter directions and speeds. (In later models we also flag each parent to indicate whether it is from the dayside or the nightside of the nucleus, see below.) From this information it is straightforward to determine the inversion weight for the OH radical as well as its beam weight. Finally, we determine the velocity of the OH radical with respect to the Earth and add its contribution to the appropriate velocity bin. For this stage of the modeling we need both parent and daughter velocity distributions, the acceleration of an OH radical due to resonant scattering, and an inversion curve.

- The last step in the modeling process is to check the number of daughter molecules we have created. If that number is less than  $2 \times 10^5$ , a number chosen to minimize the statistical noise inherent in a Monte Carlo model such as this, while still producing results in a manageable amount of computer time, we go back to the top and select another candidate parent molecule.

In addition to the above mentioned input parameters, we also require the geometry of the observations. This includes the Sun–Comet distance ( $R_h$ ), the Earth–Comet distance ( $\Delta$ ), the Sun–Comet–Earth angle ( $\beta$ , also known as the phase angle), and the heliocentric velocity of the comet ( $\dot{R}_h$ ). For these parameters we use noise weighted values as described in Chapter 2, Section 2.2. Below we describe each step in the modeling process in greater detail.

### 3.2 The Birth of the Parents ( $H_2O$ Molecules)

Since, by their very nature, Monte Carlo simulations are subject to statistical fluctuations, it is important to suppress such fluctuations as much as possible. We accomplish this in two ways. First, as mentioned above, each of our simulations consists of  $2 \times 10^5$  OH radicals. Second, the length of time over which we allow  $H_2O$  molecules to be generated and dissociated into OH radicals before the system is observed is of sufficient length to properly sample the parent and daughter lifetime distributions. This observation time,  $t_{obs}$ , is chosen to be five times the sum of the parent and daughter lifetimes against

photodissociation (see Sections 3.3 and 3.4). We assume that there is constant production rate of molecules over the course of each simulation and therefore we use a random distribution of parent creation times over the length of each model simulation. Since all parent creation times ( $t_i$ 's) are equally probable in this case, they are determined from the expression  $t_i = r t_{\text{obs}}$ , where  $r$  is a random number chosen without bias on the interval  $[0,1)$ <sup>1</sup>, such that  $t_i$  values fall uniformly within the range  $0 \leq t < t_{\text{obs}}$ . We note that Combi and Smyth (1988a) have recently detailed a means of modeling a gas production rate which is variable over the course of a simulation such as this. However, the times at which surges in the gas production rate occur for any given comet are uncertain, thus use of such a scheme to model variable production rates seems unwarranted at this time.

### 3.3 The Death of the Parents

In order to make our model code more efficient we first ask whether each parent molecule we generate will produce a daughter molecule (an OH radical) before the time of our observation. If it will not generate a daughter it is ignored and another candidate parent is produced. To determine whether the parent is a viable one we must establish the time of its photodissociation. Our calculation of this time is in complete analogy with the determination of

---

<sup>1</sup>To generate this and all other random numbers used in this model we rely on the standard VAX-11 FORTRAN pseudo-random number generation function RAN which uses the algorithm  $X_{i+1} = ((2^{16} + 3) \times X_i) \bmod 2^{32}$  followed by scaling  $X_{i+1}$  to lie on the interval  $[0,1)$  to generate random number  $r_{i+1}$  from its predecessor  $r_i$ . All further reference to random numbers implies numbers lying in the range  $[0,1)$ .

the distance a particle travels in an infinite, homogeneous medium between collisions. Following on the work of Cashwell and Everett (1959), the probability of a photodissociation happening during the interval from  $t$  to  $t+dt$  is given by

$$p(t)dt = e^{-F\sigma t}F\sigma dt ,$$

where  $F$  is the flux of dissociating photons and  $\sigma$  is the photoabsorption cross section. This expression can be written in terms of the probability weighted average lifespan for molecules,  $\tau$ , which is given by

$$\tau = \frac{\int_0^{\infty} tp(t) dt}{\int_0^{\infty} p(t) dt} = \frac{1}{F\sigma} .$$

Thus, the probability density for dissociation in such a photon field is

$$p(t) = \frac{e^{-t/\tau}}{\tau} .$$

The probability *distribution* function is defined as the integral of the probability *density*, or

$$P(t) = \int_0^t p(t') dt' ,$$

which ranges in value from 0 (at  $t = 0$ ) to 1 (at  $t = \infty$ ). As random numbers chosen in the fashion described above also lie in the range  $[0,1)$ , it is easy to see that by setting  $P(t)$  equal to a random number one can uniquely determine  $t$  while uniformly sampling the probability distribution function. This latter point ensures that the probability of the photodissociation being between  $t$  and

$t + dt$  is given by  $p(t) dt$ . So, the lifespan of a molecule is determined from

$$r = P(t) = 1 - e^{-t/\tau}$$

(where  $r$  is a random number) which implies

$$t = -\tau \ln(1 - r).$$

Since  $(1 - r)$  is uniformly distributed on the interval  $[0,1]$  if  $r$  itself is, this expression can be simplified to

$$t = -\tau \ln(r).$$

Making the above equation specific to the case of the water molecule, we have

$$t_d = t_i - \tau_{\text{H}_2\text{O}} \ln(r),$$

where  $t_d$  signifies the time at which a daughter molecule is created.

For the water lifetime value we use the result of Festou (1981b) who bases his value of  $8.2 \times 10^4$  sec on the  $\text{H}_2\text{O}$  absorption cross section of Watanabe, Zelikoff, and Inn (1953) and the solar flux as reported in Thekackara (1970) and Widing, Purcell, and Sandlin (1970). This value is in agreement with the  $8.33 \times 10^4$  sec lifetime quoted by Huebner and Carpenter (1979), as well as the  $7.94 \times 10^4$  sec lifetime quoted by Crovisier (1988). All of these values are for a heliocentric distance of 1 A.U. We assume that

this lifetime is proportional to  $R_h^2$  (which follows from simple conservation of photodissociating flux).

### 3.4 The Death of the Daughters (OH Radicals)

In contrast with the parent molecules, we ask whether the daughter molecule produced during the photodissociation of the parent will *survive* until the observation time. If it is dissociated before this time it is ignored and another candidate parent is produced. In analogy with the above treatment of the parent molecules, the time at which the OH molecule produces a granddaughter molecule is given by

$$t_g = t_d - \tau_{\text{OH}} \ln(r),$$

where  $t_g$  is the time at which a granddaughter radical is created and  $\tau_{\text{OH}}$  is the lifetime of the OH radical.

Values for the lifetime of OH in a cometary coma have been determined by a number of authors (Jackson 1980; van Dishoeck and Dalgarno 1984 (hereafter vDD); Schleicher and A'Hearn 1988), with results differing by as much as a factor of 3. The cause for these disparities lies, in part, in the solar spectrum which is adopted. Jackson (1980), building on the earlier work of Potter and Del Duca (1964), demonstrated that a Swings-like effect (see Chapter 1, Section 1.2) works in influencing the photodissociation lifetime of OH. That is, since the photodissociation proceeds via excitation into discrete

levels above the dissociation threshold and since this excitation is heliocentric velocity dependent, the lifetime of OH is a function of the velocity of the comet. On a more detailed level, the lifetime of each molecule depends on its own particular velocity with respect to the sun, although this subtle effect is ignored in this work. Thus, slight variations between adopted solar spectra can lead to small differences in the derived OH lifetime at many velocities.

The complexity of the calculations also plays a critical role in the derivation of the lifetime of OH. For example, since the excitation of the OH molecules into these superdissociative energy levels takes place from the ground state the population inversion of that ground state (see Chapter 1, Section 1.2) is important to consider. Figure 3 of vDD, which shows that the difference between the OH lifetimes which are calculated with and without consideration of the ground state inversion can be as much as a factor of  $\sim 1.3$  at some heliocentric velocities, illustrates this point quite well.

Finally, calculated OH lifetimes depend on the number of possible upper levels considered, as is illustrated in Figure 2 of vDD. They have modeled absorption into the  $A^2\Sigma^+$  ( $v' = 2, 3$ ),  $1^2\Sigma^-$ ,  $1^2\Delta$ ,  $B^2\Sigma^+$ ,  $D^2\Sigma^-$ , and  $2^2\Sigma-3^2\Sigma$  states and included the inversion of the ground state (from Schleicher and A'Hearn 1982) into their calculation of  $\tau_{OH}$ . Because their modeling was the most complete and used the most up-to-date solar spectrum at the time this work began, we have adopted their (solar minimum) lifetime curve for use in our analysis. Recently, however, Schleicher and A'Hearn (1988) have suggested

that the vDD work may not properly model the physics of the OH dissociative process. Their first criticism is that vDD assumed that all molecules dissociate after being excited into the  $A^2\Sigma^+$  ( $v' = 2$ ) vibrational level. On the contrary, Schleicher and A'Hearn have found that one molecule in six radiatively decays from this level rather than dissociating. Furthermore, Schleicher and A'Hearn include the effect of heliocentric velocity in the excitation to the  $A^2\Sigma^+$  ( $v' = 3$ ) level which was ignored by vDD. Our model results (see Chapter 4) suggest, however, that the true lifetime of OH is nearer to that determined by vDD.

When using the vDD OH lifetime we are always careful to make it an explicit function of the heliocentric velocity of the comet. We do this by spline fitting the lifetime curve and determining the value of this spline at the appropriate heliocentric velocity<sup>2</sup>. We have neglected the more subtle effect of the lifetime of each *individual* OH radical having a lifetime which is a function of its particular heliocentric velocity (that is, a Greenstein-like effect for the lifetime). Finally, we also assume an  $R_h^2$  dependence for this lifetime.

### 3.5 Parent Velocity Distribution

After each successful parent/daughter pair is generated we determine their respective velocities. The parent velocity is taken to be a superposition of a Maxwellian velocity due to the temperature of the gas and a bulk flow velocity due to the expansion of the coma into the vacuum of space. Since

---

<sup>2</sup>To spline fit and interpolate this and all other curves in this model (see Section 3.8) we rely on the routines SPLINE and SPLINT as listed in Press *et al.* (1987). When using SPLINE we regard the slope at either endpoint as being “natural”, *i.e.* 0.



the water molecule has only weak resonance lines in the strongest portion of the solar spectrum, acceleration of water molecules by resonant scattering is unimportant. Therefore, the original parent velocity remains unchanged throughout the course of the life of the parent.

To generate the Maxwellian component of this velocity we sample the Maxwellian probability distribution and employ an acceptance-rejection scheme. A candidate speed ( $V_{\text{cand}}$ ) is generated by multiplying a random number by  $5 \times$  the most probable speed ( $V_{\text{mp}}$ ) for the chosen kinetic temperature. That is,

$$V_{\text{cand}} = r_1 (5) \sqrt{\frac{2 k T_k}{m_{\text{H}_2\text{O}}}}.$$

This assignment ensures that all parent velocities lie in the range  $[0, 5 V_{\text{mp}})$ , but since the fraction of all molecules traveling faster than  $5 V_{\text{mp}}$  is less than 1 in  $10^{10}$  we lose no generality in choosing this upper speed cutoff. We then choose a second random number ( $r_2$ ) and compare it to the value of the Maxwellian probability distribution (which has been normalized by its value at  $V_{\text{mp}}$ ) at the candidate speed. If

$$r_2 \leq \frac{m_{\text{H}_2\text{O}} V_{\text{cand}}^2}{2 k T_k} \exp\left(\frac{-m_{\text{H}_2\text{O}} V_{\text{cand}}^2}{2 k T_k} + 1\right)$$

we take the thermal component of the parent velocity to be  $V_{\text{cand}}$ . Otherwise, a new candidate speed is chosen and this whole process is repeated until the parent speed is successfully generated. For the kinetic temperature in this Maxwellian distribution, we use 50 K. For comets with gas production rates

of  $\sim 10^{29}$  molecules  $\text{sec}^{-1}$  such temperatures are typical for the region of the coma where the gas decouples from itself and ballistic flow ensues (Crifo 1986a; Bockelée-Morvan and Crovisier 1987). In any event, our choice for this kinetic temperature is not very critical since the thermal component of the parent velocity is small compared to the bulk outflow component, and the temperature only enters in through a square root.

For the bulk outflow velocity component of the parent velocity we use a range of values. Constraints for our parameter search come from both theoretical and observational evidence for what realistic outflow velocities should be. On the theoretical side, many authors (Marconi and Mendis 1983, 1984; Crovisier 1984; Huebner 1985; Bockelée-Morvan and Crovisier 1987; see also Crifo 1986b and references therein) have shown that for comets of average gas productivity velocities of  $\sim 0.8$  km  $\text{sec}^{-1}$  are expected near the point in the coma where the gas decouples from itself.

Observationally, Larson *et al.* (1986) estimate outflow velocities of  $0.9 \pm 0.2$  and  $1.4 \pm 0.2$  km  $\text{s}^{-1}$  from their pre- and post-perihelion infrared observations of water in Comet Halley. Radio observations of the hydrogen cyanide molecule in the coma of Comet Halley have led to outflow velocity estimates of  $1.5$  km  $\text{s}^{-1}$  (Despois *et al.* 1986) and from  $0.8$  km  $\text{s}^{-1}$  to  $1.15$  km  $\text{s}^{-1}$  (Schloerb *et al.* 1986b). In addition, Krankowsky *et al.* (1986) report an outflow velocity of  $0.9 \pm 0.2$  km  $\text{s}^{-1}$  for Halley based on Giotto neutral mass spectrometer (NMS) measurements. Although the above

estimates were made for only a few heliocentric distances they serve as an excellent basis for comparison with our model results.

In this work we span a range of outflow velocities from 0.2–0.4 km s<sup>-1</sup> up to whatever outflow velocity is necessary to fit our spectra given a minimum  $\chi^2_{\nu}$  criterion. Originally, we only simulated one parent outflow velocity at a time. However, the constant need for making our modeling effort more efficient has prompted us to make it possible to simulate 5 different parent outflow velocities simultaneously. This cuts down the CPU consumption of the model by a factor of about 3.5 (additional overhead prevents this factor from being 5). Chapter 4 contains details on our parent outflow velocity results.

### 3.6 Parent Outflow Morphology

In the following discussion, we will use the terms dayside and nightside to describe regions of the coma and nucleus of a comet. Before we do so, we must describe the geometry used in our model. As shown in Figure 3.2, the origin of both the antisun (unprimed) and anti-earth (primed) coordinate systems lies at the center of the comet. We take the +z-axis to point in the antisun direction, while the +y-axis lies perpendicular to the sun-comet-earth plane. The utility of defining the axes in this fashion is that conversion of the coordinates of a molecule (and its velocity) in the antisun system to the anti-earth system for purposes of beamweighting (and line-of-sight velocity determination, see below) involves only rotation about the y-axis by the phase

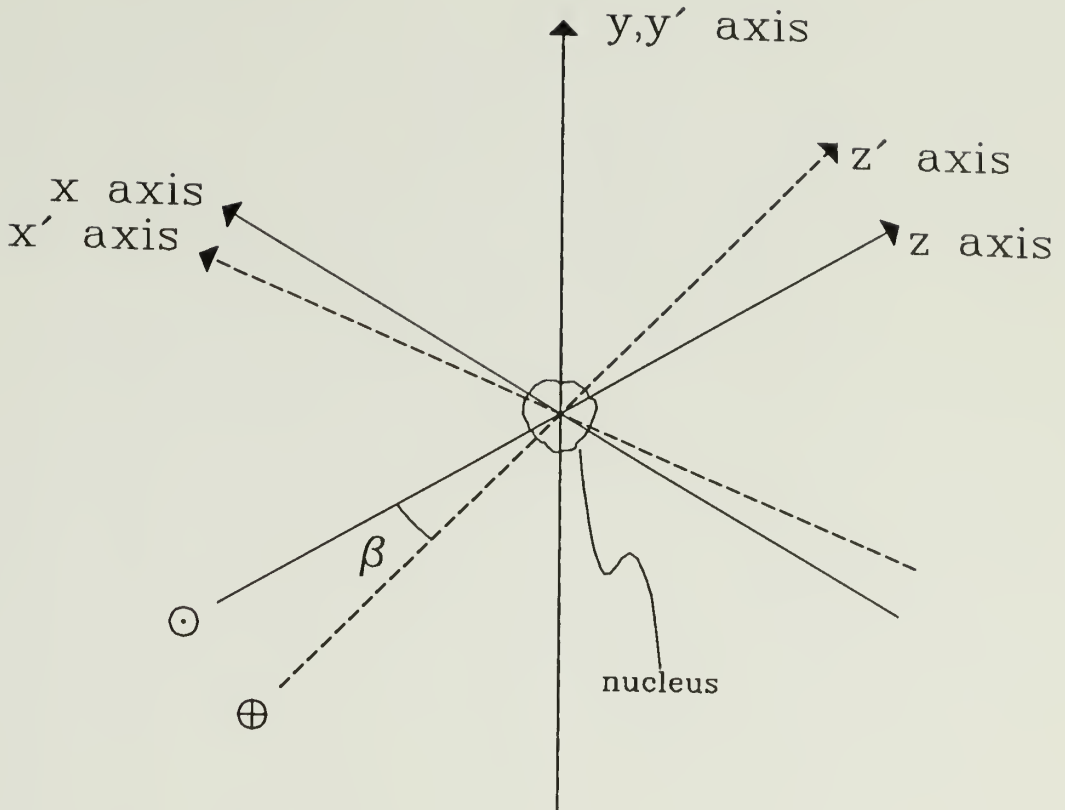


**Figure 3.2:** The coordinate systems used in our modeling. The origin for both coordinate systems is the nucleus of the comet. The  $x$ ,  $x'$ ,  $z$ , and  $z'$  axes all lie in a common plane which passes through the sun, the earth, and the comet. The  $y$  and  $y'$  axes are coincident and perpendicular to this plane. The  $z$  axis points away from the sun, while the  $z'$  axis points away from the earth. Transformation of coordinates in the unprimed frame to the prime frame is accomplished by rotation through the angle  $\beta$ , known as the phase angle.

angle (the sun-comet-earth angle,  $\beta$ ) for the epoch being modeled (see Section 3.9). Based on this coordinate definition, it is easy to see that the dayside of the comet is defined by the relations

$$\frac{\pi}{2} \leq \theta \leq \pi$$

and

$$0 \leq \phi < 2\pi,$$

where  $\theta$  and  $\phi$  have their usual spherical coordinate meanings.

Now, in our initial modeling the direction in which each parent molecule travels was established by a two-step method. The first of these steps is to force which hemisphere (day or night) of the coma the water molecule enters by imposing a predefined day/night outflow ratio. The governing parameter for this determination is called the anisotropy parameter. This parameter, hereafter referred to as AP, is defined as follows,

$$AP \equiv \log [Q_{\text{day}}/Q_{\text{night}}],$$

where  $Q_{\text{day(night)}}$  represents the production rate into the day (night) hemisphere. Thus, the fraction of all molecules which enter the night hemisphere of the coma is given by

$$f_n = \frac{Q_{\text{night}}}{Q_{\text{total}}} = \frac{1}{1 + 10^{AP}}$$

(hereafter,  $f \equiv 10^{AP}$ ). In practice, we choose a random number ( $r$ ) and

compare it to  $f_n$ , determining which hemisphere the molecule enters as follows:

$$\text{hemisphere} = \begin{cases} \text{day,} & f_n < r < 1; \\ \text{night,} & 0 \leq r \leq f_n. \end{cases}$$

Within each hemisphere, we treat the emission as being isotropic. This technique is quite schematic, but the results of such modeling are illustrative of the gross outflow properties of the coma. Any strong jets of emission, for example, would show up in our model results in the form of large derived AP values (or large negative values in the somewhat unlikely event that the jet originates on the nightside). The only artifact of this modeling scheme is an outflow discontinuity at the terminator which we feel is a minor problem in light of its utility.

The second step in determining the direction in which the parent travels is to distribute the molecules within the two hemispheres. To accomplish this, we use the same random number which was used to make the day/night decision. That is, for molecules which enter the day hemisphere, the cosine of the spherical angle  $\theta$  is given by

$$\cos \theta = \frac{1 - r(1 + f)}{f},$$

while for the other hemisphere we use

$$\cos \theta = 1 - r(1 + f).$$

Both of these forms reduce to the standard

$$\cos \theta = 1 - 2r$$

for the case of pure isotropic emission ( $f = 1$ ; see Cashwell and Everett 1959).

Finally, we determine the azimuthal angle,  $\phi$ , by the formula

$$\phi = r'(2\pi),$$

where  $r'$  is another random number.

More recently, however, we have made our model perform more efficiently and we have adopted a new strategy for simulating differing day/night outflow ratios. Rather than the laborious method of using a different day-to-night ratio for each model simulation, we now model only isotropic outflow. Within each simulation, each water molecule is assigned a flag indicating whether it came from the dayside or the nightside of the nucleus. We then accumulate two spectra for each parent outflow velocity, one which represents the contribution from the dayside molecules and one arising from the nightside molecules. To simulate different day-to-night ratios we simply construct linear combinations of these two spectra. This whole process is faster than the prior technique by a factor of about  $n$ , where  $n$  is the number of different day-to-night ratios being simulated, and the model results are identical to those obtained with the old technique.

### 3.7 Daughter Velocity and Spatial Distributions

The daughter molecules receive an additional velocity component in a random direction at the time of their creation. This additional velocity arises from the excess energy of the dissociating photon. This process has been studied in detail by Festou (1981b) who divides the photons shortward of  $1860\text{\AA}$  (the wavelength below which the water absorption cross section has non-negligible values) into three regimes.

The first of these regimes is defined by the range  $1357\text{\AA} < \lambda < 1860\text{\AA}$ , the first absorption band ( $\tilde{X}^1A_1 - \tilde{A}^1B_1$ ) of water. Photons in this regime are responsible for the bulk of the photodissociation of water in the coma; about 72% of all water molecules are destroyed by such photons during periods of relative solar inactivity. Festou also found this regime to be important because the excess photon energy was insufficient to either vibrationally or electronically excite the offspring molecules. Thus the excess energy was distributed amongst the daughter molecules as kinetic energy. He derived a velocity for the OH radicals which had a Gaussian distribution with a mean velocity of  $1.15 \text{ km s}^{-1}$  and a dispersion of  $0.08 \text{ km s}^{-1}$ .

The second of Festou's photodissociation regimes covers the range  $\lambda < 1357\text{\AA}$ ,  $\lambda \neq 1216.6\text{\AA}$  (the second ( $\tilde{X}^1A_1 - \tilde{B}^1A_1$ ) and subsequent absorption bands), while the third regime corresponds to  $\lambda = 1216.6\text{\AA}$  (Ly  $\alpha$ ).

Photodissociation of water by photons in these two wavelength regions is less common and accounts for only about one quarter of the total number of water



molecule dissociations within the coma. Therefore, since first band absorption is the dominant water photodissociative channel and Festou had done the most complete treatment of the water dissociation problem at the time, most analyses of the coma requiring knowledge of the gas kinematics since that time have used an OH velocity of  $1.15 \text{ km s}^{-1}$ .

More recent theoretical and experimental results, however, have shown that in fact the OH radicals may be created in vibrationally excited states (for first band absorption) and rotationally excited states (for second band absorption; see references in Crovisier 1988). Allowing for this excitation, Crovisier (1988) derives an OH velocity distribution which has a mean value of  $1.05 \text{ km s}^{-1}$  ( $0.1 \text{ km s}^{-1}$  lower than the mean velocity derived by Festou for first band absorption) and a longer tail towards small velocity than the distribution derived by Festou. Since the important velocity in affecting the scale length of the coma is the *vectorial sum* of the parent and daughter velocities, it is imperative that we use the daughter velocity distribution which is based on the most complete treatment of the water dissociation problem. Thus, for our modeling we have adopted the daughter velocity distribution as derived by Crovisier (1988). When using this OH velocity distribution, we take into account the fact that the OH molecule has some strong resonance lines in its 0-0 band which give rise to an appreciable radiative acceleration via scattering. Dolginov, Gnedin, and Novikov (1971) have determined this

acceleration to be  $0.01 R_h^{-2} \text{ cm s}^{-2}$  and we have adopted their value for our modeling.

In the true spirit of the vectorial model, the distribution of directions taken by daughter molecules following the destruction of their parents is isotropic *in the rest frame of the parent molecule*. That is, each OH radical leaves the scene of the dissociation in a direction defined by the spherical angles  $\theta_d$  and  $\phi_d$ , which are determined from the following relations:

$$\cos \theta_d = 1 - 2r_1$$

and

$$\phi_d = r_2 (2\pi),$$

where both  $r_1$  and  $r_2$  are random numbers. The origin for the “sub-d” coordinates is the site of the photodissociation, where the +z-axis points away from the sun.

### 3.8 Inversion Weighting

Having established the complete trajectory of the OH radicals, it is straightforward to determine both their positions within the coma and their velocities at the observation time. Finally, to produce spectra we must weight each molecule by its inversion value (thereby directly modeling the Greenstein effect), apply a beamweighting factor, and add its contribution

to the appropriate velocity bin. These processes are discussed in this and the following two sections.

Although the inversion curve of Schleicher and A'Hearn (1988) is based on a more recent (and therefore more reliable) solar atlas than that used to derive the Despois *et al.* (1981) curve, Schleicher and A'Hearn themselves have compared data from the literature with the predictions of both inversion curves and conclude that neither curve is uniformly better than the other over the entire range of heliocentric velocities. Therefore, we have chosen to use both inversion curves. This leads to two different results for any given model spectrum, and the resulting disparity of results have been folded into our error analysis.

In practice, whichever inversion curve is used is first spline fit. The inversion weight of each molecule is determined by the value of this spline curve at the heliocentric velocity of the molecule. Finally, this inversion weight is taken to be independent of heliocentric distance (*cf.* Schleicher and A'Hearn 1988).

### 3.9 Beam Weighting and Velocity Binning

In our model we are capable of simulating a variety of observations. It is possible to generate a model map of as many as five beams with offsets expressed in terms of RA and Dec or  $x'$  and  $y'$ -coordinates (see Figure 3.2). We also can generate simultaneously the spectra that would be seen if up to

five different observatories had pointed their telescopes at the nuclear position. For any model observing mode, we begin determining the beam weight(s) for each molecule by transforming its coordinates in the unprimed coordinate system  $(x_{\text{OH}}, y_{\text{OH}}, z_{\text{OH}})$  to the plane of the sky (the  $x'y'$ -plane). That is,

$$x'_{\text{OH}} = x_{\text{OH}} \cos \beta - z_{\text{OH}} \sin \beta$$

and

$$y'_{\text{OH}} = y_{\text{OH}},$$

where  $\beta$  is the sun-comet-earth angle. Next, if the coordinates of the beam center(s) is(are) given in the RA and Dec system we further transform the coordinates of the OH radical as follows

$$\alpha_{\text{OH}} = x'_{\text{OH}} \sin \rho - y'_{\text{OH}} \cos \rho$$

and

$$\delta_{\text{OH}} = x'_{\text{OH}} \cos \rho + y'_{\text{OH}} \sin \rho.$$

In these expressions,  $\rho$ , the angle between the comet-sun line (the  $-z$ -axis) and true north (the  $+Dec$ -axis), is found by the Laws of Sines and Cosines for spherical triangles (see Figure 3.3) and is given by

$$\rho = \arcsin \left[ \frac{\cos \delta_{\odot} \sin(\Delta\alpha)}{\sin(\arccos(\sin \delta_c \sin \delta_{\odot} + \cos \delta_c \cos \delta_{\odot} \cos(\Delta\alpha)))} \right],$$

where  $\alpha_{\odot(c)}$  and  $\delta_{\odot(c)}$  are the RA and Dec for the sun (comet) and

$\Delta\alpha = \alpha_{\odot} - \alpha_c$ . For either the RA/Dec or the  $x'/y'$  system, then, we are able

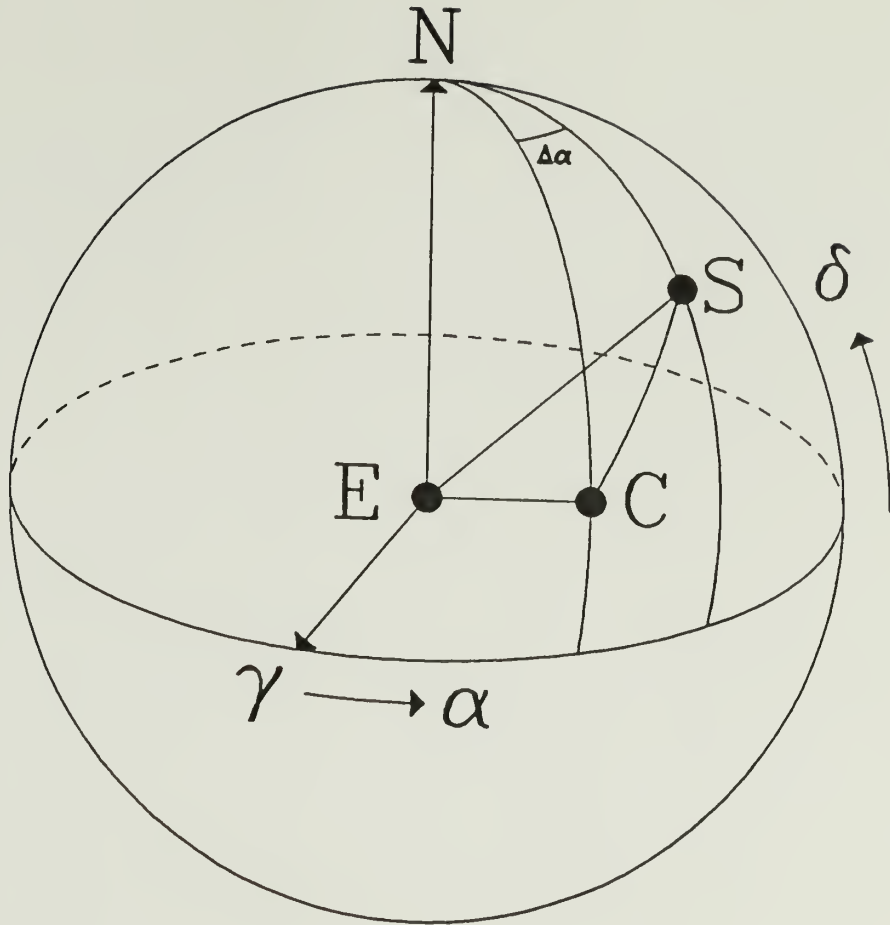


**Figure 3.3:** The Earth-Sun-Comet geometry. In this figure the Earth (E) is shown lying at the center of the celestial sphere. The complete ellipse (half of which is dashed) in the center of the figure represents the celestial equator. The directions towards true north (N) and the Vernal Equinox ( $\gamma$ ) are shown. Also in this figure are arrows indicating the directions in which Right Ascension ( $\alpha$ ) and Declination ( $\delta$ ) increase. The line joining the comet (C) and the sun (S;  $\overline{CS}$ , seen as an arc when projected onto the celestial sphere) is defined to be the  $-z$  axis (see text). Thus, the angle  $\rho$  is  $\angle NCS$ .

to determine the offset(s) of the OH radical from the beam center(s). Finally, the beam weight(s) are found using the formula

$$\text{beam weight}_i = \exp\left(-4 \ln(2) \sum_j \frac{\text{off}_{i,j}^2}{B_{i,j}^2}\right),$$

where  $\text{off}_{i,j}$  is the  $j$ th coordinate of the  $i$ th beam offset and  $B_{i,j}$  is the  $j$ th dimension of beam  $i$ .

The final step in generating a model spectrum is to add the product of the inversion and beam weights for each OH molecule to the appropriate velocity channel of the modeled 256-channel spectrometer. Thus, we need to know the velocity of the molecule with respect to the earth (*i.e.* in the primed coordinate frame). Its heliocentric velocity is easily transformed to this plane by the expression

$$\dot{z}'_{\text{OH}} = \dot{z}_{\text{OH}} \cos \beta + \dot{x}_{\text{OH}} \sin \beta.$$

This velocity is then used to determine the proper channel index and the product of the beam and inversion weights is added to the running sum for that channel.

## CHAPTER 4

### MODEL RESULTS

#### 4.1 Introduction

The outstanding success of radio observations of Halley's Comet by the International Halley Watch has shown that there is much to be learned from observations of the 18-cm OH transitions. The OH emission is not only a useful probe of the composition of gas in the comae of comets (see, for example, Snyder 1985 and references therein) but can also be exploited to study the gas kinematics within the coma (Bockelée-Morvan and Gérard 1984, Bockelée-Morvan *et al.* 1985, Tacconi-Garman and Schloerb 1987a, b).

In this chapter we investigate the roles that cometary gas productivity and heliocentric distance play in influencing the coma kinematics. Since gas productivity in comets tends to increase with decreasing heliocentric distance (see *e.g.* Ney 1982), we must have some way of separating the influence of the heliocentric distance on the coma kinematics from that of the gas production rate alone. We are able to accomplish this separation through the analysis of spectra from a number of comets at a few common heliocentric distances (see Section 4.3.3).

However, the gas production rate is not the only factor which can determine the parent gas flow properties. Indeed, it is well known that parent molecules flow more rapidly as the comet nears the sun (*e.g.* Delsemme 1982

and references therein). Delsemme presents both theoretical reasoning and observational evidence (from Whipple 1980) which points to a velocity law of the form

$$V_P = (V_P)_0 R_h^{-n} ,$$

where  $R_h$  is expressed in A.U. and  $n = 0.5$  (theoretical) or  $0.6$  (observational). In order to determine if our observed OH line profiles are consistent with a dependence of this form, we have modeled the high S/N ( $\gtrsim 3$ ) data from P/Halley, as well as from P/Giacobini-Zinner, C/Hartley-Good, C/Thiele, and C/Wilson. These data represent a wide range of heliocentric distances from that taken in September 1985 ( $R_h = 2.47$  A.U.) through perihelion for Comet Halley in February 1986 ( $R_h = 0.63$  A.U.) to that taken in May 1986 ( $R_h = 1.67$  A.U.). For the presentation and preliminary discussion of these data the reader is referred to Chapter 2 of this thesis.

We begin our discussion in Section 4.2 with the calculations of the gas production rates and the comparisons of these values to those derived by other authors from other observations. Following that, we present and discuss our model results in light of other recent observations and theoretical endeavors (Section 4.3).

## 4.2 Gas Production Rates

We have calculated gas production rates for all the cometary spectra in this thesis via the method outlined in Schloerb and Gérard (1985). Thus, we



begin by adopting their expression for the average flux density of a cometary OH line,

$$S_\nu = \frac{A_{ul} i k T_{BG}}{4\pi\Delta^2} \frac{c}{2\nu V_{max}} \frac{2F_u + 1}{8} \Gamma$$

(equation 11 of Schloerb and Gérard). In this equation  $A_{ul}$  is the Einstein spontaneous emission term,  $i$  is the inversion of the ground state  $\Lambda$ -doublet levels,  $T_{BG}$  is the background temperature,  $F_u$  is the statistical weight of the upper level of the transition,  $\Delta$  is the earth-comet distance, and  $V_{max}$  is the maximum expansion velocity of the gas in the coma.  $\Gamma$  is defined to be the product of  $Q_P$ , the production rate of all possible OH parent species, and  $\tau_{OH}$ , the lifetime of the OH molecules. Since  $2V_{max}S_\nu$  is simply the velocity-integrated flux, which we will call  $I_{OH}$ , the expression for the production rate of OH reduces to

$$Q_{OH} = \frac{7.06 \times 10^{25}}{i} \left[ \frac{3.3 \text{ K}}{T_{BG}} \right] \left[ \frac{10^5 \text{ sec}}{\tau_{OH}} \right] \left[ \frac{\Delta}{1 \text{ AU}} \right]^2 \left[ \frac{I_{OH}}{1 \text{ mJy km s}^{-1}} \right] \text{ mol s}^{-1}.$$

For this expression, which we have written for the 1667 MHz line, we have taken the value for  $A_{ul}$  from Destombes *et al.* (1977). We have also assumed a constant background temperature of 3.3 K for all comets. Lastly, since our model results provide few clues as to which inversion curve is more appropriate for a given heliocentric velocity (Section 4.3), we use an average of the inversion values from the inversion curve of Despois *et al.* (1981; hereafter Despois) and from that of Schleicher and A'Hearn (1988; hereafter SA) in our calculation of the production rates; the error determination for these production rates reflect

the disparity in the inversion curves. The exception to this approach is the case of the May 1986 P/Halley observations (see Chapter 2, Section 2.3; see also below). To account for the effects of beam resolution on our observed  $I_{OH}$  values, we have used both the parameters of the Festou vectorial model (Festou 1981a, b) and Radio Model 1986a (Schloerb, Claussen, and Tacconi-Garman 1987). Our adopted gas production rates are based exclusively on the Radio Model 1986a values as its parameters are closest to those derived in our models (see below).

We have made further approximate corrections to the derived production rates to account for the effects of quenching of the OH  $\Lambda$ -doublet (Schloerb 1988). To obtain the multiplicative factors used for this correction we have interpolated between values listed in Table 2 of Schloerb using an inverted 4-point bilateral interpolation scheme; as the spacing between values in this table is rather coarse, and this is a simplified approach to the quenching problem, we stress that these corrections should be viewed as “zeroth order” corrections. Furthermore, for one set of observations, those of Comet Halley in February 1986, we have had to extrapolate to a higher resolution parameter than was listed in that table. In all cases we have assumed a value of 0.1% for the ion/electron fraction. The maximum multiplicative correction factor for the Radio Model 1986a results was 4.54 (Comet Halley for the May 1986 observations), and in cases where the uncorrected gas production rates were

lower than  $2 \times 10^{28}$  molecules  $\text{sec}^{-1}$  we have not corrected for quenching effects.

The error in these production rate determinations comes from a variety of sources. First, the observational 18-cm line integrals,  $I_{\text{OH}}$ , have intrinsic error in them. In addition, there is an error which arises from the epoch averaging procedure. That is, the average data are from a range of heliocentric and geocentric distances and heliocentric velocities. The heliocentric distance enters into the production rate calculation through the lifetime of the OH radical, which is taken to vary as  $R_h^2$ . The variation in heliocentric velocity over the course of a series of observations results in an inversion which is time variable. However, a larger source of inversion error arises from the differences in the values of the inversion at particular heliocentric velocities indicated by the two inversion curves. In addition, there is the uncertainty associated with the choice of kinematic parameters used to describe the coma. The relative contributions of all of these error sources vary from epoch to epoch but in most cases the dominant source of error *for a given kinematic model* is the uncertainty in the inversion. Therefore, our adopted production rates are the averages of those derived using the Despois and SA inversion curves and the errors on these values are derived from the discrepancy between the two values. In cases where this discrepancy is less than 15% we have assumed a nominal error of 15% to account for the other error contributions.

In Tables 4.1 and 4.2 we present a summary of our production rate calculations for the cometary observations of this thesis. In Figure 4.1, we compare our production rates for Comet Halley with those obtained from IUE OH data using the Festou vectorial model (Feldman *et al.* 1986). In the top portion of this figure we present our Festou vectorial model OH production rates, while in the bottom panel we show our Radio Model 1986a results. The agreement between our results and the UV results shown in the top panel of this figure illustrates that the long standing disparity between UV and radio gas production estimates can be attributed to the effects of quenching of the OH  $\Lambda$ -doublet (see Schloerb 1988 and references therein). For reasons cited above, however, we will adopt our Radio Model 1986a quenching-corrected production rates for the remainder of this work. These production rates are also compatible with the results of Feldman *et al.* (1986)(Figure 4.1, bottom panel).

### 4.3 The Model Results

#### 4.3.1 General Remarks

As fully detailed in Chapter 3, our model for the kinematics of the gas in the coma of a comet follows the original work of Combi and Delsemme (1980a). It is a vectorial model which fully incorporates the Greenstein effect, and accounts for the effects of beam resolution. Many parameters must be specified in a Monte Carlo simulation such as this one. First of all, it is necessary to

Epoch	$R_h$ A.U.	$I_{OH}$ Jy km s <sup>-1</sup>	Festou		Radio Model 1986a	
			$(Q_{OH})_{RADIO}$ 10 <sup>28</sup> mol s <sup>-1</sup>	$Q_{OH}^1$ 10 <sup>28</sup> mol s <sup>-1</sup>	$(Q_{OH})_{RADIO}$ 10 <sup>28</sup> mol s <sup>-1</sup>	$Q_{OH}^1$ 10 <sup>28</sup> mol s <sup>-1</sup>
Sept 1985	2.47	0.055	0.91 (0.14)	0.91 (0.14)	1.25 (0.19)	1.25 (0.19)
Oct 1985	2.09	0.273	3.31 (0.50)	4.70 (0.71)	4.43 (0.66)	7.85 (1.18)
Nov 1985	1.71	0.642	5.03 (0.76)	9.50 (1.50)	6.41 (0.96)	15.72 (2.58)
Dec 1985	1.34	0.473	6.94 (1.17)	11.69 (2.59)	9.71 (1.63)	21.82 (5.03)
Jan 1986	0.97	0.406	13.16 (2.79)	20.85 (5.33)	22.87 (4.85)	69.36 (28.22)
Feb 1986	0.63	0.224	26.09 (5.39)	38.93 (10.65)	50.57 (10.35)	168.86 (58.19)
Mar 1986	0.94	0.426	16.58 (4.23)	31.26 (11.09)	27.71 (7.07)	120.42 (59.63)
May 1986	1.67	0.208	11.79 (1.77)	27.32 (4.10)	15.69 (2.35)	71.25 (10.69)

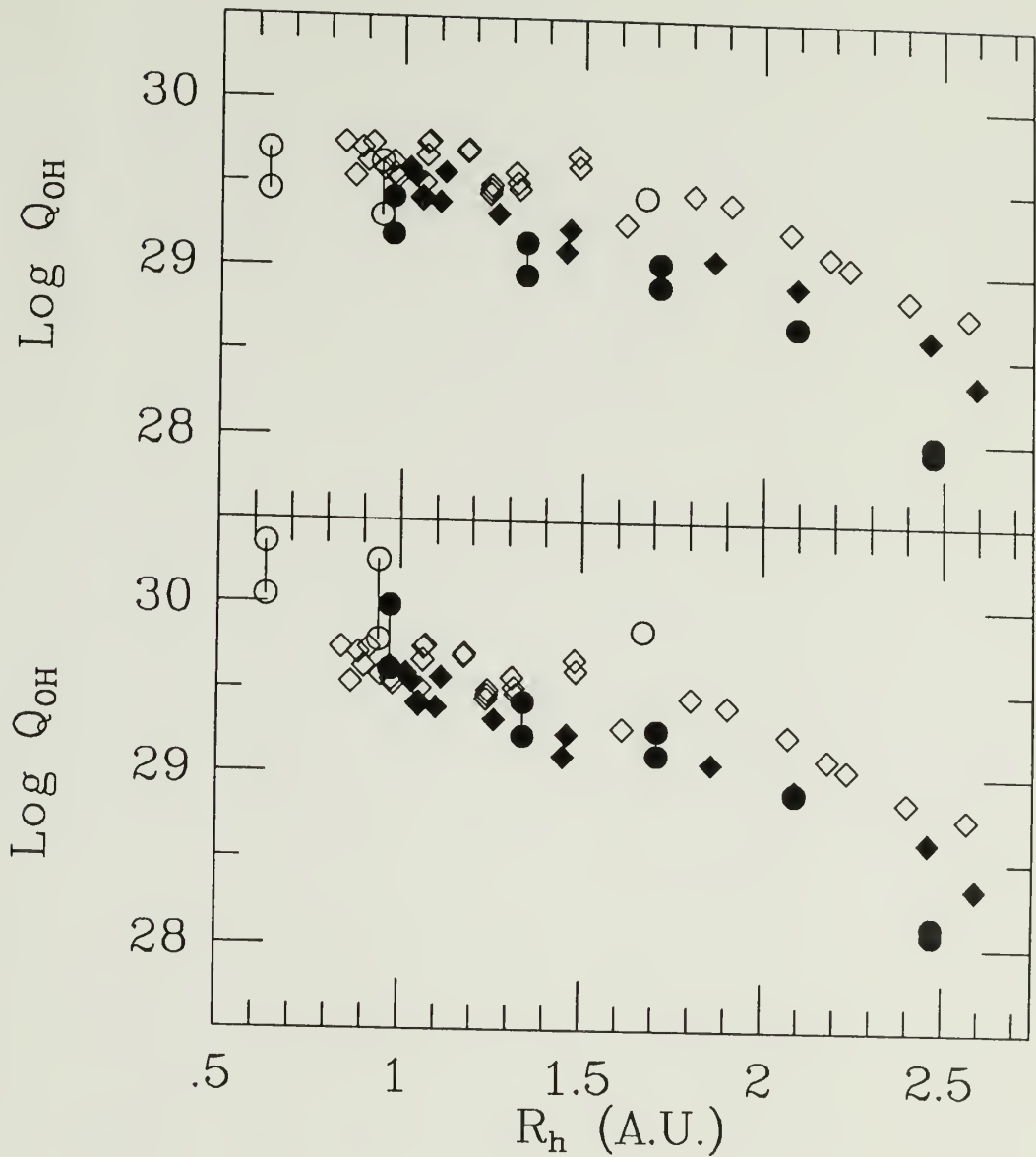
<sup>1</sup>Corrected for quenching of the OH  $\Lambda$ -doublet

Table 4.2

Line Integrals and Production Rates for Comets Giacobini-Zinner, Hartley-Good, Thiele, and Wilson

Comet	Epoch	$R_h$ A.U.	$I_{OH}$ Jy km s <sup>-1</sup>	Festou		Radio Model 1986a	
				$(Q_{OH})_{RADIO}$ 10 <sup>28</sup> mol s <sup>-1</sup>	$Q_{OH}^1$ 10 <sup>28</sup> mol s <sup>-1</sup>	$(Q_{OH})_{RADIO}$ 10 <sup>28</sup> mol s <sup>-1</sup>	$Q_{OH}^1$ 10 <sup>28</sup> mol s <sup>-1</sup>
P/GZ	Jul 1985	1.29	0.183	2.65 (0.66)	3.14 (1.15)	3.80 (0.94)	5.91 (1.97)
P/GZ	Aug 1985	1.04	0.433	3.62 (0.54)	4.85 (0.73)	5.15 (0.77)	8.90 (1.33)
P/GZ	Oct 1985	1.21	0.100	1.18 (0.18)	1.18 (0.18)	1.69 (0.25)	1.69 (0.25)
C/HG	Oct 1985	1.19	0.295	1.73 (0.26)	1.73 (0.26)	2.40 (0.36)	2.40 (0.36)
C/HG	Nov 1985	0.85	0.178	1.75 (0.26)	1.75 (0.26)	3.01 (0.45)	3.01 (0.45)
C/Thiele	Nov 1985	1.41	0.148	1.03 (0.15)	1.03 (0.15)	1.37 (0.21)	1.37 (0.21)
C/Wilson	Mar 1987	1.25	0.461	8.33 (1.25)	12.76 (1.91)	13.52 (2.03)	28.40 (4.26)
C/Wilson	May 1987	1.28	0.264	6.45 (0.97)	10.00 (1.50)	9.59 (1.44)	19.87 (2.98)

<sup>1</sup>Corrected for quenching of the OH  $\Lambda$ -doublet



**Figure 4.1:** Comparison of radio and UV gas production rates. In each panel the diamonds show the UV gas production results for Comet Halley (Feldman 1986) and the circles show our results. Pre-/Post-perihelion results are represented by filled/open symbols. The top panel illustrates our Festou vectorial model results while the bottom panel shows Radio Model 1986a production rates. In each case Despois and SA values are connected by a vertical line.

specify the distribution of the OH parent molecules as they emerge from the nucleus. Then parent molecules are sent outward from the nucleus with a particular velocity,  $V_P$ . At some later time, photodissociation occurs and the OH radical is formed. From this point OH goes in a random direction until the time of its photodestruction with an additional velocity,  $V_{OH}$ , which is added vectorially to  $V_P$ . Thus, the important parameters of this model are:

- parent production distribution
- parent outflow velocity
- parent lifetime against photodissociation
- OH velocity attained during parent photodestruction
- OH lifetime against photodissociation

Of these many parameters, the last three are related to the properties of the molecules themselves, rather than the comet, and they are all known (or knowable) from theoretical calculations. For this work, we adopt the theoretical values of these parameters and attempt to constrain the remaining parameters through fits to the data. The parent production distribution is schematically modeled through the anisotropy parameter, AP, while the parent outflow velocity,  $V_P$ , is directly modeled.

We have run a grid of models covering AP- $V_P$  parameter space for each comet. The grid spacing for AP values is typically 0.3 units, or roughly a factor of 2 in the ratio of day-to-night emission, while the parent outflow



velocity grid spacing is characteristically  $0.2 \text{ km sec}^{-1}$ . Both parameters are allowed to vary until a best fitting solution is obtained.

For each combination of AP and  $V_P$ , we have computed model spectra and fit these spectra to the appropriate data, representing the quality of the fits by values of  $\chi^2_\nu$ . We have searched AP- $V_P$  parameter space for the combination which produces the best fitting model for each spectrum. To arrive at this combination we first determine a  $\chi^2_\nu$  value for each point in the AP- $V_P$  grid. We then fit a three-dimensional paraboloid to the  $\chi^2_\nu$  surface in the vicinity of the minimum. From the minimum of that parabola we derive the best parameter combination while the curvature of the paraboloid is indicative of the errors in these parameters. In cases where the region near the minimum  $\chi^2_\nu$  value on our (coarse) grid was not symmetric with respect to either AP or  $V_P$  we refined the grid spacing to properly isolate the true minimum (Bevington 1969). For the July and October 1985 epochs of P/Giacobini-Zinner we are only able to derive a lower limit for AP since the quality of the fits are insensitive to changes in AP above a threshold value.

Our resulting  $\chi^2_\nu$  surfaces are shown in Figures 4.2a-p. In each of these figures, the top panel is the  $\chi^2_\nu$  surface for models in which we used the SA inversion curve, while the lower panel in each case shows the surface which results from models in which we used the Despois inversion curve. In both panels of each of these figures we have indicated the position of the derived best AP and  $V_P$  parameter combination along with their associated errors.

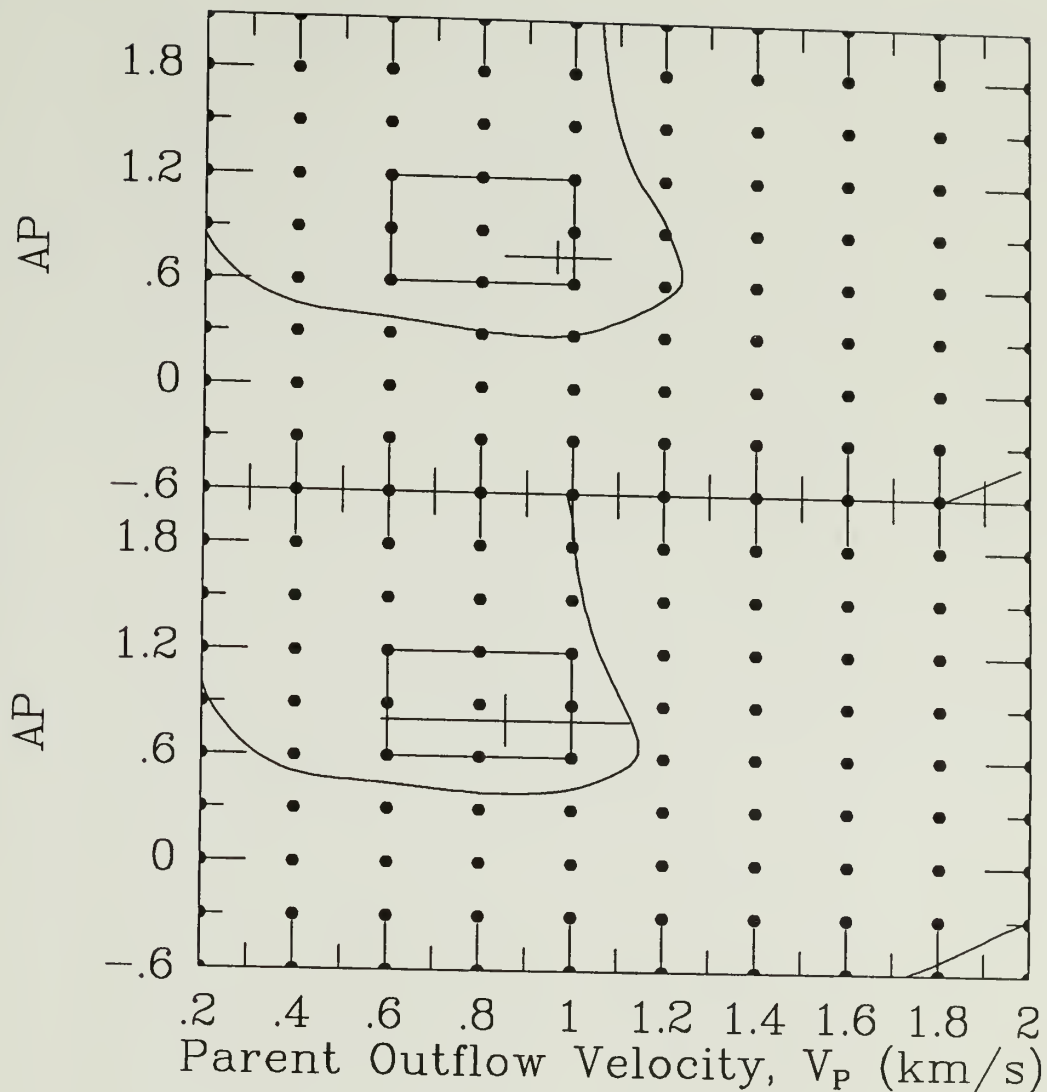


**Figure 4.2a:** The  $\chi^2_\nu$  surfaces derived from model fits to the September 1985 P/Halley spectrum. The top panel illustrates the surface from models using the Despois inversion curve, while the bottom panel shows the surface from models using the inversion curve of SA. The lowest contour is at a  $\chi^2_\nu$  value of 1.0 and the contour spacing is 0.5. The dots represent grid locations at which model spectra were generated. The inset boxes represent regions in which we have sampled parameter space more finely.

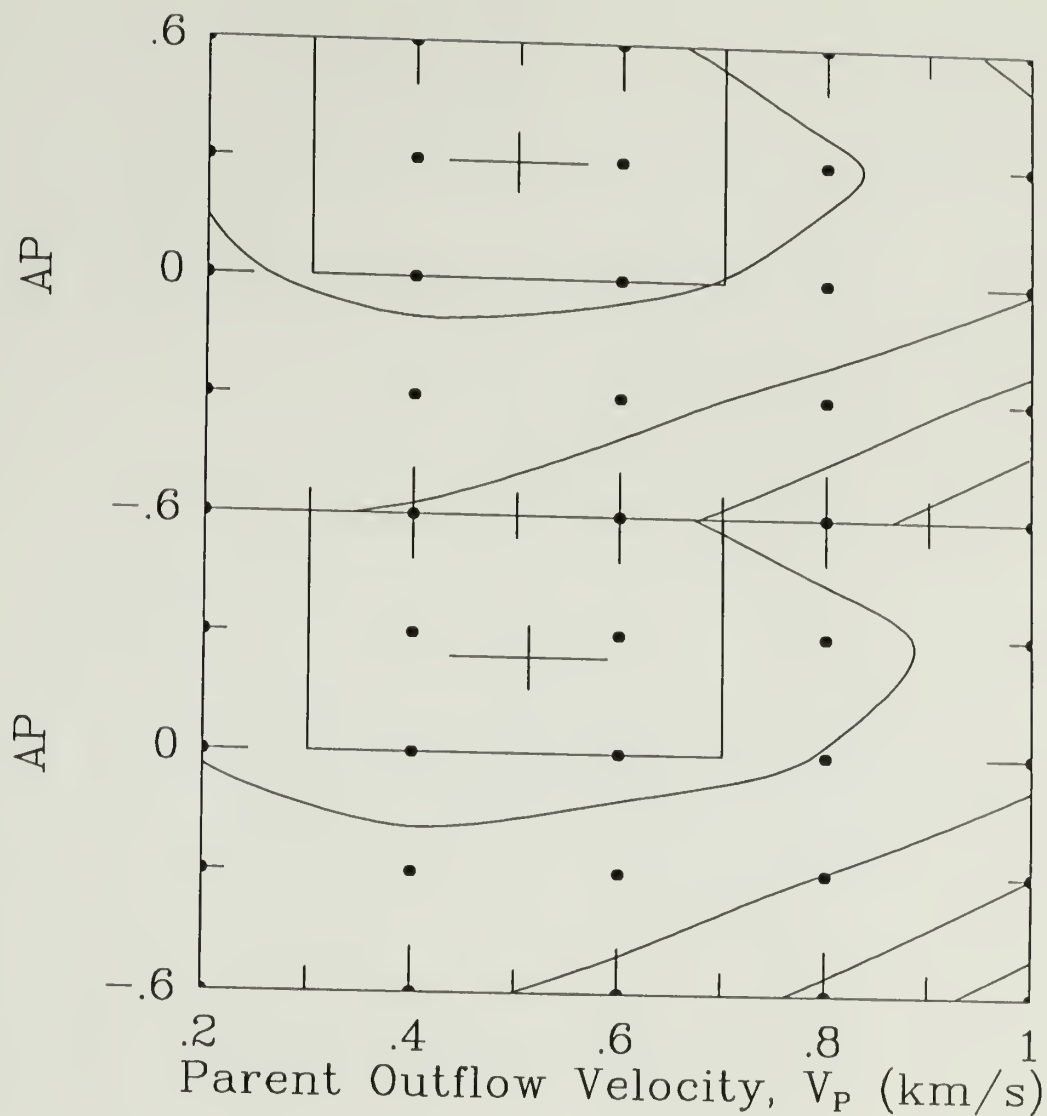


**Figure 4.2b:** The  $\chi^2_\nu$  surfaces derived from model fits to the October 1985 P/Halley spectrum. The top panel illustrates the surface from models using the Despois inversion curve, while the bottom panel shows the surface from models using the inversion curve of SA. The lowest contour is at a  $\chi^2_\nu$  value of 1.0 and the contour spacing is 0.5. The dots represent grid locations at which model spectra were generated. The inset boxes represent regions in which we have sampled parameter space more finely.

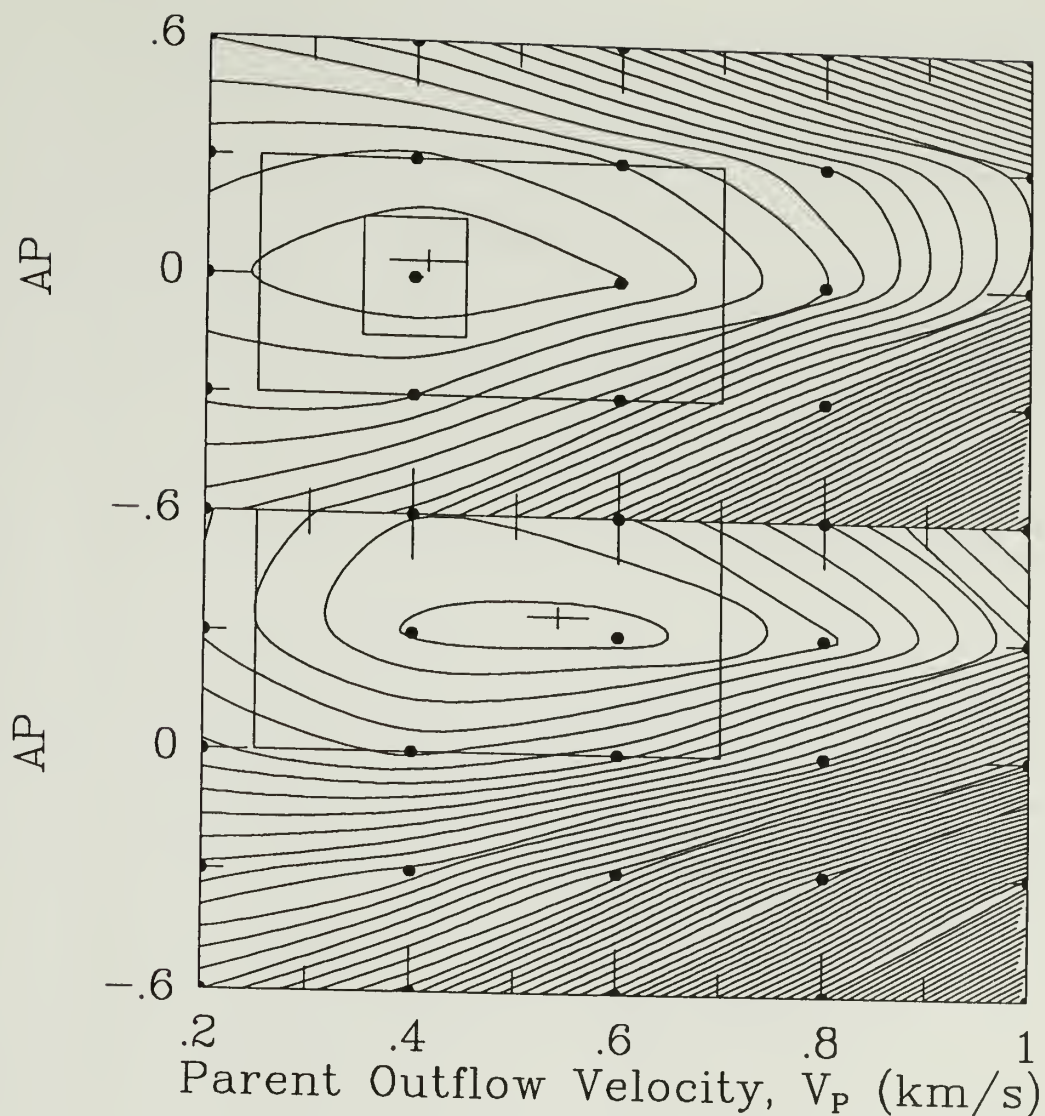
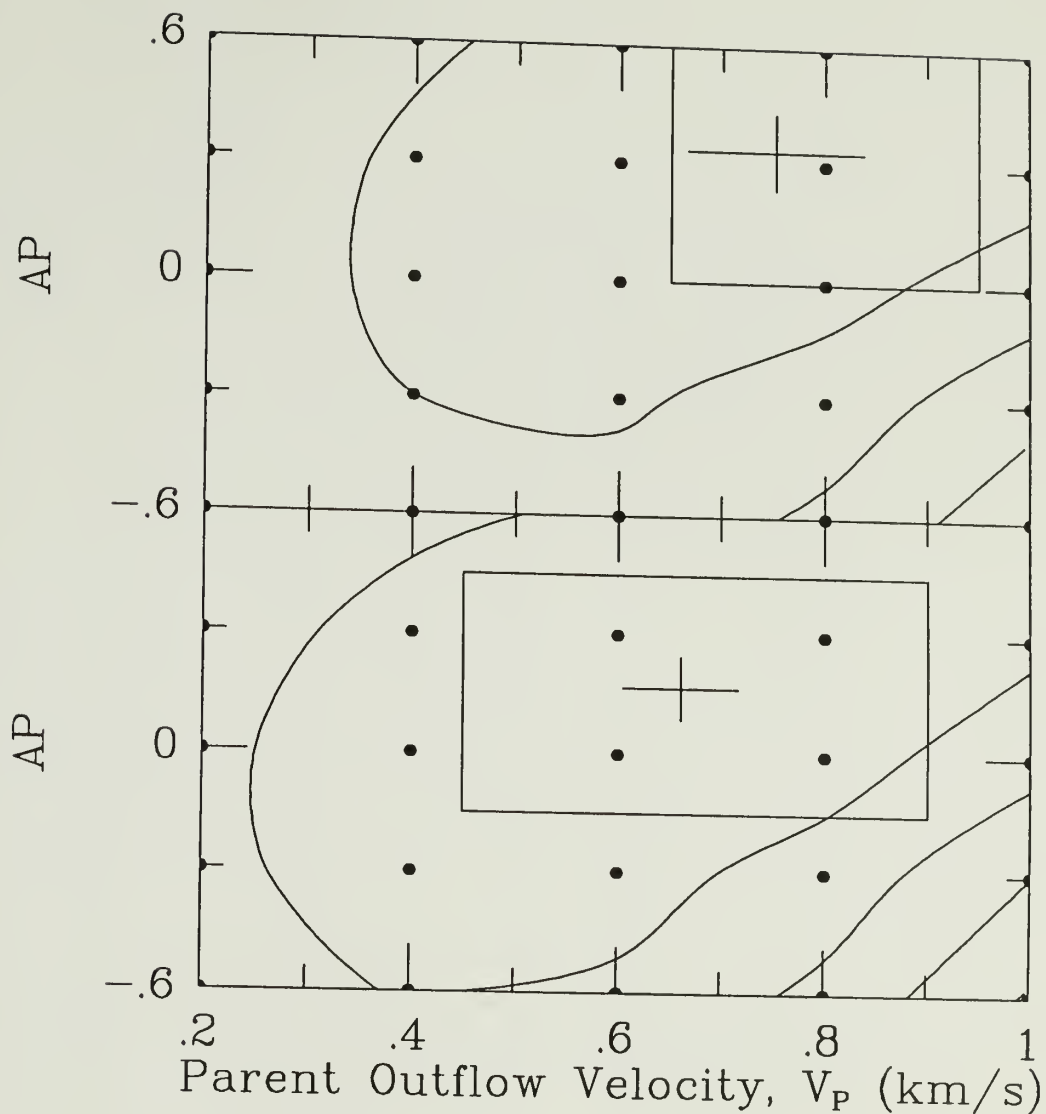


Figure 4.2c: The  $\chi^2_\nu$  surfaces derived from model fits to the November 1985 P/Halley spectrum. The top panel illustrates the surface from models using the Despois inversion curve, while the bottom panel shows the surface from models using the inversion curve of SA. The lowest contour is at a  $\chi^2_\nu$  value of 1.0 (top) and 1.5 (bottom) and the contour spacing is 0.5. The dots represent grid locations at which model spectra were generated. The inset boxes represent regions in which we have sampled parameter space more finely. The (unfortunate) touching/crossing of contours is an artifact of the contouring scheme.



**Figure 4.2d:** The  $\chi^2_\nu$  surfaces derived from model fits to the December 1985 P/Halley spectrum. The top panel illustrates the surface from models using the Despois inversion curve, while the bottom panel shows the surface from models using the inversion curve of SA. The lowest contour is at a  $\chi^2_\nu$  value of 1.5 and the contour spacing is 0.4. The dots represent grid locations at which model spectra were generated. The inset boxes represent regions in which we have sampled parameter space more finely.

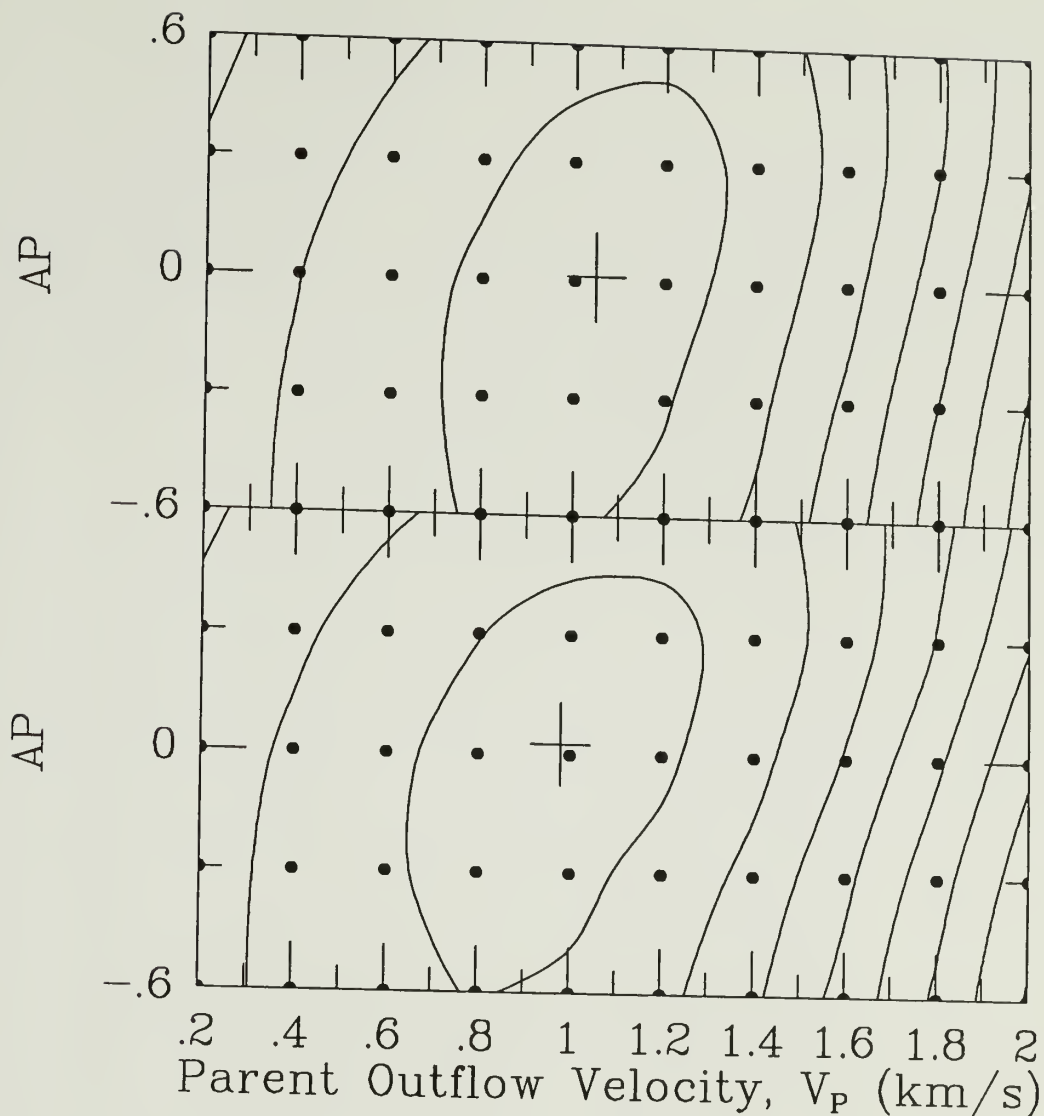
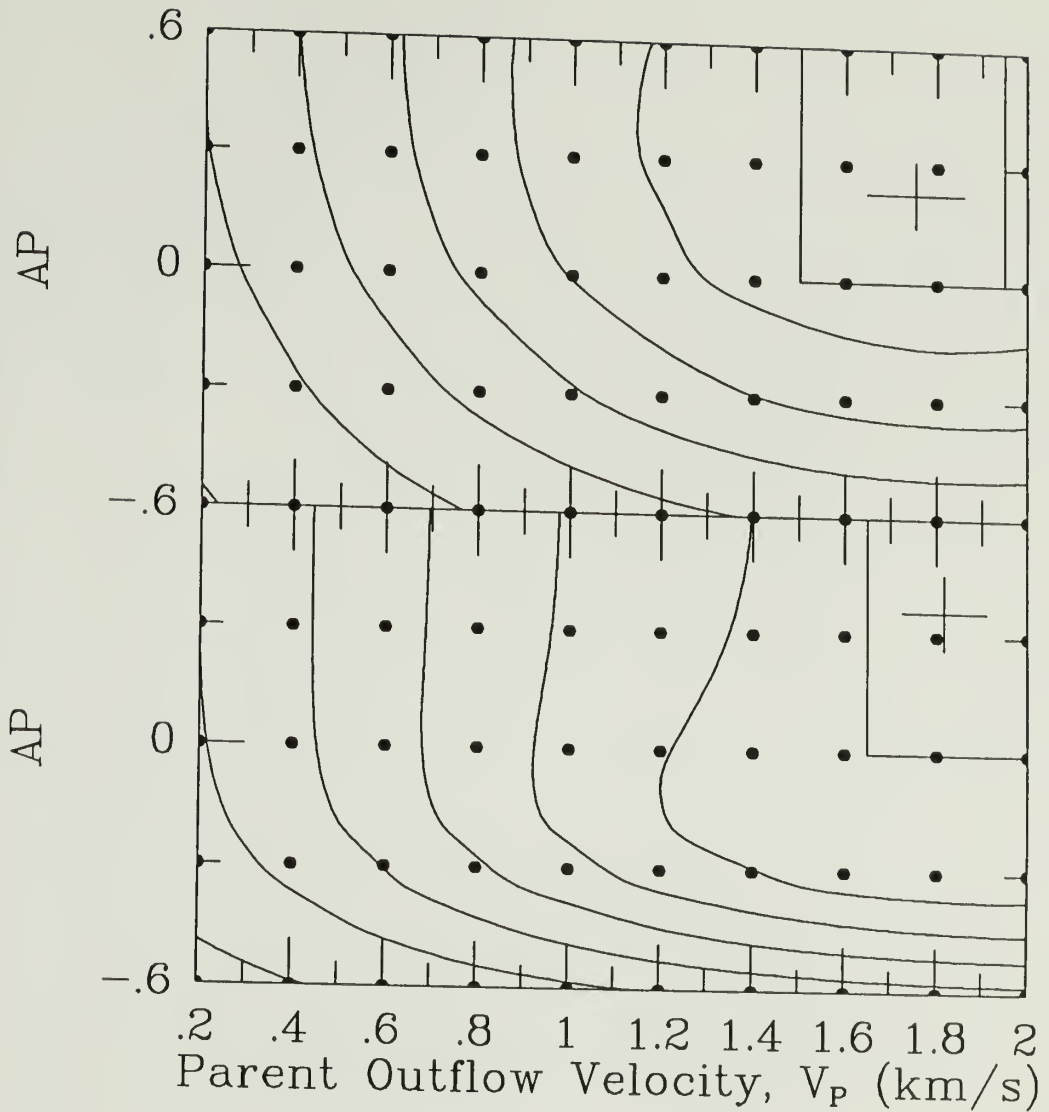


Figure 4.2e: The  $\chi^2_\nu$  surfaces derived from model fits to the January 1986 P/Halley spectrum. The top panel illustrates the surface from models using the Despois inversion curve, while the bottom panel shows the surface from models using the inversion curve of SA. The lowest contour is at a  $\chi^2_\nu$  value of 1.0 and the contour spacing is 0.5. The dots represent grid locations at which model spectra were generated.



**Figure 4.2f:** The  $\chi^2_\nu$  surfaces derived from model fits to the February 1986 P/Halley spectrum. The top panel illustrates the surface from models using the Despois inversion curve, while the bottom panel shows the surface from models using the inversion curve of SA. The lowest contour is at a  $\chi^2_\nu$  value of 1.5 and the contour spacing is 0.5. The dots represent grid locations at which model spectra were generated. The inset boxes represent regions in which we have sampled parameter space more finely.

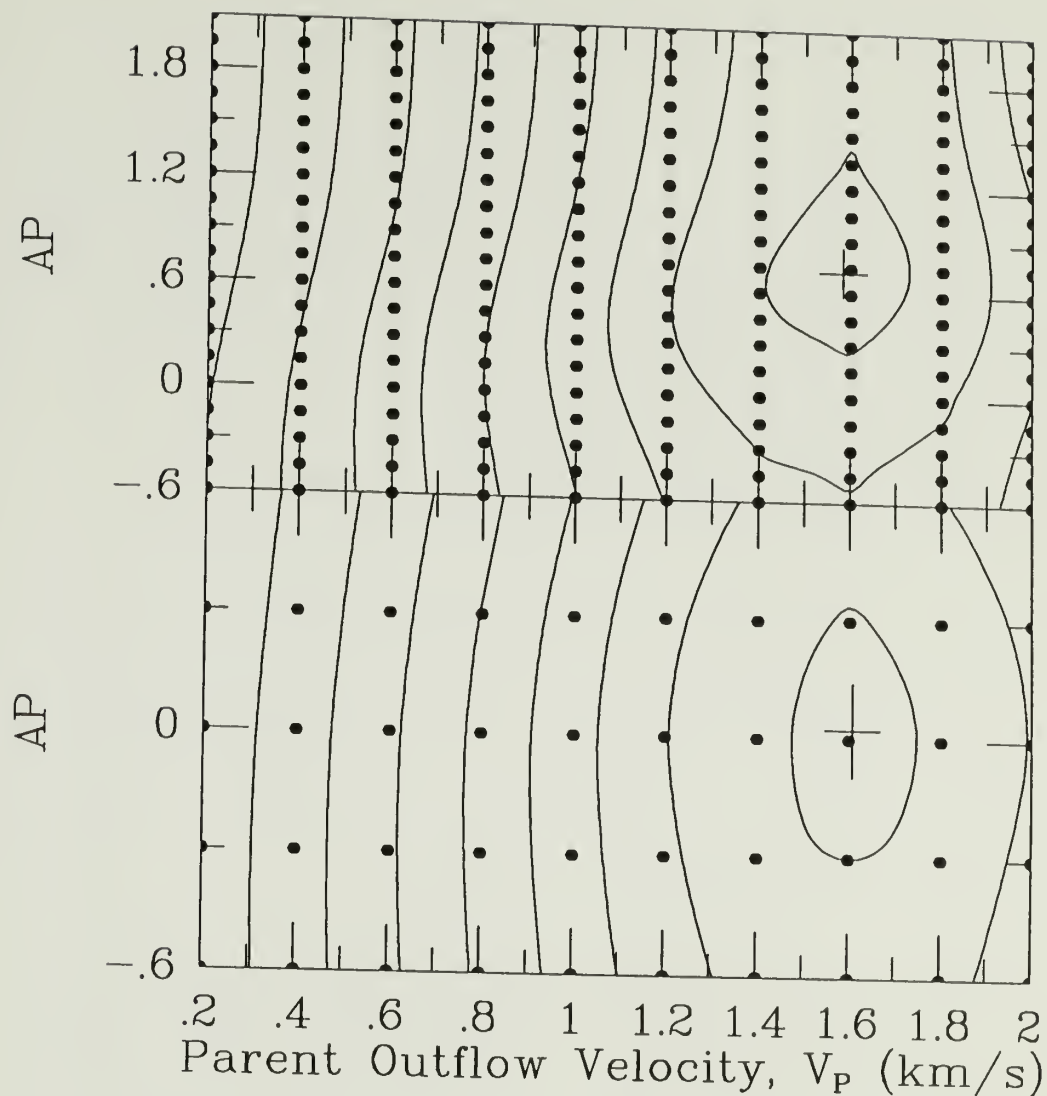
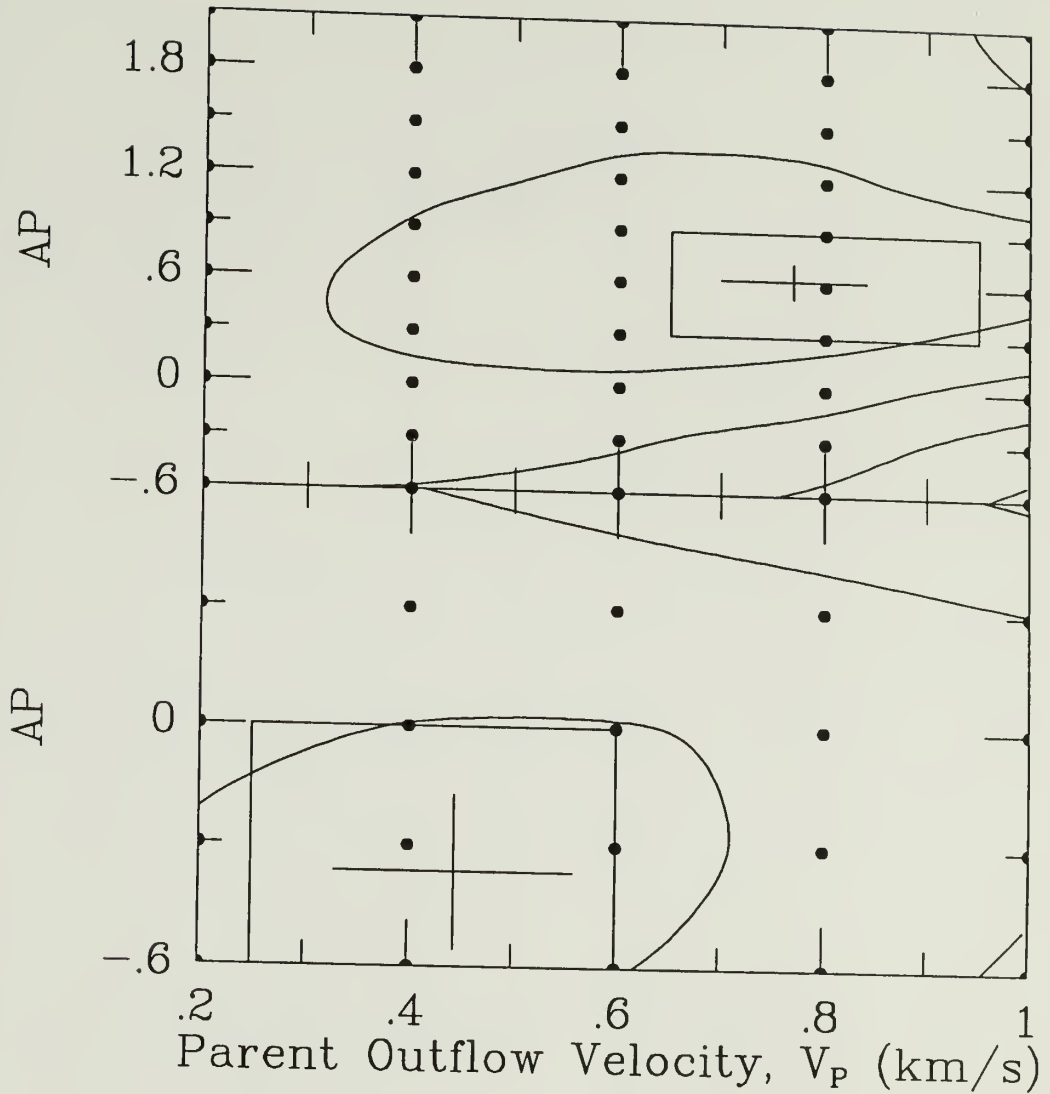


Figure 4.2g: The  $\chi^2_\nu$  surfaces derived from model fits to the March 1986 P/Halley spectrum. The top panel illustrates the surface from models using the Despois inversion curve, while the bottom panel shows the surface from models using the inversion curve of SA. The lowest contour is at a  $\chi^2_\nu$  value of 1.5 and the contour spacing is 0.5. The dots represent grid locations at which model spectra were generated.





**Figure 4.2h:** The  $\chi^2_\nu$  surfaces derived from model fits to the May 1986 P/Halley spectrum. The top panel illustrates the surface from models using the Despois inversion curve, while the bottom panel shows the surface from models using the inversion curve of SA. The lowest contour is at a  $\chi^2_\nu$  value of 1.5 and the contour spacing is 0.5. The dots represent grid locations at which model spectra were generated. The inset boxes represent regions in which we have sampled parameter space more finely.

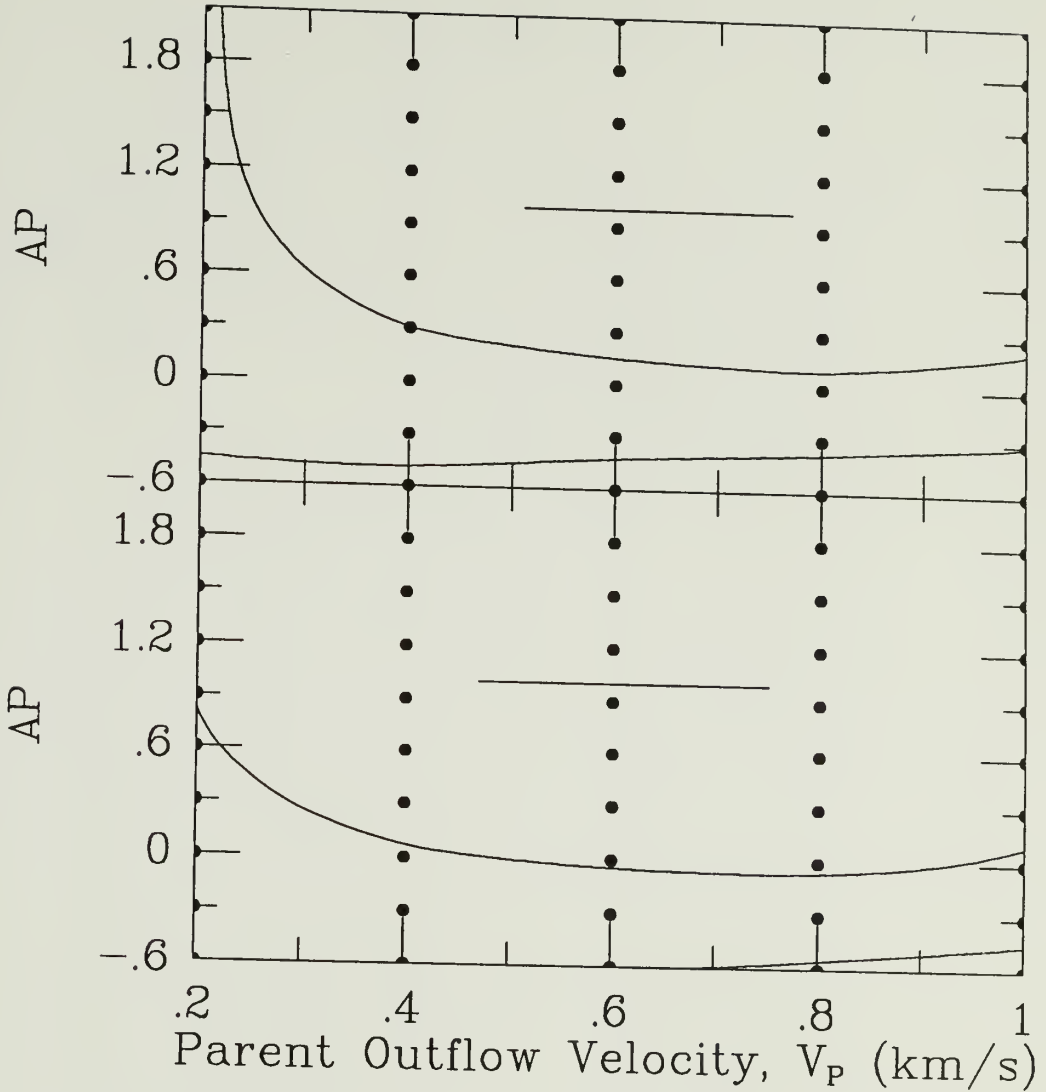
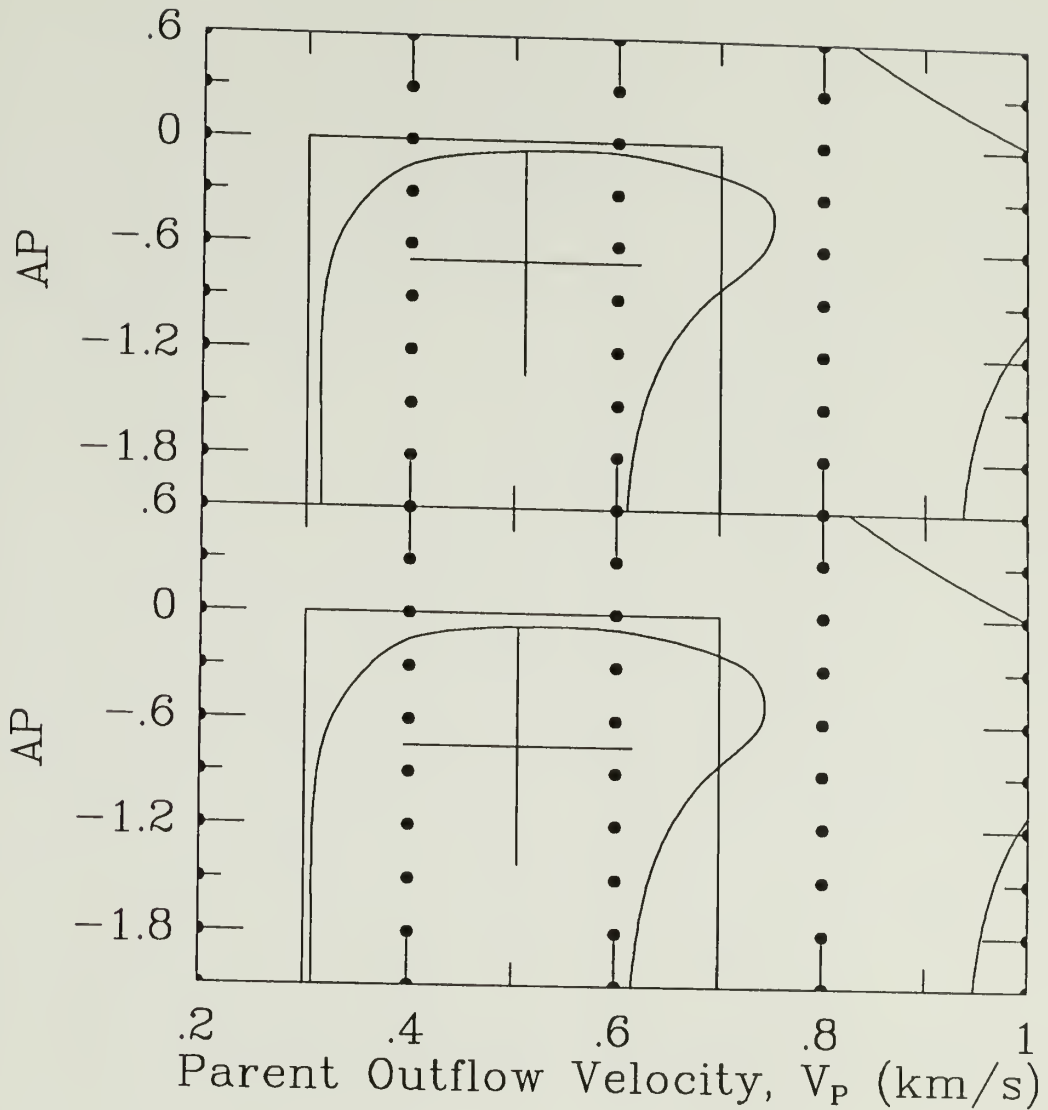
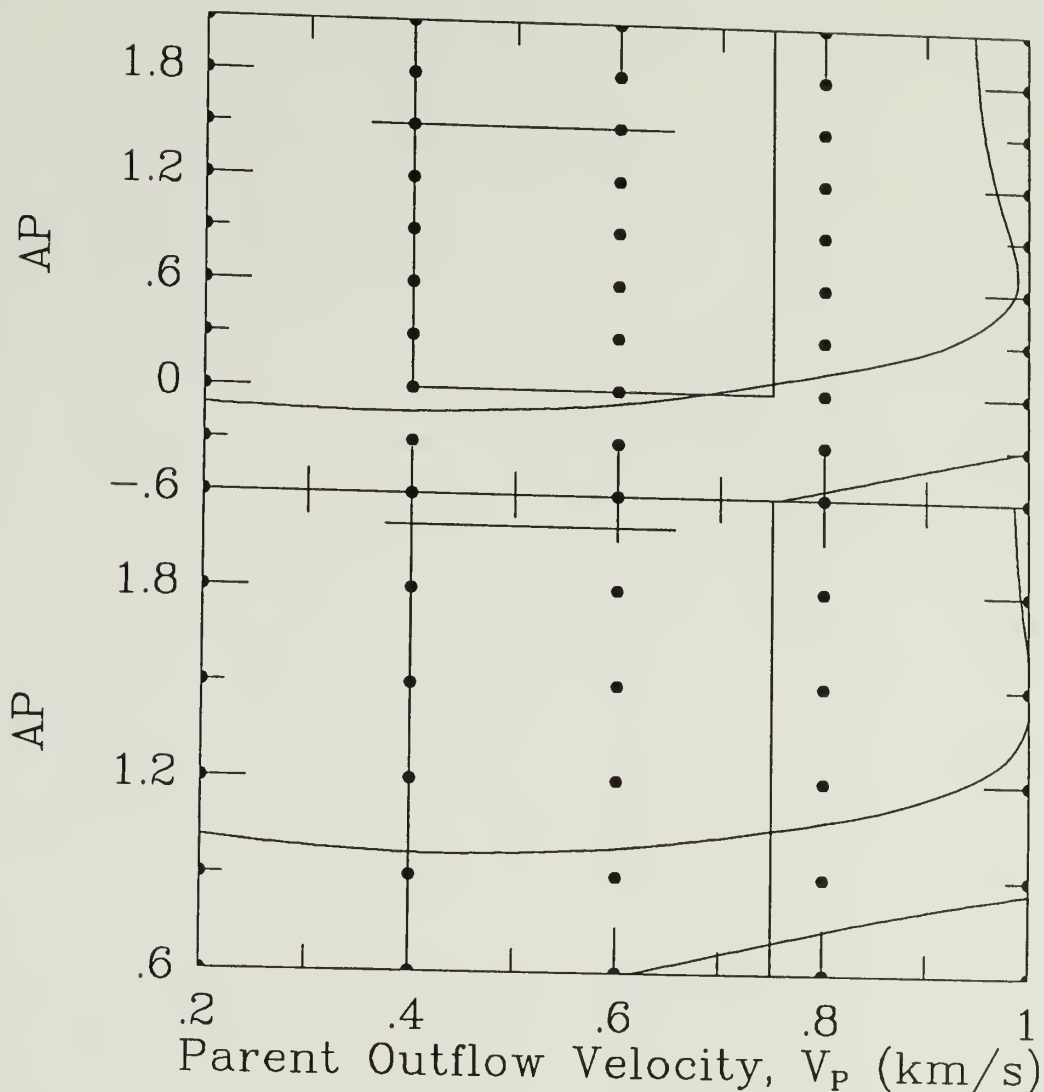


Figure 4.2i: The  $\chi^2_\nu$  surfaces derived from model fits to the July 1985 P/Giacobini-Zinner spectrum. The top panel illustrates the surface from models using the Despois inversion curve, while the bottom panel shows the surface from models using the inversion curve of SA. The lowest contour is at a  $\chi^2_\nu$  value of 1.4 and the contour spacing is 0.25. The dots represent grid locations at which model spectra were generated.



**Figure 4.2j:** The  $\chi^2_\nu$  surfaces derived from model fits to the August 1985 P/Giacobini-Zinner spectrum. The top panel illustrates the surface from models using the Despois inversion curve, while the bottom panel shows the surface from models using the inversion curve of SA. The lowest contour is at a  $\chi^2_\nu$  value of 0.9 and the contour spacing is 0.125. The dots represent grid locations at which model spectra were generated. The inset boxes represent regions in which we have sampled parameter space more finely.



**Figure 4.2k:** The  $\chi^2_\nu$  surfaces derived from model fits to the October 1985 P/Giacobini-Zinner spectrum. The top panel illustrates the surface from models using the Despois inversion curve, while the bottom panel shows the surface from models using the inversion curve of SA. The lowest contour is at a  $\chi^2_\nu$  value of 0.9 and the contour spacing is 0.0625. The dots represent grid locations at which model spectra were generated. The inset boxes represent regions in which we have sampled parameter space more finely.

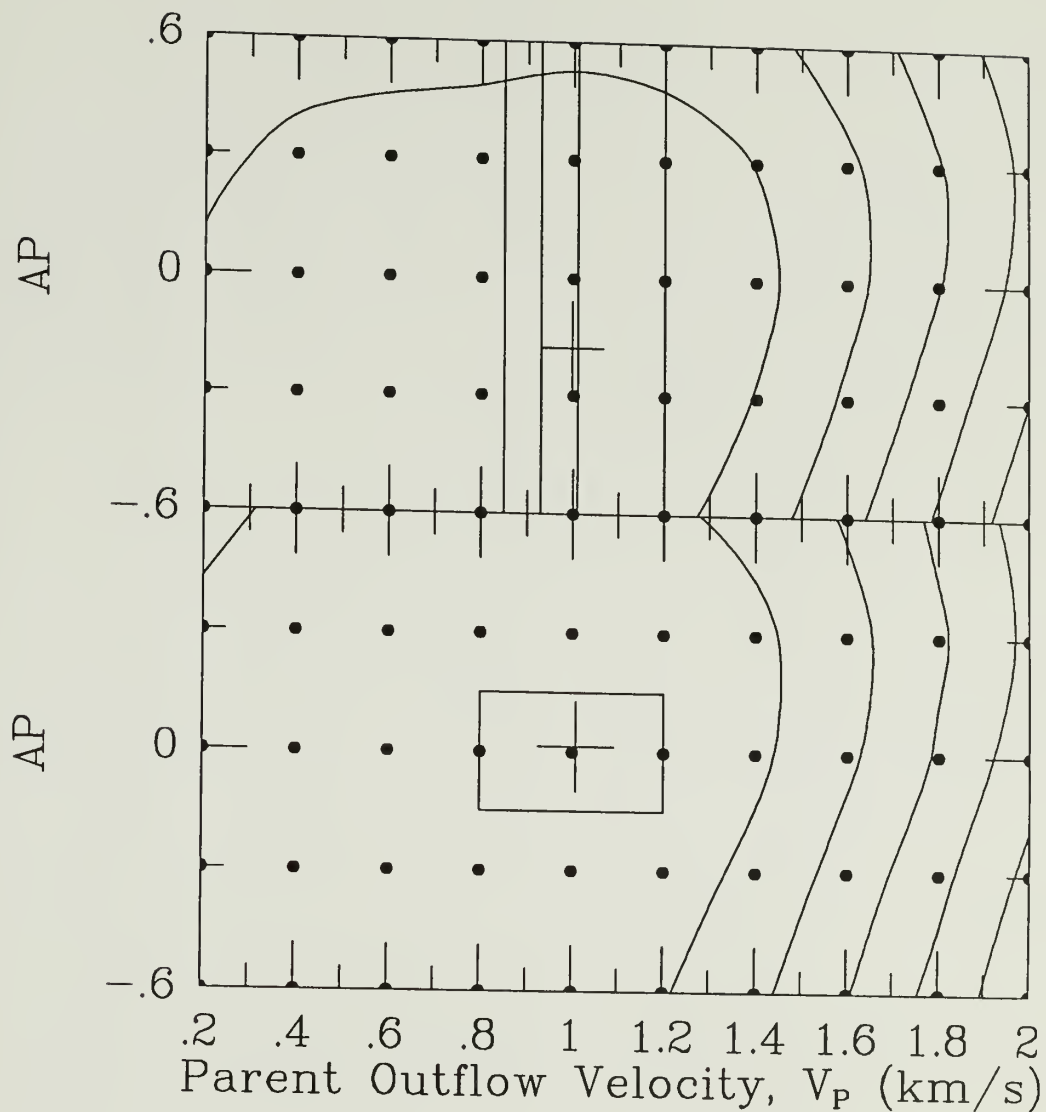
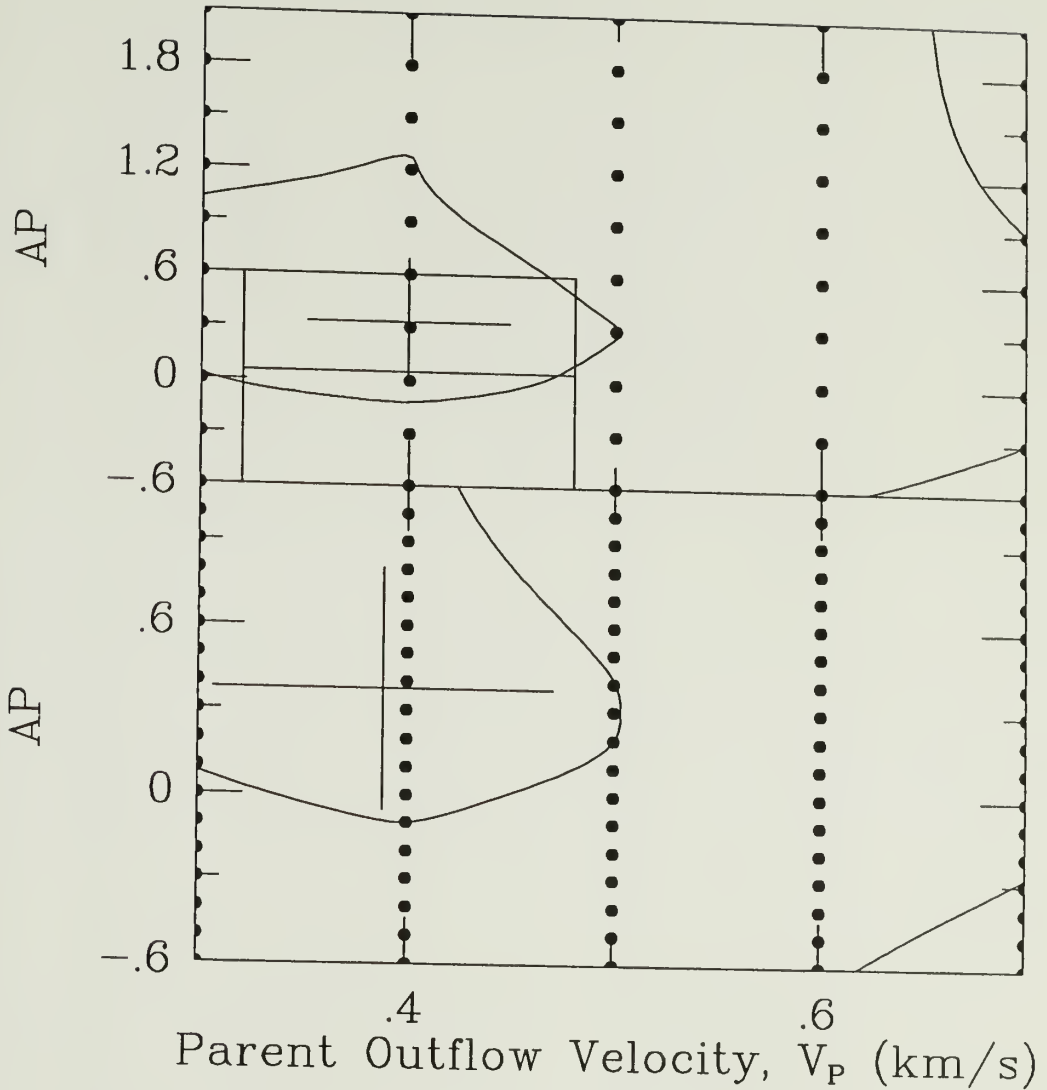
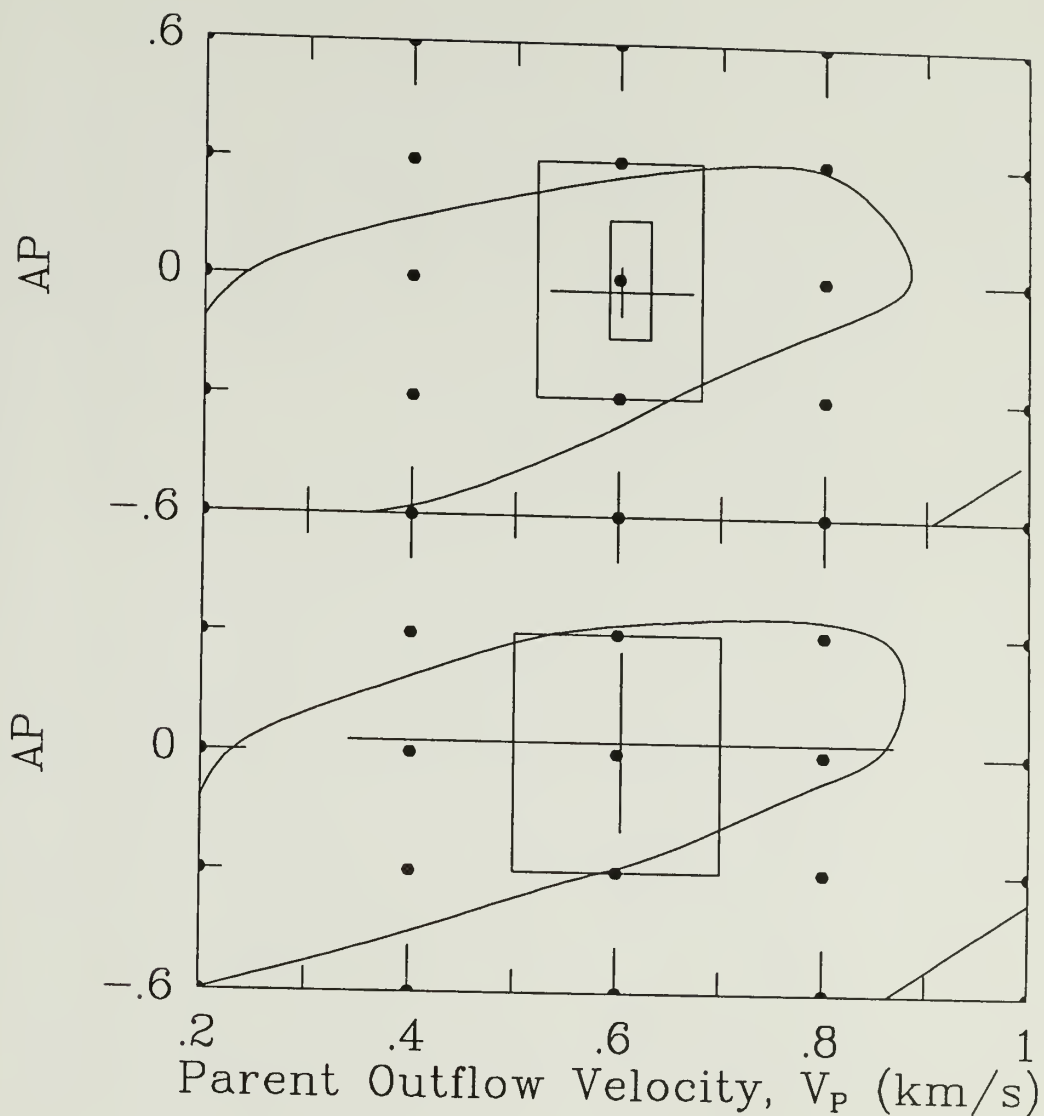


Figure 4.21: The  $\chi^2_\nu$  surfaces derived from model fits to the October 1985 C/Hartley-Good spectrum. The top panel illustrates the surface from models using the Despois inversion curve, while the bottom panel shows the surface from models using the inversion curve of SA. The lowest contour is at a  $\chi^2_\nu$  value of 1.0 (top) and 1.5 (bottom) and the contour spacing is 0.5. The dots represent grid locations at which model spectra were generated. The inset boxes represent regions in which we have sampled parameter space more finely.



**Figure 4.2m:** The  $\chi^2_\nu$  surfaces derived from model fits to the November 1985 C/Hartley-Good spectrum. The top panel illustrates the surface from models using the Despois inversion curve, while the bottom panel shows the surface from models using the inversion curve of SA. The lowest contour is at a  $\chi^2_\nu$  value of 0.9 and the contour spacing is 0.125. The dots represent grid locations at which model spectra were generated. The inset boxes represent regions in which we have sampled parameter space more finely.



**Figure 4.2n:** The  $\chi^2_\nu$  surfaces derived from model fits to the November 1985 C/Thiele spectrum. The top panel illustrates the surface from models using the Despois inversion curve, while the bottom panel shows the surface from models using the inversion curve of SA. The lowest contour is at a  $\chi^2_\nu$  value of 1.25 and the contour spacing is 0.25. The dots represent grid locations at which model spectra were generated. The inset boxes represent regions in which we have sampled parameter space more finely.

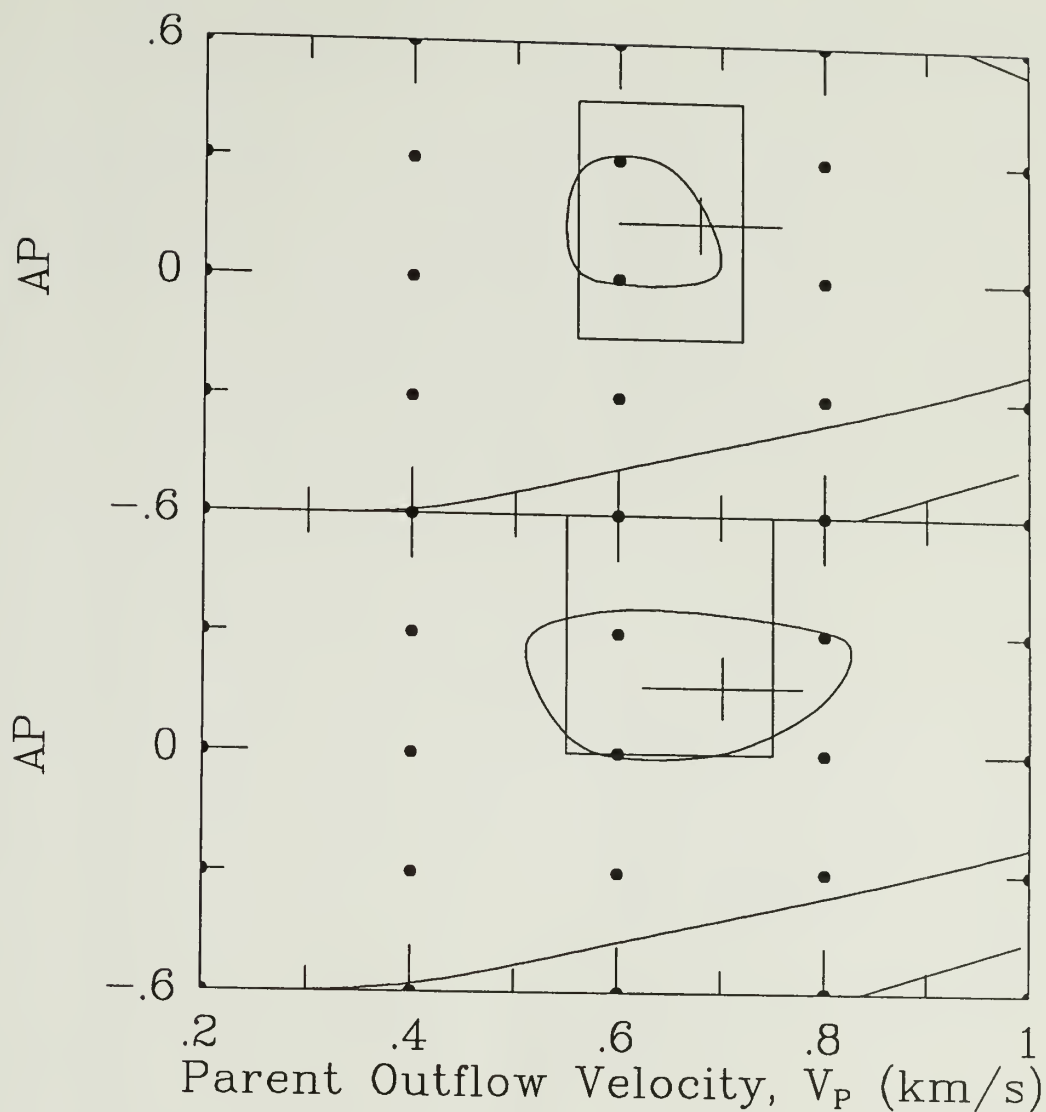


**Figure 4.20:** The  $\chi^2_\nu$  surfaces derived from model fits to the March 1987 C/Wilson spectrum. The top panel illustrates the surface from models using the Despois inversion curve, while the bottom panel shows the surface from models using the inversion curve of SA. The lowest contour is at a  $\chi^2_\nu$  value of 1.0 and the contour spacing is 0.5. The dots represent grid locations at which model spectra were generated. The inset boxes represent regions in which we have sampled parameter space more finely.



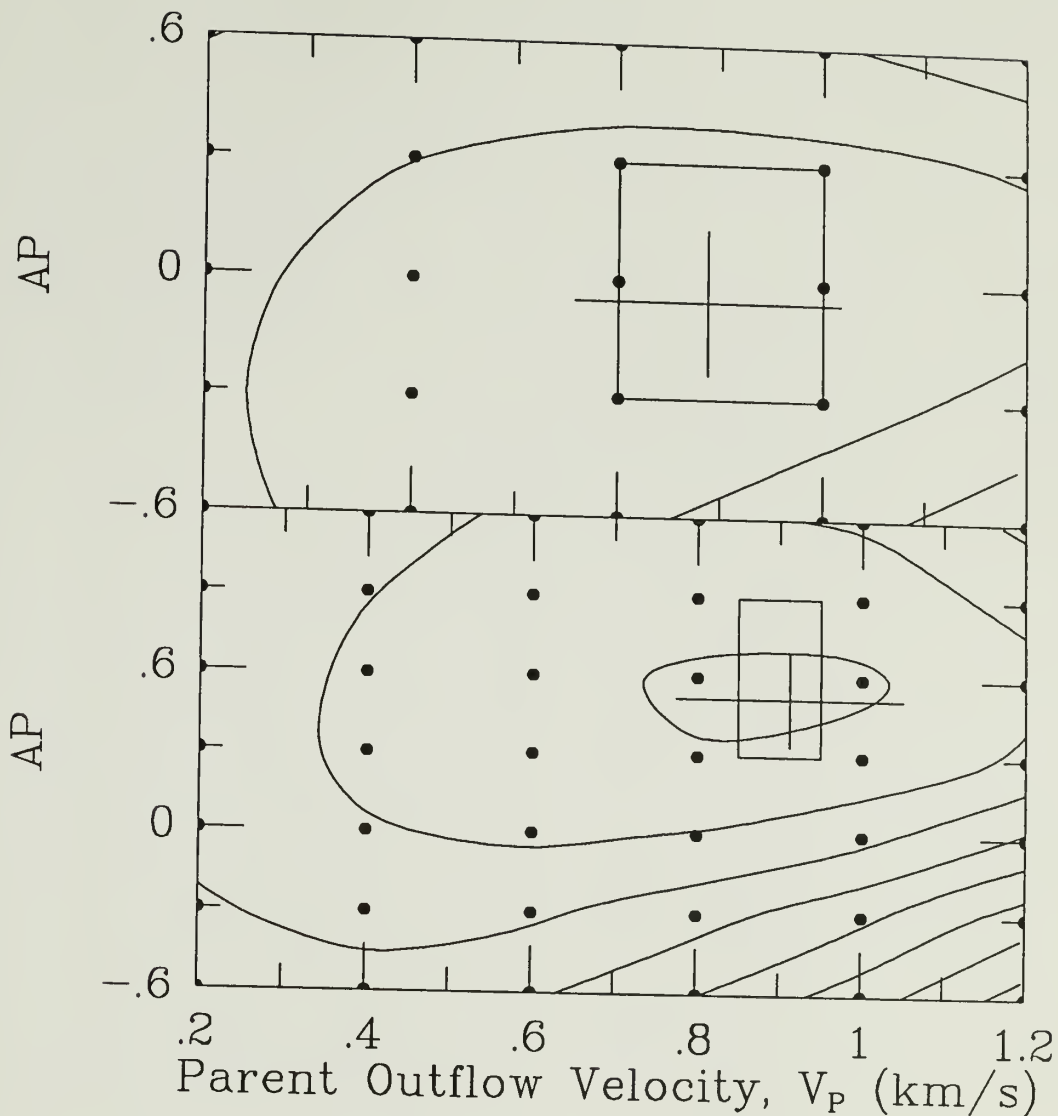


**Figure 4.2p:** The  $\chi^2_\nu$  surfaces derived from model fits to the May 1987 C/Wilson spectrum. The top panel illustrates the surface from models using the Despois inversion curve, while the bottom panel shows the surface from models using the inversion curve of SA. The lowest contour is at a  $\chi^2_\nu$  value of 0.85 and the contour spacing is 0.0625. The dots represent grid locations at which model spectra were generated. The inset boxes represent regions in which we have sampled parameter space more finely.

This series of figures illustrates the relative sensitivity of our model fits to variations in the input parameters. To further illustrate this point, we present in Figures 4.3a–p representative model spectra taken from the regions of the Despois  $\chi^2_{\nu}$  surfaces near the minima superimposed on their respective data. Offset from these model-data pairs are the residuals of the fits. In Figures 4.4a–p we show the SA counterparts to Figures 4.3a–p. In both series of figures, the model in the center panel is that which results from the parameter combination which is closest to the minimum on the  $\chi^2_{\nu}$  surface;  $V_P$  increments by  $0.2 \text{ km sec}^{-1}$  ( $0.1 \text{ km sec}^{-1}$  for the November 1985 epoch of C/Hartley-Good; Figures 4.3m and 4.4m) from left to right, while AP increments by 0.3 from bottom to top.

Examination of Figures 4.3a–p and 4.4a–p reveals that the degree to which the model fits are dependent on the model parameters is a function of the signal-to-noise of the data, as one should expect. Moreover, there are cases where, on a fine scale, the synthetic spectrum obtained with one inversion curve fits the data better than does that obtained with the other curve. Fine examples of this are the model spectra for the October and November 1985 epochs of Comet Halley. The synthetic spectra generated using the SA curve fit the data from these two epochs quite well except for at the very top of the profile near  $V_{\text{COMET}} = 0 \text{ km sec}^{-1}$  (Figures 4.4b and c for October and November 1985, respectively). On the other hand, the model spectra generated with the Despois inversion curve fit the data very well everywhere, *including*

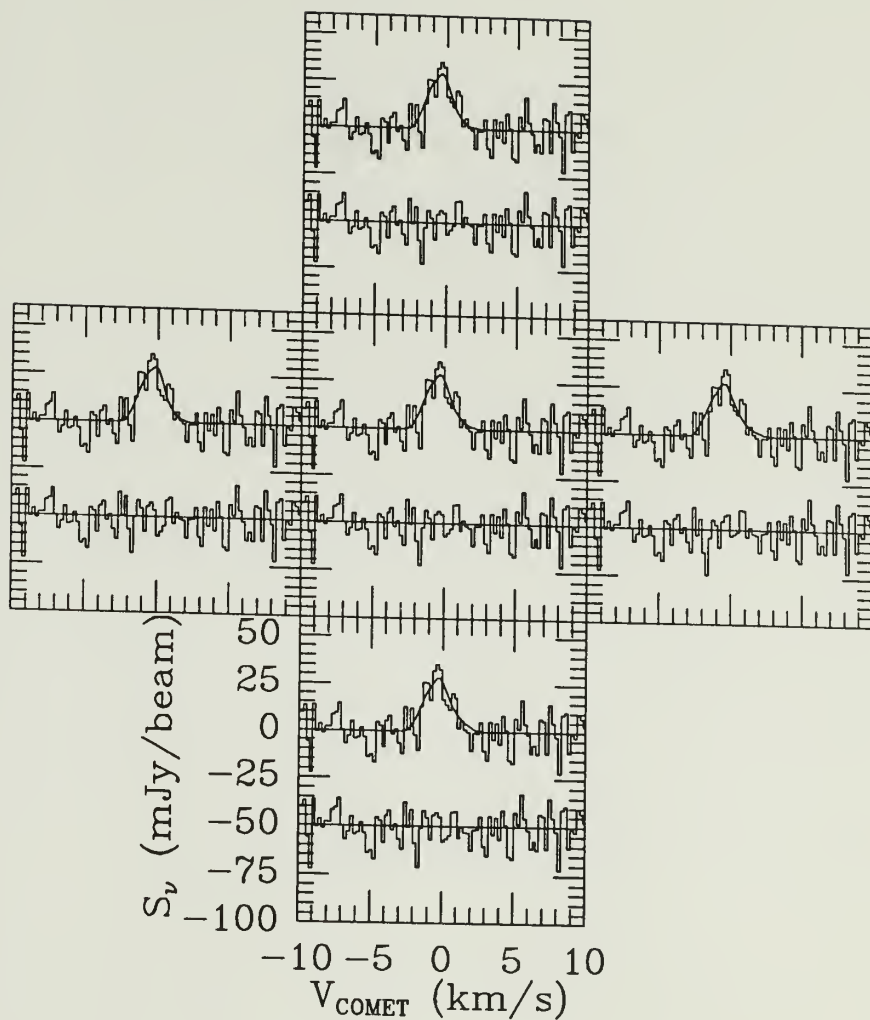
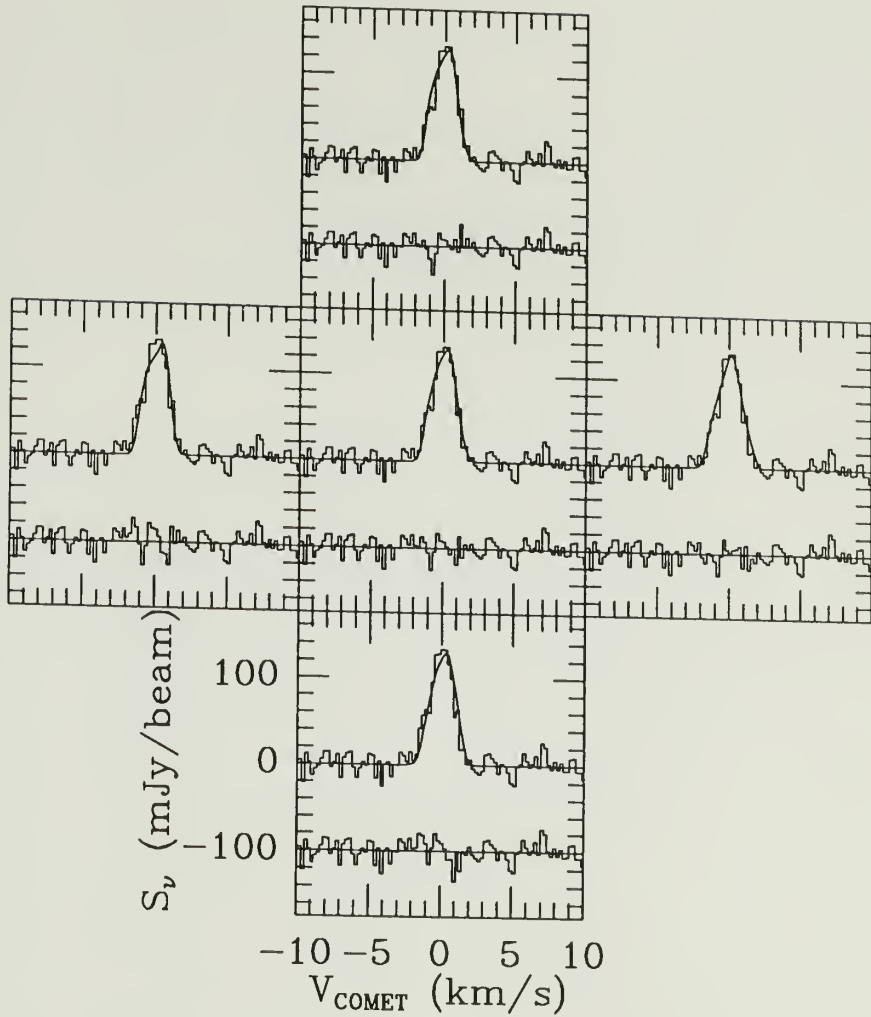


Figure 4.3a: A representative sample of model spectra generated using the Despois inversion curve superimposed on the spectrum of P/Halley from September 1985. The parameters for the center spectra are  $AP = +0.9$  and  $V_P = 1.0 \text{ km sec}^{-1}$ ; the left-right velocity increments are  $0.2 \text{ km sec}^{-1}$  and the bottom-top AP increments are 0.3 units. Offset from the model/data pair are the residuals from the model fit.



**Figure 4.3b:** A representative sample of model spectra generated using the Despois inversion curve superimposed on the spectrum of P/Halley from October 1985. The parameters for the center spectra are  $AP = +0.3$  and  $V_P = 0.4 \text{ km sec}^{-1}$ ; the left-right velocity increments are  $0.2 \text{ km sec}^{-1}$  and the bottom-top  $AP$  increments are  $0.3$  units. Offset from the model/data pair are the residuals from the model fit.

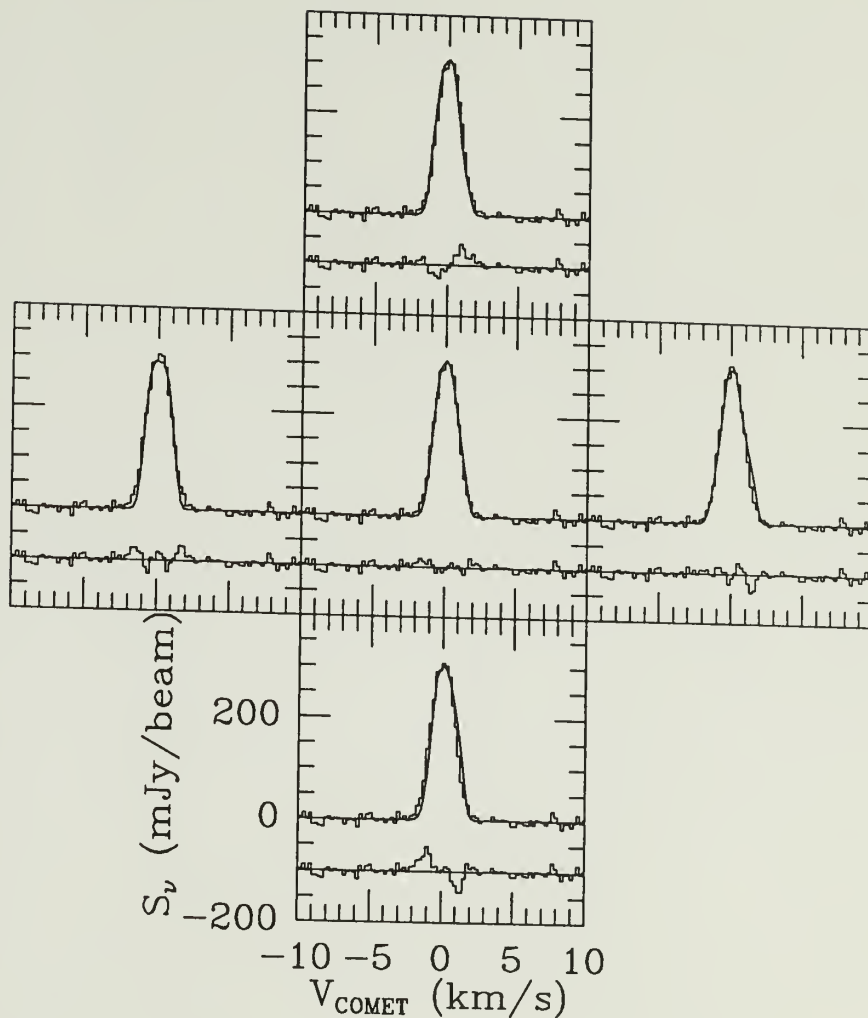


Figure 4.3c: A representative sample of model spectra generated using the Despois inversion curve superimposed on the spectrum of P/Halley from November 1985. The parameters for the center spectra are  $AP = 0.0$  and  $V_P = 0.4 \text{ km sec}^{-1}$ ; the left-right velocity increments are  $0.2 \text{ km sec}^{-1}$  and the bottom-top  $AP$  increments are  $0.3$  units. Offset from the model/data pair are the residuals from the model fit.

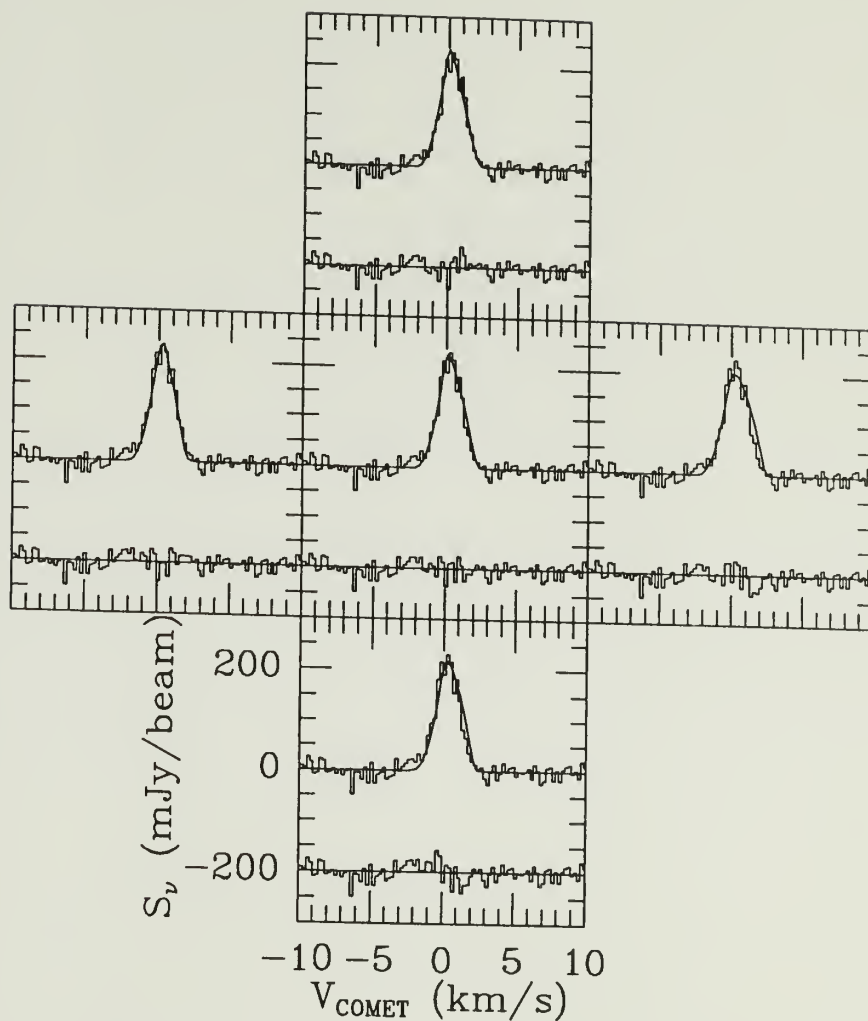
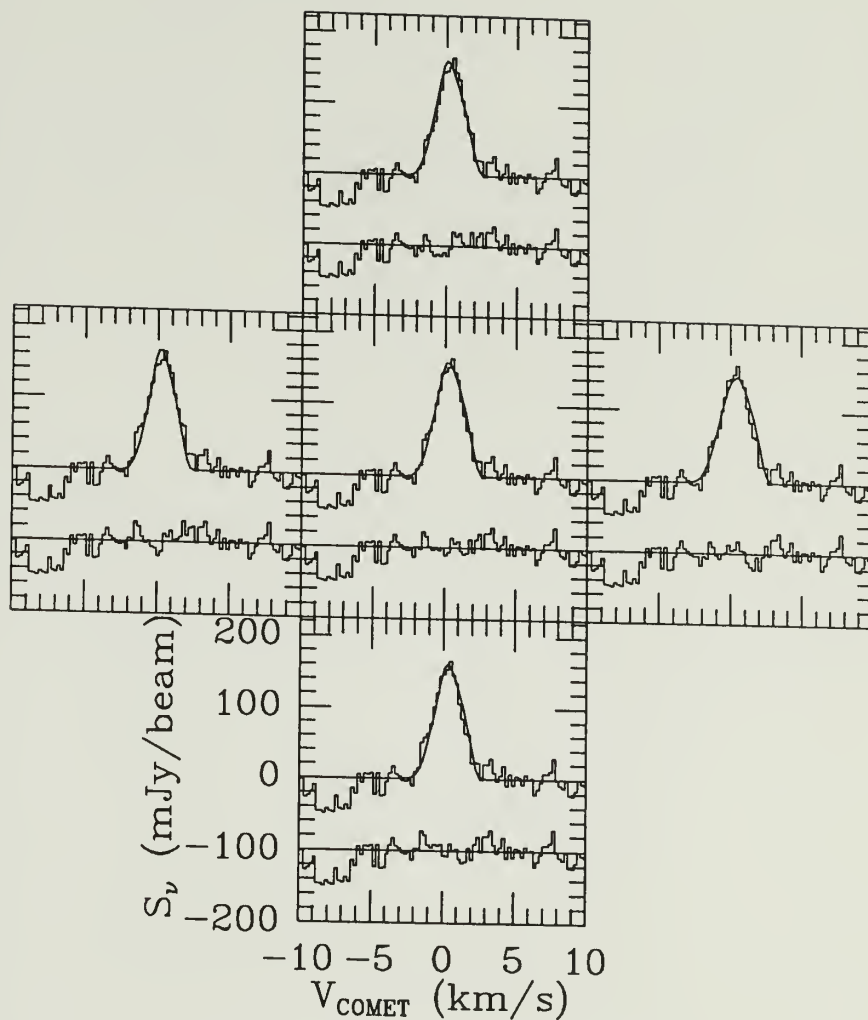
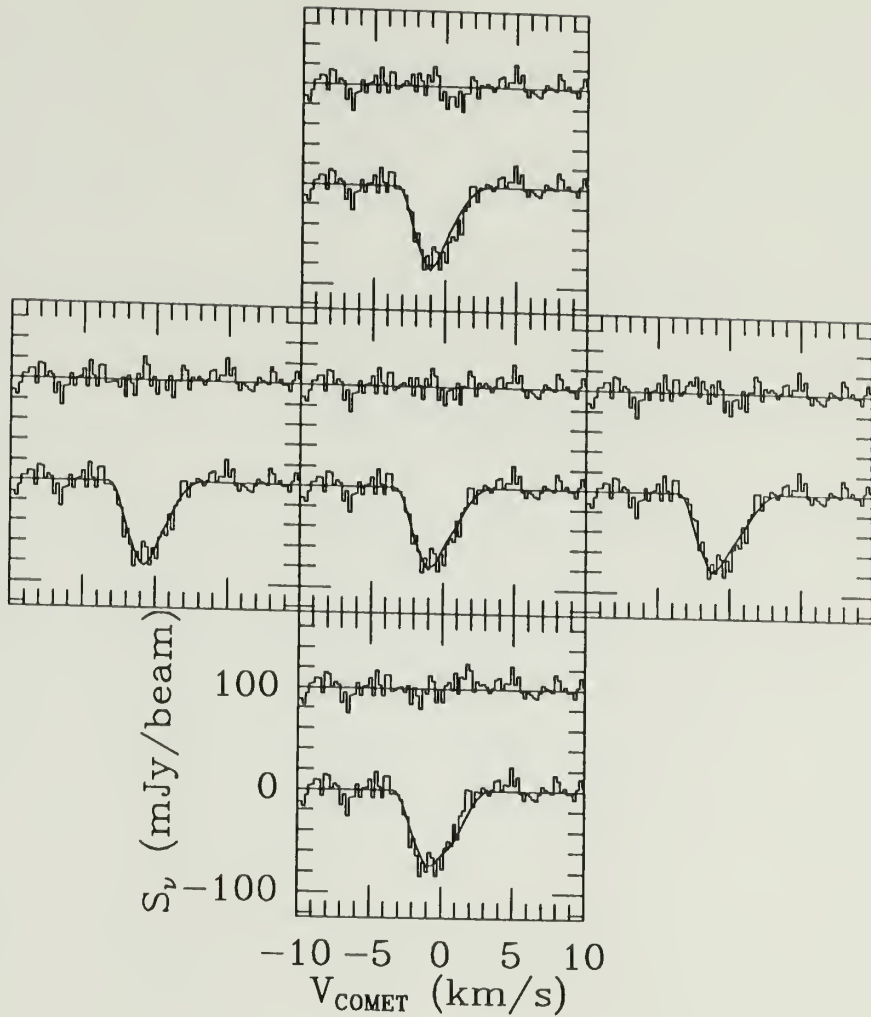


Figure 4.3d: A representative sample of model spectra generated using the Despois inversion curve superimposed on the spectrum of P/Halley from December 1985. The parameters for the center spectra are  $AP = +0.3$  and  $V_P = 0.8 \text{ km sec}^{-1}$ ; the left-right velocity increments are  $0.2 \text{ km sec}^{-1}$  and the bottom-top AP increments are 0.3 units. Offset from the model/data pair are the residuals from the model fit.



**Figure 4.3e:** A representative sample of model spectra generated using the Despois inversion curve superimposed on the spectrum of P/Halley from January 1986. The parameters for the center spectra are  $AP = 0.0$  and  $V_P = 1.0 \text{ km sec}^{-1}$ ; the left-right velocity increments are  $0.2 \text{ km sec}^{-1}$  and the bottom-top AP increments are 0.3 units. Offset from the model/data pair are the residuals from the model fit.



**Figure 4.3f:** A representative sample of model spectra generated using the Despois inversion curve superimposed on the spectrum of P/Halley from February 1986. The parameters for the center spectra are  $AP = +0.3$  and  $V_p = 1.8 \text{ km sec}^{-1}$ ; the left-right velocity increments are  $0.2 \text{ km sec}^{-1}$  and the bottom-top AP increments are 0.3 units. Offset from the model/data pair are the residuals from the model fit.



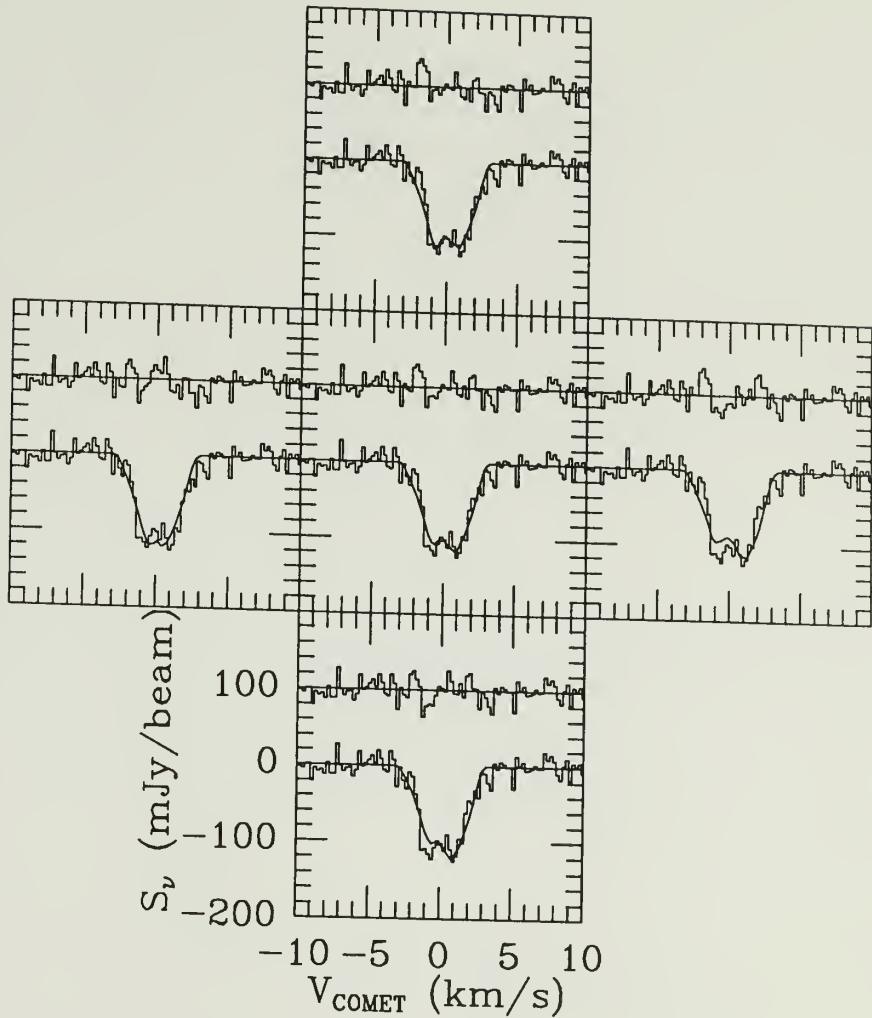


**Figure 4.3g:** A representative sample of model spectra generated using the Despois inversion curve superimposed on the spectrum of P/Halley from March 1986. The parameters for the center spectra are  $AP = +0.75$  and  $V_P = 1.6 \text{ km sec}^{-1}$ ; the left-right velocity increments are  $0.2 \text{ km sec}^{-1}$  and the bottom-top AP increments are 0.3 units. Offset from the model/data pair are the residuals from the model fit.

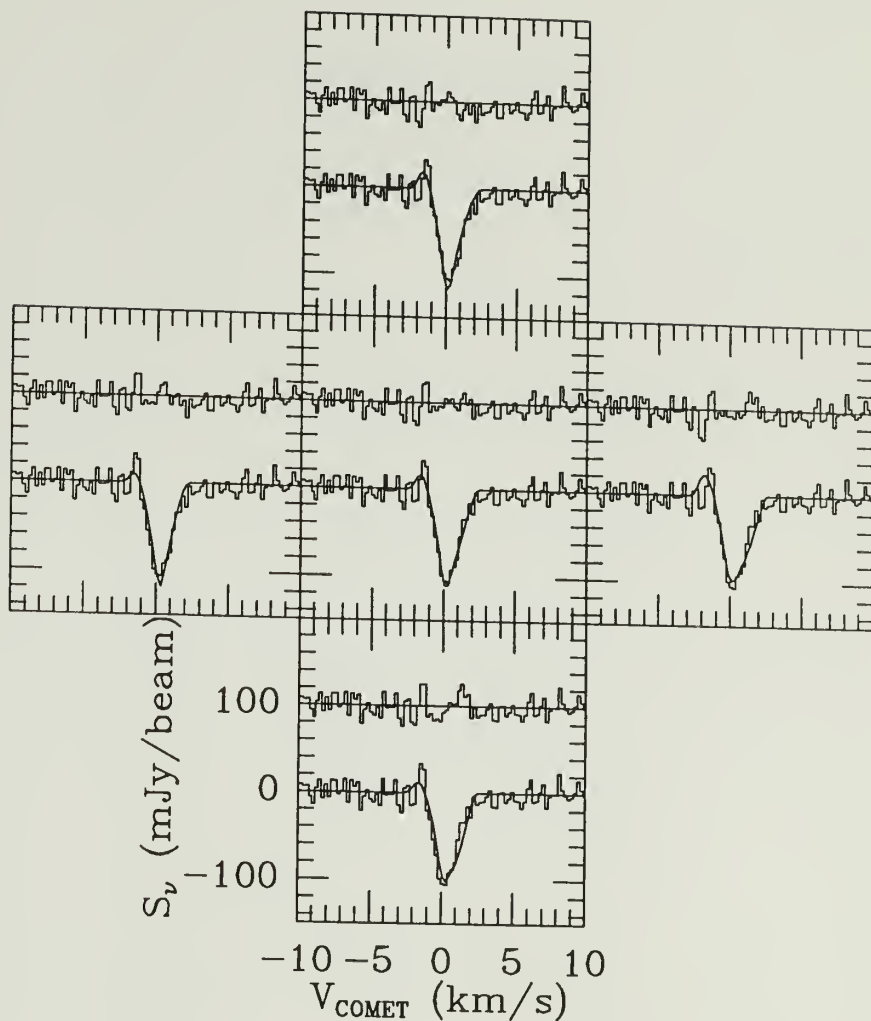


**Figure 4.3h:** A representative sample of model spectra generated using the Despois inversion curve superimposed on the spectrum of P/Halley from May 1986. The parameters for the center spectra are  $AP = +0.6$  and  $V_P = 0.8$  km sec<sup>-1</sup>; the left-right velocity increments are 0.2 km sec<sup>-1</sup> and the bottom-top AP increments are 0.3 units. Offset from the model/data pair are the residuals from the model fit.

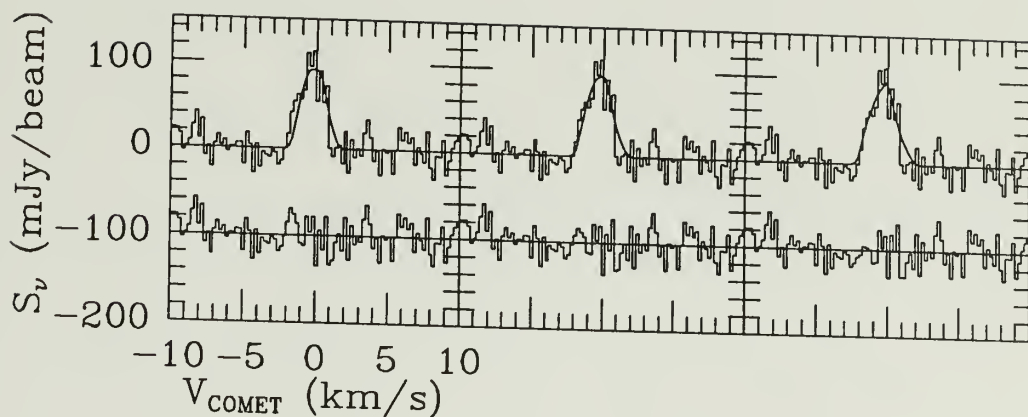


**Figure 4.3i:** A representative sample of model spectra generated using the Despois inversion curve superimposed on the spectrum of P/Giacobini-Zinner from July 1985. The parameters for the center spectra are  $AP = +0.9$  and  $V_P = 0.6 \text{ km sec}^{-1}$ ; the left-right velocity increments are  $0.2 \text{ km sec}^{-1}$ . Offset from the model/data pair are the residuals from the model fit.

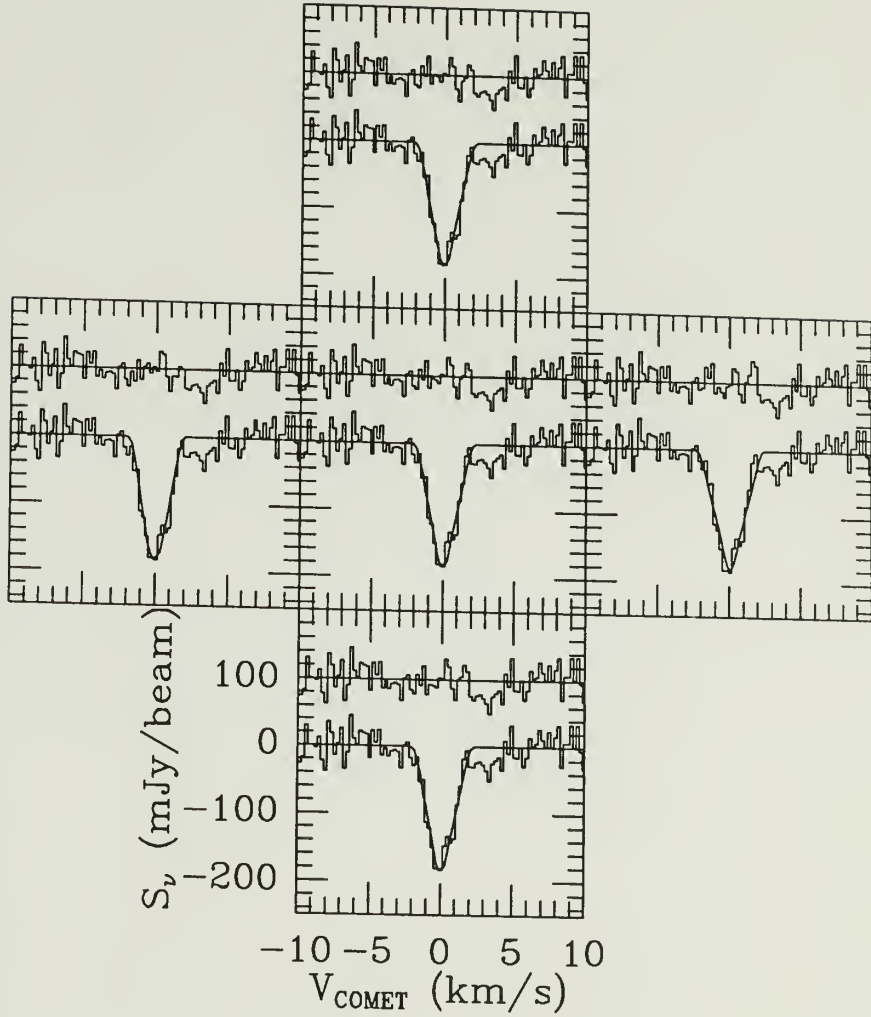


**Figure 4.3j:** A representative sample of model spectra generated using the Despois inversion curve superimposed on the spectrum of P/Giacobini-Zinner from August 1985. The parameters for the center spectra are  $AP = -0.6$  and  $V_P = 0.6 \text{ km sec}^{-1}$ ; the left-right velocity increments are  $0.2 \text{ km sec}^{-1}$  and the bottom-top  $AP$  increments are  $0.3$  units. Offset from the model/data pair are the residuals from the model fit.

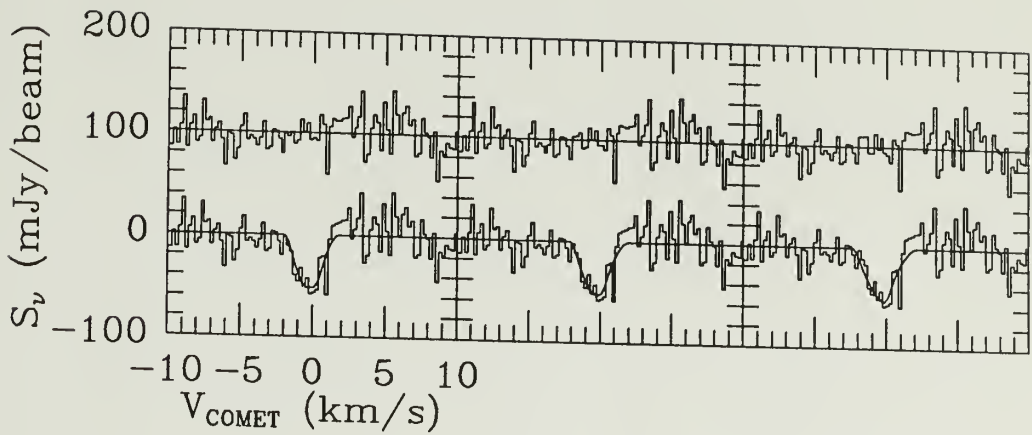


**Figure 4.3k:** A representative sample of model spectra generated using the Despois inversion curve superimposed on the spectrum of P/Giacobini-Zinner from October 1985. The parameters for the center spectra are  $AP = +1.5$  and  $V_P = 0.6 \text{ km sec}^{-1}$ ; the left-right velocity increments are  $0.2 \text{ km sec}^{-1}$ . Offset from the model/data pair are the residuals from the model fit.

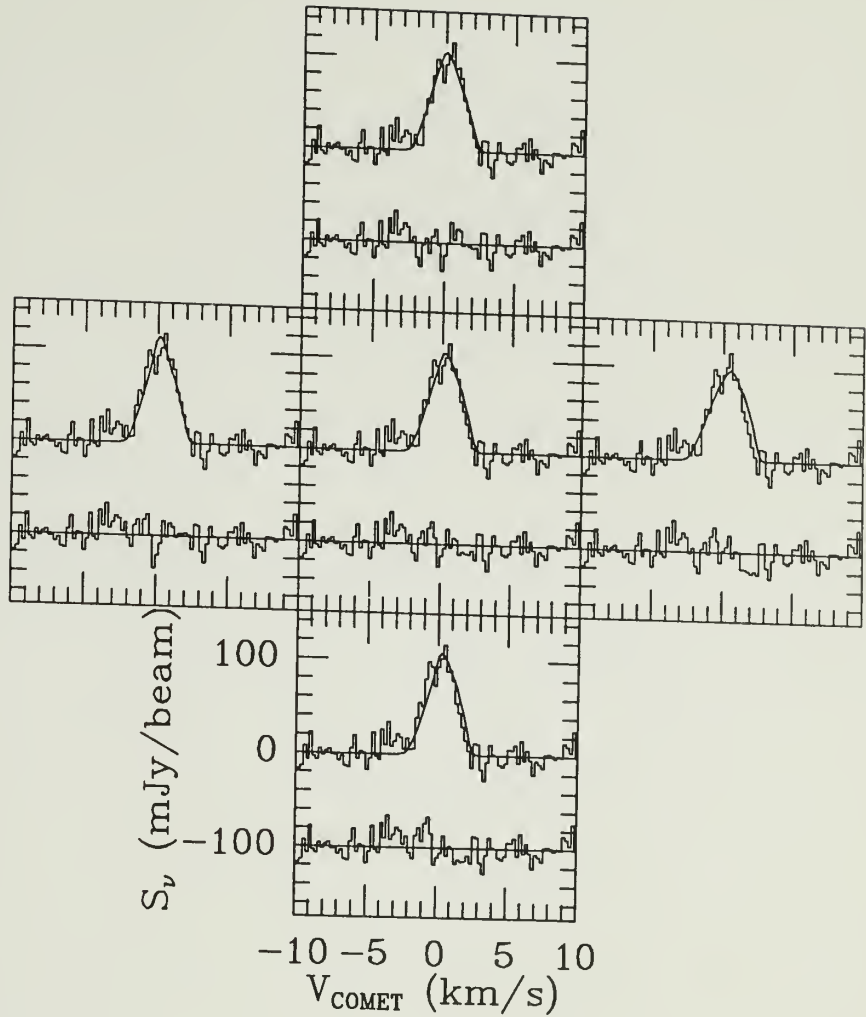


**Figure 4.31:** A representative sample of model spectra generated using the Despois inversion curve superimposed on the spectrum of C/Hartley-Good from October 1985. The parameters for the center spectra are  $AP = -0.3$  and  $V_P = 1.0 \text{ km sec}^{-1}$ ; the left-right velocity increments are  $0.2 \text{ km sec}^{-1}$  and the bottom-top AP increments are 0.3 units. Offset from the model/data pair are the residuals from the model fit.

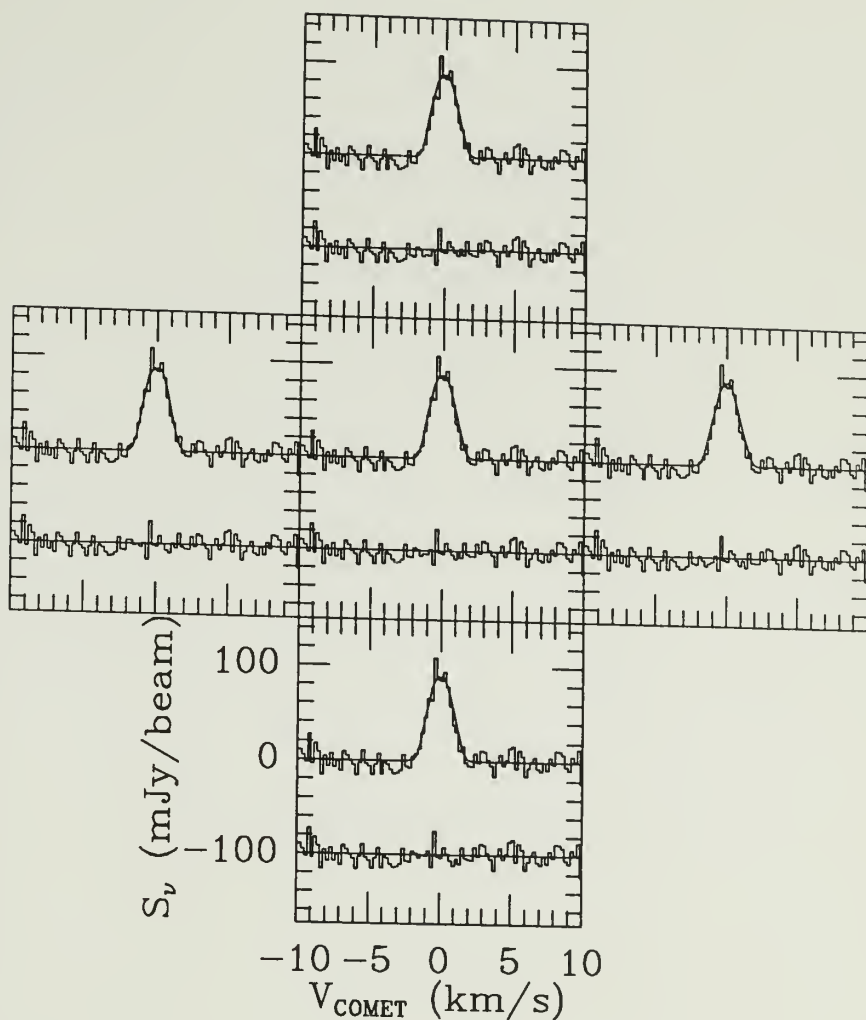


**Figure 4.3m:** A representative sample of model spectra generated using the Despois inversion curve superimposed on the spectrum of C/Hartley-Good from November 1985. The parameters for the center spectra are  $AP = +0.3$  and  $V_P = 0.4 \text{ km sec}^{-1}$ ; the left-right velocity increments are  $0.1 \text{ km sec}^{-1}$  and the bottom-top AP increments are 0.3 units. Offset from the model/data pair are the residuals from the model fit.

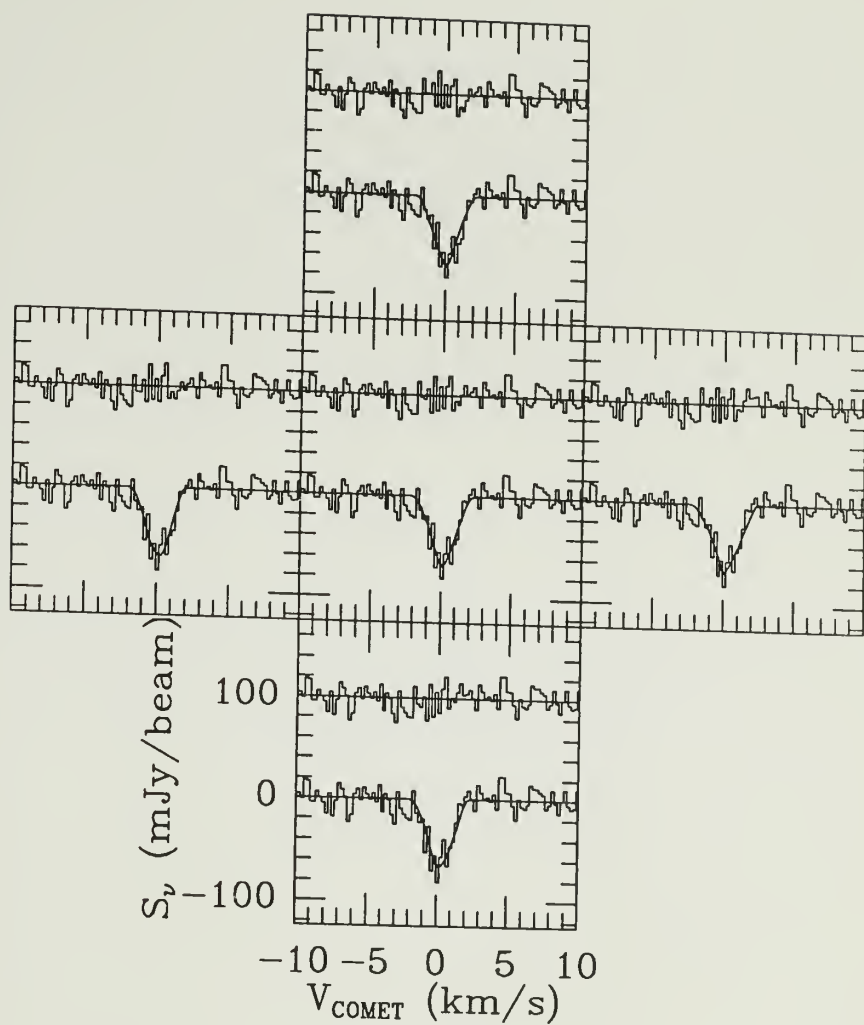


**Figure 4.3n:** A representative sample of model spectra generated using the Despois inversion curve superimposed on the spectrum of C/Thiele from November 1985. The parameters for the center spectra are  $AP = 0.0$  and  $V_P = 0.6 \text{ km sec}^{-1}$ ; the left-right velocity increments are  $0.2 \text{ km sec}^{-1}$  and the bottom-top AP increments are 0.3 units. Offset from the model/data pair are the residuals from the model fit.



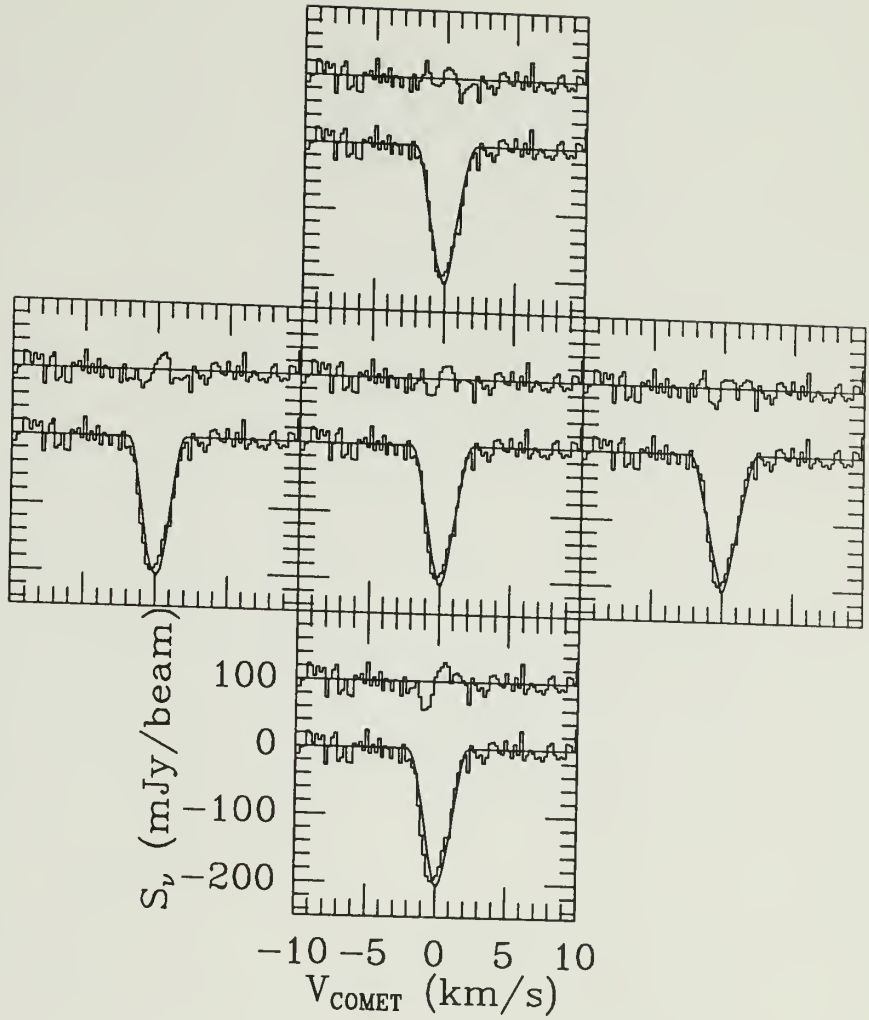


**Figure 4.30:** A representative sample of model spectra generated using the Despois inversion curve superimposed on the spectrum of C/Wilson from March 1987. The parameters for the center spectra are  $AP = 0.0$  and  $V_P = 0.6 \text{ km sec}^{-1}$ ; the left-right velocity increments are  $0.2 \text{ km sec}^{-1}$  and the bottom-top AP increments are 0.3 units. Offset from the model/data pair are the residuals from the model fit.

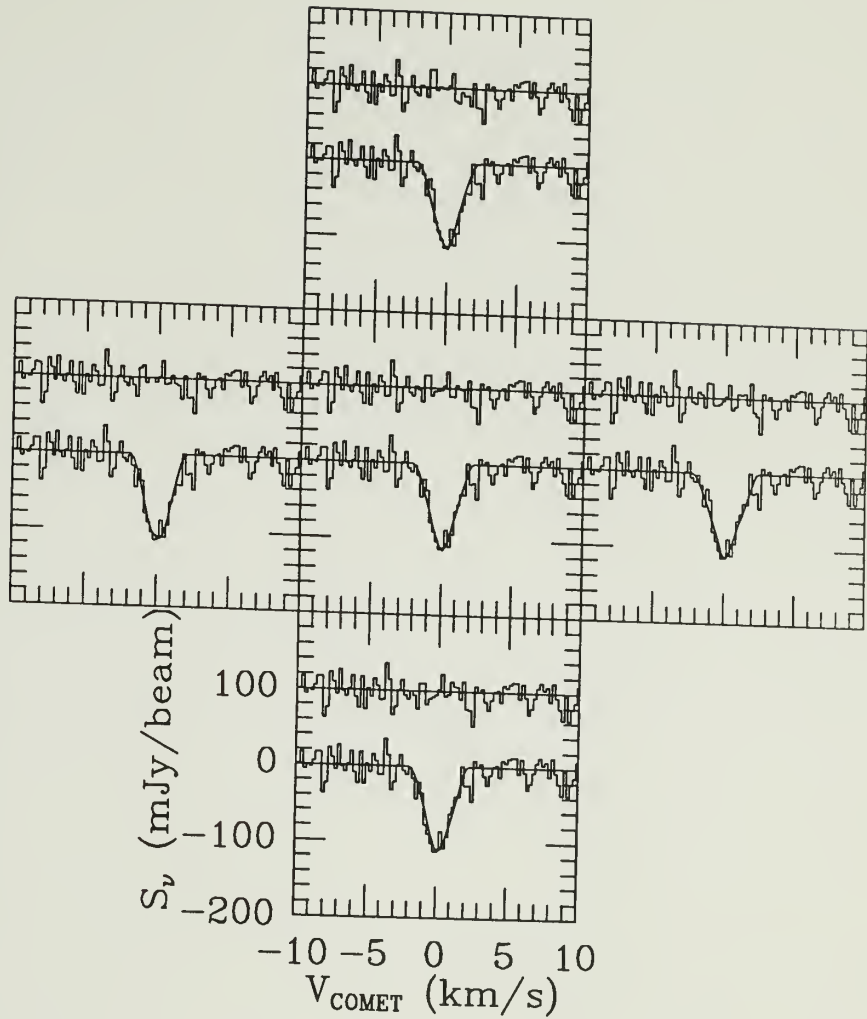


**Figure 4.3p:** A representative sample of model spectra generated using the Despois inversion curve superimposed on the spectrum of C/Wilson from May 1987. The parameters for the center spectra are  $AP = 0.0$  and  $V_P = 0.6$   $\text{km sec}^{-1}$ ; the left-right velocity increments are  $0.2 \text{ km sec}^{-1}$  and the bottom-top AP increments are 0.3 units. Offset from the model/data pair are the residuals from the model fit.

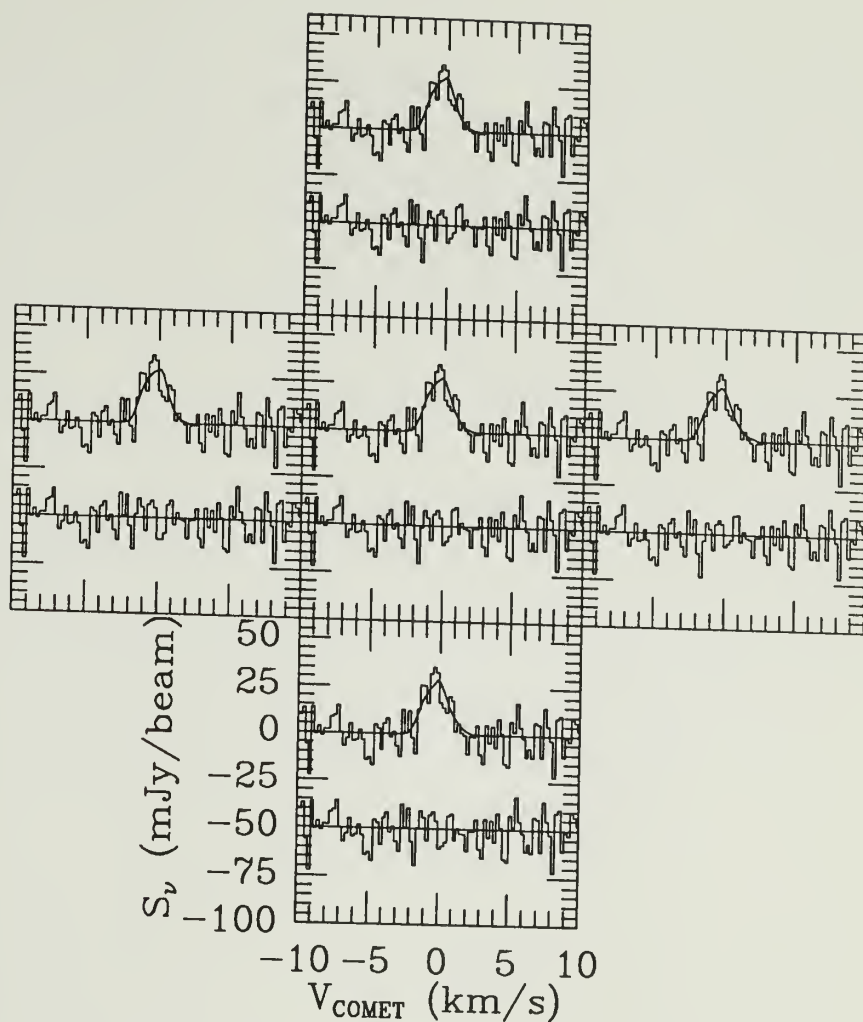


**Figure 4.4a:** A representative sample of model spectra generated using the inversion curve of SA superimposed on the spectrum of P/Halley from September 1985. The parameters for the center spectra are  $AP = +0.9$  and  $V_P = 0.8 \text{ km sec}^{-1}$ ; the left-right velocity increments are  $0.2 \text{ km sec}^{-1}$  and the bottom-top AP increments are 0.3 units. Offset from the model/data pair are the residuals from the model fit.

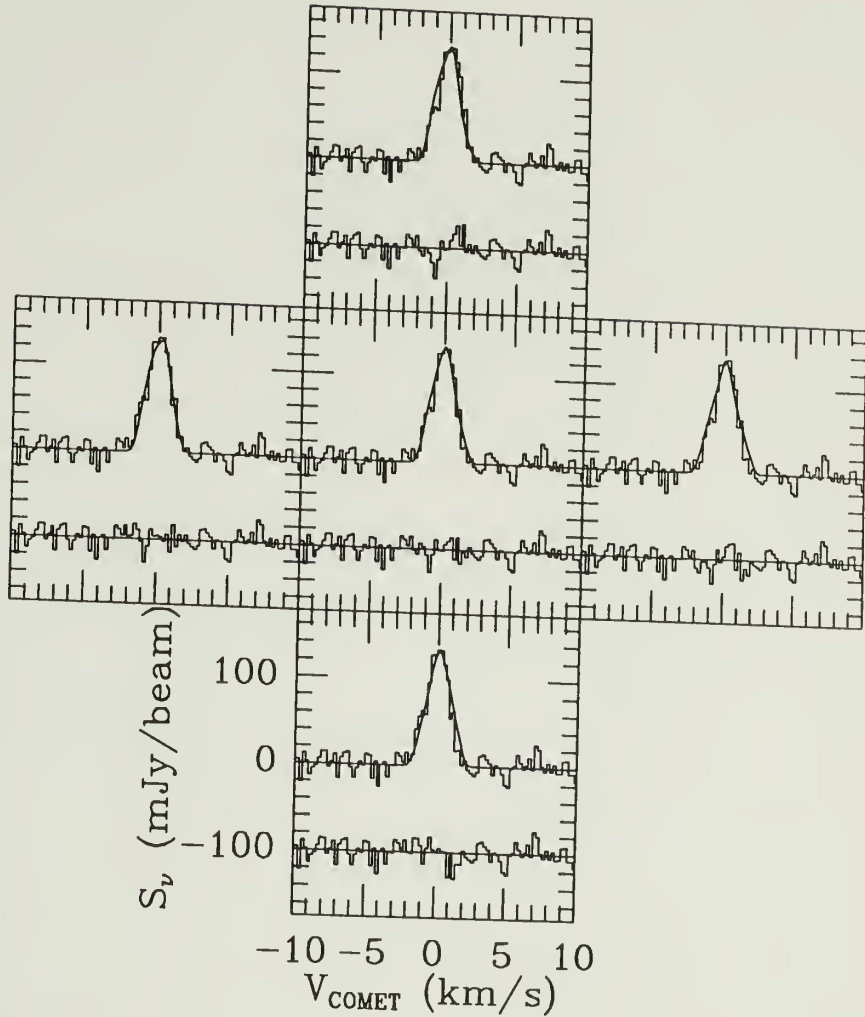
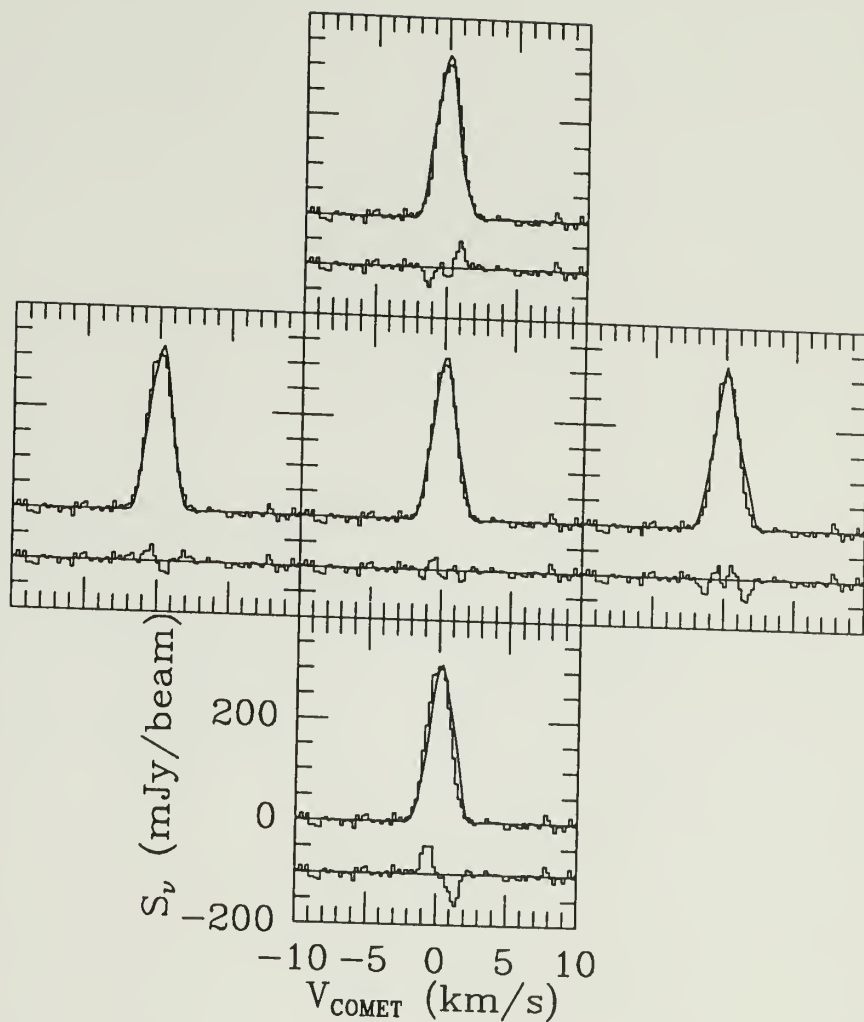
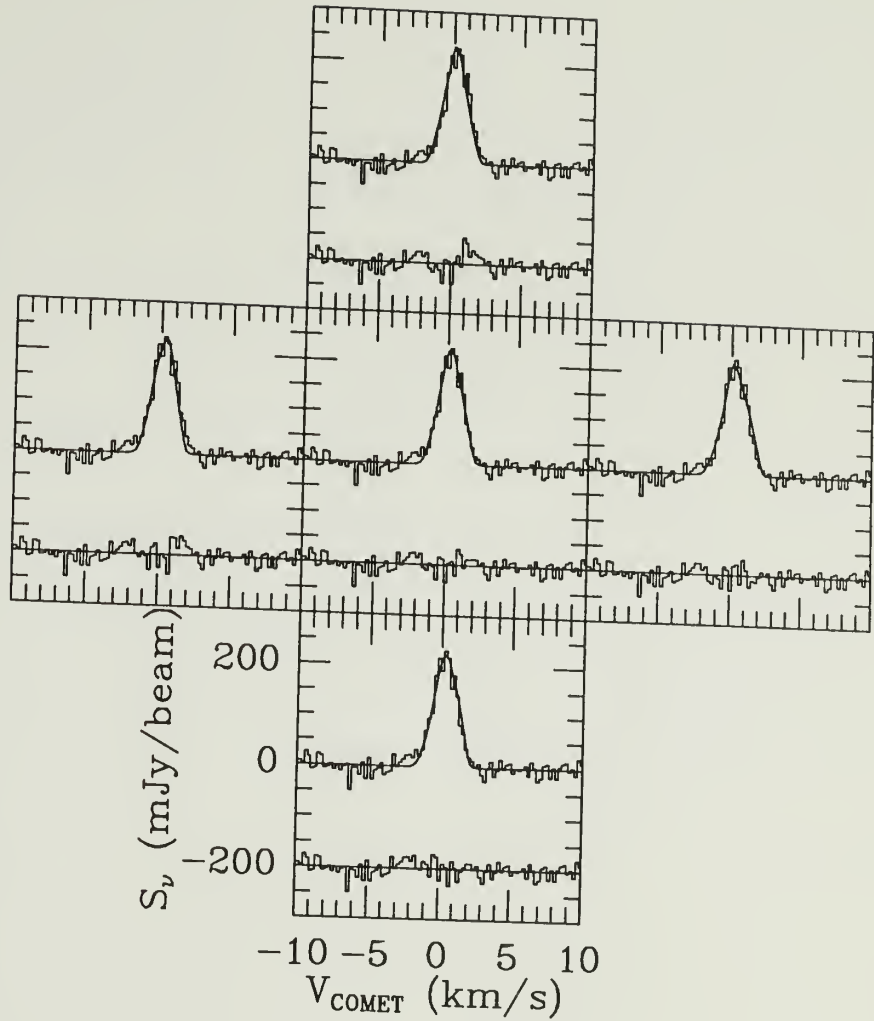


Figure 4.4b: A representative sample of model spectra generated using the inversion curve of SA superimposed on the spectrum of P/Halley from October 1985. The parameters for the center spectra are  $AP = +0.3$  and  $V_P = 0.6 \text{ km sec}^{-1}$ ; the left-right velocity increments are  $0.2 \text{ km sec}^{-1}$  and the bottom-top AP increments are 0.3 units. Offset from the model/data pair are the residuals from the model fit.



**Figure 4.4c:** A representative sample of model spectra generated using the inversion curve of SA superimposed on the spectrum of P/Halley from November 1985. The parameters for the center spectra are  $AP = +0.3$  and  $V_P = 0.6 \text{ km sec}^{-1}$ ; the left-right velocity increments are  $0.2 \text{ km sec}^{-1}$  and the bottom-top AP increments are 0.3 units. Offset from the model/data pair are the residuals from the model fit.



**Figure 4.4d:** A representative sample of model spectra generated using the inversion curve of SA superimposed on the spectrum of P/Halley from December 1985. The parameters for the center spectra are  $AP = +0.3$  and  $V_P = 0.6 \text{ km sec}^{-1}$ ; the left-right velocity increments are  $0.2 \text{ km sec}^{-1}$  and the bottom-top AP increments are 0.3 units. Offset from the model/data pair are the residuals from the model fit.

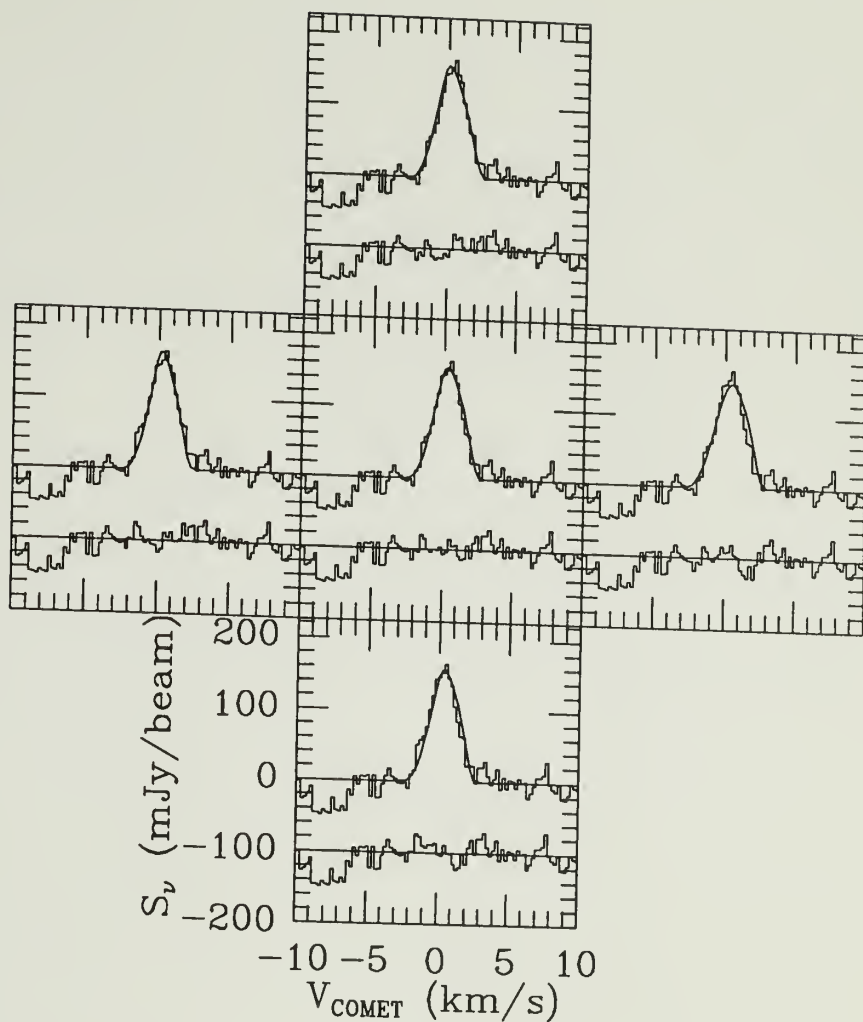


**Figure 4.4e:** A representative sample of model spectra generated using the inversion curve of SA superimposed on the spectrum of P/Halley from January 1986. The parameters for the center spectra are  $AP = 0.0$  and  $V_P = 1.0 \text{ km sec}^{-1}$ ; the left-right velocity increments are  $0.2 \text{ km sec}^{-1}$  and the bottom-top AP increments are 0.3 units. Offset from the model/data pair are the residuals from the model fit.

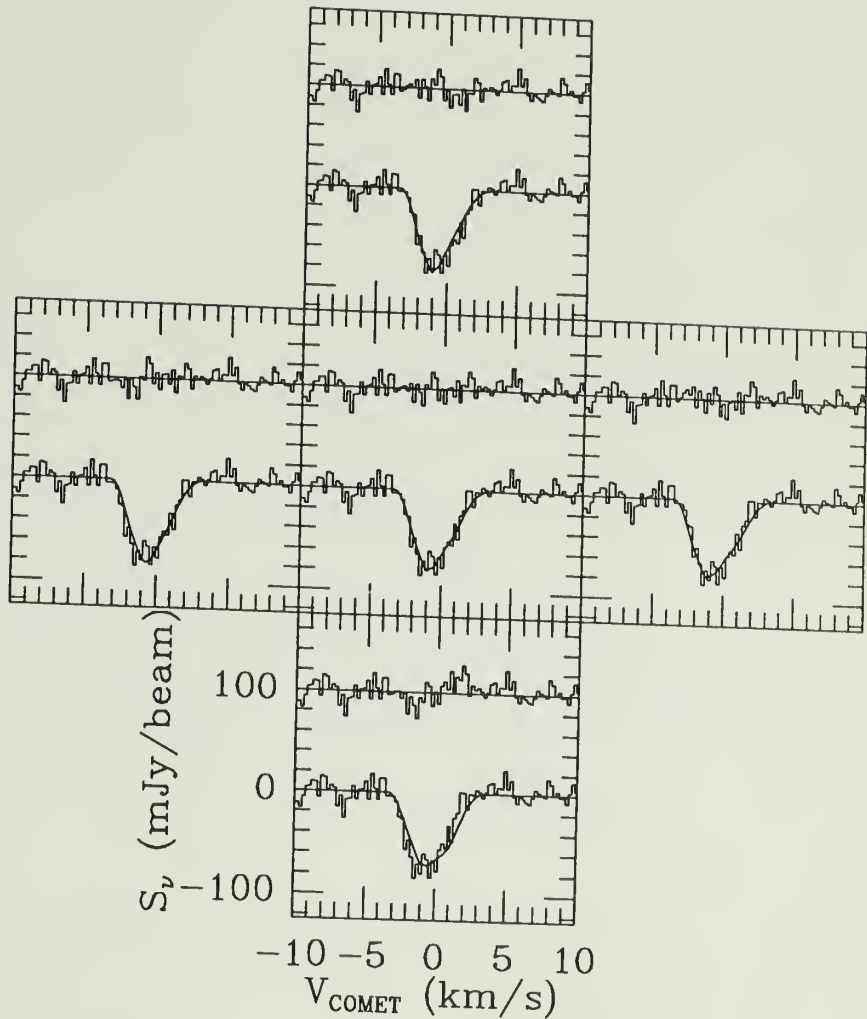
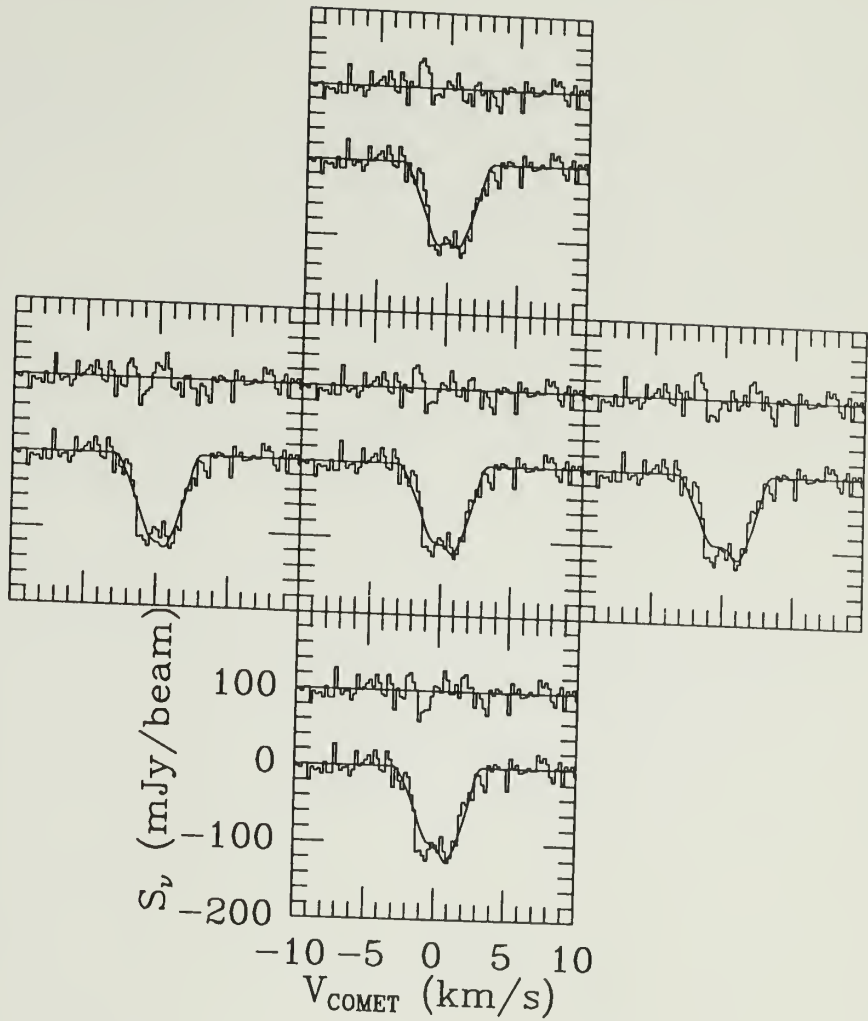
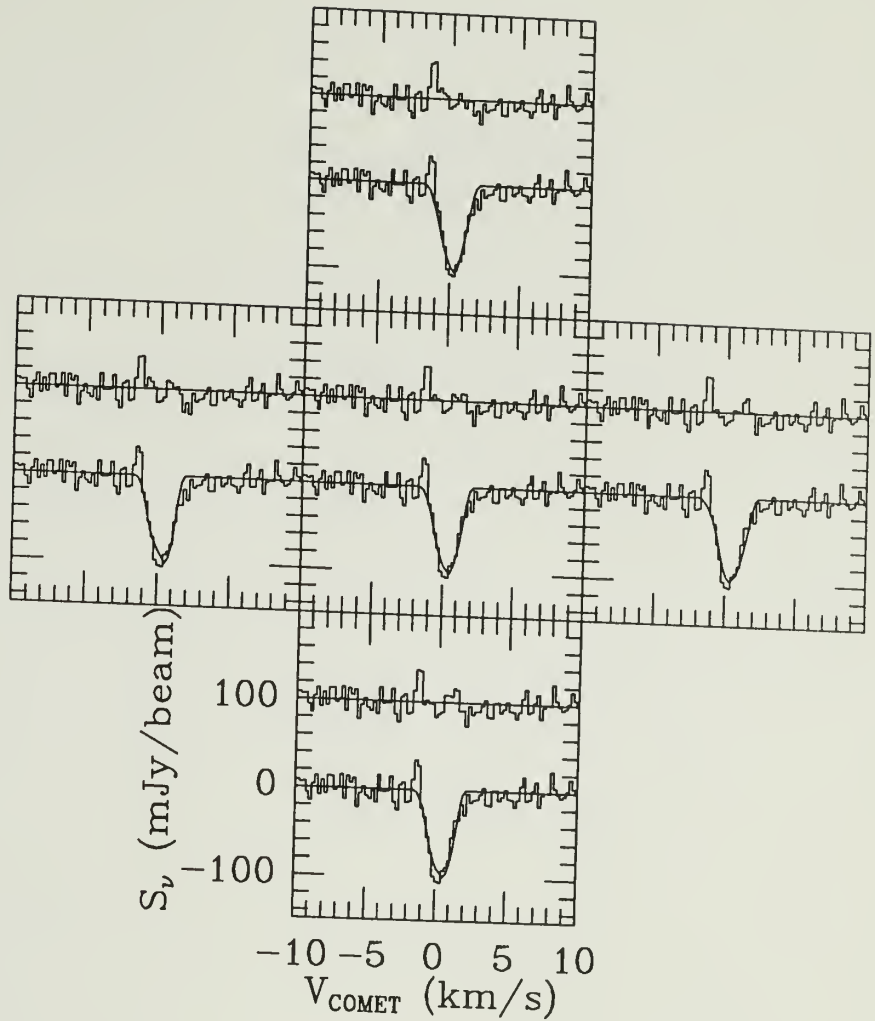


Figure 4.4f: A representative sample of model spectra generated using the inversion curve of SA superimposed on the spectrum of P/Halley from February 1986. The parameters for the center spectra are  $AP = +0.3$  and  $V_P = 1.8 \text{ km sec}^{-1}$ ; the left-right velocity increments are  $0.2 \text{ km sec}^{-1}$  and the bottom-top AP increments are 0.3 units. Offset from the model/data pair are the residuals from the model fit.





**Figure 4.4g:** A representative sample of model spectra generated using the inversion curve of SA superimposed on the spectrum of P/Halley from March 1986. The parameters for the center spectra are  $AP = 0.0$  and  $V_P = 1.6 \text{ km sec}^{-1}$ ; the left-right velocity increments are  $0.2 \text{ km sec}^{-1}$  and the bottom-top AP increments are 0.3 units. Offset from the model/data pair are the residuals from the model fit.



**Figure 4.4h:** A representative sample of model spectra generated using the inversion curve of SA superimposed on the spectrum of P/Halley from May 1986. The parameters for the center spectra are  $AP = -0.3$  and  $V_P = 0.4 \text{ km sec}^{-1}$ ; the left-right velocity increments are  $0.2 \text{ km sec}^{-1}$  and the bottom-top AP increments are  $0.3$  units. Offset from the model/data pair are the residuals from the model fit.

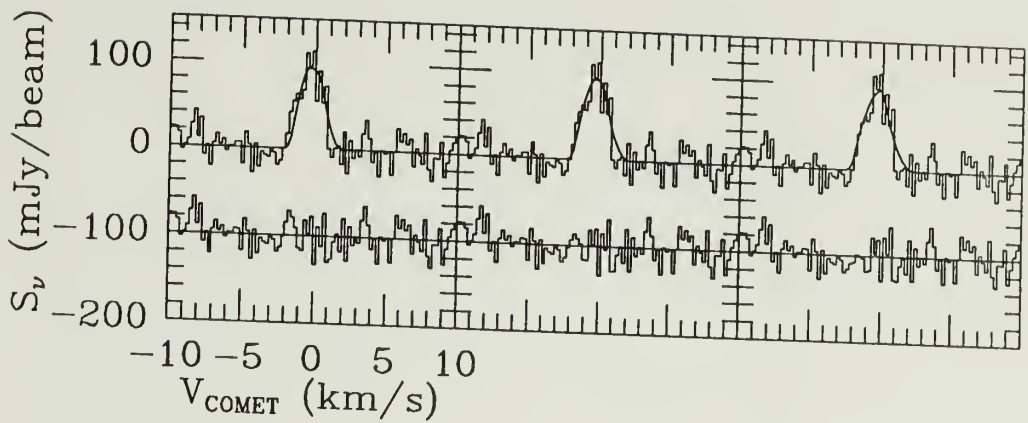


**Figure 4.4i:** A representative sample of model spectra generated using the inversion curve of SA superimposed on the spectrum of P/Giacobini-Zinner from July 1985. The parameters for the center spectra are  $AP = +0.9$  and  $V_P = 0.6 \text{ km sec}^{-1}$ ; the left-right velocity increments are  $0.2 \text{ km sec}^{-1}$ . Offset from the model/data pair are the residuals from the model fit.

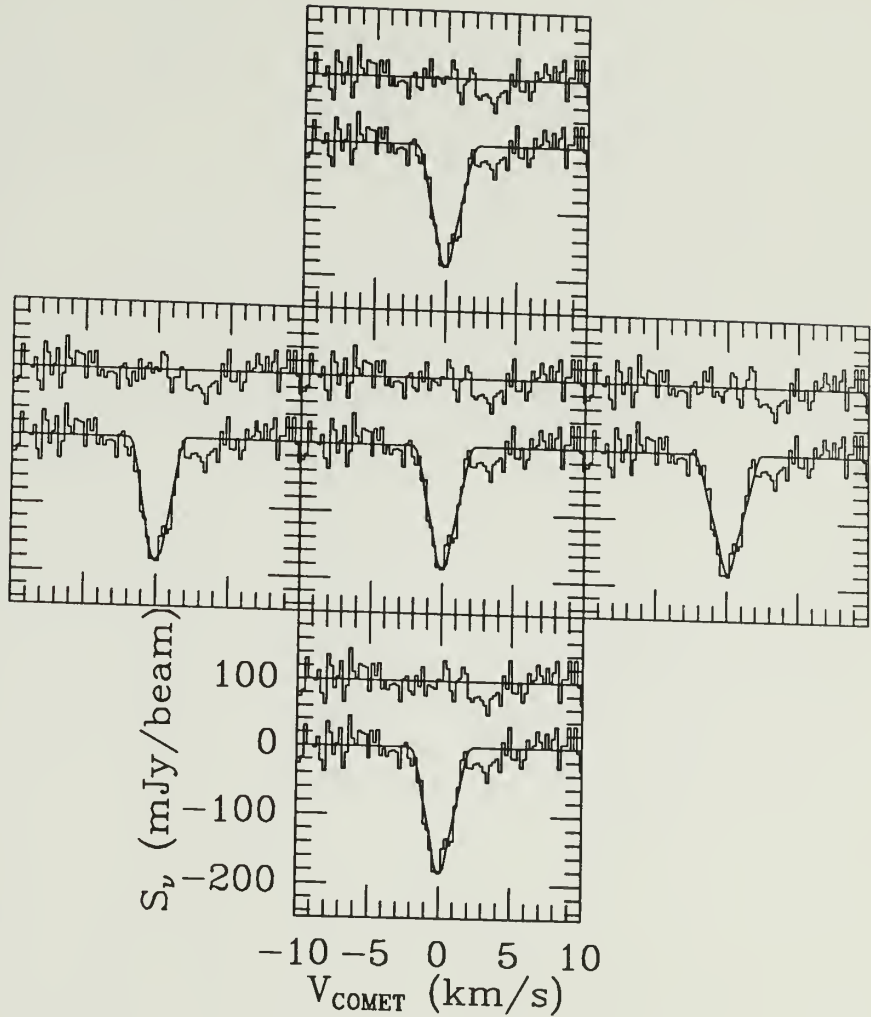


**Figure 4.4j:** A representative sample of model spectra generated using the inversion curve of SA superimposed on the spectrum of P/Giacobini-Zinner from August 1985. The parameters for the center spectra are  $AP = -0.6$  and  $V_P = 0.6 \text{ km sec}^{-1}$ ; the left-right velocity increments are  $0.2 \text{ km sec}^{-1}$  and the bottom-top AP increments are 0.3 units. Offset from the model/data pair are the residuals from the model fit.

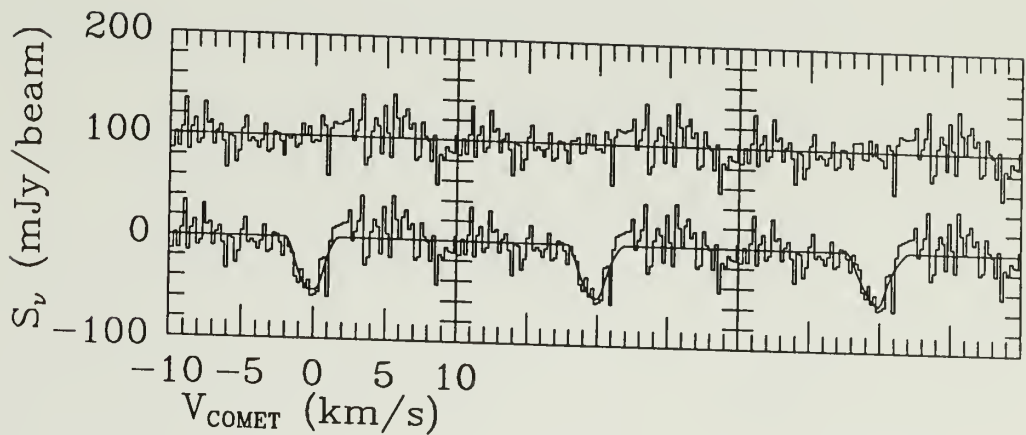


**Figure 4.4k:** A representative sample of model spectra generated using the inversion curve of SA superimposed on the spectrum of P/Giacobini-Zinner from October 1985. The parameters for the center spectra are  $AP = +2.1$  and  $V_P = 0.6 \text{ km sec}^{-1}$ ; the left-right velocity increments are  $0.2 \text{ km sec}^{-1}$ . Offset from the model/data pair are the residuals from the model fit.

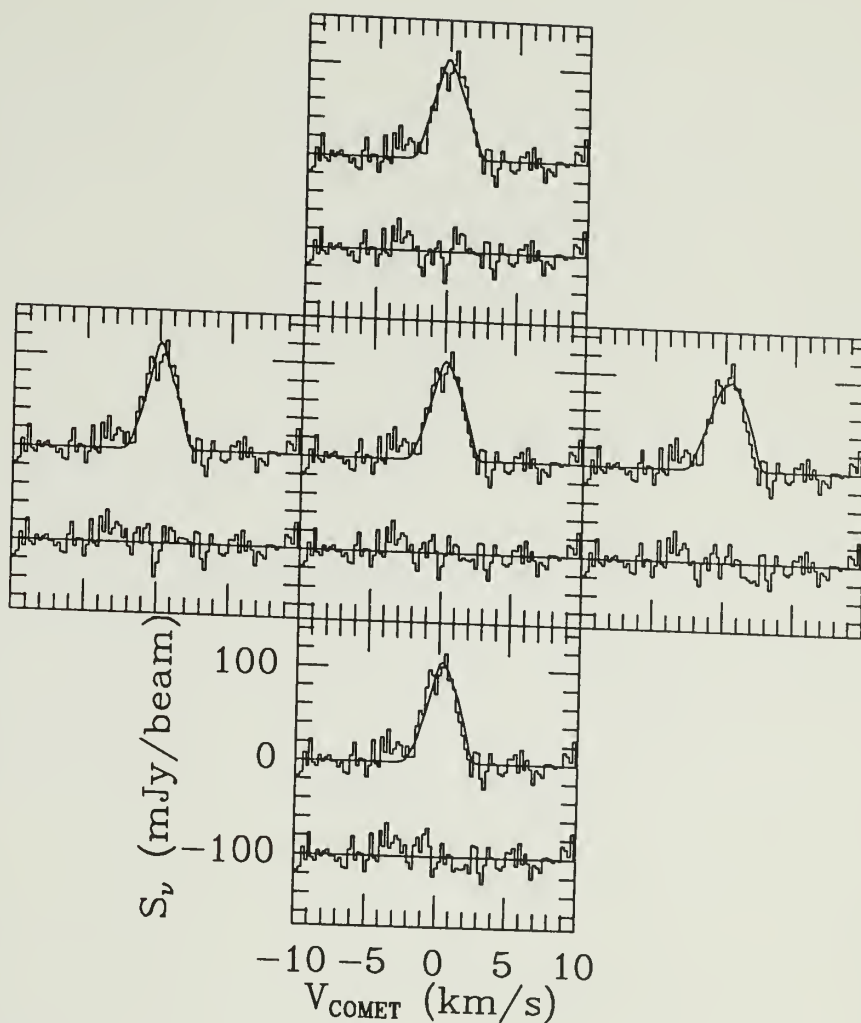


Figure 4.41: A representative sample of model spectra generated using the inversion curve of SA superimposed on the spectrum of C/Hartley-Good from October 1985. The parameters for the center spectra are  $AP = 0.0$  and  $V_P = 1.0 \text{ km sec}^{-1}$ ; the left-right velocity increments are  $0.2 \text{ km sec}^{-1}$  and the bottom-top AP increments are 0.3 units. Offset from the model/data pair are the residuals from the model fit.

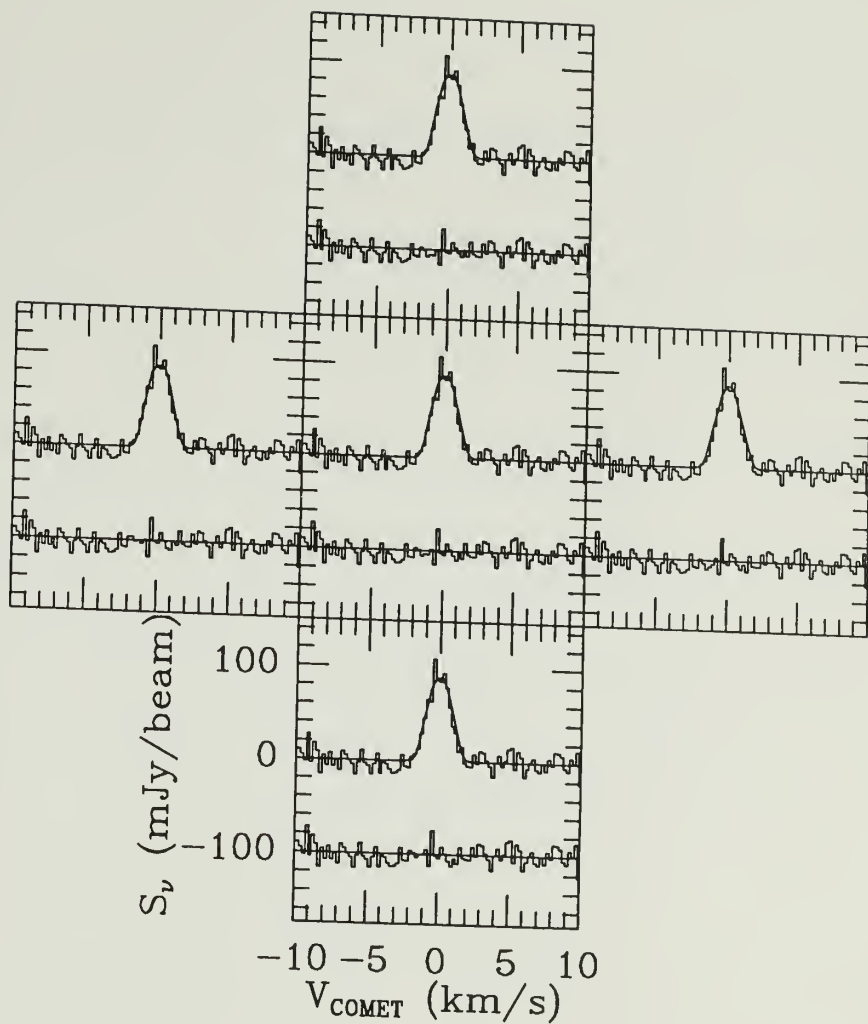


Figure 4.4m: A representative sample of model spectra generated using the inversion curve of SA superimposed on the spectrum of C/Hartley-Good from November 1985. The parameters for the center spectra are  $AP = +0.3$  and  $V_P = 0.4 \text{ km sec}^{-1}$ ; the left-right velocity increments are  $0.1 \text{ km sec}^{-1}$  and the bottom-top AP increments are 0.3 units. Offset from the model/data pair are the residuals from the model fit.

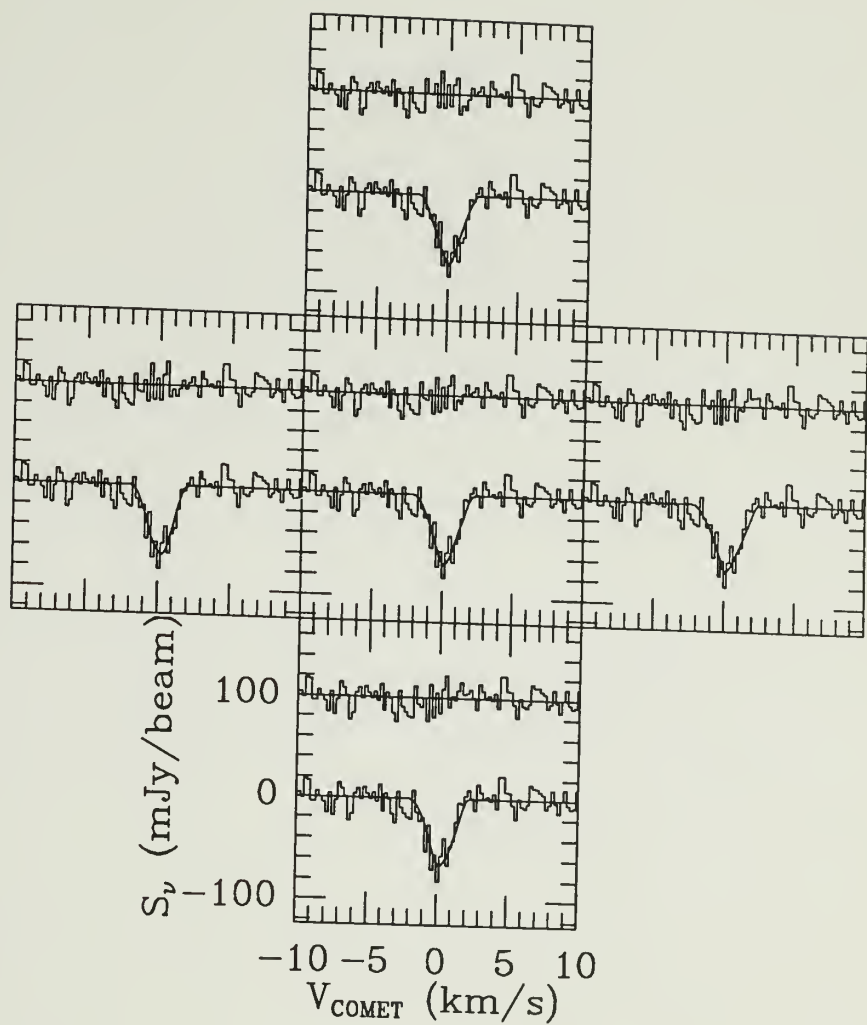
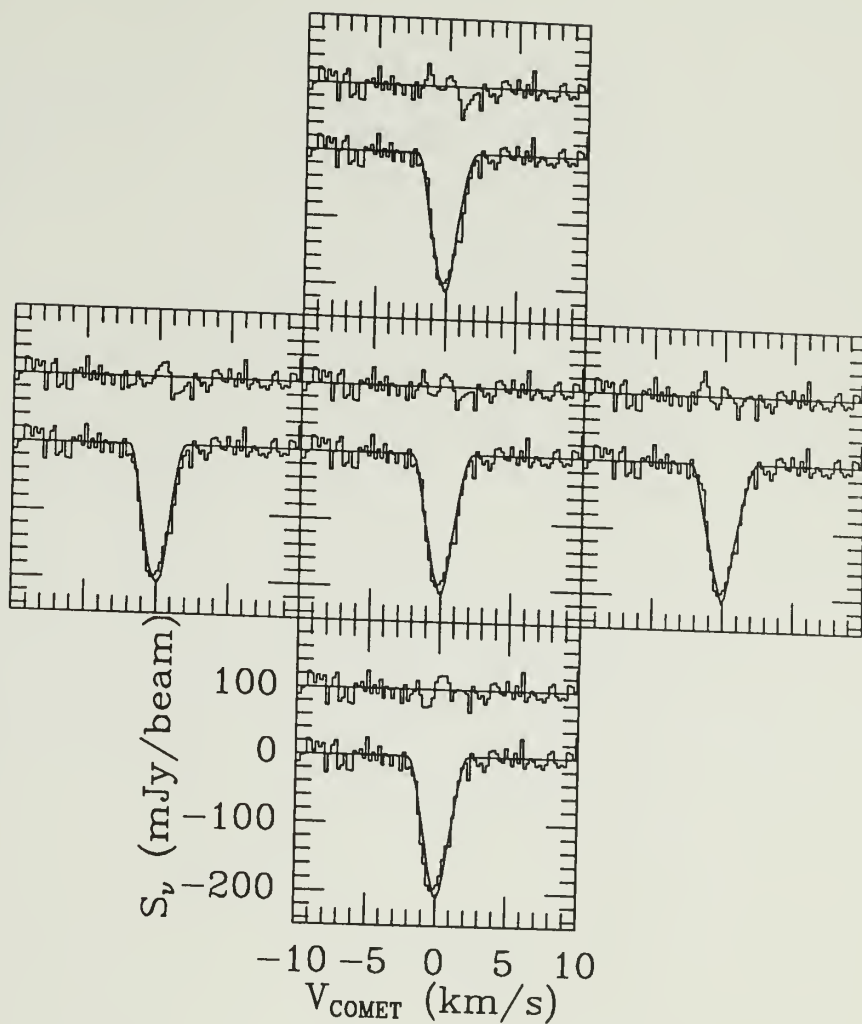


Figure 4.4n: A representative sample of model spectra generated using the inversion curve of SA superimposed on the spectrum of C/Thiele from November 1985. The parameters for the center spectra are  $AP = 0.0$  and  $V_P = 0.6 \text{ km sec}^{-1}$ ; the left-right velocity increments are  $0.2 \text{ km sec}^{-1}$  and the bottom-top AP increments are 0.3 units. Offset from the model/data pair are the residuals from the model fit.





**Figure 4.40:** A representative sample of model spectra generated using the inversion curve of SA superimposed on the spectrum of C/Wilson from March 1987. The parameters for the center spectra are  $AP = +0.3$  and  $V_P = 0.6 \text{ km sec}^{-1}$ ; the left-right velocity increments are  $0.2 \text{ km sec}^{-1}$  and the bottom-top AP increments are 0.3 units. Offset from the model/data pair are the residuals from the model fit.

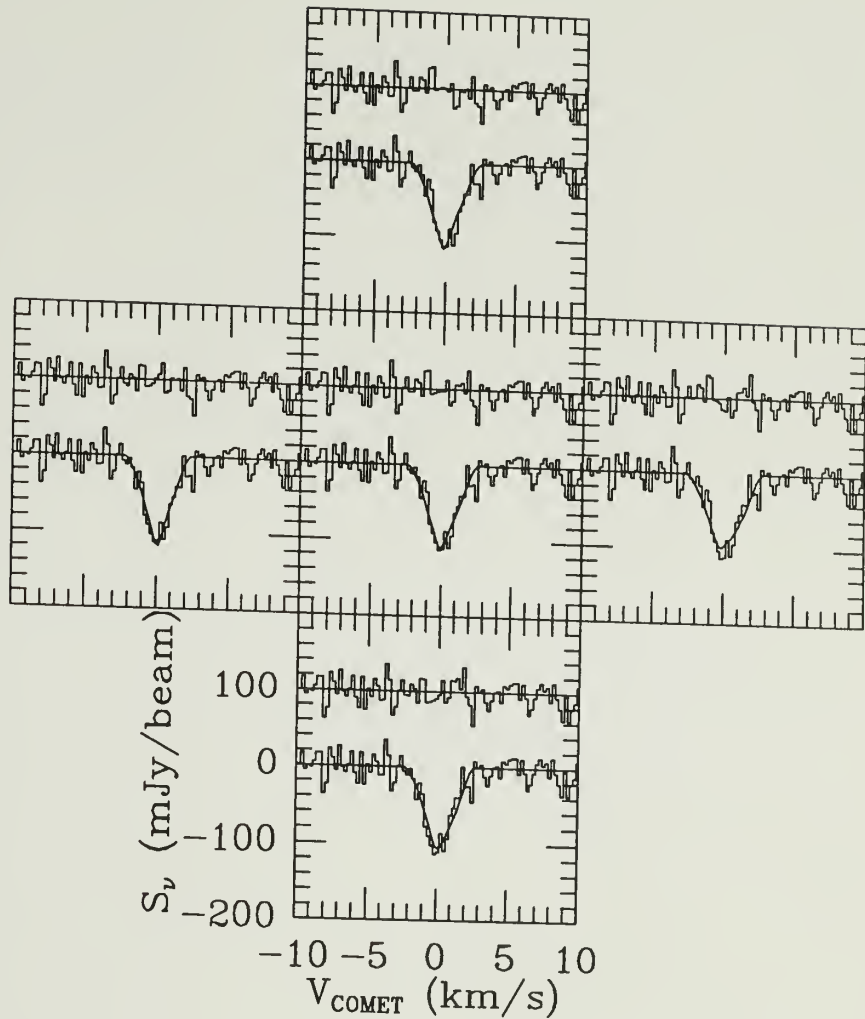


Figure 4.4p: A representative sample of model spectra generated using the inversion curve of SA superimposed on the spectrum of C/Wilson from May 1987. The parameters for the center spectra are  $AP = +0.6$  and  $V_P = 1.0 \text{ km sec}^{-1}$ ; the left-right velocity increments are  $0.2 \text{ km sec}^{-1}$  and the bottom-top AP increments are 0.3 units. Offset from the model/data pair are the residuals from the model fit.

the tops of the profiles (Figures 4.3b and c). The inability of models using the SA inversion curve to properly fit the top of the November 1985 P/Halley spectrum was noticed originally by Tacconi-Garman and Schloerb (1987b; see also Schloerb, Claussen, and Tacconi-Garman 1987). Other cases where models using one inversion curve fit the data marginally better than those using the other curve are in March 1986 (P/Halley; Figures 4.3g and 4.4g) and in March 1987 (C/Wilson; Figures 4.3o and 4.4o). In the former case the model spectrum generated using the Despois curve has a more pronounced "dimple" at the bottom than does the SA spectrum. Thus, the Despois generated spectrum does a slightly better job of matching the flat bottom of the data. Both synthetic spectra, however, are wider than the data. In the case of the models for the March 1987 observations of C/Wilson, we note that the model using the SA inversion curve fits the edges of the observed profile a bit better than the model using the Despois curve does. Both model spectra fall short, however, in properly reproducing the very bottom of the spectrum.

The only example, however, where a model using one inversion curve *clearly* represents the data better than a model which uses the other curve is in the case of the May 1986 epoch of P/Halley. As mentioned in Chapter 2 (see also Figure 2.1h), there is a real emission feature to the blue side of the dominant absorption line in this data. Close examination of Figures 4.3h and 4.4h show that, in fact, only the Despois model has an emission feature which corresponds to the emission in the data. To demonstrate that emission

at this velocity naturally follows from the Despois inversion curve, we present in Figure 4.5 the data from this epoch (top) and appropriate portions of the Despois and SA inversion curves (bottom). For this figure the velocity scales of the inversion curves have been corrected for the velocity of the comet with respect to the earth and the phase angle of the observations,  $\beta$ . Here we see that the range of gas velocities in the coma during that epoch actually span a crossing point of the Despois inversion curve, whereas the SA curve crosses zero at a lower velocity. Molecules traveling with velocities less than  $1.22 \text{ km sec}^{-1}$  with respect to the earth should have positive inversions, according to the Despois curve, and hence should be seen in emission. This is precisely what is seen in the data.

In the majority of cases, though, there is little significant difference in the quality of the fits generated from models using either inversion curve. This is hardly surprising in light of the fact that *at the heliocentric velocities of the epochs in this study* there is little difference in the *shape* of the inversion curves (Figure 4.6)<sup>1</sup>. This similarity is also reflected in the agreement between most of the  $\chi^2_{\nu}$  surfaces and the derived values for AP and  $V_P$  for the two models. To further demonstrate this lack of sensitivity to the inversion curve used, we have plotted in Figure 4.7 the difference in derived  $V_P$  values versus

---

<sup>1</sup>This does not contradict statements in the last section referring to large differences between the curves. Since we scale our model spectra in a “brute force” manner to fit the data, the magnitude of the inversion is not very critical to our model results, assuming we are not near a crossing point for either curve. On the contrary, what is important for reproducing the observed line profiles is the shape of the inversion curve over the velocity range covered by the gas in the coma. In deriving the production rates, on the other hand, we use a single value at a particular heliocentric velocity.

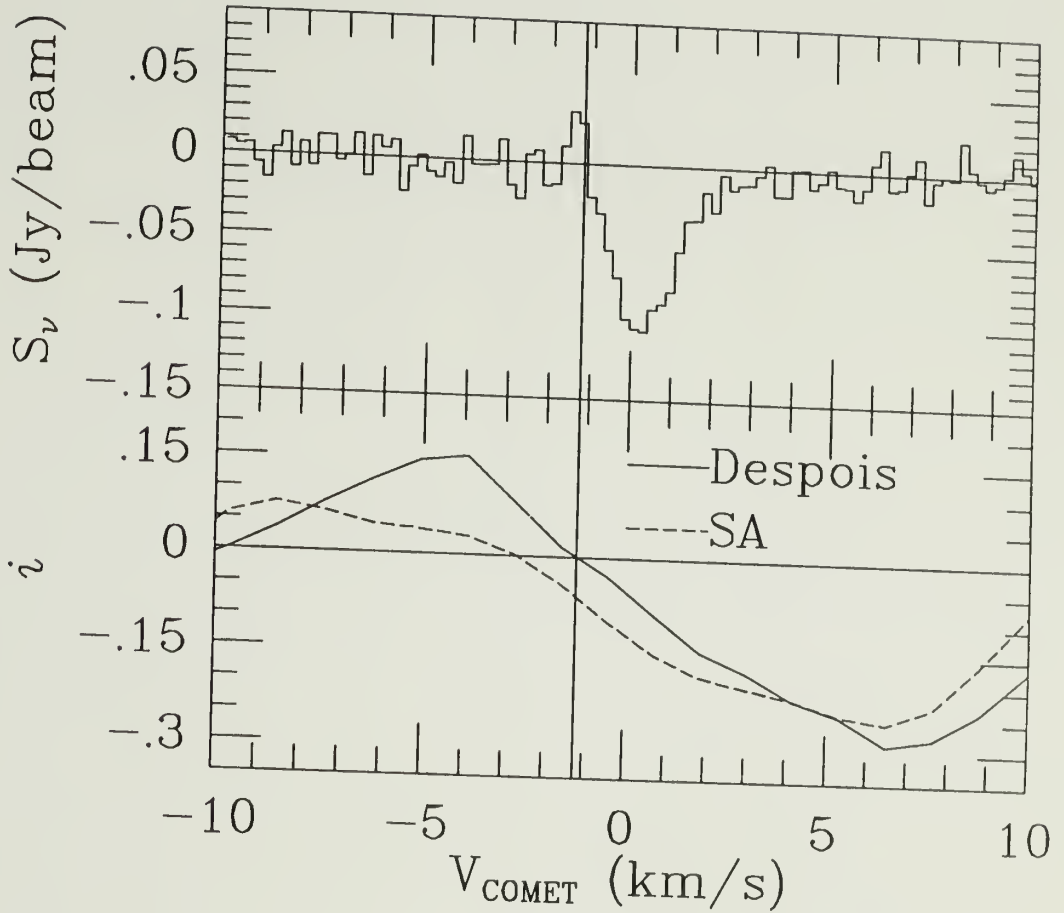


**Figure 4.5:** The May 1985 P/Halley spectrum (top) and relevant portions of the Despois and SA inversion curves (bottom). Note the coincidence between the crossing point of the Despois curve and the transition from absorption to emission in the data.

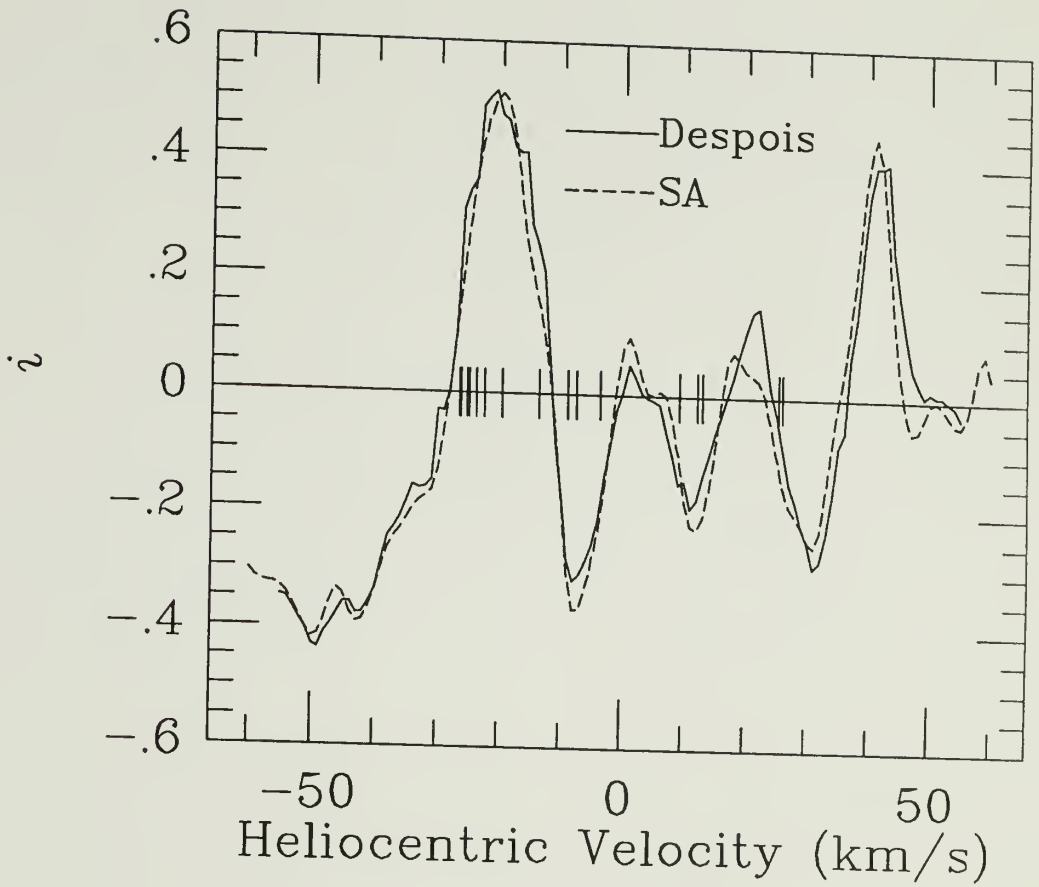


**Figure 4.6:** The Despois and SA inversion curves. The tick marks on the x-axis represent the heliocentric velocities of the comets in this thesis.

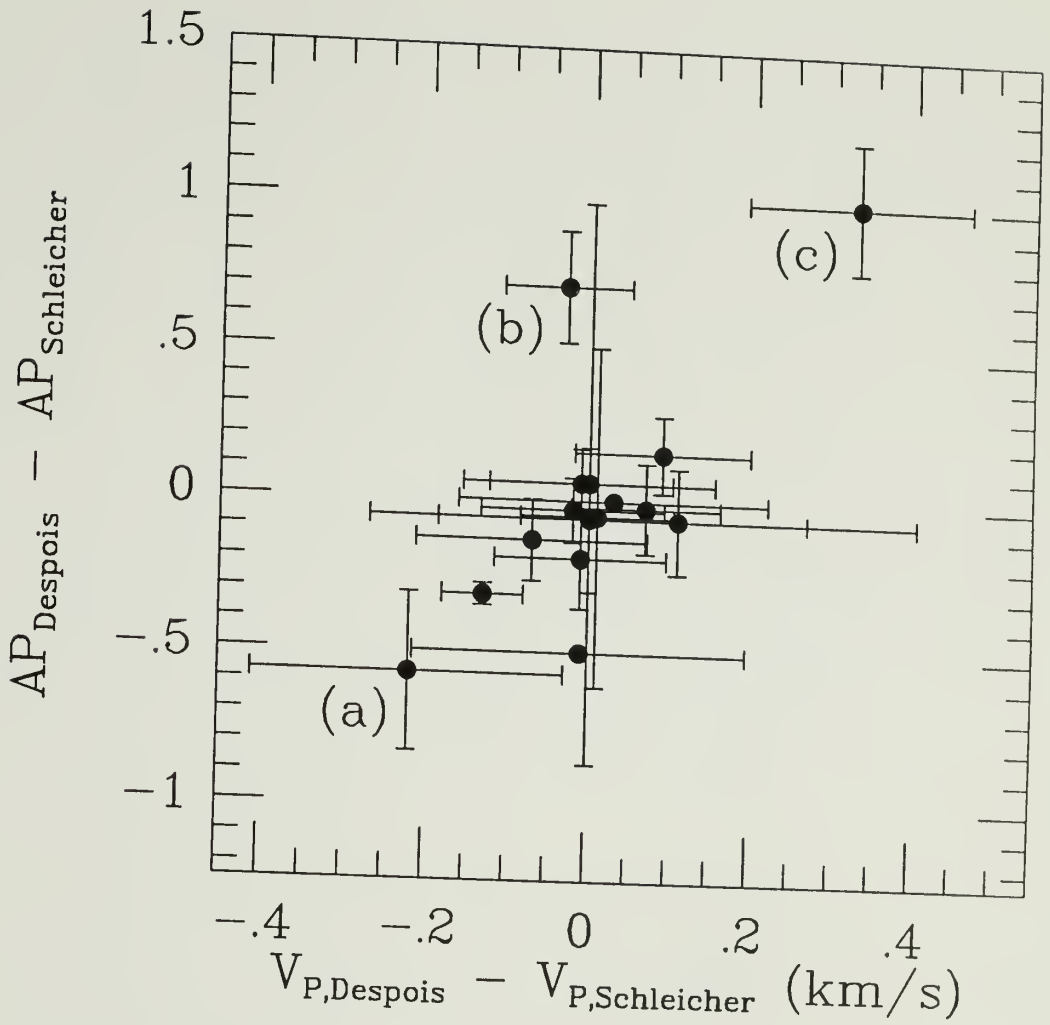


**Figure 4.7:** The difference between AP and  $V_P$  values derived using the Despois and SA inversion curves. The cluster near the origin indicates an insensitivity in the model fits to the choice of inversion curves. Points (a), (b), and (c) are described in the text.

the difference in derived AP values. The cluster of points near the origin of this plot indicates that the values we derive for these kinematic parameters are primarily independent of the inversion curve used. For one of the three outlying points in this plot, C/Wilson in May 1987 (a) we derive AP values which differ by 0.57, or a factor of  $\sim 3.5$  in the day-to-night gas outflow ratio. Point (b) in Figure 4.7 represents the March 1986 Comet Halley epoch, which was mentioned above. In neither of these cases is there compelling evidence to prefer one inversion curve over the other. The final discrepant point, P/Halley in May 1986 (c), was also discussed above.

To determine final values for the modeled kinematic parameters we have averaged the AP and  $V_P$  values obtained using the Despois and SA inversion curves. The exception to this, of course, is the May 1986 epoch of Halley for which we use the AP and  $V_P$  values derived using the Despois inversion curve. The errors on our adopted AP and  $V_P$  values are derived from the difference in values when using these two inversion curves. A complete summary of our derived AP and  $V_P$  values is found in Tables 4.3 and 4.4.

### 4.3.2 AP Results

Except for the cases of the P/Giacobini-Zinner model results, which are discussed at the end of this section, *all* of our adopted AP values fall in the range  $\sim 0$  to 0.8, with errors in individual determinations roughly scaling with the cosine of the phase angle,  $\beta$ . We expect such a dependence for this



Table 4.3  
Kinematic Model Results for Comet Halley

Epoch	$R_h$ A.U.	$AP_{Despois}$	$AP_{SA}$	$V_{P,Despois}$ $km\ s^{-1}$	$V_{P,SA}$ $km\ s^{-1}$	$AP^1$	$V_P^1$ $km\ s^{-1}$
Sept 1985	2.47	+0.75 (0.09)	+0.81 (0.15)	0.97 (0.12)	0.86 (0.27)	+0.78 (0.18)	0.92 (0.33)
Oct 1985	2.09	+0.30 (0.08)	+0.24 (0.08)	0.50 (0.08)	0.51 (0.08)	+0.27 (0.11)	0.51 (0.08)
Nov 1985	1.74	+0.04 (0.03)	+0.35 (0.02)	0.41 (0.04)	0.54 (0.03)	+0.25 (0.24)	0.49 (0.12)
Dec 1985	1.34	+0.33 (0.10)	+0.17 (0.08)	0.75 (0.09)	0.66 (0.06)	+0.25 (0.18)	0.71 (0.13)
Jan 1986	0.97	+0.01 (0.11)	+0.03 (0.10)	1.05 (0.06)	0.98 (0.07)	+0.02 (0.12)	1.02 (0.10)
Feb 1986	0.626	+0.23 (0.09)	+0.36 (0.10)	1.75 (0.11)	1.82 (0.09)	+0.30 (0.16)	1.79 (0.15)
Mar 1986	0.94	+0.73 (0.14)	+0.02 (0.12)	1.58 (0.05)	1.61 (0.06)	+0.38 (0.49)	1.60 (0.07)
May 1986	1.67	+0.63 (0.10)	-0.37 (0.19)	0.77 (0.07)	0.44 (0.12)	+0.63 (0.10)	0.77 (0.07)

<sup>1</sup> Adopted value.

Table 4.4

Kinematic Model Results for Comets Giacobini-Zinner, Hartley-Good, Thiele, and Wilson

Comet	Epoch	R <sub>h</sub> A.U.	AP <sub>Despois</sub>	AP <sub>SA</sub>	V <sub>P,Despois</sub> km s <sup>-1</sup>	V <sub>P,SA</sub> km s <sup>-1</sup>	AP <sup>1</sup>	V <sub>P</sub> <sup>1</sup> km s <sup>-1</sup>
P/Giacobini-Zinner	Jul 1985	1.29	≥1.00	≥1.00	0.64 (0.13)	0.61 (0.14)	≥1.00	0.63 (0.16)
P/Giacobini-Zinner	Aug 1985	1.04	-0.69 (0.64)	-0.75 (0.67)	0.51 (0.11)	0.51 (0.11)	-0.72 (0.70)	0.51 (0.11)
P/Giacobini-Zinner	Oct 1985	1.21	≥1.50	≥2.00	0.51 (0.15)	0.52 (0.14)	≥1.50	0.52 (0.16)
C/Hartley-Good	Oct 1985	1.19	-0.18 (0.12)	+0.01 (0.11)	1.00 (0.07)	1.01 (0.08)	-0.08 (0.22)	1.00 (0.09)
C/Hartley-Good	Nov 1985	0.85	+0.33 (0.36)	+0.38 (0.43)	0.40 (0.05)	0.39 (0.08)	+0.35 (0.46)	0.40 (0.09)
C/Thiele	Nov 1985	1.41	-0.03 (0.06)	+0.02 (0.22)	0.60 (0.07)	0.56 (0.56)	-0.01 (0.23)	0.58 (0.23)
C/Wilson	Mar 1987	1.25	+0.14 (0.07)	+0.21 (0.08)	0.68 (0.08)	0.61 (0.08)	+0.18 (0.11)	0.65 (0.12)
C/Wilson	May 1987	1.28	-0.05 (0.19)	+0.57 (0.18)	0.69 (0.13)	0.84 (0.14)	+0.26 (0.49)	0.77 (0.21)

<sup>1</sup> Adopted value

error since our sensitivity to the day/night outgassing ratio depends on the component of the day-night outflow differential which lies on the line-of-sight to the comet. That is, our observations at small phase angles are far more sensitive to the effects of anisotropic emission than our observations at large phase angles.

In addition, we derive an average value for AP of  $0.29 \pm 0.04$ , implying that typically twice as much gas flows into the day hemisphere of the coma as flows into the night hemisphere. In addition, we find that the coma anisotropy is independent of both heliocentric distance (Figure 4.8) and gas production rate (Figure 4.9). Gas anisotropies this low are in contrast with that found for the dust in the coma (Keller *et al.* 1986a, b; Edenhofer *et al.* 1987). These AP values are *not* surprising, however, when viewed in light of coma gas distributions derived by a number of authors (see below).

To put things in perspective for comparison to the results of other authors, we must first consider the length scales over which our results are most appropriate. As listed in Tables 2.1 and 2.2, the 18' beam of the 43-meter telescope at NRAO corresponds to a physical dimension of  $\sim 10^6$  km at the distance of the comets during our observations. Therefore, our model results indicate that at distances of  $\sim 5 \times 10^5$  km from the nucleus there is still evidence for gas anisotropies of factors of 2–4. Specifically, for the March 1986 epoch (our closest to the time of the spacecraft encounters) we infer an

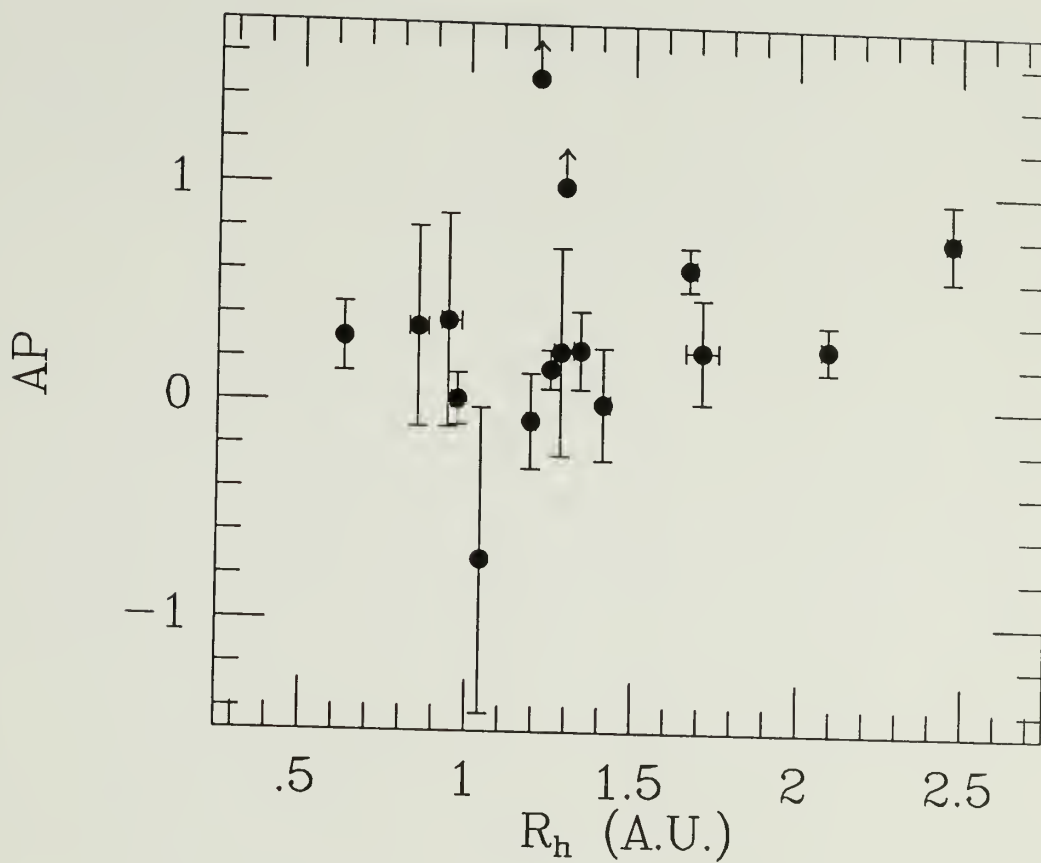
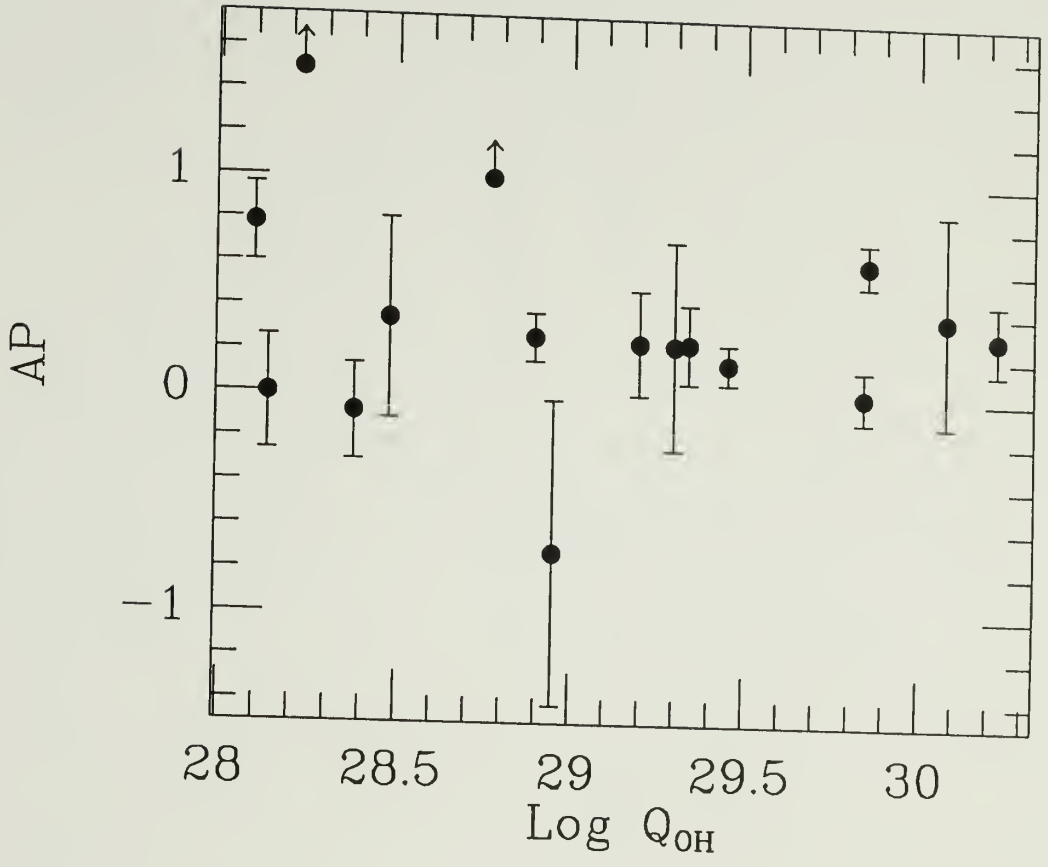


Figure 4.8: Adopted AP values as a function of heliocentric distance.



**Figure 4.9:** Adopted AP values as a function of the Log of the derived gas production rate.

AP of  $0.38 \pm 0.49$  within  $3.5 \times 10^5$  km of the nucleus. This corresponds to a day/night asymmetry of a factor of  $2.4 \begin{smallmatrix} (+5.0) \\ (-1.6) \end{smallmatrix}$ .

Evidence for anisotropies in the gas distribution at smaller radii comes from a variety of sources. Krasnopolsky *et al.* (1987) have modeled  $1.38 \mu\text{m}$  water data taken by the three-channel spectrometer (TKS; Krasnopolsky *et al.* 1986) onboard the Vega 2 spacecraft and find that 40% of the water in the inner 1000–2000 km of the coma of Halley was confined to a cone with an opening angle of  $20 \pm 5^\circ$ . Assuming that the remaining 60% is evenly distributed about the nucleus, this implies a day-to-night ratio of  $\sim 2$  in this region. Larger regions of the coma ( $r \lesssim 12500$  km) were probed on 24 December 1985 and 22 March 1986 (close to the time of the spacecraft encounters) by the  $2.65 \mu\text{m}$  water observations of Larson *et al.* (1986). They find that both their pre- and post-perihelion data are consistent with a coma gas outflow morphology which is a superposition of an isotropic flow and a sun-directed enhanced flow. That is, their data are compatible with a slightly anisotropic flow. In addition, similarly sized regions in Comet Halley were probed by the HCN observations of Schloerb *et al.* (1987). They find a net blueshifting of the main ( $F=2-1$ ) hyperfine component which, given the phase angles at the times of their observations, is suggestive of an enhancement in the emission into the day hemisphere.

That such anisotropies can persist to large distances is demonstrated by the neutral particle density profiles deduced from data collected by the

PLASMAG-1 instruments on Vega 1 and Vega 2 (Remizov *et al.* 1986). Remizov *et al.* present experimental results which indicate that there were factors of 2–3 difference in the neutral gas densities at distances of  $3 \times 10^5$  km from the nucleus of Comet Halley between the inbound and outbound legs of the encounters. Similar inbound-outbound gas asymmetries were measured out to a distance of  $10^5$  km by the Neutral Gas Experiment (NGE) on the Vega 1 spacecraft (Curtis *et al.* 1986). Hsieh *et al.* (1987) have explained this observed inbound-outbound discrepancy in terms of an coma gas asymmetry of a factor of 2–6 at this distance from the nucleus.

Finally, the VLA images of the 18-cm line of OH (de Pater, Palmer, and Snyder 1986) provide further evidence for anisotropies of factors of  $\sim 2$  at distances of  $10^5$  km from the nucleus. Since anisotropy in our model is treated as strictly day-night, one must be careful in directly comparing our results to any others which treat only the dayside of the coma. However, the coma gas anisotropies that we derive from the 18-cm OH line profiles are consistent with those inferred from a variety of other observations.

As mentioned above, however, our AP results for Comet Giacobini-Zinner are unlike all others. For this comet we infer grossly anisotropic flows into either the day hemisphere of the coma (in July and October 1985) or the night hemisphere of the coma (in August 1985). This extreme inferred anisotropy could be evidence for a phase lag in the outflow of gas from the nucleus of this comet. If the gas productivity of the nucleus was strongest in the afternoon

on the comet, then it is possible, given the phase angle of these observations, that the outflowing gas was directed primarily towards the earth. As we model strictly day-night anisotropies, the large shift in the line profile produced by this afternoon outflow would be mapped into an anomalously high value for our parameter AP. However, if this explanation is correct we are confronted with the question of why we such effects are not seen for observations of any other comets at large phase angles.

### 4.3.3 $V_P$ Results

Unlike the AP results we have derived, the parent outflow velocities we infer *are* a function of heliocentric distance. This is shown in Figure 4.10 where the filled circles represent our adopted parent outflow velocities. This figure is strikingly similar to Figure 2.3 in which the line widths of the data are plotted as a function of heliocentric distance. Therefore, the natural explanation for the broadening of the 18-cm OH lines as a comet nears the sun is an increase in the parent gas velocity.

A comparison of our outflow velocity results to values derived by other authors from a variety of observations is shown in Figure 4.11. We see in this figure that this analysis of 18-cm OH line spectra has yielded outflow velocities (filled circles) which are consistent with these other measures (HCN [open circles]: Bockelée-Morvan *et al.* 1986, Schloerb *et al.* 1987; H<sub>2</sub>O [filled squares]: Lämmerzahl *et al.* 1986, Larson, Mumma, and Weaver 1987; CN Jets/Shells



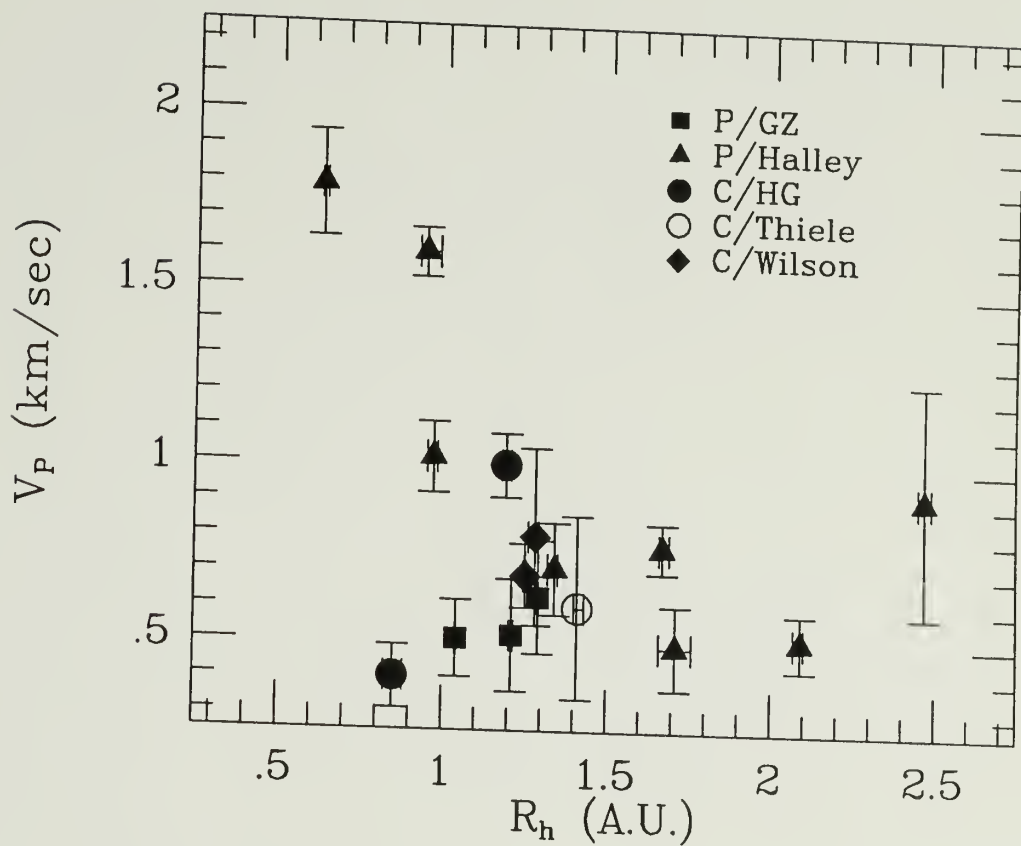


Figure 4.10: Adopted parent gas outflow velocity as a function of heliocentric distance. Note the similarity between this figure and Figure 2.3.

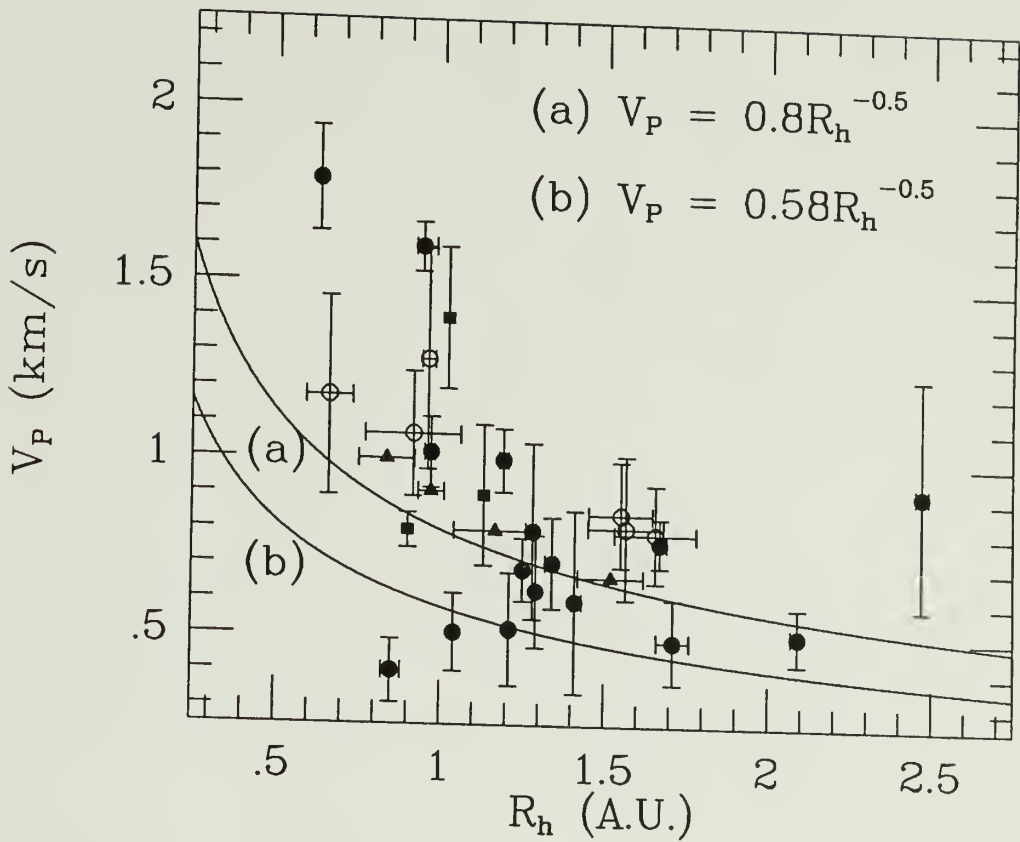


Figure 4.11: Comparison of adopted  $V_P$  values and other indicators of the coma gas expansion velocity. Curve (b) shows the velocity dependence of Delsemme (1982). Curve (a) shows the same heliocentric distance dependence with a rescaling to the often used  $0.8 \text{ km s}^{-1}$  outflow at  $R_h = 1 \text{ A.U.}$

[filled triangles]: A'Hearn *et al.* 1986, Schlosser, Schultz, and Koczet 1986).

From this we infer that our choices for such model parameters as the parent and daughter lifetimes are likely correct. Since at large heliocentric distances the velocity of the OH molecules is larger than that of the parent molecules, linewidths for comets far from the sun are more strongly influenced by the daughter velocity than for comets near the sun. Therefore, the suggestion of low inferred outflow velocities at larger heliocentric distances may indicate that the average OH velocity given by the work of Crovisier (1988) is too large.

Also shown in this figure is the outflow velocity law derived by Delsemme (1982; curve (b)) from observations of a number of comets. Clearly this law is inadequate for representing the derived outflow velocities from this and other studies. Most of our derived outflow velocities lie above this line, as was found previously by Schloerb *et al.* (1987) in their study of HCN lines in Comet Halley.

The exponent in the Delsemme outflow velocity relationship was derived by equating the coma heating and cooling rates. For heating mechanisms, Delsemme cites photoexcitation of molecules followed by collisional de-excitation and photodissociation or photoionization of molecules yielding superthermal fragments which then collide with the ambient gas (photolytic heating). Since these processes depend on the solar flux for their start, their heliocentric distance dependence should follow conservation of flux. That is,

$$\text{heating rate} \propto N R_h^{-2},$$

where  $N$  is the gas density (note this presentation of equation (8) of Delsemme uses slightly different notation from the original). For cooling processes, he adopts the work of Shimizu (1976) who suggested that water rotational transitions were efficient and argued that the cooling should be modeled as

$$\text{cooling rate} \propto T^2 N$$

where  $T$  is the temperature of the gas. Equating these two expressions and using the fact that the thermal speed of a gas is proportional to the square root of its temperature, Delsemme arrives at an  $R_h^{-0.5}$  dependence for the outflow velocity.

Since that time, Crovisier (1984) and Bockelée-Morvan (1987) have reexamined the radiative transfer of water lines in the comae of comets and have found that the water rotational lines invoked by Shimizu (and adopted by numerous others, see references in Crovisier 1984) for cooling the gas are actually optically thick in the inner coma. This means that the efficiency of these lines as coolants is lower than previously thought. Therefore, photolytic heating plays a more dominant role in determining the temperature, and hence, velocity distribution in the coma.

Since the coma expansion velocity is a strong function of the photolytic heat input, it must follow the heating rate dependence cited above. That is, the steep rise in parent gas velocity as a comet nears the sun must be not only a function of the decrease in heliocentric distance but also of the

increase in coma gas density owing to an increase in the gas productivity of the nucleus. This is supported by the thermodynamic coma modeling of Crovisier (1984) and Bockelée-Morvan and Crovisier (1987) who find an increase in the coma expansion velocity with gas productivity above a threshold of  $\sim 10^{29}$  molecules  $\text{sec}^{-1}$  (at 1 A.U.) when all other parameters are held constant. Additional theoretical work on this subject includes the dusty-gas-dynamic/Monte Carlo coma modeling of Combi (1989). He finds that an increase in the gas productivity of the nucleus results in greater collisional coupling between the fast H atoms (created during the photodissociation of water) and the molecules of the coma at large distances from the nucleus. That is, the point at which the fast H atoms decouple from the rest of the gas is pushed further out into the coma as the gas production rate increases. This increased collisional rate results in a hotter coma which, in turn, increases the outflow velocity.

Observational evidence for this effect was cited by Colom *et al.* (1987) in their recent paper on OH radio lines in comets. They have determined line widths from a series of observations of Comets Halley and Wilson and see an increase with decreasing heliocentric distance. Without attempting to disentangle the OH and parent gas velocities from their profiles, they have suggested that an increase in parent gas velocity through photolytic heating is responsible for this broadening trend. As support for this they show in their Figure 9 the measured line widths as a function of  $Q_P/R_h^2$  (note that our

notation is slightly different from theirs) in which a rise in line width above a threshold value of  $10^{29}$  molecules  $\text{sec}^{-1}$   $\text{AU}^{-2}$  is clearly seen, in agreement with the model calculations of Bockelée-Morvan and Crovisier (1987).

Our derived parent gas outflow velocities are completely consistent with this scenario. We have found that our results do not agree with the curve of Delsemme which was derived under the assumption that the cooling of the coma through water rotational lines was as important to the thermodynamics of the coma gas as the heating due to photolytic processes. Instead, our results illustrate that the net heating of the coma as the comet nears the sun must be more rapid. And, as with the study of Colom *et al.*, we argue that the increase in gas productivity as a comet approaches the sun directly results in an increase in the expansion velocity of the coma.

Furthermore, our data provides evidence that the difference in pre- and post-perihelion gas production rates at a fixed heliocentric distance are sufficient to result in differences in the coma kinematics. Although the January and March 1986 observations of Comet Halley were both made at times when the comet was at a heliocentric distance of 1 A.U. we infer parent outflow velocities of  $1.02 \pm 0.10$   $\text{km s}^{-1}$  and  $1.60 \pm 0.07$   $\text{km s}^{-1}$ , respectively. Within a few days of these observations, Larson *et al.* (1986) made their observations of the water molecule in Comet Halley. From these observations they infer similar gas outflow velocities ( $0.9 \pm 0.2$   $\text{km s}^{-1}$  in late December 1985 and  $1.4 \pm 0.2$   $\text{km s}^{-1}$  in March 1986), while their derived gas production rates are

$10^{29}$  and  $10^{30}$  molecules  $\text{sec}^{-1}$ , respectively. Using these production rates in his model Combi (1989) is able to reproduce a pre-/post-perihelion velocity disparity of the size observed. The production rates deduced from our OH observations of January and March 1986 are  $(7\pm 3) \times 10^{29}$  and  $(1.2\pm 0.6) \times 10^{30}$  molecules  $\text{sec}^{-1}$  which are consistent with those derived from the water observations and used in the model of Combi. Therefore, the difference in the outflow velocities derived from the OH data is most likely an effect of the increased post-perihelion gas production rate.

We finally note that our assertion here that the gas production rate has a direct impact on the inferred outflow velocity is *not* weakened by the derived parent outflow velocities for the few comets observed at a heliocentric distance of  $1.3\pm 0.1$  A.U. (Tables 4.3 and 4.4) In Figure 4.12 we show the derived parent outflow velocity as a function of gas production rate for all the comets in this study. This plot illustrates that at all heliocentric distances the parent outflow is relatively insensitive to the gas production rates for low production rates.

To illustrate that this is indeed what one expects based on simple one-dimensional pure-gas thermodynamic models of the coma, we present in Figure 4.13 the results of our model calculations based on the work of Bockelée-Morvan and Crovisier (1987). For this figure we have run a grid of models covering  $\log Q_{\text{OH}}\text{-}R_h$  parameter space. For each model run we have defined the point in the coma where the gas decouples to be where the collisional

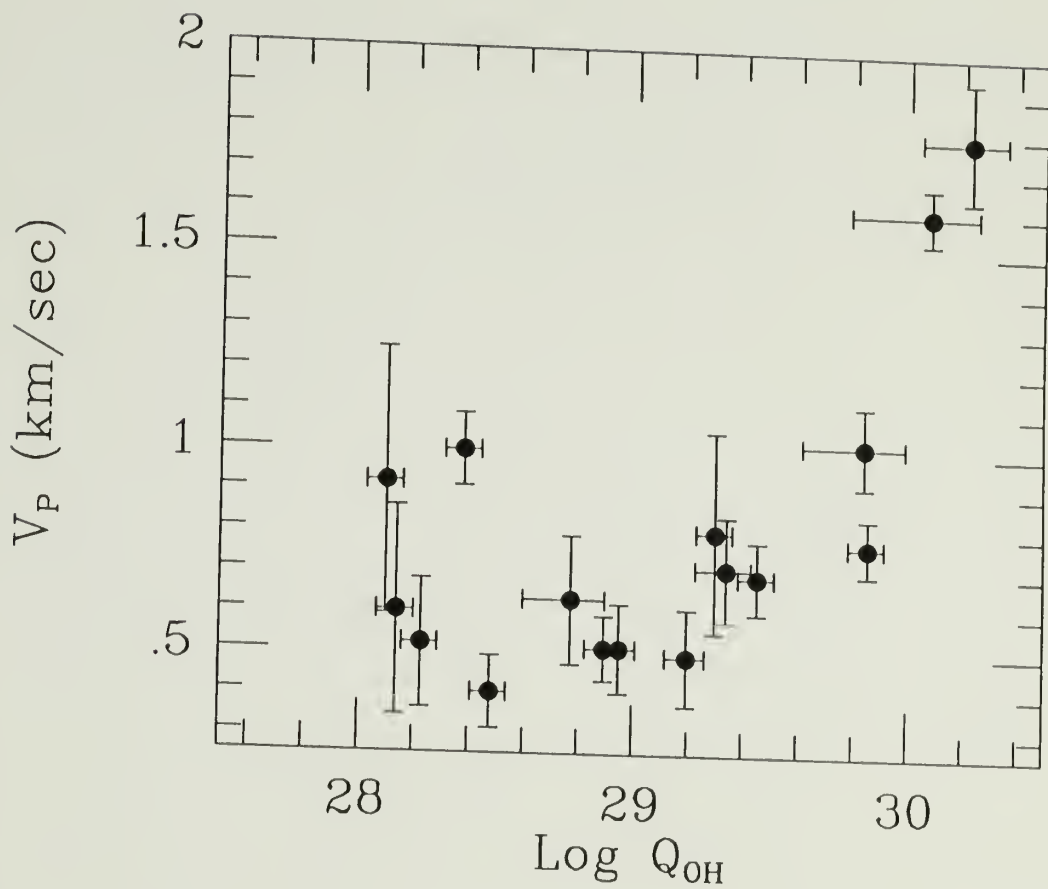
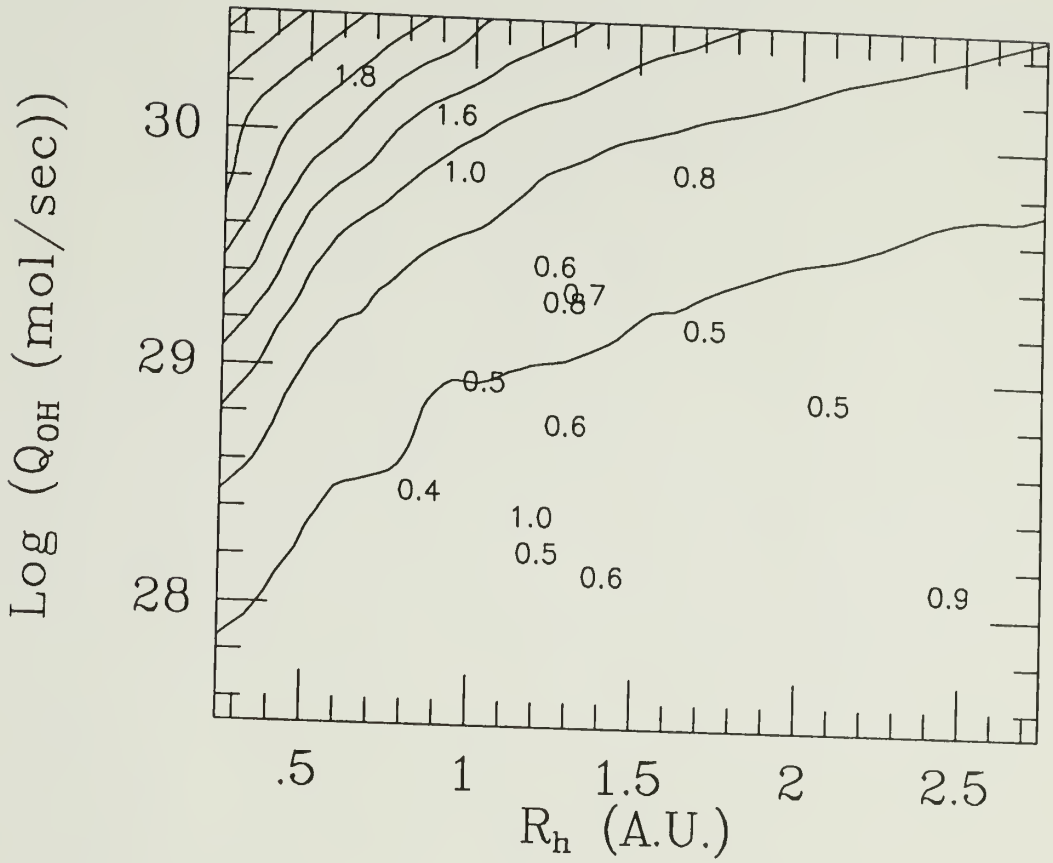


Figure 4.12: Adopted parent gas outflow velocity as a function of the log of the gas production rate.





**Figure 4.13:** Outflow velocity as a function of the log of the gas production rate and heliocentric distance. The numbers within the plot are our derived  $V_P$  values. The contours are in steps of  $0.2 \text{ km sec}^{-1}$  (increasing towards the upper left) and the minimum contour is at  $1.0 \text{ km sec}^{-1}$ .

mean free path equals the distance from the nucleus. The velocities at that point, which should correspond to our inferred  $V_P$  values, have been used to draw the contours in Figure 4.13. Our derived outflow velocities appear as numbers in the  $\log Q_{OH}-R_h$  plane. We see from this figure that such models predict an increase in the outflow velocity with both heliocentric distance and gas production rate. However, we note that our derived values for the outflow velocity typically fall below those predicted by the thermodynamic model. To test whether the introduction of dust into a model such as this results in gas outflow velocities which are more consistent with those we have derived from the data (see below), we have compared our results for Comet Halley to those of the dusty-gas-dynamic/Monte Carlo coma modeling of Combi (1989), shown in Figure 4.14. We see in this figure that the predicted gas outflow velocity agrees rather well with our derived values for small heliocentric distances (the discrepancy for the March epoch is likely due to differences in adopted gas production rates) but that at large heliocentric distances our derived outflow values lie systematically below the predicted values. This disparity remains a puzzling issue. One suggestion for its cause is that the simplification of such models to one-dimensional treatments may result in an overestimation of the parent gas outflow velocity. As mentioned above, the low inferred outflow velocities at larger heliocentric distances could also indicate that the average OH velocity given by the work of Crovisier (1988) is too large.

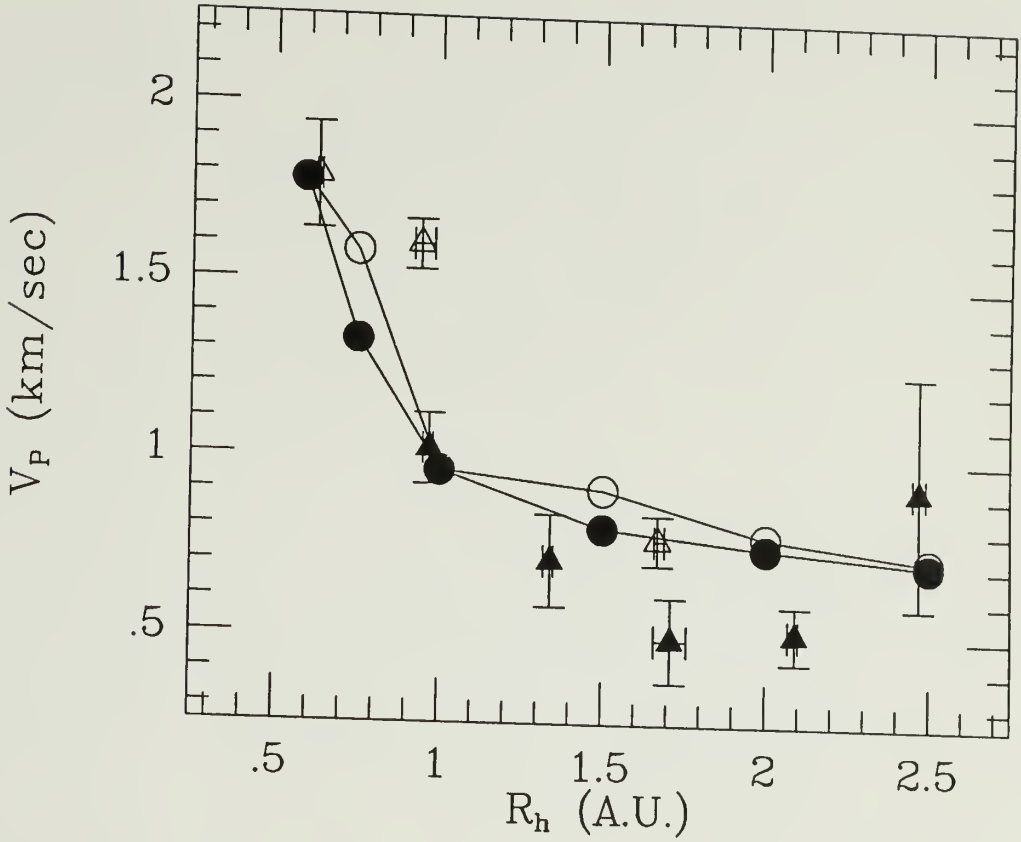


**Figure 4.14:** Comparison of derived parent gas outflow velocities with dusty-gas-dynamic/Monte Carlo modeling predictions. Circles represent the model results of Combi (1989), while the triangles show our Comet Halley results. Filled symbols are used for preperihelion values, while open symbols are used for postperihelion values.

We finally remark that there are large portions of the  $\log Q_{\text{OH}}\text{-}R_h$  plane for which we have no high resolution, high signal to noise data. To truly put models of the coma such as those of Bockelée-Morvan and Crovisier (1987) and Combi (1989) to the test we need a sample of spectra from comets of a wide range of gas productivities, at many heliocentric distances, especially low heliocentric distances. Until such a complete sample is available, however, we should be content with analyzing data from the low productivity comets at many heliocentric distances. Such comets are quite common and interesting kinematically. We have already mentioned P/Giacobini-Zinner as an example of such a comet. Another example from this thesis is Comet Hartley-Good. The interesting feature of this comet is its unusually narrow OH line for a comet at a heliocentric distance less than 1 A.U. (during the November 1985 epoch; Figures 2.1m and 2.3). In fact, this comet shows a narrowing of the line profile with decreasing heliocentric distance, and we have inferred a corresponding decrease in the parent gas outflow velocity. This phenomenon could possibly be explained if the dust-to-gas ratio in the coma increased during the November epoch. The net result of the introduction of large quantities of dust into a cometary coma is to mass load the outflowing gas thereby slowing it down (Combi 1989). We find no evidence in the literature, however, to indicate such an increase in the coma dust content for this comet and the exact cause for the decrease in outflow velocity remains uncertain.

## CHAPTER 5

### SUMMARY

Comet Halley has a unique place in history. Since the time of Halley himself the reappearance of this comet has been awaited with great anticipation. This latest apparition was no exception, as the International Halley Watch and the astronomical community as a whole poised at the ready to undertake an unprecedented observational campaign. The fruits of this labor have begun to appear. There have been several large and small conferences on the subject of cometary science or some facet of cometary science. In addition, an entire volume of *Astronomy and Astrophysics* has been devoted to the results from observational studies of Halley's Comet.

As part of this wave of exciting cometary studies, we have made a series of observations of the 18-cm lines of OH in Comets Halley, Giacobini-Zinner, Hartley-Good, Thiele, and Wilson. These are the highest sensitivity, highest spectral resolution cometary radio OH data ever taken and as such they have served as the impetus behind this project. These data also represent the observational backbone for this thesis.

We have calculated gas production rates from the OH spectra in this thesis. Since the parameters for Radio Model 1986a (Schloerb, Claussen, and Tacconi-Garman 1987) are closer to our chosen and derived parameters than those of the Festou vectorial model (Festou1981a, b)(see below) we have adopted Radio Model 1986a to correct our observed integrated intensities

for the effects of beam resolution and we encourage others to do the same. Furthermore, we have corrected the observed radio integrated intensities for the effects of quenching of the OH  $\Lambda$ -doublet (Schloerb 1988). This is the first time such a correction has been systematically applied to radio OH data. We find, as was suggested by Schloerb, that through this quenching correction the radio gas production rate estimates can be made to agree with those derived from UV observations of OH in comets, which do not suffer from the effects of quenching. Indeed, this illustrates that the long standing UV/radio gas production rate disparity has been explained at last. The problem which remains is to ascertain which inversion curve is most appropriate for any given heliocentric velocity. We have found one range of heliocentric velocity over which the inversion curve of Despois *et al.* (1981) is most appropriate (see below). However, at present uncertainties as to which inversion curve to adopt for most heliocentric velocities leads to large uncertainties in radio determinations of the gas production rate.

To model the observed spectra we have constructed a Monte Carlo model for the coma of a comet. This model, which is based on the fundamental work of Combi and Delsemme (1980a), is a ballistic vectorial simulation of a cometary coma which incorporates a wide variety of physical processes. For the best constrained input parameters we have adopted nominal values from the literature (Table 5.1). To describe the excitation of the OH  $\Lambda$ -doublet we have used both the inversion curve of Despois *et al.* (1981) and that of

Table 5.1		
Model Parameters		
Parameter	Value	Source
Parent (Water) Lifetime	$8.2 \times 10^4 R_n^2$ sec	Festou 1981b
OH Lifetime	$\sim 1 \times 10^5 R_n^2$ sec	van Dishoeck and Dalgarno 1984
OH Velocity Distribution		Crovisier 1988
OH inversion		Despois <i>et al.</i> 1981 Schleicher and A'Hearn 1988

Schleicher and A'Hearn (1988). We have then solved for the remaining coma kinematic parameters, the parent gas outflow velocity ( $V_P$ ) and the anisotropy of that flow (through the anisotropy parameter, AP).

For each combination of outflow velocity and outflow anisotropy parameter we have generated a spectrum. Each of these spectra are fit to the respective data through a "brute force" scaling and we define the quality of that fit in terms of the  $\chi^2_\nu$  statistic. The best kinematic parameter combination for any given epoch is that combination which produces the lowest value for  $\chi^2_\nu$ . We find from this analysis that, in general, our model results are insensitive to the particular inversion curve being used. In only a few cases does the model spectrum generated using one inversion curve fit the observed profile slightly better than the model spectrum resulting from the other inversion curve. The prime exception to the relative insensitivity of our model results to the choice of inversion curve is for the case of the May 1986 observations of Comet Halley. At the heliocentric velocity of the comet

at this epoch only the inversion curve of Despois *et al.* predicts the presence of an emission feature on the blue side of the main absorption feature, as is seen in the data from that epoch. Therefore, over heliocentric velocities from  $\sim 23$  to  $\sim 27 \text{ km s}^{-1}$  the inversion of OH in cometary comae is best characterized by that inversion curve.

The anisotropy in the coma gas outflow is independent of heliocentric distance, except perhaps for the case of Comet Giacobini-Zinner. In addition, we have inferred an average day-to-night anisotropy of 2:1 for the parent gas. This is in contrast to that found for the dust in the coma of Halley's Comet (Keller *et al.* 1986a, b; Edenhofer *et al.* 1987) but is consistent with the anisotropy derived from a wide variety of ground based and *in situ* observations (see references in Chapter 4). P/Giacobini-Zinner, on the other hand, shows anomalously anisotropic gas emission. This phenomenon could be explained in terms of an enhancement of gas productivity during the afternoon on the nucleus of this comet. Observations of this comet during future apparitions may help to confirm this explanation for the origin of this peculiar gas flow morphology.

Our derived outflow velocities are consistent with those inferred from a number of other indicators of the coma expansion (see references in Chapter 4). From this concurrence we infer that our choices for such model parameters as the parent and daughter lifetimes. The suggestion of unusually low outflow velocities at large heliocentric distances may indicate that the mean OH



velocity of Crovisier (1988) may be too high. We also see a rise in the outflow velocity for heliocentric distances smaller than about 1 A.U. It is this increase which is responsible for the broad 18-cm OH lines seen for comets near the sun. This rise in outflow velocity cannot be attributed strictly to the effect of heliocentric distance. Rather, the increased gas production rate normally associated with comets near the sun must result in a hotter coma which in turn leads to increased coma expansion velocities (Crovisier 1984; Bockelée-Morvan and Crovisier 1987; Combi 1989). A striking demonstration of this phenomenon is seen in the data from the January and March 1986 epoch for Comet Halley. At these times the comet was at a heliocentric distance of 1 A.U. but we infer gas outflow velocities of 1.02 and 1.60 km sec<sup>-1</sup> for these two epochs, respectively. Our estimated production rate difference is sufficient to account for this difference in outflow velocities (see Combi 1989 and references therein).

No signature of the dependence of the outflow velocity on the productivity of comets is seen in a sample of our data from comets near a heliocentric distance of 1.3 A.U. From this we conclude that at this heliocentric distance the gas production rate must be larger than  $3 \times 10^{29}$  molecules sec<sup>-1</sup> to influence the coma expansion. We also find that one-dimensional dynamic models of the coma (Bockelée-Morvan and Crovisier 1987, Combi 1989) cannot account for the low outflow velocities we derive from data from Comet Halley far from perihelion. In addition, a peculiar trend

is seen in the case of the relatively faint Comet Hartley-Good. The width of the observed 18-cm line for this comet actually decreases with decreasing heliocentric distance. We have derived a corresponding decrease in the parent gas expansion velocity. The cause for this decrease is unknown.

Finally, we would like to have more high quality cometary 18-cm OH data. This would allow us to fill in the  $\log Q_{\text{OH}}-R_h$  plane to really put coma gas dynamic models to the test. We would also be able to determine how common it is for coma outflow velocities to decrease with decreasing heliocentric distance and perhaps through coma modeling find an origin for this phenomenon. As mentioned above, because of its unusual gas outflow properties we would like to have observations of future apparitions of P/Giacobini-Zinner. Additional observations of a wide variety of comets will help to determine if this comet is alone in the kinematic behavior of its coma. In short, high spectral resolution, high sensitivity observations of the 18-cm lines of OH in comets have been and should continue to be very enlightening in the important study of the kinematics of cometary comae.

## BIBLIOGRAPHY

- Abell, G.O. 1982, *Exploration of the Universe (4th Edition)*. Saunders College Publishing, New York, p. 362.
- A'Hearn, M.F., Hoban, S., Birch, P.V., Bowers, C., Martin, R., Klinglesmith III, D.A. 1986, *Nature*, **324**, 649.
- Baars, J.W.M., Genzel, R., Pauliny-Toth, I.I.K., and Witzel, A. 1977, *Astr. Ap.*, **61**, 99.
- Bailey, M.E., Clube, S.V.M., and Napier, W.M. 1986, *Vistas in Astron.*, **29**, 53.
- Bevington, P.R. 1969, *Data Reduction and Error Analysis for the Physical Sciences*. McGraw-Hill Book Company, New York.
- Biermann, L. 1951, *Zs. Ap.*, **29**, 274.
- Biraud, F., Bourgois, G., Crovisier, J., Fillit, R., Gérard, E., and Kazès, I. 1974, *Astr. Ap.*, **34**, 163.
- Bockelée-Morvan, D. 1987, *Astr. Ap.*, **181**, 169.
- Bockelée-Morvan, D. and Crovisier, J. 1987, in "Symposium on the Diversity and Similarity of Comets", eds. Rolfe, E.J. and Battrick, B., Brussels, ESA SP-278, p. 235.
- Bockelée-Morvan, D., Crovisier, J., Despois, D., Forveille, T., Gérard, E., Schraml, J., and Thum, C. 1986, in "Proc. 20th ESLAB Symposium on the Exploration of Halley's Comet", eds. Battrick, B., Rolfe, E.J., and Reingard, R., Heidelberg, ESA SP-250, vol. I, p. 365.
- Bockelée-Morvan, D., Crovisier, J., Gérard, E., Henkel, C., Jewell, P.R., Snyder, L.E., Clemens, C.A., Molloy, A.R., and Schloerb, F.P. 1985, *A.J.*, **90**, 2586.
- Bockelée-Morvan, D. and Gérard, E. 1984, *Astr. Ap.*, **131**, 111.
- Cashwell, E.D. and Everett, C.J. 1959, *The Monte Carlo Method for Random Walk Problems*. Pergamon Press, New York.
- Clark, D.H. and Stephenson, F.R. 1977, *The Historical Supernovae*. Pergamon Press, New York, pp. 22, 40ff.

- Claussen, M.J. and Schloerb, F.P. 1987, in "Cometary Radio Astronomy", Proceedings of NRAO Workshop no. 17, eds. Irvine, W.M., Schloerb, F.P., and Tacconi-Garman, L.E., Green Bank, West Virginia, p. 135.
- Colom, P., Bockelée-Morvan, D., Bourgois, G., Crovisier, J., and Gérard, E. 1987, in "Symposium on the Diversity and Similarity of Comets", eds. Rolfe, E.J. and Battrick, B., Brussels, ESA SP-278, p. 241.
- Combi, M.R. 1980, *Ap.J.*, **241**, 830.
- \_\_\_\_\_ 1989, *Icarus*, submitted.
- Combi, M.R. and Delsemme, A.H. 1980a, *Ap.J.*, **237**, 633.
- \_\_\_\_\_ 1980b, *Ap.J.*, **237**, 641.
- Combi, M.R. and Smyth, W.H. 1988a, *Ap.J.*, **327**, 1026.
- \_\_\_\_\_ 1988b, *Ap.J.*, **327**, 1044.
- Crifo, J.F. 1986a, in "Proc. 20th ESLAB Symposium on the Exploration of Halley's Comet", eds. Battrick, B., Rolfe, E.J., and Reinhard, R., Heidelberg, ESA SP-250, vol. I, p. 533.
- \_\_\_\_\_ 1986b, in "Proceedings of the 15th International Symposium on Rarified Gas Dynamics", vol. II, p. 229.
- Crovisier, J. 1984, *Astr. Ap.*, **130**, 361.
- \_\_\_\_\_ 1987, in "Symposium on the Diversity and Similarity of Comets", eds. Rolfe, E.J. and Battrick, B., Brussels, ESA SP-278, p. 235.
- \_\_\_\_\_ 1988, *Astr. Ap.*, submitted.
- Curdt, W., Wilhelm, K., Craubner, A., Krahn, E., and Keller, H.U. 1988, *Astr. Ap.*, **191**, L1.
- Curtis, C.C., Fan, C.Y., Hsieh, K.C., Hunten, D.M., Ip, W.-H., Keppler, E., Richter, A.K., Umlauf, G., Afonin, V.V., Dyachkov, A.V., Erö, J., Jr., and Somogyi, A.J. 1986, in "20th ESLAB Symposium on the Exploration of Halley's Comet", eds. Battrick, B., Rolfe, E.J., and Reinhard, R., Heidelberg, ESA SP-250, vol. I, p. 391.

- Delsemme, A.H. 1982, *Comets*. University of Arizona Press, Tucson, Arizona, pp. 85-130.
- Delsemme, A.H. and Moreau, J.L. 1973, *Ap. Lett.*, **14**, 181.
- de Pater, I., Palmer, P., and Snyder, L. E. 1986, *Ap.J. (Letters)*, **304**, L33.
- Deslandres, M.H.A. 1909, *Comptes Rendus*, **148**, 809.
- Despois, D., Crovisier, J., Bockelée-Morvan, D., Schraml, J., Forveille, T., and Gérard, E. 1986, *Astr. Ap.*, **160**, L11.
- Despois, D., Gérard, E., Crovisier, J., and Kazès, I. 1981, *Astr. Ap.*, **99**, 320.
- Destombes, J.L., Marliere, C., Baudry, A., and Brillet, J. 1977, *Astr. Ap.*, **60**, 55.
- Dolginov, A.Z., Gnedin, Yu.N., and Novikov, G.G. 1971, *Planet. Space Sci.*, **19**, 143.
- Edenhofer, P. Bird, M.K., Brenkle, J.P., Buschert, H., Kursinski, E.R., Mottinger, N.A., Porsche, H., Stelzreid, C.T., and Volland, H. 1987, *Astr. Ap.*, **187**, 712.
- Elitzur, M. 1981, *Ap.J.*, **246**, 354.
- Feldman, P.D. 1982, *Comets*. University of Arizona Press, Tucson, Arizona, pp. 461-479.
- Feldman, P.D., Festou, M.C., A'Hearn, M.F., Arpigny, C., Butterworth, P.S., Cosmovici, C.B., Danks, A.C., Gilmozzi, R., Jackson, W.M., McFadden, L.A., Patriarchi, P., Schleicher, D.G., Tozzi, G.P., Wallis, M.K., Weaver, H.A., and Woods, T.N. 1986, in "Proc. 20th ESLAB Symposium on the Exploration of Halley's Comet", eds. Battrick, B., Rolfe, E.J., and Reinhard, R., Heidelberg, ESA SP-250, vol. I, p. 325.
- Festou, M.C. 1981a, *Astr. Ap.*, **95**, 69.
- 1981b, *Astr. Ap.*, **96**, 52.
- Fowler, A. 1910, *M.N.R.A.S.*, **70**, 37.
- Gérard, E. 1985, *Astr. Ap.*, **146**, 1.

- Gérard, E., Bockelée-Morvan, D., Bourgois, G., Colom, P., and Crovisier, J. 1987a, *Astr. Ap.*, **187**, 455.
- Gérard, E., Bockelée-Morvan, D., Bourgois, G., Colom, P., and Crovisier, J. 1987b, in "Cometary Radio Astronomy", Proceedings of NRAO Workshop no. 17, eds. Irvine, W.M., Schloerb, F.P., and Tacconi-Garman, L.E., Green Bank, West Virginia, p. 125.
- Greenstein, J.L. 1958, *Ap.J.*, **128**, 106.
- Harwit, M. 1981, *Cosmic Discovery*. Basic Books, Incorporated, New York, p. 73.
- Haser, L. 1957, *Bull. Acad. Roy. Soc. Belgique*, **43**, 740.
- 1966, *Mém. Soc. Roy. Sci. Liège*, **12**, series 5, 233.
- Herzberg, G.H. 1950, *Molecular Spectra and Molecular Structure. I. Spectra of Diatomic Molecules*. Van Nostrand, New York.
- Hsieh, K.C., Curtis, C.C., Fan, C.Y., Hunten, D.M., Ip, W.-H., Keppler, E., Erö, J., Jr., and Somogyi, A.J. 1987, *Astr. Ap.*, **187**, 375.
- Huebner, W.F. 1985, in "Molecular Astrophysics", Ed. G. H. F. Diercksen *et al.* D. Reidel, Dordrecht, p. 311.
- Huebner, W.F. and Carpenter, C.W. 1979, LASL Informal Report, LA-8085-MS.
- Irvine, W.M., Schloerb, F.P., and Gérard, E. 1983, in "Cometary Exploration. III.", ed. Gombosi, T.I., Budapest, pp. 83-93.
- Jackson, W.M. 1980, *Icarus*, **41**, 147.
- Keller, H.U., Arpigny, C., Barbieri, C., Bonnet, R.M., Cazes, S., Coradini, M., Cosmovici, C.B., Delamere, W.A., Heubner, W.F., Hughes, D.W., Jamar, C., Malaise, D., Reitsema, H.J., Schmidt, H.U., Schmidt, W.K.H., Seige, P., Whipple, F.L., and Wilhelm, K. 1986a, *Nature*, **321**, 320.
- Keller, H.U., Delamere, W.A., Huebner, W.F., Reitsema, H., Schmidt, H.U., Schmidt, W.K.H., Whipple, F.L., and Wilhelm, K. 1986b, in "20th ESLAB Symposium on the Exploration of Halley's Comet", eds. Battrick, B., Rolfe, E.J., and Reinhard, R., Heidelberg, ESA SP-250, vol. II, p. 359.

- Kitamura, Y. 1986, *Icarus*, **66**, 241.
- 1987, *Icarus*, **72**, 555.
- Krankowsky, D., Lämmerzahl, P., Herrwerth, I., Woweries, J., Eberhardt, P., Dolder, U., Herrmann, U., Schulte, W., Berthelier, J.J., Illiano, J.M., Hodges, R.R., and Hoffman, J.H. 1986, *Nature*, **321**, 326.
- Krasnopolsky, V.A., Gogoshev, M., Moreels, G., Moroz, V.I., Krysko, A.A., Gogosheva, Ts., Palazov, K., Sargoichev, S., Clairemidi, J., Vincent, M., Bertaux, J.L., Blamont, J.E., Troshin, V.S., and Valníček, B. 1986, *Nature*, **321**, 269.
- Krasnopolsky, V.A., Tkachuk, A.Yu., Moreels, G., and Gogoshev, M. 1987, in "Symposium on the Diversity and Similarity of Comets", eds. Rolfe, E.J. and Battrick, B., Brussels, ESA SP-278, p. 185.
- Lämmerzahl, P., Krankowsky, D., Hodges, R.R., Stubbemann, U., Woweries, J., Herrwerth, I., Barthelier, J.J., Illiano, J.M., Eberhardt, P., Dolder, U., Schulte, W., and Hoffman, J.H. 1986, in "Proc. 20th ESLAB Symposium on the Exploration of Halley's Comet", eds. Battrick, B., Rolfe, E.J., and Reinhard, R., Heidelberg, ESA SP-250, vol. I, p. 179.
- Larson, H.P., Davis, D.S., Mumma, M.J., and Weaver, H.A. 1986, *Ap.J. (Letters)*, **309**, L95.
- Larson, H.P., Mumma, M.J., and Weaver, H.A. 1987, *Astr. Ap.*, **187**, 391.
- Marconi, M.L. and Mendis, D.A. 1983, *Ap.J.*, **273**, 381.
- 1984, *Ap.J.*, **287**, 445.
- McKellar, A. 1942, *Rev. Mod. Phys.*, **14**, 179.
- 1943, *Ap.J.*, **98**, 1.
- Mies, F.H. 1974, *Ap.J. (Letters)*, **191**, L145.
- Mumma, M.J., Weaver, H.A., Larson, H.P., Davis, D.S., and Williams, M. 1986, *Science*, **232**, 1523.
- Newburn, R.L., Jr. 1983, in "Cometary Exploration. III.", ed. Gombosi, T.I., Budapest, pp. 19-32.

- Ney, E.P. 1982, *Comets*. University of Arizona Press, Tucson, Arizona, pp. 323-340.
- Öhman, Y. 1941, *Stockholm Obs. Ann.*, **13**, no. 11.
- Oort, J.H. 1950, *Bull. Astr. Inst. Neth.*, **11**, 91.
- Öpik, E.J. 1932, *Proc. Am. Acad. Arts and Sc.*, **67**, 169.
- Potter, A.E. and Del Duca, B. 1964, *Icarus*, **3**, 103.
- Press, W.H., Flannery, B.P., Teukolsky, S.A., and Vetterling, W.T. 1987, *Numerical Recipes*. Cambridge University Press, New York.
- Remizov, A.P., Verigin, M.I., Gringauz, K.I., Apáthy, I., Szemerey, I., Gombosi, T.I., and Richter, A.K. 1986, in "20th ESLAB Symposium on the Exploration of Halley's Comet", eds. Battrick, B., Rolfe, E.J., and Reinhard, R., Heidelberg, ESA SP-250, vol. I, p. 387.
- Sagdeev, R.Z., Blamont, J., Galeev, A.A., Moroz, V.I., Shapiro, V.D., Shevchenko, V.I., and Szegő, K. 1986a, *Nature*, **321**, 259.
- Sagdeev, R.Z., Szabó, F., Avanesov, G.A., Cruvellier, P., Szabó, L., Szegő, K., Abergel, A., Balazs, A., Barinov, I.V., Bertaux, J.-L., Blamont, J., Detaille, M., Demarelis, E., Dul'nev, G.N., Endröczy, G., Gardos, M., Kanyo, M., Kostenko, V.I., Krasikov, V.A., Nguyen-Trong, T., Nyitrai, Z., Reny, I., Ruzsnyak, P., Shamis, V.A., Smith, B., Sukhanov, K.G., Szabó, F., Szalai, S., Tarnopolsky, V.I., Toth, I., Tsukanova, G., Valníček, B.I., Varhalmi, L., Zaiko, Yu. K., Zatsepin, S.I., Ziman, Ya.L., Zsenei, M., and Zhukov, B.S. 1986b, *Nature*, **321**, 262.
- Schenewerk, M.S., Palmer, P., Snyder, L.E., and de Pater, I. 1986, *A.J.*, **92**, 166.
- Schleicher, D.G. 1983, *Ph.D. Thesis*, University of Maryland.
- Schleicher, D.G. and A'Hearn, M.F. 1982, *Ap.J.*, **258**, 864.
- \_\_\_\_\_ 1988, *Ap.J.*, **331**, 1058.
- Schloerb, F.P. 1988, *Ap.J.*, **332**, 524.



- Schloerb, F.P., Claussen, M.J., and Tacconi-Garman, L. 1986, in "Proceedings of the 20th ESLAB Symposium on the Exploration of Halley's Comet", eds. Battrick, B., Rolfe, E.J., and Reinhard, R., Heidelberg, ESA SP-250, vol. I, p. 583.
- Schloerb, F.P., Claussen, M.J., and Tacconi-Garman, L. 1987, *Astr. Ap.*, **187**, 469.
- Schloerb, F.P. and Gérard, E. 1985, *A.J.*, **90**, 1117.
- Schloerb, F.P., Kinzel, W.M., Swade, D.A., and Irvine, W.M. 1986a, *Ap.J. (Letters)*, **310**, L55.
- \_\_\_\_\_ 1986b, in "Proc. of the 20th ESLAB Symposium on the Exploration of Halley's Comet", eds. Battrick, B., Rolfe, E.J., and Reinhard, R., Heidelberg, ESA SP-250, vol. I, p. 577.
- Schloerb, F.P., Kinzel, W.M., Swade, D.A., and Irvine, W.M. 1987, *Astr. Ap.*, **187**, 475.
- Schlosser, W., Schultz, R., and Koczet, P. 1986, in "Proc. 20th ESLAB Symposium on the Exploration of Halley's Comet", eds. Battrick, B., Rolfe, E.J., and Reinhard, R., Heidelberg, ESA SP-250, vol. III, p. 495.
- Schwarzschild, K. and Kron, E. 1911, *Ap.J.*, **34**, 342.
- Shimizu, M. 1976, *Astrophys. Space Sci.*, **40**, 149.
- Snyder, L.E. 1985, *A.J.*, **91**, 163.
- Spinrad, H. 1987, *Ann. Rev. Astr. Ap.*, **25**, 231.
- Stief, L.J. 1966, *J. Chem. Phys.*, **44**, 277.
- Stief, L.J., De Carlo, V.J., and Mataloni, R.S. 1965, *J. Chem. Phys.*, **42**, 3113.
- Swings, P. 1943, *M.N.R.A.S.*, **103**, 86.
- Tacconi-Garman, L. and Schloerb, F.P. 1987a, *B.A.A.S.*, **18**, 1019.

- Tacconi-Garman, L. and Schloerb, F.P. 1987b, in "Cometary Radio Astronomy", Proceedings of NRAO Workshop no. 17, eds. Irvine, W.M., Schloerb, F.P., and Tacconi-Garman, L.E., Green Bank, West Virginia, p. 143.
- Thekackara, M.P. 1970, *J. Environmental Science*, **13**, 6.
- van Dishoeck, E.F. and Dalgarno, A. 1984, *Icarus*, **59**, 305.
- van Woerkom, A.J.J. 1948, *Bull. Astr. Inst. Neth.*, **10**, 445.
- Watanabe, K., Zelikoff, M., and Inn, E.C.Y. 1953, *A.F.C.R.L. Technical Report*, **52**, 23.
- Whipple, F.L. 1950, *Ap.J.*, **111**, 375.
- \_\_\_\_\_ 1951, *Ap.J.*, **113**, 464.
- \_\_\_\_\_ 1955, *Ap.J.*, **121**, 750.
- \_\_\_\_\_ 1976, *Nature*, **263**, 15.
- \_\_\_\_\_ 1980, *A.J.*, **85**, 305.
- Widing, K.G., Purcell, S.D., and Sandlin, G.D. 1970, *Solar Phys.*, **12**, 52.
- Wurm, K. 1934a, *Zs. Ap.*, **8**, 218.
- \_\_\_\_\_ 1934b, *Zs. Ap.*, **9**, 62.
- Zanstra, H. 1928, *M.N.R.A.S.*, **89**, 178.

